BREAST CANCER SURGICAL NAVIGATION:
AN IMAGE GUIDANCE SYSTEM LEVERAGING COMPUTER VISION

By

Winona L. Richey

Dissertation

Submitted to the Faculty of the

Graduate School of Vanderbilt University

in partial fulfillment of the requirements

for the degree of

DOCTOR OF PHILOSOPHY

in

Biomedical Engineering

May 31, 2022

Nashville, Tennessee

Approved:

Michael I. Miga, Ph.D.

Ingrid M. Meszoely, M.D.

Ipek Oguz, Ph.D.

Brett C. Byram, Ph.D.

Yunkai K. Tao, Ph.D.

Richard Alan Peters, Ph.D.

ACKNOWLEDGMENTS

The work in this thesis would not have been possible without the unending support from mentors, colleagues, friends, and family. I have been incredibly fortunate to be surrounded by sharp and gracious people willing to ride the research roller coaster with me, cheering me on at the peaks, and pushing me along at the valleys.

I would first like to thank all the members of my committee for their mentorship and insights over the years; Dr. Miga, Dr. Meszoely, Dr. Oguz, Dr. Tao, Dr. Byram and Dr. Peters. I am particularly grateful to Dr. Meszoely for showing me the realities of breast cancer care in the clinic and in the operating room. She facilitated many important opportunities for observation and her continued input was critical for development of the guidance system presented here. Most of all, I would like to thank my thesis advisor, Dr. Miga, who has an incredible ability to strike the perfect balance between support and freedom for each of his students. His constant readiness for scientific discussion and debate has improved my work and made me a more thoughtful and thorough scientist. He imparts to his trainees the importance of clinical experience to inform engineering solutions, and his dedication to improved training benefits his students and the patients they go on to help.

I am also immensely grateful to have shared my time in graduate school with such brilliantly talented colleagues who have become some of my most treasured friends. Jon Heiselman has provided generous guidance. His intellect and scientific creativity pull all around him towards new heights. Ma Luo has been an unwavering beacon of light throughout graduate school. His kindness and grit combine to make him one of the most valuable members of any team lucky enough to have him. Saramati Narasimhan has continuously lifted me up, serving as an invaluable source of motivation and helping build and strengthen the community wherever she goes. Morgan Ringel has inspired and challenged me. She is astonishingly efficient and her hard work will continue to propel this project into the future.

I'd also like to thank the current and former members of the Biomedical Modeling Laboratory: Dr. Rebekah Griesenauer, Dr. Jarrod Collins, Dr. Xiaochen Yang, Alice Ding, Shannon Taylor, Frankangel Servin, Kush Hari, Bowen Xiang, and Dr. Kyvia Pereira. Thank you for laying the groundwork for this thesis, and thank you for making Stevenson a wonderful place to spend my days and nights. Additionally, I would like to thank all the colleagues and friends who have offered their ideas and their company throughout my journey. I also owe a special thanks to the volunteers who participated in these studies and made this work possible.

Lastly, I would like to thank my family. My parents have given me everything; thank you for saying—and believing—that I can do anything I set my mind to. My brother, Alex, has always had confidence in my ability to make a dent in science, even when I didn't, and my extended family—by blood and by love—has been rooting for me through it all.

To Matt, who has strengthened me each step of the way: I'm so lucky to have you on my team.

TABLE OF CONTENTS

LIST OF TABLES

LIST OF FIGURES

CHAPTER 1

Introduction

1.1 Specific Aims

Breast cancer is the most common cancer in American women and the second most deadly [1]. About 70 - 80% of breast cancer patients are eligible for breast conserving therapy, or breast conserving surgery (BCS) (removal of the lesion with a margin of healthy tissue) followed by radiation [2, 3]. This procedure has shorter surgical times, shorter post-operative hospital stays, and improved cosmetic outcomes, as the breast usually retains its original shape, and symmetry with the contralateral breast is maintained. In eligible patients, breast conserving therapy has equivalent survival outcomes to mastectomy (removal of breast tissue, nipple, areola, and skin) [4–7], or even improved survival [8–11]. However, these outcomes are dependent on complete excision, or negative margins. High reoperation rates set breast cancer apart from other common general surgeries with an observed versus expected morbidity (O/E) ratio nearly three times higher than that of other general surgeries [12]. In the last few years, BCS reoperation rates have been reported around 5-30% [13–16]. These high and variable rates of positive margins in breast cancer surgeries have been referred to as "the other breast cancer epidemic" [17].

Current approaches to reduce these high reoperation rates focus on intraoperative margin assessment and lesion localization. Intraoperative margin assessment techniques evaluate the border of an excised specimen so that more tissue can be excised in regions that correspond to a positive margin, or residual cancer. Unfortunately, difficulty orienting the excised mass can lead to increased resection volumes and the need for repeat surgeries. Ideally, margins would be managed before cuts are made and before the tissue loses its in-situ shape. Lesion localization works towards this but is confounded by the dynamic movements of breast tissue and the stark differences in patient positioning between preoperative imaging and surgery. Most localization methods focus on identifying the center of a lesion using an implanted marker, or seed. These systems guide towards the intraoperative location of the seed, but can not indicate the lesion border. Using preoperative images as a reference, surgeons rely on spatial reasoning to understand the location of the seed with respect to the lesion boundaries, even though the shape of the tumor is likely distorted by imaging-to-surgery deformations [18, 19]. Understanding lesion position and extent is critically important to obtaining negative margins. When tumor boundaries can be visualized with intraoperative ultrasound (IOUS), positive margin rates are relatively low at 0-14% [20–25]. However, only 50% of non-palpable tumors are visible on ultrasound (US) [26], and US underestimates size in over 40% of those tumors [23, 27]. Excising the lesion with a margin

of healthy tissue helps compensate for border estimation inaccuracies, but reoperation rates for BCS remain high. There remains a need for a lesion localization method that provides accurate lesion position and extent.

In this thesis, an intraoperative guidance system is proposed to offer improved understanding of tumor margins. A data collection system pairing stereo cameras, an optical tracker, and tracked ultrasound is proposed for breast data acquisition and visualization. This intraoperative data acquisition framework is incorporated into an image guidance software platform along with high sensitivity preoperative supine MR images that most closely represent surgical positioning. A nonrigid patient-specific biomechanical model utilizing the linearized iterative boundary reconstruction method [28] and automatic skin fiducial tracking set this work apart from previous intraoperative breast guidance. We hypothesize that high-sensitivity MR imaging coupled with computer vision technology and patient specific biomechanical models can be utilized to provide lesion position and extent before and during BCS. Towards this end, this thesis aims to improve localization accuracy in breast tissue by addressing the following specific aims:

Aim 1: **Characterize supine breast deformations between preoperative imaging and surgical presentation**. The proposed guidance system is used to characterize supine breast deformation *in vivo* for ten breasts across six healthy volunteers. Breast deformations are examined in the context of simple arm motion and image-to-surgery repositioning.

Aim 2: **Correct for image-to-surgery breast deformations with a sparse-data-driven model-based framework.** An existing iterative model-based correction strategy [28] is extended to deform preoperative supine breast MR images to fit intraoperative data. Novel boundary condition reconstruction is tailored to reflect anatomical support regions of the breast. Registration accuracy is evaluated at surface and subsurface features across seven healthy volunteers and one breast cancer patient.

Aim 3: **Monitor soft tissue deformations with computer vision tracking of skin fiducials.** To provide intraoperative sparse-data measurements of the breast surface, stereo cameras are used to measure precise ink-based skin fiducials throughout arm motion in the supine position for eight breasts across six healthy volunteers. Fiducial localization accuracy is compared to tracked stylus designated points. Data extent and tracking fidelity are quantified.

1.2 Clinical Significance

In the United States, one in eight women will be diagnosed with breast cancer in their lifetime, and an estimated 290,560 people will be diagnosed with breast cancer in 2022 [1]. It is the leading cause of cancer death in women worldwide, falling second only to lung cancer in the US [1, 29]. In the last several decades, there has been a shift from more extensive surgeries, such as radical and total mastectomy, towards less extensive surgeries, such as breast conserving therapy, with no change in outcomes [4–7]. Breast conserving

therapy, or BCS coupled with post-operative radiation, has been shown to have a significantly decreased rate of recurrent cancer in the ipsilateral breast when compared with mastectomy and BCS without radiation [4]. More recent studies suggest that, in addition to improved cosmesis, breast conserving therapy may actually have better survival outcomes, with lower rates of complications and disease specific mortality [8–11, 30, 31]. However, these equivalent or superior outcomes associated with breast conserving therapy are dependent on complete excision, or negative margins. Resecting the entire lesion in a single pass surgery is critical, as reoperations are associated with a two to eight fold increase in local recurrence [32]. Unfortunately, positive margin rates in BCS are high, around 5-30% in the last few years [33–37], with the most averages around 10-20% [13–16].

Current approaches to reduce reoperation rates focus mainly on two areas: margin assessment and lesion localization. During surgery, margin assessment techniques evaluate the removed tissue after excision to determine if the margins are positive (requiring re-excision) or negative (indicating successful surgery). If margins are determined to be positive, re-excision is performed, removing further tissue from the region associated with the specimen's positive margin. However, margin assessment suffers from a loss of spatial orientation upon excision. Breast tissue is highly deformable and once it is cut, it recoils, changing shape and moving away from its original position. As soon as the tissue is cut, exact correspondence is lost between the excised mass and the remaining tissue. After it is removed, the specimen usually compresses significantly, and distinct boundaries are lost. The dramatic shape changes and the irregular shape of the mass result in difficulty re-excising the correct location during the first surgery. These difficulties lead to an increase in volume of resected tissue, and/or a need for reoperation.

Lesion localization aims to intraoperatively guide surgeons, however this remains challenging. During surgery, geometric and spatial cues are lost as BCS involves few landmarks, highly deformable tissue, and extreme movements. Recent localization methods are mainly seed-based. Seed-based methods generally implant a marker into the lesion under cross-sectional image guidance. These seeds can then be localized during surgery, giving audio and visual feedback on the magnitude of the distance between the handheld probe and the implanted marker. Seeds are generally considered accurately placed if they are within 10 mm of the lesion centroid. The distance from the probe to the seed allows surgeons to approximate the lesion position. However, to estimate the lesion borders during surgery, the surgeon must rely on spatial reasoning and preoperative images of the breast where the breast is in a different orientation. When tumor boundaries are visible during surgery, such as with IOUS, outcomes are improved [38–40], though only 50% of non-palpable tumors are visible on US [26]. The promising results of intraoperative US show the benefits of tumor extent information during surgery, but many patients have non-echogenic tumors and cannot benefit from this technique.

Tumor displacements between prone and supine breast positions are reported between 18–68 mm [18, 19, 41–43]. Due to this large change, we propose a single supine preoperative MR to initialize our model, and provide additional information to surgeons. For a supine MR, the patient is lying face up, just as in surgery, and no deformation is applied. Of the three imaging modalities used for breast lesions (mammography, ultrasound, and MR), each method over-estimates lesion size in some patients, and underestimates size in others [23, 27]. Though more expensive than mammography or ultrasound, MR offers a three-dimensional representation of the breast and is generally considered the most accurate imaging modality for breast cancer, offering high sensitivity [27, 41, 44, 45]. Furthermore, rising evidence shows that supine preoperative imaging better estimates breast geometry and tumor size than prone MRI [19, 42, 46, 47]. It is important to note here that while supine MR images are taken with patient in a similar position to surgical presentation, the arm cannot be outstretched in the surgical position during imaging in a closed bore MR scanner. Finite element models to predict the large changes in breast position from standing to supine often require estimating a stress-free geometry [48, 49]. Because the induced deformation is more limited here, depending mainly on rotations of the operating room table and the change in arm position, the supine MR can be used to directly produce the initial mesh, and breast displacements can be sparsely measured intraoperatively. From these measured displacements, an inverse modeling approach can be employed to solve for the true displacement field. This displacement field can be applied to the preoperative mesh to produce volumetric images of the deformed, intraoperative state. In related work, Barth *et al.* used 6–8 surface fiducials to rigidly register a preoperative supine MR image to the intraoperative three dimensional (3D) breast surface [50]. Their optically tracked surface fiducials can only be used for surgical planning and must be removed for surgery. Using supine MR to guiding surgery resulted in a reoperation rate of 12% with this rigid registration framework. This thesis presents a novel expansion on this, incorporating nonrigid inverse modeling to accurately capture the deformations between supine MR and intraoperative positioning. Additionally, with the use of stereo cameras and 26 drawn fiducials, the surface of the breast can be obtained intraoperatively throughout surgery.

With respect to inclusion of subsurface data, it is intuitive that subsurface data would improve model prediction accuracy, and this path has been pursued for decades. For diagnostic and screening purposes, subsurface features have been used to improve registration between breast images of different modalities [51, 52]. Herein, subsurface information around the target lesion is used to improve prediction accuracy over purely boundary-data based methods. This work evaluates the impact of subsurface features on nonrigid registration.

Stereo cameras are well suited for intraoperative surface monitoring as data collection can be automated and integrate into existing surgical workflows. Stereo cameras provide fast and rich surface measurements, with high pixel density and color information. This thesis demonstrates that stereo cameras work well with

ink-based skin fiducials that are hand-drawn directly onto the breast surface. These inked skin fiducials can be easily sterilized and remain on the patient for the duration of procedure (compared to optically tracked fiducials that can be used for an initial alignment, but must be removed at the start of surgery).

This work is a novel contribution to image-guided breast surgery for: (1) use of stereo-camera and computer vision strategies for near-real-time automatic skin surface acquisition, (2) rapid inverse model-based registration of supine MR to intraoperative presentation, and (3) comprehensive evaluation of model-based correction across over 150 clinically relevant regions of interest. Here we propose a customized, automated approach for lesion localization in BCS. Use of stereo cameras in breast surgery is novel and practical for obtaining the surface quickly. This methodology extends guidance past initial surgical planning, and into the operating theater during surgery. This work aims to shift the paradigm of breast cancer treatment and reduce the reoperation rates, demonstrating the success of automated accurate image guidance that is easily integrated into operating rooms.

CHAPTER 2

Background

This chapter provides an overview of breast anatomy, a review of breast cancer imaging, and the surgical options for breast cancer patients. The summary of breast cancer discusses difficulties contributing to high reoperation rates and current strategies for reducing the rates of positive margins. Next, this chapter provides a review of intraoperative lesion localization approaches with a quantitative comparison of existing methods. Finally, this section introduces previous biomechanical breast modeling approaches and intraoperative measurement techniques in the context of image-guided approaches.

2.1 Breast Anatomy

The female breast is comprised of adipose and glandular tissues (Figure 2.1). Adipose tissue is fatty tissue, while glandular tissue is comprised of the lobes that create milk and the ducts that carry milk to the nipple. The nipple lies on the skin surface and is surrounded by the areola. The lymphatic system helps to maintain fluid balance and filter waste materials, with a large role in immune defense. Most lymphatic fluid from the breast drains towards axillalary lymph nodes [53]. These lymph nodes are primary sites for initial breast cancer metastasis, and are often biopsied after a cancer diagnosis.

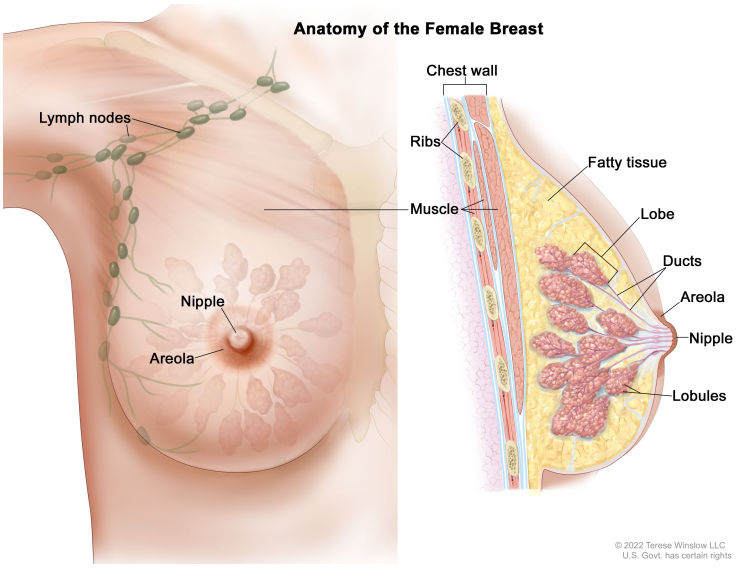

Figure 2.1: Breast anatomy reprinted from [54] with permission.

Also within the breast tissue are Cooper's ligaments that provide shape and support. Cooper's ligaments are fibrous connective tissue distributed throughout the breast, generally anchored at the underlying chest

muscles or clavicle, traversing throughout the breast tissue, and attaching to the skin. The sternum lies on the mid-sagittal line between the two breasts, forming the center front of the rib cage. Between the rib cage and breast tissue (anterior to the ribs, posterior to the breast tissue) lie the pectoralis major and minor muscles. In this text, the "chest wall" refers to the boundary between the breast tissue and the underlying structures: the pectoralis muscles, rib cage and intercostal muscles. The pectoralis muscles stabilize the shoulder and are responsible for adduction of the arm, or bringing the arm closer to the body along the same plane as the torso. Abduction, the opposite of adduction, describes the movement of the arm away from the body. Abduction and adduction are illustrated in Figure 2.2. Each breast is divided into four quadrants. These quadrants and relevant anatomical directions are shown in Figure 2.3.

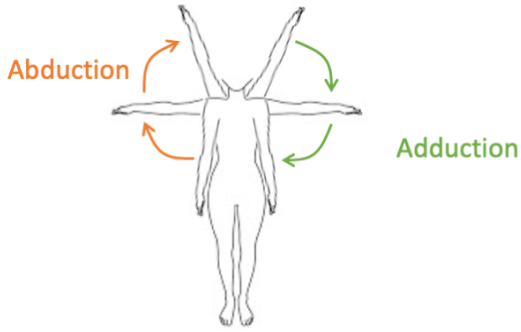

Figure 2.2: Abduction and adduction of the arm.

2.2 Breast Cancer

2.2.1 Diagnostic Breast Imaging

The three main modalities for breast imaging are: mammography, ultrasound and magnetic resonance (MR). For mammography, a patient is standing with the breast compressed between two plates. Breast tomosynthesis, a newer imaging technique that expands upon conventional mammography, combines many 2D images to provide a 3D rendering of the anatomy, though these images are still taken with the patient standing and the breast compressed. During diagnostic MR imaging, the patient is typically lying prone with both arms at her sides and the breast pendant in a cylindrical coil. Finally, for ultrasound imaging, a patient is lying supine with her arm above her head, and the tissue is compressed with pressure applied to the transducer. None of these configurations is representative of the surgical presentation: lying supine with the arms outstretched in a T shape. These positional differences between imaging and surgery are visualized in Figure 2.4.

2.2.2 Image-to-Surgery Breast Deformations

One factor that can confound localization in BCS is the large deformations between preoperative imaging and surgical presentation. It can be very difficult to understand the relationship between the tumor location

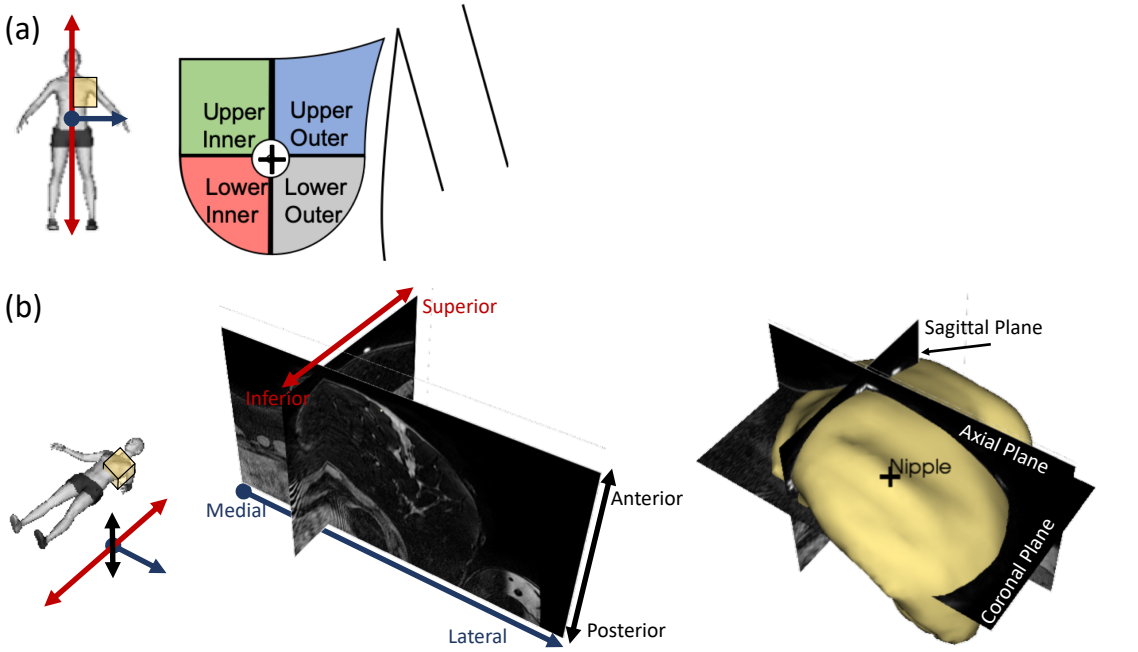

Figure 2.3: Anatomical directions shown at left with superior/inferior axis in red, medial/lateral axis in blue, and anterior/superior axis in black. Nipple is marked +. Locations of the right images are marked on the corresponding human figure in yellow. (a) Quadrants of the breast. (b) Supine breast MR image with anatomical directions marked (center) and body, or image, planes with the breast volume segmented in yellow (right).

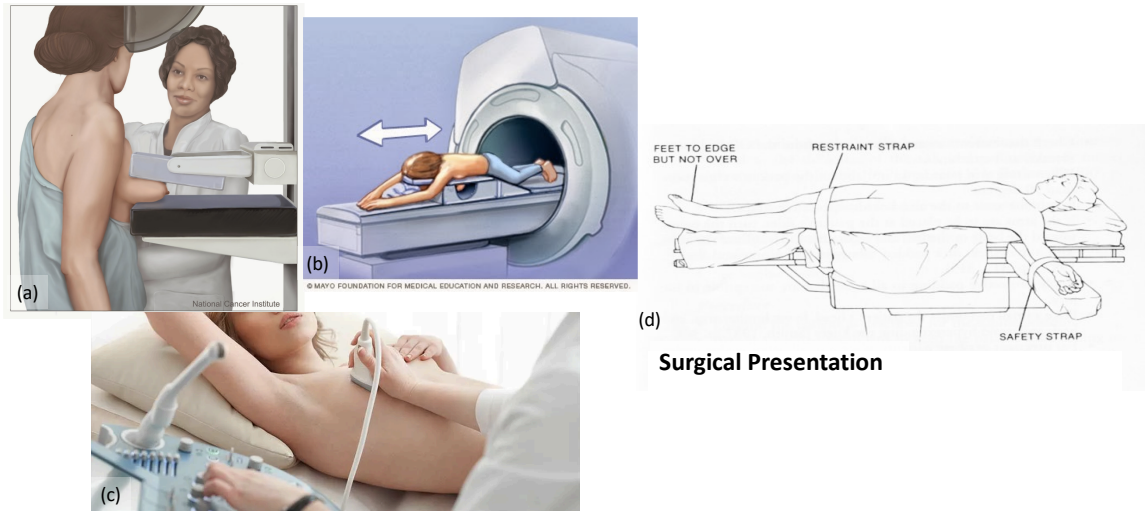

Figure 2.4: Breast imaging positions compared to the surgical position. (a) mammography reprinted from [55] (b) prone MR imaging reprinted from [56] (c) ultrasound reprinted from [57] and (d) surgical position reprinted from [58].

in a diagnostic image and the tumor location during surgery. Large displacements occur between imaging and surgery for breast cancer. Breast deformation has been characterized in a number of ways, with a focus on displacement between prone imaging and the surgical presentation – supine with the arm abducted to 90°. Tumor displacements from prone to supine MR have been reported between 18-68 mm [18, 41–43]. An example is shown in Figure 2.5. The nature of these displacements has been characterized with respect to breast features, and tumor positions were shown to vary with respect to all available landmarks: the nipple, chest wall, as well as superior, inferior, medial and lateral planes [18, 19, 43]. Tumors were also shown to vary with regards to sphericity and volume [18, 19]. Breast deformation has also been characterized from standing upright to lying supine [59], showing that the breast surface moves significantly with respect to musculoskeletal structures and other fixed points. Stretch was measured to be larger near the axilla, and for larger breast volumes. Though these breast deformations are all shown to be large, and supine positioning is more representative of surgical positioning, no previous studies have quantified deformations from supine imaging to surgical position.

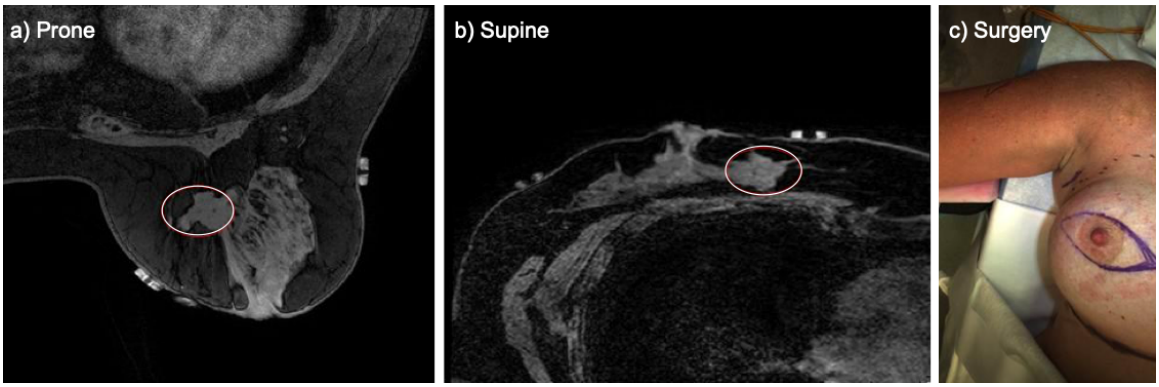

Figure 2.5: Deformation of a single patient's breast from (a) prone MR image of breast (b) supine MR image of breast and (c) surgical presentation. Tumor location is delineated with a circle in the MR images. Image reproduced from [60] with permission.

2.2.3 Supine Magnetic Resonance Imaging

Diagnostic MR imaging is performed in the prone position, with the patient's breast pendant within a breast coil as shown in Figure 2.4b. As discussed above, this position is starkly different from the supine surgical position, and the breast undergoes large displacements between these two positions. Breast MR imaging can also be performed in the supine position, where the patient orientation is much more representative of the surgical positioning. This section discusses supine breast MR imaging with regards to: feasibility, image quality, and lesion localization. The utility during surgery is discussed later on in this chapter in Section 2.3.3.7.

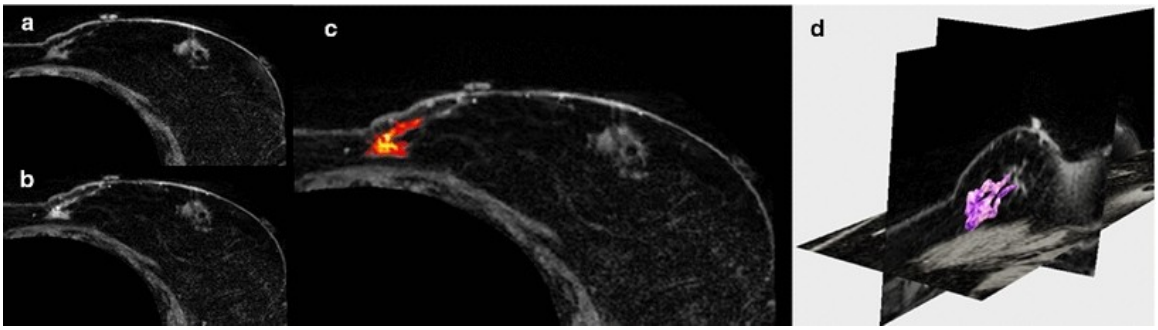

Figure 2.6: Axial slices of supine MRI of patient volunteer with a precontrast, b post-contrast injection,c contrast-enhanced tumor, and d 3D segmentation of tumor (magenta). Image reprinted from [60] with permission.

MR imaging is particularly useful in visualizing breast cancer. Overall, MR imaging is the most sensitive imaging modality for breast cancer, meaning that the majority of cancers can be seen on MR images, especially when performed with dynamic contrast enhancement [45, 61] as shown in Figure 2.6. For dynamic contrast enhanced MR imaging, images are acquired before and after a gadolinium contrast agent is inserted intravenously. As breast cancers grow, new blood vessels are created to provide sufficient nutrients. A lesion's vascular environment, indicative of malignancy, can be characterized by evaluating the kinetic behavior of contrast accumulation.

Alderliesten *et al.* [62] noted that supine MR was minimally impacted by cardiac and respiratory motions, stating "although several techniques currently exist to reduce the impact of periodic patient motion such as from breathing, the image quality of the supine breast scans in all subjects were found to be sufficient to allow image navigation without need for additional measures." Beyond the image quality sufficient for guidance observed by [62], [47] and [63] found that supine MRI provided image quality comparable to diagnostic breast MRI. However, breath-hold supine breast MRI was also found to be feasible using commercially available coils and sequences [46].

Supine MR images have been widely demonstrated to be more representative of tumors in the surgical position. Displacements between conventional diagnostic prone MR imaging and surgical position are large and well documented [42, 43]. Beyond simple positional changes, between prone and supine positioning, breast tumors have been shown to also change in volume, shape, and relationship to available landmarks (chest wall, nipple, skin) [18, 19, 47]. Relatedly, [46] found supine MRI useful in the precise preoperative localization of breast lesions, due to its ability to accurately predict size and area of lesions. Information gained from a supine MR can also be used to generate 3D tumor models to more accurately represent true tumor shapes [64].

2.2.4 Surgical Options

Surgical excision is the standard of care for the majority of breast cancer cases. When diagnosed with breast cancer, most patients are offered the choice between mastectomy and breast conserving therapy. Mastectomy is the surgical removal of the breast tissue, the nipple, areola and the surrounding skin. Breast conserving therapy is the removal of the lesion with a margin of healthy tissue surrounding the lesion followed by radiation. The surgical component of breast conserving therapy is called lumpectomy, or breast conserving surgery (BCS). Mastectomy is the only option for patients with locally widespread disease, multicentricity, diffuse (malignant) microcalcifications, I or II trimester of pregnancy, mutated BRCA genes, or previously irradiated chest wall [65]. Tumors larger than 20 mm are also generally recommended for mastectomy [66].

About 60-80% of breast cancer patients are eligible for breast conserving therapy [2, 3]. Given negative margins, or complete lesion excision, breast conserving therapy offers shorter surgical times, shorter post-operative hospital stays, and improved cosmetic outcomes, as the breast usually retains its original shape and symmetry with the contralateral breast. In eligible patients, breast conserving therapy has equivalent survival outcomes to mastectomy [4–7]. Breast conserving therapy has even been shown to have significantly decreased rates of recurrent cancer in the ipsilateral breast when compared with mastectomy and lumpectomy without radiation [4]. More recent studies suggest that, in addition to improved cosmesis, breast conserving therapy may actually have better survival outcomes, with lower rates of complications and disease specific mortality [8–11, 30, 31]. However, these equivalent or superior outcomes associated with BCT are dependent on complete excision, or negative margins. Resecting the entire lesion in a single pass surgery is critical, as reoperations are associated with a two to eight fold increase in local recurrence [32]. Unfortunately, positive margin rates in BCS remain high, with most averages in the last few years reported around 10-20% [14–16].

2.3 Reducing Positive Margin Rates

In an attempt to reduce re-excision rates, surgical guidelines were updated in 2014. While this has made a great impact on BCS re-excision rates, the underlying difficulties of breast tumor excision have remained relatively unchanged. Current approaches to reduce reoperation rates focus mainly on two areas: margin assessment and lesion localization. Margin assessment, or analysis of the excised volumes during surgery, is difficult due to the loss of precise spatial orientation after excision. After excision, specimens do not maintain their original in vivo structure or shape, and matching positive specimen margin locations to the corresponding cavity locations can be difficult. An ideal excision achieves negative margins on the first pass. This necessitates accurate lesion localization before and during surgery. Lesion localization techniques aim to guide the surgeon to and around a breast lesion. Due to the soft tissue properties of the breast and the imaging modalities used to take diagnostic images, major displacements occur between preoperative images

and intraoperative tumor locations. The breast is virtually featureless and the features that are present, such as the nipple and chest wall are not constant distances from the tumor, further confounding the intraoperative tumor position. This section covers the recent developments aimed at reducing re-excision rates in BCS.

2.3.1 Surgical Margins in Breast Conserving Surgery (BCS)

Prior to 2014, there was no consensus on acceptable surgical margins for BCS. Each center could decide the margins necessary to deem a tumor completely resected (with negative margins). In 2010, Houssami *et. al.* reported that increasing margin distance was weakly associated with decreased local recurrence, but the significance of this effect was eliminated with the addition of radiation [67]. In 2014 "no ink on tumor", or 0 mm margins, began to be endorsed by the Society of Surgical Oncology, the American Society for Radiation Oncology (ASTRO), National Comprehensive Cancer Network (NCCN) and the American Society of Breast Surgeons [68]. In 2016, 2 mm margins were shown to be necessary for ductal carcinoma in situ and the consensus guideline shifted, while remaining unchanged (no ink on tumor, 0mm) for invasive breast carcinoma [69]. This guideline was then also echoed by the European Society for Medical Oncology (ESMO) [66].

As expected, recent reports show an overall decrease in re-excision rates [15, 69–71], and some specify a direct reduction in re-excision due to close margins [71]. Similarly, though less intuitively, the reduction in re-excision rates varies widely across institutions ranging from 4-30% [72, 73]. One retrospective application of this guideline showed the decrease in re-excision rates was not significant [33] and another reported that while this guideline would halve their reoperation rates, it would leave patients with residual tumor [74], though neither of these studies could retrospectively account for radiation's affect on residual disease. It is important to note that breast conserving therapy couples surgery with radiation, and the addition of radiation may have been sufficient to clear this residual disease. This could not be investigated retrospectively in [74], and prospective reports show no compromise of oncological outcomes under the new guideline [70]. This guideline change has decreased re-excision rates, saving many patients from unnecessary reoperations. Unfortunately, re-excision rates still remain high and widely variable with inter-quartile range spanning about 10-20% and some reoperation rates well above 40% [15] as summarized in Figure 2.7.

2.3.2 Margin Assessment

Margin assessment techniques evaluate the removed tissue to determine if the margins are positive (requiring re-excision) or negative. When a specimen is excised, it is immediately marked with ink to delineate the tissue orientation with regards to the anatomical directions. Different colors are used for each of the six sides of the volume. If positive margins are found, the color of the ink indicates the location of residual cancer

# Physicians	**1,398**	**1,413**	**1,434**	**1,464**	**1,540**	**701**
Median re-excision rate	18.8%	17.9%	15.4%	15.0%	15.0%	13.3%
% Outliers	22.2%	19.6%	13.7%	11.1%	10.4%	8.8%

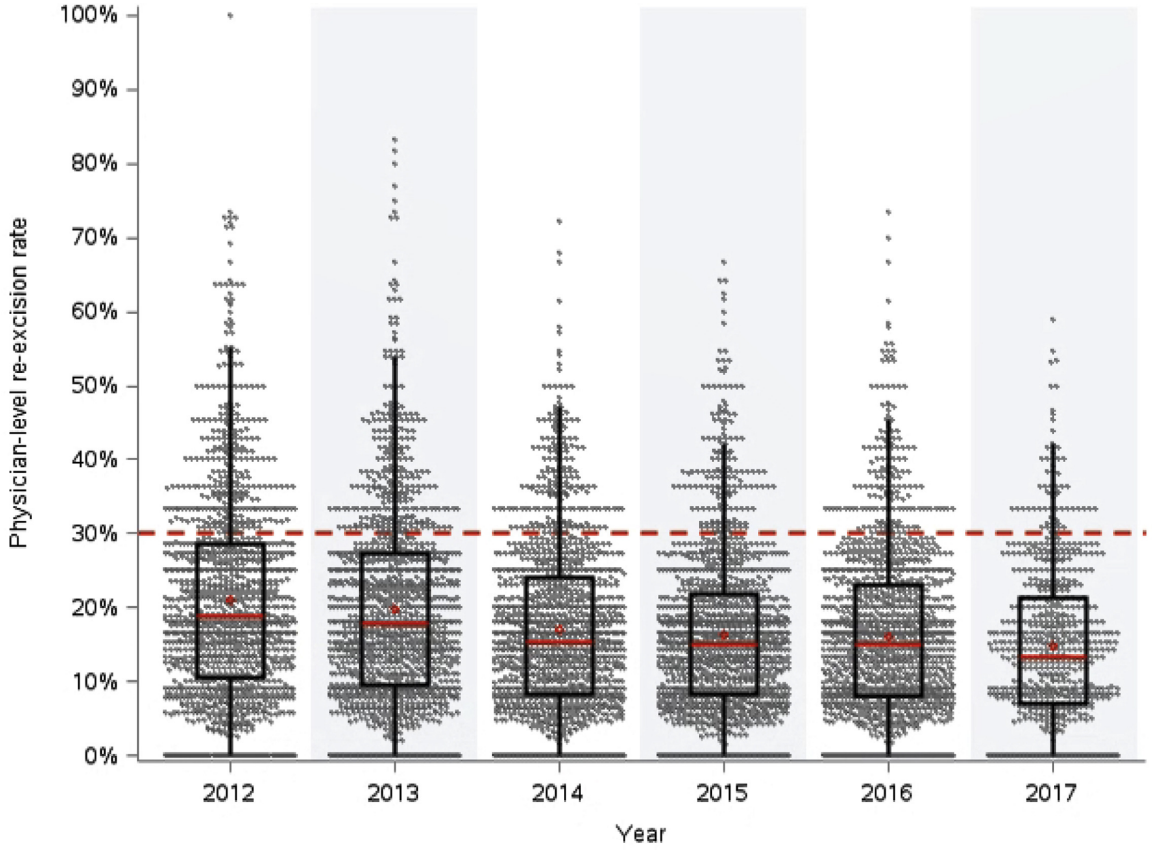

Figure 2.7: Variation in physician-level breast re-excision rate from 2012 to 2017. Each gray diamond represents an individual physician. Box-plot overlaid with the red bar marking the median physician re-excision rate and the red diamond marking the mean physician re-excision rate. Red dashed line represents the consensus threshold of an outlier physician set by the authors in [15]. Reprinted with permission from [15], ©Elsevier.

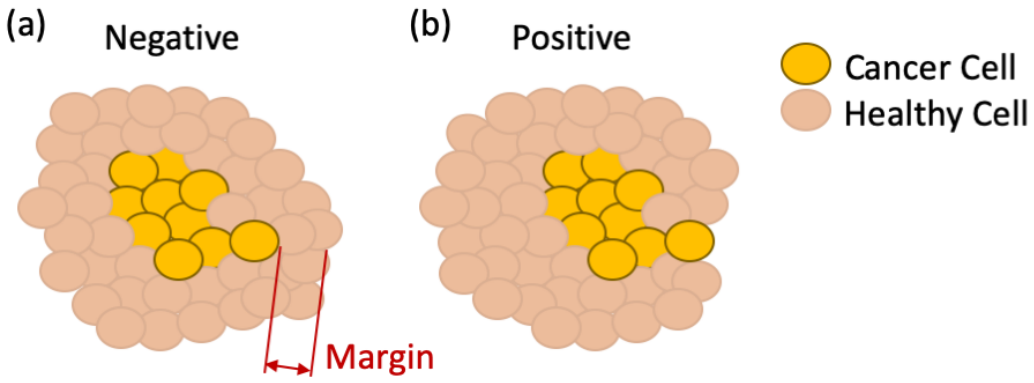

Figure 2.8: Tumor margin status in an excised tissue volume. The margin is measured by the closest distance between cancer and the edge of the excised tissue. (a) negative margin; tumor cells are entirely surrounded by healthy cells. (b) positive margin; tumor cells extend to the boundary of the excised tissue.

with respect to the existing excision cavity. Negative and positive margins are shown in Figure 2.8. Frozen section analysis involves freezing the specimen, then slicing it for observation under a microscope. Though this technique has high sensitivity and specificity (75% and 97% on average), it requires about 30 minutes to perform, limiting its intraoperative use [75]. For imprint cytology, the faces of the specimen are pressed to a glass slide, where residual cancer cells are much more likely to adhere to the glass [76, 77]. This alternative is much faster and offers a sensitivity of 63–91% and a specificity of 99–100%. Another common approach is specimen imaging, though sensitivity and specificity are low (49% and 77%), images can be used to help infer margin status from the orientation of features in the excised volume. Features such as biopsy clips, localization devices, or microcalicifications can be used to estimate the tumor position within the excised volume [78]. A final technique should be noted, though it does not assess margins. Cavity shaving, or the practice of taking another layer of additional tissue after the primary tissue excision has been shown to significantly reduce reoperation rates, though it naturally causes larger excision volumes [79]. Newer margin assessment techniques include the MarginProbe [80, 81], optical coherence tomography (OCT) with deep learning [82], spectroscopic photoacoustic (sPA) and fluorescence imaging [83], and a cathepsin-activated fluorescent imaging system [84].

Intraoperative margin assessment can reduce surgical costs, as a re-excision can be performed during the initial surgery avoiding the need for a reoperation. However, these techniques suffer from a loss of spatial orientation upon excision, as resected tissue often compresses without the support of surrounding tissue and ligaments. While margin assessment is an important tool in evaluating margins and determining a need to re-excise, an ideal surgery would result in negative margins on the first pass with minimized resection volumes. This requires accurate lesion localization before and during the initial excision.

2.3.3 Lesion Localization Methods

Current localization methods for breast excisions generally fall into two main categories: preoperative target marking and intraoperative image guidance. Most methods for localization identify and mark the target preoperatively, and this marker serves as a guide throughout breast motion. With known lesion size and orientation with respect to the marker, the surgeon can move towards and around the marker to excise the lesion. There are a variety of methods for marking the lesion location including wire guided localization (WGL), radioactive seed localization (RSL), radio occult lesion localization (ROLL), Scout® Radar localization (SRL), magnetic seed localization (MSL), and SmartClips. Image guidance strategies provide information on location and extent of lesions without depositing a marker. IOUS is a common guidance approach, and the use of supine MR in BCS continues to expand. This section will serve to summarize these localization methods and their surgical outcomes. Understanding state of the art localization strategies is important in the design and implementation of a new localization method to overcome current obstacles.

The analysis in this section discusses re-resection rates and positive margin rates as defined by the 2014 standards: "no ink on tumor". Inclusion criteria were at least 20 patients who underwent lumpectomy or surgical biopsy for malignancies, reports of positive margins with respect to malignancies, and reports from single target localization (not bracketing). The definition of positive margins is inconsistent and is therefore listed.

Here the positive margin rate is reported in Table 2.1 as the percentage of patients with positive margins out of the number of malignant (DCIS and cancer) diagnoses. There are conflicting definitions for re-resection in the literature, here two uses are defined. Some groups report re-resection as a second excision during the initial surgery (due to intraoperative margin evaluation), this is hereafter referred to as re-excision. Other groups report re-resection as a return to the operating room for a secondary surgery, hereafter referred to as reoperation. Many studies that report re-excisions describe them as a return to the operating room—in these cases, the report is designated as a reoperation. When the definition is ambiguous, the term is taken as written by the authors, though correspondence with the definitions prescribed here may be confounded. While reoperation rates may include factors outside of localization (e.g. intraoperative margin assessment, or tumor response to other treatment options), re-excision rates indicate a failed first attempt at localization. For this reason, re-excision rates are reported wherever possible. Ideally, a localization method would achieve negative margins with only one surgery and only one excision. Though some institutions re-operate based solely on positive margin rates, discrepancies between positive margin rates, re-excision rates and reoperation rates are due to a variety of considerations. Clinicians decide whether or not to reoperate based on factors beyond simple positive/negative margins. These decisions depend on the tumor characteristics and position,

the surgeon's preference and experience, and the patient specifics and preference.

Lesion localization serves as an intraoperative guide for surgeons. Wire guided localization (WGL) was the standard of care for many years, but recently it is being replaced in favor of seed-based methods such as radioactive seed localization (RSL), magnetic seed localization (MSL), and Scout® Radar localization (SRL). Methods such as these implant a marker under image guidance. These seeds can be localized during surgery, giving a read out of the distance between a probe and the implanted marker. The distance from the probe to the seed allows surgeons to approximate their instrument position in relation to the lesion centroid. Metrics for the included papers are reported in Table 2.1. Median specimen sizes are not averaged across papers due to inconsistent units (g and cm^3), and the relationship to unreported statistics on lesion sizes. This metric is most useful in the case of comparison studies, many of which are included in Table 2.1.

Table 2.1: Aggregated metrics for breast lesion localization methods, and the number of patients with malignant lesions. Re-excision rates reported as the number of patients with positive margins after the first excision. Statistics for each method are summarized in its first row, with mean values ($\pm$ standard deviation).

Method	Study	Margins (mm)	Number of Patients	Positive Margins (%)	Re-excision Rates (%)	Median Specimen Size
Wire-Guided Localization		*1.1*	*344*	*15.9 $\pm$ 9.5*	*21.8 $\pm$ 19.8*	
	Burkholder, 2007 [85]	3	125	25.6	28.0	–
	Chu, 2010 [86]	1	38	31.2	31.2[2]	56.4 cm^3
	Barentsz, 2012 [25]	0	138	6.5	10.9	56.6 cm^3
	Postma, 2012 [87]	0	152	11.8	9.9[2]	64 cm^3
	Luiten, 2015 [88]	0	78	25.6	16.7	47.0 cm^3
	In't Hout,2018 [89]	4	149	15.4	15.4	32.5 g
	Rubio, 2016 [20]	0	45	6.6	13.3	43.7 cm^3
	Langhans, 2017 [35]	2	4118	17.6	17.6	–
	Langhans, 2017 [90]	2	195	12.3	53.8	26.0 g
	Theunissen, 2017 [91]	0	76	32.9	17.1[2]	81.8 cm^3
	Tran, 2017[92]	0	141	2.8	6.4	–
	Patel, 2018 [93]	0	42	7.1	9.5	16.3 cm^3
	Stelle, 2018 [94]	0	60	16.7	71.7	35.9 g
	Zacharioudakis, 2019 [95][1]	1	100	14.0	14.0	95.6 cm^3
	Barth, 2019 [50]	1	69	23.2	21.7[2]	70.0 cm^3
	Hu, 2020 [96]	4	258	19.4	24.0	–
	Joukainen, 2021 [97]	0[3]	65	1.5	1.5	60.0 g 124.0 g[4]
Raidoactive Seed Localization		*0.6*	*228*	*8.1 $\pm$ 4.7*	*25.0 $\pm$ 21.4*	
	McGhan, 2011 [98]	0	767	3.3	15.4	–
	Sung, 2013 [99]	0	232	6.9	–	–
	vanderNoordaa, 2015 [100]	0	128	9.4	2.3[2]	30 g (DCIS) 43 g (invasive)
	In't Hout,2018 [89]	4	87	6.9	6.9	38.0 g

[1] study included bracketing in some patients; multiple seeds/wires used to identify a lesion

[2] re-operation rate; return to the operating room for a secondary surgery; excluded from method average when re-excision rates are available

[3] 2016 American Society of Clinical Oncology consensus guidelines were followed; 0 mm margins (no-tumor-on-ink) for invasive cancer and 2 mm margins for ductal carcinoma in situ

[4] with oncoplastic methods in addition to tumor resection

Method	Study	Margins (mm)	Number of Patients	Positive Margins (%)	Re-excision Rates (%)	Median Specimen Size
	Nolano, 2017 [101]	0	35	11.4	–	100.39 cm^3
	Langhans, 2017 [90]	2	186	12.6	53.2	29.0 g
	Theunissen, 2017 [91]	0	69	7.2	7.2[2]	97.5 cm^3
	Tran, 2017 [92]	0	161	1.9	7.1	–
	Velazco, 2017 [102]	0	522	3.3	–	–
	Stelle,2018 [94]	0	94	17.0	42.6	36.3 g
Scout® Radar Localization		*0.00*	*51*	*10.7 ± 2.8*	*10.5 ± 4.7*	
	Cox, 2016 [103]	0	41	7.3	7.3	–
	Cox, 2016 [104]	0	99	14.8	17.2	–
	Nolano, 2017 [101]	0	35	11.4	–	81.28 cm^3
	Jadeja, 2018[105]	0	39	10.5	10.5	–
	Patel, 2018 [93]	0	42	9.5	7.1	15.2 cm^3
Magnetic Seed Localization		*0.75*	*84*	*14.6 ± 1.7*	*12.6 ± 3.9 %*	
	Price, 2018 [106]	0	58	15.5	7.3	–
	Reid, 2019 [107]	1	58	12.1	12.1	–
	Thekkinkattil, 2019 [108][1]	1	121	14.8	14.8	–
	Zacharioudakis, 2019[95][1]	1	100	16.0	16.0	–
Radioguided Occult Lesion Localization		*0.25*	*157*	*14.4 ± 3.3*	*11.6 ± 3.7*[2]	
	Chu, 2010 [86]	1	55	16.4	16.4[2]	81.6 cm^3
	Postma, 2012 [87]	0	162	13.6	11.7[2]	71 cm^3
	van der Noordaa, 2015 [100]	0	275	10.2	7.3[2]	22.5 g (DCIS) 37.0 g (invasive)
	Theunissen, 2017 [91]	0	137	17.5	10.9[2]	86.3cm^3
IntraOperative Ultrasound		*0.625*	*136*	*6.6 ± 5.3*	*12.6 ± 8.2*	
	Barentsz, 2012 [25]	0	120	6.7	12.5	62.8 cm^3
	Eggeman, 2014 [23]	0	147	14.3	8.8[2]	89.4 cm^3
	Karanlik, 2015 [22]	0	84	6.0	28.6	89.9 cm^3
	Rubio, 2016 [20]	0	112	4.4	11.6	54.18 cm^3
	Volders,2017 [21]	0	65	0.0	1.5	38 cm^3
	Cakmak, 2017 [24]	0	208	2.4	8.2	–
	Gerrard, 2019 [109]	1	95	14.7	14.7	–
	Hu, 2020 [96]	4	262	4.6	11.1	–
PreOperative Supine MR for IntraOperative Guidance		*0.50*	*51*	*5.9 ± 8.3*	*5.9 ± 8.3*	
	Barth, 2019 [50]	1	68	11.8	11.8[2]	70.0 cm^3
	Joukainen, 2021 [97]	0[3]	33	0.0	0.0	205 g

2.3.3.1 Wire Guided Localization (WGL)

WGL was the standard of care for many years, but recently has been phasing out of use in favor of seed-based methods. For wire guided localization, a few hours before surgery, a wire is placed into the center of the targeted area using a needle under mammographic or ultrasound guidance. If the lesion is echogenic, the needle can be inserted parallel to the chest wall and visualized directly with ultrasound. If the lesion is not echogenic, mammography can be used. Distance to landmarks such as the chest wall and nipple are used to calculate placement. The needle is positioned based on these calculations and then imaged for confirmation. This process is repeated until the needle tip is determined to be in the center of the desired

target. Once properly placed, a hooked wire is deployed. The breast with the inserted hook is then imaged to re-confirm placement. During surgery, the surgeon follows the path of the wire to excise the lesion. Note that the noticeably higher re-excision rates in Stelle *et al.*, are reported explicitly as additional margins performed intraoperatively, and that for [97], results are pooled for breast conservation surgery with and without oncoplastic methods, as wire guidance was used for localization in both groups. In the 17 studies included, WGL had a positive margin rate of 1.5–32.9% with a mean of $15.9 \pm 9.5\%$. Overall, the re-excision rate ranged from 1.5–71.7% with a mean of $21.8 \pm 19.7\%$ (see Table 2.1).

Another form of wire guided localization has recently been presented that includes electromagnetic tracking of the implanted needle [110] and incorporation of a 4-panel image guidance platform. An EM tracker was attached to the implanted needle, and intraoperative ultrasound (IOUS) was used to segment the lesion. The position of the lesion was then displayed in a 3D scene with respect to the needle, tracked surgical tools, and IOUS planes. The addition of this technology that expands upon wire-guidance was shown to reduce re-excision rates from 50% to 14.3%. Because it expands upon WGL, this study is not included in the summaries, although the 14.3% re-excision rate is on par with the observed results reported in Table 2.1.

Despite being the standard procedure, WGL has many drawbacks. As the patient waits for surgery, the end of the wire protrudes from the patient's breast. Localization is performed the same day as the excision, ideally close together, to minimize patient discomfort and risk of wire displacement, but scheduling localization and surgery close together leads to logistical problems. Wire guidance cannot be used in the first operating room slot of the day, and delays in radiology lead to costly delays in the operating room. Because the wire is placed under cross-sectional image guidance, the path taken by the radiologist is frequently not the ideal surgical path for aesthetics or invasiveness. Furthermore, the embedded tip of the wire in the center of the lesion is not visible to the surgeon. The surgeon must estimate the relative position of the wire tip in the lesion and approximate margins surrounding the unseen wire tip. While much less common, other serious issues may arise during WGL. The wire can be transected during surgery, and wire fragments may remain in the breast [111]. This was reported in 0.02% of cases over an eight year period [112]. One patient out of ten reported cases in [112] experienced discomfort in certain positions, however most patients were asymptomatic. With no external component, the wire fragments showed no change in position for years [112]. Wire migration, or deviation from the intended image-confirmed location, is also possible, though unlikely [113–115].

2.3.3.2 Radioactive Seed Localization (RSL)

For RSL, a radioactive seed is inserted into the target lesion under ultrasound or mammographic guidance. Similar to WGL, a needle is inserted into the lesion for resection and the location marker is deployed upon reaching the correct location, except here the needle is then removed and the location marker is a radioactive

seed instead of a hooked wire. The radioactive seeds have a titanium shell and contain 3.7 to 10.7 MBq of 125I, which has a half life of 60 days and emits 27 keV of gamma radiation [116]. During surgery, a handheld gamma counter is swabbed over the breast and outputs audible and numerical feedback corresponding to the distance to the isotope. The surgeon can then place the excision at the point of greatest feedback strategically over the lesion. The seed is excised with the lesion, and the gamma probe is used to confirm that the seed is within the resected specimen. In the 10 studies included, RSL had a positive margin rate of 1.9–17.0% with a mean of 8.1 $\pm$ 4.7%. The re-excision rate ranged from 2.3–53.2% with a mean of 25.0 $\pm$ 21.4% (see Table 2.1).

One of the main drawbacks of this technique is the strict care that must be taken when dealing with radioactive materials. In the United States, Radioactive materials are regulated by the United States Nuclear Regulatory Commission (NRC) [117]. These guidelines were updated in late 2016 to eliminate burdensome requirements not pertinent to the procedure, however strict protocol remains necessary for adequate safety. Institutions must obtain a license to perform RSL, personnel must become authorized users through documented training and experience, a radiation safety committee or officer must ensure safe handling protocols, emergency plans must be developed, and proper disposal must be carried out. Materials must be kept in locked cabinets, and chain of possession must be recorded to maintain constant accountability for the seeds. There have also been several reported cases of seed rupture in pathology during removal from the specimen [117]. A rupture of the seed in the operating room, or in pathology, could lead to airborne 125I and is considered an emergency. Other types of adverse events that need to be addressed in the written emergency procedures are loss of a seed, inability to locate an implanted seed during surgery, or patient with an implanted seed not returning for surgery. After excision, the seed must be returned to the manufacturer, transferred to a licensed radioactive waste broker, or placed in a lead container and returned to nuclear medicine for long term decay [117].

In contrast to the drawbacks associated with radioactive materials, RSL has many advantages. The implanted seed does not cause the patient discomfort or pain after the initial placement procedure, and intraoperatively surgeons are free to plan their surgical approach for optimal cosmesis and minimal resection. The RSL procedure is straightforward for surgeons and associated with no evidence of a learning curve [98, 102]. The isotope commonly used for sentinel lymph node mapping has a much shorter half-life and a stronger gamma emission, and can easily be differentiated from the 125I seed intraoperatively. Current gamma probe systems in most operating rooms can easily switch between detection of 125I, the isotope used for radioseeds, and 99Tc, the isotope used for sentinel lymph node mapping, with the press of a button [116]. This allows a single probe console to be used for localizing the lesion and sentinel lymph nodes.

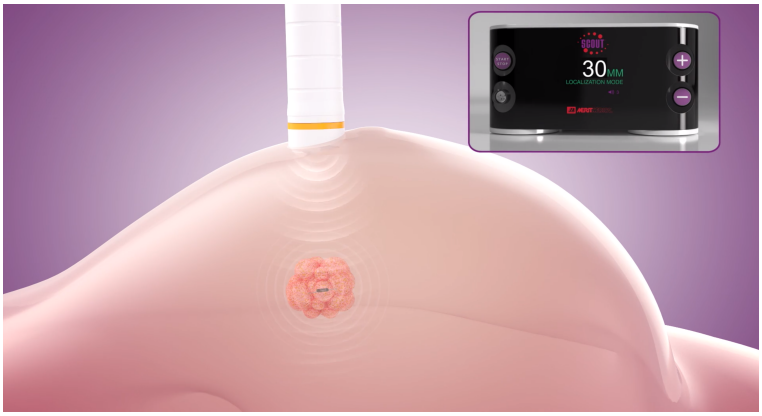

Figure 2.9: Illustration of the use of a Scout® radar reflector and handheld probe. The reflector is shown implanted in the center of a spherical tumor. The distance between the probe and the reflector is shown in mm on the display at bottom left (Merit Medical, Jordan UT, USA).Reprinted with permission from [121].

2.3.3.3 Scout® Radar Localization (SRL)

The Scout® Radar Localization surgical guidance system (Merit Medical, Jordan UT, USA), formerly the SAVI Scout System, utilizes micro-impulse radar to localize an implanted reflector, as shown in Figure 2.9. A 12 mm long reflector is inserted into the breast with a 16 gauge delivery needle under sonographic or mammographic guidance [104]. The reflector is implanted near a target such as a biopsy clip, or the centroid of the suspicious region. During surgery, a handheld probe provided by the manufacturer emits micro-impulse radar. The implanted device reflects these radar waves and the system console outputs an audible signal and a numerical readout corresponding to the distance between the probe and the reflector. In the 5 studies included, SRL had a positive margin rate of 7.3–14.8% with a mean of $10.8 \pm 2.9\%$. The re-excision rate ranged from 7.1–17.2% with a mean of $10.5 \pm 4.7\%$ (see Table 2.1)).

More recent comprehensive studies continue to report low reoperation rates, though these studies do not meet our strict inclusion criteria for the table. Across 320 patients, [118] reports a positive margin rate of 5.6% (with 1 mm margins), though patients with benign tumors were considered successful excisions. In a systematic review and pooled analysis of 842 cases, [119] found a reoperation rate of 12.9%.

The SRL reflector can be placed up to 30 days before surgery, allowing the localization and surgery to be performed on different days, improving efficiency, and multiple reflectors can be implanted for lesion bracketing. Most SRL reflector placements were less than 4 cm from the skin, although one study limited included patients to those with lesions $\leq$3 cm deep [103]. Multiple groups have reported difficulties detecting reflectors past depths ranging from 4–5 cm [103, 105, 120].

2.3.3.4 Magnetic Seed Localization (MSL)

MSL involves implantation of a small stainless-steel marker under mammographic or sonographic guidance. The markers, one example commercially produced as Magseeds (Endomagnetics, Inc., Austin, TX), are metallic, nonradioactive, and cylindrical with 1 mm diameter and 5 mm height. In the operating room, surgeons can localize the marker with the manufacturer's probe that temporarily magnetizes the marker. Similar in use to RSL and SRL, the handlheld probe outputs a numerical readout as well as an audible tone corresponding to the distance to the marker. Magnetic markers cost more than radioactive seeds and wire guidance, and the cost has not yet been compared to Scout® (SRL). MaMaLoc produces a similar, smaller device measuring 1.5mm $\times$ 3.5 mm [122]. As the MaMaLoc has not been validated to the same extent as Magseeds, this section focuses on Magseed.

Several MSL studies have been reported in the last two years, though they are excluded from the aggregated analysis based on cavity shaving, or excision of additional tissue after the initial lesion excision. In 2022, Kelly *et al.* reported cavity shaving at the discretion of the surgeon after MSL, achieving 19.1% reoperation rates[123] . Across 395 patients in Miller *et al.*, MSL resulted in a positive margin rate of 17.2% and a reoperation rate of 15.2% though these results are not included in the table due unspecified margin widths [124]. In this study from 2021, cavity shaving was performed in the majority of cases (68.9%). In Murphy *et al.* from 2021, cavity shaving was performed at the surgeon's discretion following intraoperative x-ray margin analysis. Across 85 patients, MSL resulted in 9.4% reoperation rates, though neither the positive margin rate nor the frequency of cavity shavings are reported [125].

Because they are approved for implantation up to 30 days prior to surgery, seed placement can be scheduled separate from surgery leading to improved surgical center efficiency [126]. The metallic marker precludes the use of MR evaluation, and specialized nonferromagnetic surgical instruments must be used because metallic instruments, including standard electrocautery, interfere with the magnetic signal and require the probe to be recalibrated. These devices are meant for detecting tumors 3–4 cm from the surface, and thus there is some selection bias in these trials [106, 127]. Bracketing, or using multiple seeds to identify multiple points in the tumor, is common in the literature for this localization technique, though placing two seeds less than 2cm apart is not recommended [125]. For this reason, multiple studies were included that used bracketing with seeds on a select number of patients [95, 108]. In addition to the studies excluded for cavity shaving, two studies conducted on the Magseed were included in our discussion but excluded from our numerical analysis due to ambiguity in margins depth used [126] and no reported margin status [127]. The positive margin rate ranged from 12.1–16.0% with a mean of 14.6 $\pm$ 1.7% and the re-excision rate ranged from 12.6 $\pm$ 3.9 % (see Table 2.1).

2.3.3.5 Radio-Occult Lesion Localization (ROLL)

In ROLL, a radiotracer solution is injected into the lesion under ultrasonographic or mammographic guidance. Generally, the radioisotope used is the same as that used for sentinal lymph node biopsy, 99mTc-nanocolloid, and it is injected the day of or up to 24 hours before surgery [128]. This radio-tracer injection allows for subsequent surgical biopsy or wide local excision to be performed under the guidance of a hand held gamma-ray detection counter [128, 129]. In the 4 studies included, ROLL had a positive margin rate of 10.2–17.5% with a mean of 14.4 $\pm$ 3.3%. The re-excision rate ranged from 7.3–16.4% with a mean of 11.6 $\pm$ 3.7% (see Table 2.1)).

The radiotracer is retained by the tumor, however it can diffuse into surrounding tissue and the liver. In Carrera *et al.*, 22.2% of patients experienced radiotracer dispersion, although only 8.6% of these cases represented a risk for incorrect lesion localization [130]. All of these lesions were correctly localized with the use of palpation when the tumors were palpable. Therefore, this is not truly directly indicative of the success of ROLL. Elevated levels of hepatic radioactivity were observed in 11.1% of patients [130]. Radiation risk to the surgeon is strongest in the fingers, but is less than 1% of the annual limit because 99mTc has a half-life of about 6 hours, resulting low dose gamma radiation [131]. With regard to patient radiation, the majority of radiated tissue is resected [131]. While radiotracer is not visible on mammograms, contrast can be injected with the tracer to overcome this issue. When inserted under mammographic guidance, the radiotracer can leak into other tissue when the breast is removed from compression. To avoid this, radiologists use less radiotracer. Use of mammography for injection can also produce minor errors in the perceived depth, which causes the inaccurate placement of the radiotracer in a compressed breast [131].

2.3.3.6 IntraOperative Ultrasound (IOUS)

Ultrasound can be used inside the sterile field throughout the procedure to visualize echogenic tumors intra-operatively. While deep lesions are not visualized as clearly as superficial lesions, the ultrasound probe can also be used throughout the procedure to investigate the resection cavity for remaining tumor cells after the initial excision. For IOUS, localization is performed entirely after the patient is anesthetized, with no preoperative localization procedure. This causes less stress and anxiety for the patient leading up to the surgery and no discomfort related to localization. In the 8 studies included, IOUS had a positive margin rate of 0–14.7% with a mean of 6.6 $\pm$ 5.3%. The re-excision rate ranged from 1.5–28.6% with a mean of 12.6 $\pm$ 8.2% (see Table 2.1)).

One of the largest drawbacks to IOUS is that not all lesions are visible on ultrasound. Unfortunately, only 50% of non-palpable tumors are visible on ultrasound [26]. While there is no risk of displacement or inaccurate target placement, not all tumors are accurately represented on ultrasound. Tumors can be over

or underestimated [23]. Eggemann *et al.* found that only 11.9% of margins were accurately represented on ultrasound, while 41.2% were underestimated, and 46.9% were overestimated [23]. Excising the tumor with a margin of healthy tissue surrounding the lesion helps compensate for the margin estimation inaccuracies.

2.3.3.7 PreOperative Supine Magnetic Resonance (MR) for IntraOperative Guidance

MR image guidance for BCS involves leveraging preoperative MR scanning to estimate the intraoperative tumor position. These techniques generally rely on registration to align preoperative images with the intraoperative presentation, providing surgeons with a visualization of the predicted tumor position and extent. To the best of our knowledge, there is currently no commercially available system leveraging supine MR in breast surgery. However, the utility of supine MR is being actively explored by several groups. Due to the aforementioned benefits of supine MR imaging (see Section 2.2.3), a range of technologies to improve breast surgery have been introduced in recent years that demonstrate the utility of supine MR data in the operating room. Here, the two studies included in aggregated analysis had both a positive margin rate and re-excision rate of $5.9 \pm 8.3\%$, with a range of 0.0–11.8% for both metrics.

The specific use of supine MR data differed between the two studies included, though in both trials, the full volumetric image data was not available to the surgeon, but was used to provide guidance information. Referencing a supine MR image and 15 MR-visible surface markers, regions to be excised were marked on the skin surface, demonstrating comparable outcomes to wire guided localization across 115 patients in Joukainen *et al.*[46, 97]. In Barth *et al.*, a guidance system was used to portray tumor positions in 3D space on a monitor and project tumor positions onto the surface within the 3D rendered scene. This rendering was used to mark predicted tumor boundaries onto the skin surface .

Though these methods both require additional imaging procedures to include preoperative supine MR, the use of supine MR for intraoperative guidance is painless for the patient requiring no wires or targets, and provides additional 3D anatomical information to the surgeon during resection. The method in [50] also requires an intraoperative system including an optical tracker and a 3D scanner. The method in [46, 97] required no additional equipment, however without the use of tracked tools to navigate the images, careful image analysis was required to delineate tumor position. In 2014, Pallone *et al.* presented a system for image guided breast surgery that included optically tracked surface fiducials and a 3D scanner to capture the intraoperative breast surface [41]. This work relied on preoperative supine MR and rigid registration. Dynamic contrast enhanced MR imaging allowed for clear visualization of tumor boundaries in the preoperative image, and MR fiducials were placed on the breast surface. In the operating room, the surface fiducial locations were tracked via conventional optical tracking. Though they can be used for initial planning, they must be removed during surgery. This guidance platform provides surgical planning based on 6–8 surface fiducials and rigid regis-

tration. In an expansion of this work included in Table 2.1, the platform was evaluated in 68 patients [50]. Outside of the two uses described so far, data extracted from MR images has also been used in a variety of other approaches. Other groups have projected supine MR data onto the skin surface itself demonstrating low positive margin rates (12.5%) [132] and low re-resection rates (0% re-excision rate and 6.7% reoperation rate in [133]), though the unquantified use of intraoperative margin evaluation excludes these from the tablular analysis. With no commercialized system and only a handful of reported trials, more investigation is needed to evaluate patient comfort, cost, and to further prove feasibility.

Though not commercially available, a few research systems have also been recently presented to 3D print surgical guides for tumor localization. These methods print breast molds based on preoperative supine MR images that are fit onto the breast surface using the nipple and at least one additional hole for a fiducial alignment [134, 135]. Based on the tumor position in the image, these rigid, bra-like forms allow the surgeon to mark the boundary of the tumor directly onto the skin surface. In addition to boundary marking ports, molds in [135] incorporate additional ports for blue dye injection and a hook wire to further aid guidance. The system accurately localized 18/19 cancers. One case was inaccurately localized due to breast deformations induced by the MR coil, though surgery was still successful since the lesion was palpable. In [134], 0% reoperation rates were achieved across 102 patients with an 11 mm median distance from tumor to margin. However, intraoperative margin assessment allowed repeated resections on positive margins until a tumor-free margin was obtained and no re-excision rates are reported. In this case, intraoperative margin assessment (frozen section) is an important factor in the reported outcomes. A similar framework was used in Ko *et al.*, but with prone MR images obtaining clear margins in 3 patients with malignant lesions [136].

Other groups are investigating BCS guidance approaches with supine MR data visualized in augmented reality. Augmented reality systems use a headset to overlay computer-generated guidance information onto a see-through lens. This integrates guidance information with the real perception of the surroundings through clear glasses. Two groups have developed prototype systems to display supine MR information in the operating room using augmented reality headsets [137, 138]. The augmented reality system in Gouvia *et al.* achieved clear margins on a 17 mm breast cancer, though positive margin definitions were not specified [137]. The system in Perkins *et al.* was evaluated on four patients by marking the perceived tumor boundaries on the skin surface using the augmented reality, surgeon intuition (called cognitive fusion), and palpation[138]. The perceived tumor boundaries using augmented reality did not always overlap with the palpated tumor boundaries, though the authors attribute this misalignment to abduction of the arm [138, 139].

2.3.3.8 SmartClip Localization

SmartClips (Elucent Medical, Eden Prairie, MN, USA) are permanently implantable clips intended to replace both conventional biopsy clips and localization seeds [140]. A SmartClip is placed to mark the location of a biopsy, and this clip can be subsequently localized during surgery. Clips are 1.4 mm $\times$ 8mm and up to three seeds can be placed and localized with unique electromagnetic signatures. This technology completely eliminates the need for the secondary radiological placement of a surgical marker, minimizing painful and invasive procedures. If the biopsy is negative, the clip remains in the breast just like a conventional biopsy clip, serving as a marker in future mammograms. If the biopsy is positive, the EnVisio™ Navigation System, offers a screen attached to the surgical instrument which gives continuous guidance to the implanted clip. Because the screen is coupled to the electrocautery device, localization information can be provided throughout surgery without switching to a probe or transducer. Unlike conventional seeds, this system provides distance, depth, and direction to the clip with visualization that mimics a sonar or radar display. To the best of our knowledge, there are currently no publicly available studies that evaluate this method.

2.3.3.9 Comparisons

With consistent margin guidelines, positive margins are the most representative of localization error. Even with the definition of re-excision indicated, it is important to note here that many factors play into re-excision. Proximity to skin or fascia can influence excision margins during surgery, as well as the decision to re-operate. These types of decisions can be seen in Table 1 when the percentage of positive margins is not equivalent to the percentages of re-excision rates. Patel reports that one patient in the SRL group with positive margins was not re-excised due to proximity to the posterior margin (fascia), and one patient in the WGL group with positive margins was not re-excised due to proximity to the anterior (skin) margin [93]. Re-excision rates are also dependent on factors external to localization, such as patient preferences. Breast conserving therapy consists of lumpectomy with radiation, but Burkholder reports that 12.3% of lumpectomy patients with negative margins opted for mastectomy instead of radiation following their initial surgery [85]. Positive margins in this review are considered at the end of the initial surgery, (i.e. 0 mm as no ink on tumor, and 1mm as no tumor within 1mm of ink). Surgical margins are indicated because the definition of positive margins has a large impact on clinical outcomes and should be noted during comparisons [74]. Reducing the guidelines from 2 mm to 0 mm, in one case represented a significant decrease of 50% in positive margins and re-excisions [74].

Placing targets accurately under mammographic guidance is associated with difficulties that are experienced by all of these methods except IOUS and supine MR [105, 131, 141]. Furthermore, once placed, the target cannot be moved for MSL, SRL, RSL, and ROLL. A target is considered accurately placed if it is

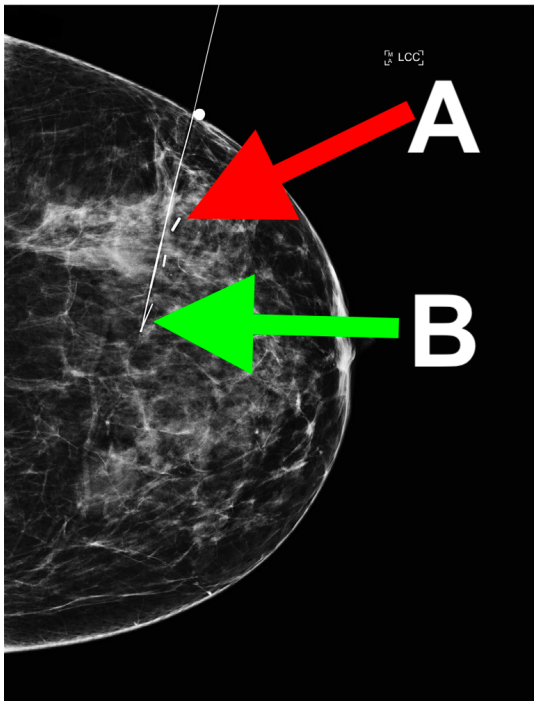

Figure 2.10: Two guidance methods viewed on craniocaudal mammograph of a ductal carcinoma in situ. A) radioactive seed for RSL, 13 mm superior and lateral to the biopsy marker; B) wire placement for WGL. Image is reproduced from [92] with permission.

within 10 mm of the lesion centroid, even if that means the target is outside the lesion altogether [106, 108]. For the patient in Figure 2.10, the radioactive seed was placed 13 mm from the biopsy clip target. Therefore, on the day of surgery a wire was inserted for guidance [92]. As you can see in Figure 2.10, the wire tip, biopsy marker, and radioactive seed are all relatively spaced out across the DCIS. This illustrates one of the drawbacks to these target-marking methods: inaccuracy in target marking leads to uncertainty in tumor location. For SRL and RSL, however, a secondary target can be placed closer to the intended destination and still be localized [88, 141]. This is not the case for ROLL or MSL. In MSL, seeds cannot be accurately localized when placed less than 2 cm apart [106], but for MaMaLoc, the small size allows for closer placement. For ROLL, once the dye and radiotracer are injected, injecting excess could lead to diffusion outside of the target region [131].

The approaches that use a seed for localization allow for scheduling efficiencies that are not provided by localization methods that must be performed day-of. In a study comparing WGL and RSL, Sharek *et al.* showed a significant improvement in workflow efficiency with RSL compared to WGL [142]. After instituting RSL, there was a 34% increase in scheduled biopsy slot utilization, 50% less time spent scheduling, and a 4.1 day average decrease in biopsy wait time for patients. These benefits are related to the ability to insert a localization marker independent of the time of surgery. For this reason, the workflow benefits can be assumed

to also apply to SRL and MSL. However, this time saving cannot be assumed to reduce costs. RSL involves increased oversight from an institution's nuclear medicine. SRL involves the purchase of a console and then continued purchase of the single-use probes. A separate cost analysis should be conducted to evaluate the overall financial impact on an institution including increased device cost and improved scheduling efficiency for MSL and SRL compared to WGL.

SRL was shown to be equivalent to RSL when comparing margin re-excision and tissue volumes [101]. It was also shown to have significantly shorter hospital stays on the day of surgery compared to WGL, due to localization being separated onto different days. [119] reports significantly lower re-excision rates for SRL compared to WGL. Selection bias also affects the SRL results reported here. A few studies used lesion depth as exclusion criteria for Scout® (SRL) placement. Cox *et al.* excluded patients with lesions deeper than 3 cm from the skin, and could not detect Scout® devices greater than 4.5 cm from the skin [103]. These excluded deeper lesions may have been more difficult to localize, and a comparison of localization methods with reported depth of lesions would be useful in analyzing the effect of this factor. Studies that did include deep lesions experienced difficulties in localizing reflectors in those cases [103, 105, 120].

MSL has been found to be safe and effective [106, 126, 127]. Compared to WGL, MSL offered significantly smaller resection volumes, shorter lumpectomy operating times and comparable reoperation rates for invasive carcinomas (14.4% MSL vs. 17.7% WGL), though for ductal carcinoma in situ MSL reoperation rates were significantly higher (35% MSL vs. 18.5% WGL)[123]. [143] reports that as their center switched from a majority WGL procedures (2016–2017) to majority MSL (2018–2019), reoperation rates decreased from 18.9% to 11.6%. Though in a comparison of SRL, MSL and WGL, [144] found marker choice was not associated with rate of re-excision, or specimen volume. The outcomes included in this review demonstrate somewhat inconclusive findings in comparison to other localization methods. MSL gives many of the benefits of RSL without the necessary precautions and dangers associated with radioactive materials. It seems that MSL offers all the benefits of SRL with the added disadvantage of requiring a nonferromagnetic operating room.

RSL is generally agreed upon to be an improvement over WGL [145], and its drawbacks are mainly due to the nature of using radioactive materials—especially small radioactive seeds that can be lost. RSL has been shown to be at least equivalent to WGL in ease of procedure, removing target lesion, volume of excised breast tissue, obtaining negative margins, avoiding a second operative intervention, and allowing for simultaneous axillary staging [116].

The superiority of ROLL versus other methods, specifically WGL, is not agreed upon in the literature. Some studies find that ROLL has similar outcomes to other methods [129, 146], some report it as superior to other methods [86, 147], and some report it as inferior [87, 91, 100]. Studies that report ROLL as superior

cite its improved patient comfort over WGL [147], and shorter localization time [86], although they cite equivalent margin clearance and need for re-excision. ROLL is reported as inferior to RSL due to higher rates of positive margins, increased specimen weight, more difficult logistics, and the ability to easily verify the radioseed location before and after resection [91, 100]. Some studies do not recommend ROLL as a replacement for WGL, due to no improvement in margin status, re-excision rates or cosmetic outcome with larger tissue volumes removed for ROLL [87, 146]. Alikhassi *et al.* reports no significant difference in patient discomfort, or disease-free margins between ROLL and WGL [148]. Generally, the literature supports that ROLL is not the best alternative to WGL considering the other localization approaches available. In recent years, the field has been moving away from ROLL and there have been fewer studies investigating the clinical outcomes of ROLL.

For cases with echogenic tumors, IOUS has improved outcomes outlined here and supported by many studies [38, 39]. Krekel *et al.* reports improved adequate margins with IOUS compared to ROLL and WGL [38]. Rates of re-excision for positive or close margins and local recurrence rates were not found to differ significantly between IOUS and WGL, and IOUS provided smaller excised volumes [20]. IOUS provided improved margin status, recurrence rates, and cosmetic outcomes when compared to WGL [40].

Information from supine MR data aligned to the surgical scene was shown to improve positive margin rates and resection volumes compared to wire guidance [132]. The guidance system in [50] was also found to be an improvement over wire guided localization with an 9% positive margin rate for the image guidance method vs. 19% for WGL. The data suggest that an image guidance system may provide lower positive margin-rates than wire guidance, though more patients should be evaluated. Nakamura *et al.* compared supine MR guidance [133] to ultrasound-guided dye application, showing an improvement in both re-excision rates and the excision area. Supine MR image guidance demonstrated comparable outcomes to WGL across 115 patients in [46, 97]. Though WGL provided shorter operation times, inclusion of a supine MR did not increase the preoperative time between diagnosis and surgery [97]. While limited, these initial comparisons demonstrate that providing full tumor boundary information could reduce reoperation rates. Despite large breast deformations between supine imaging and surgery, many of these image-alignment approaches provide similar, or improved performance to painful WGL. These methods remain to be evaluated on larger numbers of patients, and associated costs remain to be evaluated. Improved image-alignment procedures such as the one presented in this thesis may also reduce positive margins and re-excisions beyond rates presented by these rigid alignment methods.

The methods for localization produce generally comparable results, with the exception of image guidance: supine MR, and IOUS for echogenic lesions. RSL and SRL both result in relatively low rates or positive margins and re-excision rates with SRL outperforming RSL in positive margins and vice versa for re-excision

rates. The evaluation of a supine MR image guidance was successful with the lowest positive margin rates for methods not limited to echogenic tumors. Rising evidence supports that supine MR yields the best surgical outcomes, though additional studies should be conducted to verify these results as supine MR is not standard of care at any institution to the best of our knowledge. For this reason, the data support that state of the art lesion localization is IOUS when possible. When IOUS is not feasible (i.e. for nonechogenic lesions), commercially available state of the art methods are RSL and SRL. More data is needed to determine differences in cost of instrumentation for both, as well as impact of increased safety requirements for RSL.

2.3.3.10 Summary

Current seed-based technologies allow for ease of scheduling between radiology and oncology, as well as guidance to a target within 10 mm of the lesion centroid. However, they do not provide lesion extent and boundaries during surgery. Furthermore, most localization strategies offer improved patient comfort when compared but require the use of a probe or transducer, interrupting workflow for updated guidance information. Exceptions to this rule, supine MR and SmartClips, remain to be completely investigated across large clinical trials, and in the context of cost and scheduling impact on institutions. Re-excision rates for the best performing seed-based methods average around 10%. However, many institutions still use wire guidance with recent re-excision rates up to 32% [91, 149]. Cost, ease of scheduling, integration into surgical workflow, and patient comfort are all important considerations in adoptability of a novel localization paradigm. Most critical, however, is the need for a localization method that provides accurate tumor location and extent for all patients throughout surgery.

2.3.4 Breast Cancer Lesion Sizes

Fully understanding localization accuracy and margin distances requires the context of breast lesion size. Localization targets are relatively small, offering precise localization of these targets. However, localization of the lesion is considerably less precise. Markers are considered correctly implanted if they are within 10 mm of the intended location, and marker sizes range from 3–12 mm. This means that the boundary of the lesion is largely unidentified. Bracketing provides a secondary location for guidance, but still localization of the majority of the lesion boundary is left to the surgeon's spatial reasoning.

Tumor size varies slightly depending on the modality used for measurements [27]. Average, minimum and maximum breast lesion diameters are shown in Table 2.2. The distribution of lesion sizes as reported in [150], are shown in Figure 2.11. The small size of many tumors emphasizes the need for accurate localization, and provides context for understanding the typical guideline of excising the lesion as well as 10 mm of healthy tissue surrounding the lesion. These lesion sizes also describe the expected size for regions of interest in BCS.

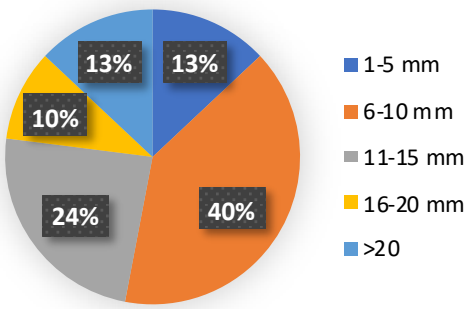

Figure 2.11: Distribution of lesion diameters across 201 patients reported in [150].

Table 2.2: Summary of breast lesion diameters.

Study	Number of Lesions	Number of Patients	Modality	Average (mm)	Minimum (mm)	Maximum (mm)
Wienbeck [151]	94	40	Pathology	20.0	2.0.	100.0
Li [152]	66	48	MRI	34.7	4.0	-
Fallenberg [153]	-	80	MRI	27.7	-	-
Mun [154]	173	169	Mammography	23.8	< 2.0	-
Liberman [155]	666	429	MRI	10.0	3.0	70.0
Brem [150]	201	201	Mammography	-	0.5	70.0
Cortadellas [156]	-	73	MRI	22.5	-	-

2.4 Modeling Breast Deformations

Similar frameworks to those presented in Section 2.3.3.7, where preoperative images registered to intraoperative data, breast modeling approaches provide image-to-physical alignments but extend the registration methods beyond a rigid transformation. These correction approaches model the deformations that occur between imaging and surgery and correct the shape changes, rendering more accurate predictions of intraoperative tumor position.

Biomechanical models can provide predicted tumor locations based on constitutive equations that govern tissues' response to force. Many groups have applied the finite element (FE) method to approximate solutions to these complex mechanics problems in breast tissues [48, 49, 157–166]. However, much of this work focuses on applications outside of surgical guidance. Breast biomechanical modeling has focused on screening and diagnostic applications [163, 167], with some groups working towards plastic surgery applications [48], and localization for biopsy procedures [165].

While there are also biomechanical modeling approaches intended for surgical guidance, many of these

works focus on registrations involving large shape changes. Due to the high sensitivity and quality of breast MR imaging, many groups have developed approaches to leverage diagnostic MR images in surgery. These works model the deformations from prone-to-supine configurations, aiming to approximate a supine MR image by deforming a diagnostic MR image [157–161, 168]. Due to the large deformations between diagnostic imaging and surgical position as discussed in "Image-to-Surgical Deformations" (Section 2.2.2) it is difficult to obtain the supine breast position from conventional volumetric diagnostic images (prone MRI or mammography). Many of these methods involve patient-specific parameters optimized from supine MR data [158, 160], with several approaches ultimately incorporating full supine MR imaging data to enhance their prone-to-supine modeling [157, 161]. Beyond accuracy limitations due to large shape changes, quantified analysis of algorithm performance is also difficult and rare. The existing body of literature generally quantifies performance with residual surface misalignment [48, 49, 158, 168] which can underestimate point-based misalignments (i.e. surface alignments can be easier to achieve than point-based alignments). This point is visible in the results of [158], where registration error was lower when measured as a surface residual (4.1 mm) than when measured as a point-wise error at the nipple point (8.1 mm). This factor is especially important in the context of surgical margin management, where it is clinically important to predict the precise locations of all points tumor margins—not only skin or chest surface alignments. Requiring supine imaging to achieve optimal algorithm performance suggests that prone imaging alone is insufficient for accurate localization in the supine position.

In 2006, Carter *et al.* used supine MR to create a patient specific model, and this model was nonrigidly registered to the prone MR image [169]. The authors use supine to prone registration to determine the location of the lesion in the supine image, as contrast was only used in the prone position. Intraoperatively, the supine breast model is nonrigidly deformed using a camera-acquired breast surface as a boundary condition, and treating the chest wall as a rigid body. Nine surface fiducials were placed on the skin and five landmarks were manually identified within the MR volume. Target error was estimated to be below 4 mm based on the system's ability to predict surface and subsurface positions in MR images after repositioning the patient in the scanner. However, the results of the intraoperative supine to supine registration were not directly quantified, nor was the stereo camera accuracy. Later, Carter *et al.* evaluated this system in one patient. A section of the tumor boundary was localized in a single tracked IOUS image, and the predicted tumor location was around 5 mm from this ground truth tumor location [170]. Though this shows promising utility of supine MR in the operating room, the accuracy remains to be more thoroughly quantified on a wider range of subjects.

Emerging works that indicate supine imaging can provide comparable diagnostic value and resolution [47, 62, 63] have driven a shift towards using supine MR images and using model correction to estimate deformations from imaging-to-surgery. In 2014, Ebrahimi *et al.* introduced a method without biomechanical

models using just thin plate splines to estimate breast displacements from 180 ° arm abudction [171]. Evaluated on data from five patients, the method reduced lesion localization error from 3–18 mm to 1–10 mm using surface data from 24–34 localized fiducials. Though these results indicate that nonrigid correction can help compensate for supine deformations, improvement was inconsistent across cases and evaluation was limited to tumor overlap metrics and centroid distances.

In 2015, Conley *et al.* presented a patient specific biomechanical breast model generated from a dynamic contrast enhanced supine MR image [60]. A rigid registration of surface fiducials was followed by a rigid registration of the chest wall. The direction of gravity was assumed to be perpendicular to the patient's bed, and the direction of gravity acting on the breast was estimated by applying the final rigid rotation to the intraoperative gravity vector. This change in gravity was used to compute the body forces. Distances between fiducials were measured in the preoperative image and the intraoperative position, and the maximum change in interfiducial distance was distributed evenly across inferior and superior boundary surfaces, and prescribed as type one displacement boundary conditions. After this non-rigid registration, residual error at surface fiducials was 2.9 mm and 7.4 mm for two cases. The resulting displacement field was computed and applied to preoperative images to obtain a model predicted tumor location. This tumor location was compared to the intraoperative tumor location as measured with compression corrected ultrasound, with resulting tumor centroid distances of 5.5 mm and 5.4 mm.

These modeling approaches show promise in reducing localization accuracy, though integrated systems for nonrigid correction have yet to be fully realized. Data collection in [60] was feasible, with the correction approach relying only on mock-intraoperative measurements using 6–7 fiducials and tracked ultrasound imaging of the chest wall. For [171], data collection in the operating room would be more extensive, requiring 20–30 fiducials for alignment. The authors discuss challenges related to the optimal number of fiducials as decreasing the number of markers reducing accuracy, and increasing the number of fiducials confounding correspondence [171]. The need for dense intraoperative localization becomes apparent. Furthermore, evaluation of accuracy improvement has been relatively limited, with main outcomes reporting tumor centroid alignment, and no previous study reporting statistical significance. Nonrigid correction of supine-to-supine breast deformation has previously been evaluated in only seven regions of interest totaled across the two relevant studies [60, 171]. While results are promising, there remains a need for more quantified accuracy, and statistical testing comparing performance to rigid registration approaches, like those leveraged in Section 2.3.3.7.

2.5 Intraoperative Measurements

2.5.1 Instrument Tracking

These image guidance approaches bring to light the need for intraoperative data collection. One common form of intraoperative data collection is tracked tools. Tracked tools allow for manual designation of points and surface swabbing to enable registration approaches that align preoperative data to the intraoperative scene. Currently there are two main methods for tracking instruments during surgery: optical tracking and electromagnetic tracking. Actively tracked tools are constantly emitting a signal, such as infrared light, while passively tracked tools reflect signal emitted by another source source—generally the tracker itself.

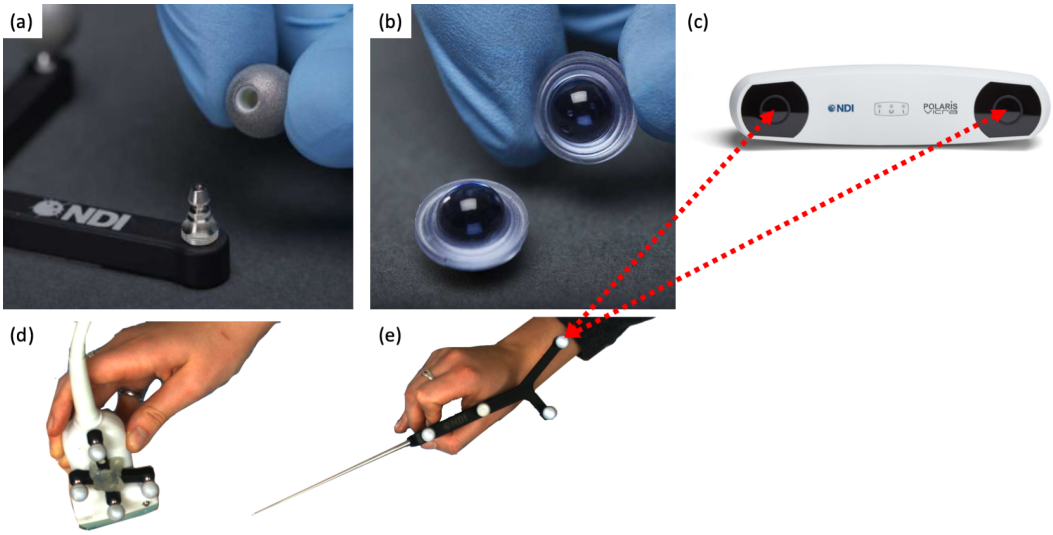

Figure 2.12: Summary of optical tracking, dotted red lines indicate the rays of infrared light reflecting off one passive marker sphere on the tracked stylus tool. (a) passive marker spheres reprinted from [172], (b) Radix™ lenses reprinted from [173], (c) Polaris Vicra optical tracker reprinted from [174], (d) ultrasound probe with optically tracked reference object rigidly fixed, and (e) optically tracked stylus.

Optical instrument tracking, shown in Figure 2.12 can use both actively and passively tracked tools. Infrared light is emitted from two cameras on the tracker and tools are tracked via reflective markers. Reflective marker spheres, like those shown in Figure 2.12a are coated in thousands of reflective microbeads [172]. The spheres are visible at $\pm 90°$ viewing angles, but are single use (i.e. cannot be re-sterilized). Reflective hemispheres called Radix™ Lenses can be wiped clean and sterilized, but have a slightly larger diameter and a smaller viewing angle ($\pm 60°$) than the reflective spheres [173]. Either of these markers can be combined in a unique geometry and rigidly fixed onto tools to enable simultaneous tracking of multiple tools.

While there are many commercial tracking systems from several companies [175] , this discussion will focus on just a few. A Polaris Vicra (Northern Digital Inc., Waterloo, ON, Canada) can track up to 6 passive and 1 active wireless tools simultaneously, a Polaris Vega can track up to 6 active wireless tools simultaneously [174, 176]. Marker localization is accurate to 0.25 mm for the Vicra, and 0.12 mm for the Vega, though

localization accuracy for a rigid body tool degrades based upon the calibration accuracy for the tool tip position, or the defined relationship between the tracked markers and the tool tip. The HX40 MicronTracker (ClaroNav Inc, Toronto, ON, Canada) is a device for optical tracking using visible light instead of infrared light. The MicronTracker reports a calibration accuracy of 0.2 mm, and can track a maximum of 100 markers concurrently [177]. In 2008, the ClaroNav and the Northern Digital optical tracking systems were compared with Northern Digital Inc proving more robust, and the MicronTracker showed to be sensitive to luminosity, shadows and motion [178]. Optical tracking, particularly with devices such as the Polaris Vicra and Vega, is well suited for intraoperative guidance due to its robust accuracy and ability to track multiple wireless tools. Optical tracking is, however, limited by line-of-sight constraints, meaning that there must be a clear path between the tool and the tracker in order for the tool to be localized.

For electromagnetic tracking, a low-intensity electromagnetic field is generated and tools contain electromagnetic micro sensors. These sensors induce a current when they enter the electromagnetic field, and this current is detected and converted to a position and orientation for tool localization. The Polaris Auora tracker, also produced by Northern Digital Inc., can have a maximum of 6 simultaneously tracked tools [179]. Since electromagnetic tracking does not depend on line-of-sight, sensors can be tracked in-vivo, though all tools must be wired and connected to a power source. Sensors' small form factors allow them to be embedded into flexible tools or needles and even embedded at the tool tip itself. However, compared to optical tracking, electromagnetic tracking accuracy is worse with sensor localization at 0.70 mm and can degrade further with field distortions due to conductive or ferro-magnetic objects in the field.

2.5.2 Surface Point Cloud Acquisition

There are many methods for obtaining surface data in the operating room. These methods can be broken down into two main categories: fixed-view surface reconstruction and handheld-mobile surface reconstruction. In the first, the device is stationary, while for the latter, the measurement device is moved around the object. Though precise surface scanning technologies exist, many of these devices are either stationary and too large to be integrated into surgical workflows, or are handheld requiring time for manual surface scanning [180]. It should also be noted that a handheld mobile surface reconstruction approach requires more time and manual digitization than a stationary method, and therefore cannot be easily integrated into an automated surface acquisition framework to provide surface updates throughout surgery.

In Simpson *et al.*, three intraoperative surface measurement approaches were compared: tracked stylus, laser range scanner, and conoprobe [181]. The specifics of an optically tracked stylus are discussed in the previous section. A laser range scanner uses a laser to pass a line of light across an object, receiving the signal with a camera and employing triangulation to locate the structure in 3D space. Also using a laser, a conoprobe

obtains a point-based measurement, reporting the distance from the laser source to the reflected light point on the object. The study found that non-contact digitization methods outperformed contact digitization, and that the conoprobe measurements were the most accurate, though still required time consuming manual swabbing [181]. Laser range scanning, the only one of these methods suited for hands-free digitization was incorporated into a guidance framework for BCS [60], with reported accuracy of 2.2 ± 1.0 mm [182]. Unfortunately, due to the time required to scan the breast, breathing motion is captured in the data measurements causing errors in the resulting surface. When evaluated on subjects with respiratory motion, all three of these measurement approaches carry inherent measurements error from capturing different time-points in the breath cycle as none of them are instantaneous. Other groups have obtained the intraoperative breast surface with a handheld structured light scanning system [50, 137]. However, none of these breast guidance systems incorporate the collected surface data into the registration approach. 3D breast surface scans acquired at the start of surgery provide texture-rich breast renderings useful for guidance visualizations, but have yet to be incorporated into a registration framework.

2.6 Computer Vision

Computer vision approaches use typical color images, and process these images to provide measurements from the scene. Images are generally composed of red, green, and blue (RGB) color channels, that are combined to create the perceived color representation. Similar to how human eyes can perceive depth by using two eyes, stereo cameras can perceive depth by using multiple views of an object. In this thesis, the term stereo-camera is used to refer to two cameras rigidly attached with largely overlapping fields of view. These two cameras are referred to as the left and right cameras. Objects in a scene can be localized in 3D space when viewed from two distinct camera positions if the stereo cameras have been properly calibrated to define the relationship between pixel coordinates in the cameras and world coordinates in the real 3D scene.

2.6.1 Fiducials from Color Images

Many technologies have been developed for reliable object detection and tracking using computer vision. Most of these fiducial markers rely on the sharp contrast between white and black and a set of known grid configurations. These fiducials give position and pose. A well known example of this type of fiducial is ArUco (Augmented Reality University of Cordoba) Tags [183–185]. ArUco Tags are freely available and implemented in the OpenCV toolkit [186], making them a popular choice for research applications, though many other similar tags exist as visualized in Figure 2.13).

Accuracy and detection rate depend on the resolution of the camera, size of the marker, and the viewing angle [187]. Localization accuracy for 14.6cm binary square tags is 17–47 mm when viewed from a distance

of 1 m [187]. For 5 cm markers localization accuracy ranges from 1–30 mm when viewed from 0.05–0.5 m distances [188], with an average accuracy of 7 mm. This study reports two types of marker tags with accuracy below 2 mm, 100% precision and over 99.9% recall even across 0–75°viewing angles [188]. However, fiducials are mounted to flat rigid objects, and the small distance between cameras and tags would be intrusive in the clinical setting. While these marker methods support large potential dictionary sizes (from 30 to over 8 million unique tags, depending on the type) [188], this high number of tags is less of a benefit intraoperatively, where less unique markers are needed and large markers sizes limits the number of points able to be applied to a patient. The large size also limits marker placement, as they should fit on the workable surface for surgery, but also should not be cut during surgery. Another limitation of these fiducial tags is that the maximum tracking distance between the cameras and tags is 1.3 m, with many marker types limited to about 1 m or less for 5 cm tags [188]. Beyond these distance limitations, Fiducial localization accuracy has not been evaluated for marker-sizes, distances, and viewing angles realistic for surgical applications.

These tags were designed for pose and location information in the context of augmented reality and robotics, and tags were therefore developed to be printed and fixed on rigid, planar surfaces. Since they were not originally intended for precise dense point detection on deformable surfaces, localization accuracy is limited on curved skin surfaces. Recently, deformable tags have been developed using full color fiducials and deep learning [189] with a high detection rate, though localization accuracy was not quantified. Tags have also been paired with depth sensors for improved pose estimates and reduce pose ambiguity at steep angles [190].

In neurosurgery, facial landmarks can be detected and used for registration [191], however the breast surface is virtually featureless adding in additional challenges. With this limitation in mind, [137] and [138] fixed binary marker tags to bony structures surrounding the breast tissue for image-to-physical registration. Unfortunately, this fiducial placement does not capture any nonrigid motions of the breast tissue. In the context of intraoperative guidance, marker tags encode valuable information that would allow for imaging-to-OR correspondence essential for many registration approaches. However, there remains a need for accurate fiducial localization on deformable, non-planar, skin surfaces. Unlike large printed tags that must be adhered to the skin surface far from an incision, fiducials should also be compatible with dense distributions to sufficiently sample breast motion, and should not interfere with resection.

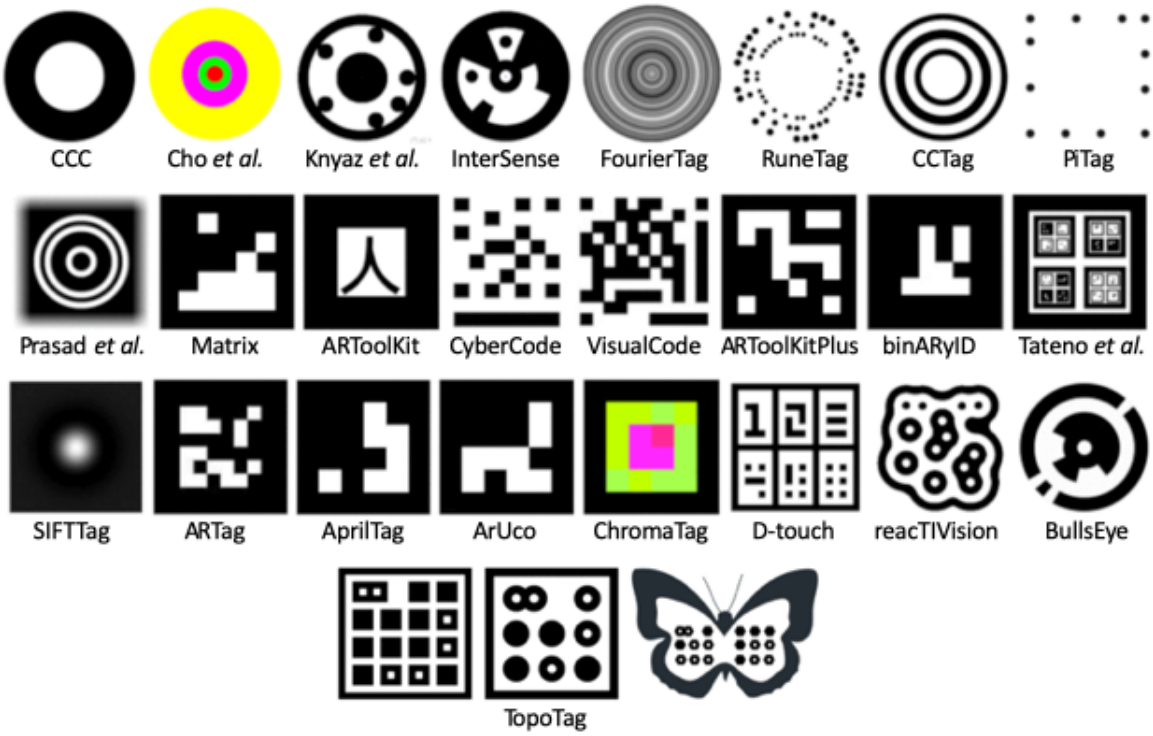

Figure 2.13: Existing fiducial marker systems. From left to right, top row: CCC [192]; Cho [193]; Knyaz *et al.* [194]; InterSense [195]; FourierTag [196, 197]; RuneTag [198, 199]; CCTag [200, 201]; Pi-Tag[202]. Second Row: Prasad *et al.* [203]; Matrix [204]; ARToolKit [205]; CyberCode [206]; VisualCode[207]; ARToolKitPlus [208]; binARyID [209]; Tateno *et al.* [210]. Third Row: SIFTTag [211]; ARTag [212]; AprilTag [213, 214]; ArUco[183–185]; ChromaTag [215]; D-touch [216, 217]; reacTIVision [218–220]; BullsEye [221]. Last Row: TopoTag [188]. Images reproduced with permission from [188] ©2020 IEEE.

.

CHAPTER 3

Methodology

3.1 Registration

Registration computes the relationship between two spaces. For example, points in a medical image volume designated with respect to the image origin at [0,0,0] can be aligned, or registered, with points in the physical world space designated with respect to a measurement device. The process of rigid registration, as described in [222] computes a rotation, **R**, and a translation, **t** between two spaces. The rotation matrix is a 3×3 matrix, and the translation matrix is a 3×1 matrix. In this work, boldfaced variables represent vectors or matrices. The matrices can be combined into a 4×4 homogenised transformation matrix $T(\mathbf{x})$ where,

$$T = \begin{bmatrix} \begin{bmatrix} & & \\ & \mathbf{R} & \\ & & \end{bmatrix} & \begin{bmatrix} t_x \\ t_y \\ t_z \end{bmatrix} \\ \begin{bmatrix} 0 & 0 & 0 \end{bmatrix} & 1 \end{bmatrix} \tag{3.1}$$

and

$$T(\mathbf{x}) = \begin{bmatrix} \begin{bmatrix} & & \\ & \mathbf{R} & \\ & & \end{bmatrix} & \begin{bmatrix} t_x \\ t_y \\ t_z \end{bmatrix} \\ \begin{bmatrix} 0 & 0 & 0 \end{bmatrix} & 1 \end{bmatrix} \begin{bmatrix} x_{1x} & x_{2x} & \dots & x_{Nx} \\ x_{1y} & x_{2x} & \dots & x_{2x} \\ x_{1z} & x_{2x} & \dots & x_{Nx} \\ 1 & 1 & \dots & 1 \end{bmatrix}. \tag{3.2}$$

Registration accuracy is typically evaluated with two metrics: fiducial registration error (FRE), and target registration error (TRE), as defined in [223]. Both measure how well a transformation describes the relationship between spaces; FRE measures accuracy at points used to compute the transformation, and TRE measures accuracy at novel points not used to compute the transformation. In order to compute these metrics, points must be identifiable in both coordinate systems.

More specifically, with N as the number of points, FRE is a measure of landmark misalignment computed as the distance between the positions in one space, denoted here as **static**, (e.g. image voxel coordinates), and the transformed points $T(\mathbf{dynamic})$ from the second space (e.g. measurements in physical world coordinates). In other words, the dynamic points are transformed to be in the same space as the static points, and

the residual error is measured as

$$FRE = \sqrt{\frac{1}{N}\sum_{i=1}^{N}(T(\mathbf{dynamic}_i) - \mathbf{static}_i)}. \tag{3.3}$$

Keep in mind that point locations $\mathbf{static}_i$ and $\mathbf{dynamic}_i$ represent coordinate vectors, where each vector has three coordinates: x, y, and z, and is homogenised to be $\mathbf{static}_i = [x, y, z, 1]^T$, where $[*]^T$ represents the transpose of a matrix, or the interchanging of columns and rows, and the subscript i represents the index of an individual point within a set of N total points.

TRE is a measure of novel target misalignment, where targets in the static space $\mathbf{q}$, are compared to their transformed counterparts in the dynamic space $T(\mathbf{p})$

$$TRE = ||(T_i(\mathbf{p}) - \mathbf{q}))||. \tag{3.4}$$

Note that in Chapter 5, instead of the root mean square (RMS) error, FRE and TRE are reported as the mean and standard deviation for euclidean distances between points and their transformed counterparts.

3.2 Image Guidance System

An novel image guidance system was developed to collect intraoperative data and display all data sources co-registered (Figure 3.1). The module is a Python based scripted module in 3D Slicer [224]. The four-panel display shows preoperative supine MR images, intraoeprative ultrasound, and a 3D scene with all data inputs co-registered (aligned and displayed in the same space).

3.2.1 Monitoring of the Surgical Scene

Monitoring of the surgical scene is important in providing an accurate and workflow friendly guidance system that can be used throughout surgery. A tracked ultrasound probe allows for intraoperative imaging correctly oriented in 3D space. Optical tracking reliably tracks multiple instruments with high accuracy, however the infrared reflecting fiducials are not well suited for surface tracking as they cannot remain on the breast surface during surgery, and they do not provide correspondence for registration approaches without additional processing that becomes increasingly cumbersome for large numbers of points. By employing stereo cameras to monitor the breast surface, fiducials can be drawn directly onto skin with indelible marker. These fiducials, drawn as letters, are workflow friendly, sterile, and provide landmarks on the previously featureless skin surface.

An optical tracker is ideal for tracking multiple rigid body instruments throughout surgery, while the rich data stream from stereo cameras is better suited for tracking the non-rigid deformations of the skin surface.

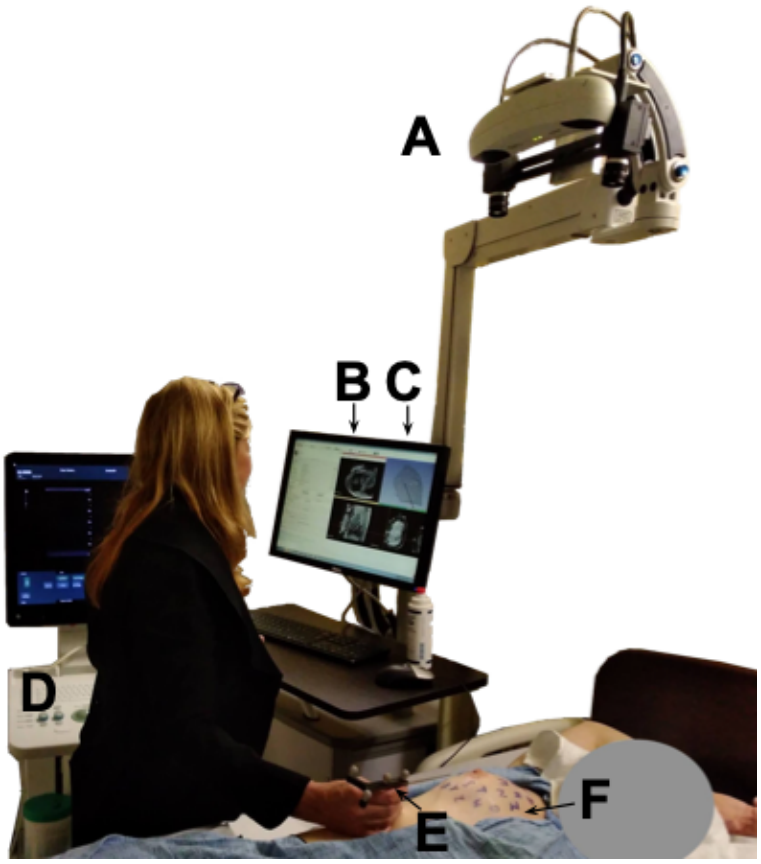

Figure 3.1: Overview of the system setup (A) coupled stereo camera and optical tracker attached to a surgical arm (B) preoperative supine breast MR image in axial, sagittal, and coronal slice views (C) patient-specific 3D breast model (gray), tracked stylus position (black) (D) Ultrasound machine (E) optically tracked stylus (F) breast with fiducial points and letter labels.

Here, a Polaris Vicra (Northern Digital Inc., Waterloo, ON, Canada) is rigidly coupled to two Grasshopper cameras (FLIR, formerly Point Grey, Richmond, BC, Canada). The devices are shown in Figure 3.1A, with the black stereo cameras behind the Vicra optical tracker. The devices are angled towards each other to increase the the functional working volume observed by both methods. These tracking devices are mounted on an adjustable surgical arm, and sit about 0.75-1.5 meters above the patient, providing a birds-eye view of the surgical scene. In Figure 3.1 the devices are approximately 1.3 m above the scene.

3.2.1.1 Surface Point Acquisition with Stereo Cameras

Stereo cameras provide intraoperative breast surface points while easily integrating into surgical workflow with minimal user interaction. The stereo cameras are optimal for surface monitoring as they can monitor precise point locations on the surface throughout surgery, providing corresponding points between preoperative imaging and the intraoperative scene. A image capture software, previously custom-built in the laboratory [225], collects image pairs from two Grasshopper stereo cameras (FLIR, formerly Point Grey Research, Richmond, BC, Canada).

3.2.1.1.1 Stereo Camera Calibration

A method for calibrating stereo calibration was presented in 2000 by Zhang [226] that computed the extrinsic and intrinsic camera parameters using images of a known planar pattern at a series of unknown orientations. There are many kinds of planar patterns that can be used for camera calibration. Two popular calibration boards are a checkerboard and a grid comprised of circles. In practice, the pattern is inconsequential provided it is (1) of known spacing and (2) easily and precisely measurable in images. Calibration boards are usually in black and white, as this color combination offers the best contrast for precise point localization, though this is not required.

Briefly, the calibration process outlined in [226] is as follows. The calibration board is imaged at several angles and the precise measured calibration feature points are localized with image processing techniques. For a checkerboard, these calibration points are the corners, or intersections of the black and white squares. For a circle grid, the centroid of each circle is used as a calibration point. The spacing of these calibration points in 3D world space is known, as prescribed by the known dimensions of the calibration pattern. Based on these 3D coordinates and the observed locations of these locations in the 2D image planes, the camera parameters can be estimated. Intrinsic camera parameters describe properties specific to each individual camera such as the optical center, or principal point, and the focal length or the distance from the image plane to the optical center. Other intrinsic camera parameters account for skew and distortion related to the camera lens. The focal length is often represented as f_x and f_y, incorporating directional skew to account

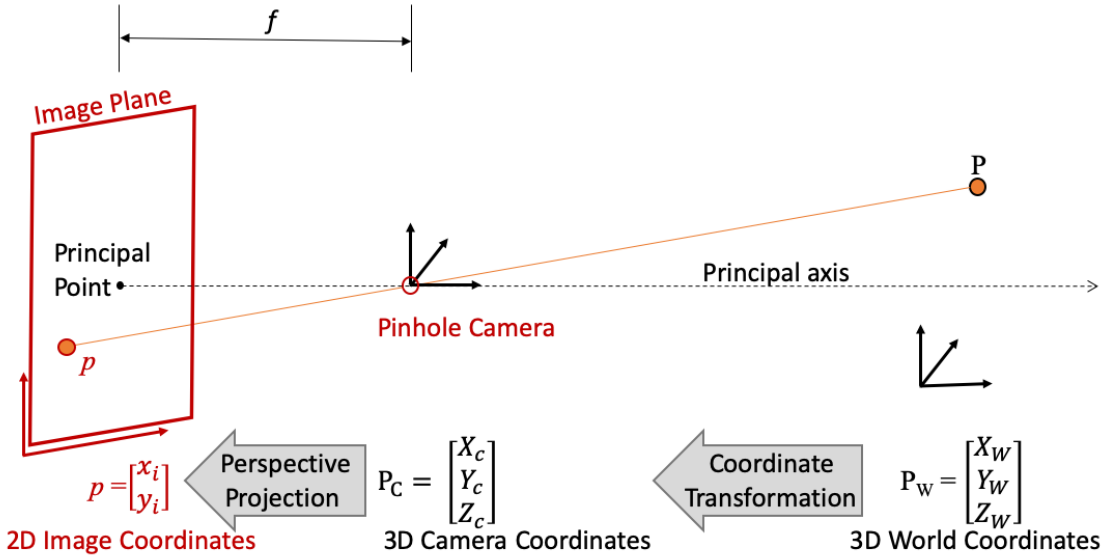

Figure 3.2: Standard pinhole camera model with the representation of a point in World, Camera, and Image coordinate spaces all in mm.

for possible discrepancies in pixel densities in the x and y directions (i.e. pixels that represent rectangles in real-world space). Extrinsic camera parameters describe the position of the camera in world coordinate space as a rotation and translation with respect to some origin in the real world. For a stereo camera system, the extrinsic parameters encode the relationship between the left and right cameras in real-world space.

More specifically, the camera parameters are estimated using the standard pinhole camera model, as visualized in Figure 3.2 [227], where the properties of similar triangles dictate that

$$\frac{x_i}{f} = \frac{x_c}{z_c}, \quad and \quad \frac{y_i}{f} = \frac{y_c}{z_c}. \tag{3.5}$$

with f as the focal distance, or the distance between the pinhole and the image plane, the point location in image coordinates $p = [x_i, y_i]^T$, and the point location in camera coordinates $P_c = [x_c, y_c, z_c]^T$

Image coordinates (e.g. mm) are related to pixel coordinates by considering the pixel density, m pixels/millimeter. When pixels are not square, the pixel density must be defined in each of the two orthogonal image directions u and v, resulting in pixel densities m_u and m_v respectively [227]. Therefore from Equation 3.5 the pixel coordinates (u, v) are defined as

$$u = m_u x_i = m_u f \frac{x_c}{z_c}, \quad and \quad v = m_v y_i = m_v f \frac{y_c}{z_c}. \tag{3.6}$$

Simplifying, the focal length is combined with the pixel density to become a general scale factor along

each of the image axes, f_u and f_v be defined with respect to the pixel density and the focal length f. To relate the focal length, f in mm, to the focal lengths as measured in pixels, f_u and f_y are defined as

$$f_u = f m_u, \quad and \quad f_v = f m_v. \tag{3.7}$$

Similarly, to relate the principal point (o_x, o_y) to pixel dimensions, o is defined with coordinates $o_u = m_u o_x$ and $o_v = m_v o_y$. The principal point can also be thought of as the offset between the center of the image plane and the origin of the pixel coordinates. Therefore the pixel coordinates for a point also take this principal point into account, with

$$u = f_u \frac{x_c}{z_c} + o_u, \quad and \quad v = f_v \frac{y_c}{z_c} + o_v. \tag{3.8}$$

The camera parameters, f_u, f_v, o_u, o_v are estimated using the method presented by [226]. A 3D point in world coordinate space is denoted as $\mathbf{P} = [X_w,\ Y_w,\ Z_w]^T$, and a 2D point in image coordinates is $\mathbf{p} = [u, v]^T$, so that the relationship between the homogeneous coordinates of the 3D point, $\tilde{\mathbf{P}} = [X_w,\ Y_w,\ Z_w,\ 1]^T$ and the homogeneous coordinates of its image projection in 2D pixel space $\tilde{\mathbf{p}} = [u,\ v,\ 1]^T$ is given by

$$s\tilde{\mathbf{p}} = \mathbf{A}[\mathbf{R} \quad \mathbf{t}]\tilde{\mathbf{P}}, \quad with\ \mathbf{A} = \begin{bmatrix} f_u & \gamma & o_u \\ & f_v & o_v \\ & & 1 \end{bmatrix} \tag{3.9}$$

where s is an arbitrary scale factor, $(\mathbf{R}, \mathbf{t})$ are now the extrinsic parameters defining the rotation and translation between the camera coordinate system and the world coordinate system, and $\mathbf{A}$ is the camera intrinsic matrix, with γ representing the skew of the two image axes. In the case of perfectly square pixels, $f_u = f_v$. In Equation 3.9, the parameters of $\mathbf{A}$ are measured in pixel coordinates. By imaging a board with known inter-point distances, $\mathbf{A}$ can be optimized. The camera parameters are estimated with a closed form solution followed by a nonlinear refinement based on maximum-likelihood criterion.

The two stereo cameras are calibrated with MATLAB's Computer Vision System Toolbox [228]. Twelve calibration images of a 6×8 checkerboard provide 576 points to solve for the calibration matrices by a least squares method [226–228]. The calibration protocol is detailed in Appendix A.

3.2.1.1.2 Triangulation

With a point localized in an image from one calibrated camera, the three dimensional location of that point is constrained to an outgoing ray, though the exact position on that ray (i.e. the depth) is still unknown. With a point localized in another image from a calibrated camera, there are then two outgoing rays. Provided

these images are taken from two different vantage points, these rays intersect at some depth, Z, allowing for triangulation of the 3D coordinates of the point in the scene. Here, assume a simple stereo system comprised of two calibrated cameras, where $\mathbf{p_L} = (u_L, v_L)$ represents the point location in the left image (l), and $\mathbf{p_R} = (u_R, v_R)$ represents the point location in the right image (r)

Given the intrinsic and extrinsic calibration parameters, the projection matrix can be defined to project a 3D coordinate point, $\mathbf{P}_C$, in one camera's coordinate frame into 2D pixel coordinates (u, v) for either camera, with $\mathbf{R}$ and $\mathbf{t}$ describing the relationship between the two cameras. Here, with $\mathbf{P}_{CL} = [X_{CL}, Y_{CL}, Z_{CL}, 1]^T$ as the 3D world point in the coordinate frame of the left camera,

$$\begin{bmatrix} u_L \\ v_L \\ 1 \end{bmatrix} = \begin{bmatrix} & & 0 \\ \mathbf{A}_L & & 0 \\ & & 0 \end{bmatrix} \begin{bmatrix} X_{CL} \\ Y_{CL} \\ Z_{CL} \\ 1 \end{bmatrix}. \tag{3.10}$$

The transformation between the cameras and the right camera's intrinsic parameters then describe the pixel coordinates in the right image as

$$\begin{bmatrix} u_R \\ v_R \\ 1 \end{bmatrix} = \begin{bmatrix} & & 0 \\ \mathbf{A}_R & & 0 \\ & & 0 \end{bmatrix} \begin{bmatrix} \begin{bmatrix} & & \\ & R & \\ & & \end{bmatrix} & \begin{bmatrix} t_x \\ t_y \\ t_z \end{bmatrix} \\ 0 \quad 0 \quad 0 & 1 \end{bmatrix} \begin{bmatrix} X_{CL} \\ Y_{CL} \\ Z_{CL} \\ 1 \end{bmatrix}. \tag{3.11}$$

For any pair of known corresponding points $\mathbf{p}_L$ and $\mathbf{p}_R$, the over-determined system of equations defined by combining Equations 3.10 and 3.11 can be solved for $\mathbf{P}_{CL}$ with a least squares solution [227, 228].

3.2.1.2 Coupled Stereo Cameras and Optical Tracker

Optical tracking is the gold standard in tool tracking, providing precise and accurate tool locations without the hassle of wired instruments. Coupling an optical tracker for instrument tracking with the surface monitoring of the stereo cameras gives a system with all the strengths of both measurement systems. The stereo cameras and optical tracker are fixed above the surgical field for optimal line of sight without obstructing the surgical workflow. The rigid coupling allows for a one-time registration aligning instrument and stereo camera spaces. These two spaces can then be rigidly aligned with the preoperative supine MR with the cancerous region identified. After this initial registration optically tracked instruments, the camera acquired breast surface, and preoperative image data can all be displayed in the same space.

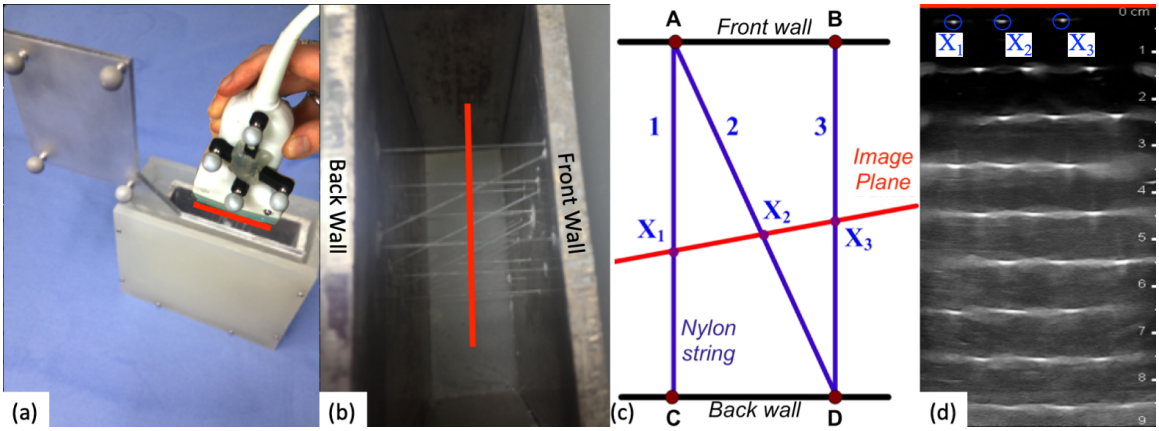

Figure 3.3: Ultrasound calibration N-wire phantom. The edge of the ultrasound transducer (the top of the image plane) is shown in each image in red. (a) the N-wire phantom, with optically tracked fiducials inside its water bath enclosure; (b) the top down view of the N-wires; (c) the internal geometry of a single "N", as viewed from the top (d) a resulting calibration image with N-wire cross sections visible as bright points.

3.2.2 Tracked IntraOperative Ultrasound (IOUS)

IOUS has been shown to reduce reoperation rates when used to localize tumors during surgery, offering valuable information for echogenic tumors. This system incorporates these benefits and expands upon them with the added utility of visualizing tracked ultrasound planes with respect to other preoperative and intraoperative data. However, the location of the ultrasound plane can be difficult to visualize at depth, and cannot be located precisely without tracking. Conventional optical tracking of an ultrasound transducer can provide the location of the ultrasound image in physical space. Once the transformation between ultrasound images and the tracked transducer is defined through calibration, the relative position of the image can be shown with respect to other patient information such as breast and tumor models, preoperative imaging, and intraoperative surface points.

Calibration of the tracked ultrasound transducer is performed with a custom Python scripted module built in 3D Slicer [224] that uses the N-wire ultrasound calibration technique [229]. Components of this N-wire calibration are shown in Figure 3.3. Briefly, using the known geometry of the N-Wire phantom, the intersection of the image plane and the diagonal line of the "N" can be located in the instrument tracker space. This point is identified in the ultrasound image as the middle dot in each of the 9 N-layers. The ultrasound image can be mapped into the scene rendering of physical space via this calibration process. The 3D Slicer module for ultrasound calibration developed for this dissertation facilitates tracking of the N-wire phantom, designation of phantom points with an optically tracked stylus, ultrasound image collection, loading of saved images, and designation of N-wire cross sections. The module computes the calibration matrix and report accuracy metrics.

The calibration process, as described in [229], determines the relationship between a pixel position in the ultrasound image (${}^{U}\mathbf{X}$) and that point's position measured in mm with respect to the ultrasound probe (${}^{P}\mathbf{X}$). This transformation from ultrasound image space (U) to transducer probe space (P) is denoted ${}^{P}_{U}T$. To achieve this, the point location is first described in the coordinate system of the N-Wire phantom (H) and the coordinate system of the optical tracker (T). The pixel coordinate in the ultrasound image (${}^{U}\mathbf{X}$) is transformed to be a location with respect N-wire phantom (${}^{H}\mathbf{X}$) as described by

$$ {}^{H}X = {}^{H}_{T}T \cdot {}^{T}_{P}T \cdot {}^{P}_{U}T \cdot {}^{U}\mathbf{X}. \tag{3.12} $$

When the transforms are nonsigular and homogenous (i.e. $({}^{B}_{A}T)^{-1} = {}^{A}_{B}T$), Equation 3.12 is equivalent to

$$ {}^{P}_{U}T \cdot {}^{U}\mathbf{X} = {}^{P}_{T}T \cdot {}^{T}_{H}T \cdot {}^{H}\mathbf{X}. \tag{3.13} $$

where the left side of Equation 3.13 describes the pixel location being transformed to a 3D coordinate with respect to the tracked probe, and the right side of the equation describes the pixel location with respect to the tracked N-wire phantom being transformed into tracker space, then probe space.

Because the front and back walls of the N-wire phantom are parallel, special triangles formed by the N-wires dictate that the ratio α between line segments is

$$ \alpha = \frac{||\mathbf{A}-\mathbf{X_2}||}{||\mathbf{A}-\mathbf{D}||} = \frac{||{}^{H}\mathbf{X_1} - {}^{H}\mathbf{X_2}||}{||{}^{H}\mathbf{X_1} - {}^{H}\mathbf{X_3}||} = \frac{||{}^{U}\mathbf{X_1} - {}^{U}\mathbf{X_2}||}{||{}^{U}\mathbf{X_1} - {}^{U}\mathbf{X_3}||} \tag{3.14} $$

where A and D are the corner vertices of the "N" wire, and X values describe intersection points between the imaging plane and the wires as shown in Figure 3.3c. The phantom's **A** and **D** vertices are measured with a tracked stylus for each N-wire layer in the phantom. Vertices on the same wall of the phantom should be co-planar, so they are fit to a plane to reduce localization errors. The position of the center point, $\mathbf{X_2}$ in the phantom frame can then be computed with

$$ {}^{U}\mathbf{X_2} = {}^{H}\mathbf{A} + \alpha \cdot ({}^{H}\mathbf{D} - {}^{H}\mathbf{A}). \tag{3.15} $$

Since the locations of $\mathbf{X_1}$, $\mathbf{X_2}$, and $\mathbf{X_3}$ can be directly measured in the ultrasound image (as seen in Figure 3.3d), the ratio α is known, and ${}^{H}\mathbf{X_2}$ can be computed by combining Equations 3.14 and 3.15.

Our initial implementation of the N-wire calibration used a least squares optimization to find ${}^{P}_{U}T$ that minimizes the distances between the two sides of Equation 3.13 as suggested in [229]. However this scheme was later updated. In order to define a transformation that is compatible with 3D slicer functionality to

stream the ultrasound image pixels into the 3D scene rendering, the transformation ${}^{P}_{U}T$ is assumed to be a transformation including rigid rotation, translation, and scaling components, as defined in [230], where the scale factors along each of the coordinate axes (s_x, s_y, s_z) are combined into a diagonal matrix, **S**, such that the relationship between ultrasound image space and N-wire phantom space is described by

$$ {}^{H}\mathbf{X_2} = {}^{H}_{U}T \cdot {}^{U}\mathbf{X_2} = \mathbf{R} \cdot \mathbf{S} \cdot {}^{U}\mathbf{X_2} + \mathbf{t} \tag{3.16} $$

The ultrasound calibration is validated via tracked optical stylus in a water bath and with residual error of N-wire images. For freehand validation, the stylus tip is placed at varying locations piercing the ultrasound plane and accuracy is measured by recording the distance between the stylus tip and the location from the calibrated ultrasound plane. The residual error of the intraoperative ultrasound calibration is also computed with novel N-wire images. Locations in optical tracker space are computed as they would be for calibration, and they are compared to the position of the center wires as manually designated in the ultrasound image [229]. This second method can alternatively be thought of as a leave-one-out validation. Though this method incorporates error associated with the N-wire phantom, it is much faster and easier than the stylus-in-water validation approach. Residual errors are on the order of 2 mm using a BK5000 18L5 linear probe (BK Medical UK Ltd., Peabody, MA) at 40-90 mm depths.

3.2.3 Integrated System

Intraoperative fiducial positions are measured with the stereo cameras and used to register the preoperative images to the patient and instrument spaces. The tracked tool tip is superimposed on the MR image to show distance and direction to the tumor. The module shows the tool with respect to tumor represenations in the three orthogonal cross-sectional slices of the preoperative MR image volume and a 3D model view. The tracked instruments are optionally used to scroll through MR slices, with the instrument visible in the MR slice. This can help orient the surgeon and allow full utilization of the information provided. This display gives an intuitive understanding of the relationship between the preoperative image and the patient on the table.

Data from the ultrasound and optical tracker are streamed continuously into the guidance module via Plus Toolkit (Perk Lab, Queen's University, Kingston, ON, Canada) [231]. The custom guidance module implemented in 3D Slicer [224] gives a 3D representation of the ultrasound plane and allows the user to view live and previously recorded ultrasound images in the scene with the aggregated information. This gives a clear understanding of the location of the ultrasound plane at depth, and helps the surgeon understand subsurface features with respect to the breast surface, intraoperative surface fiducials, and even other instruments. This

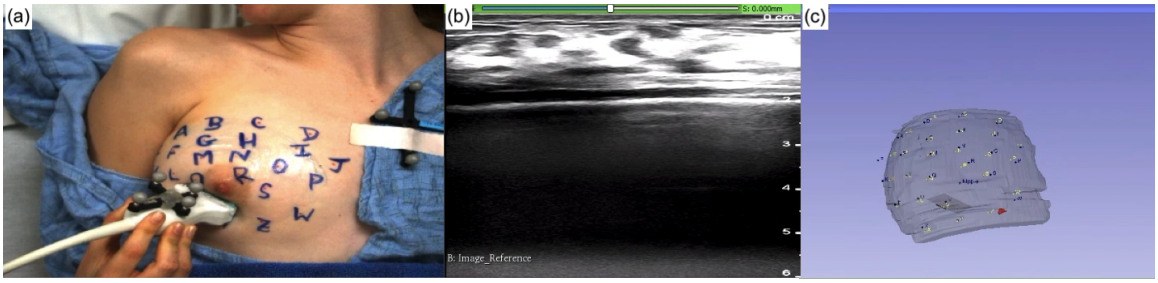

Figure 3.4: Tracked ultrasound allows for visualizing the image plane in 3D space. (a) camera view (b) ultrasound image, streamed into the integrated Slicer system (c) the 3D model view showing a semi-transparent rendering of the tracked ultrasound image plane in relation to a model of the breast, fiducial locations (blue and yellow), and a red mock tumor position.

is shown in Figure 3.4. The two sets of fiducials used for registration are seen clearly in Figure 3.4c, with preoperative fiducial positions shown in yellow, and intraopeartive fiducial positions shown in dark blue.

3.3 Biomechancial Modeling

3.3.1 The Inverse Problem

At static equilibrium, linear elasticity is governed by the Navier Cauchy equations in three dimensions [232]:

$$\frac{E}{2(1+\nu)}\nabla^2\boldsymbol{u} + \frac{E}{2(1+\nu)(1-2\nu)}\nabla(\nabla\cdot\boldsymbol{u}) + \rho(\Delta\boldsymbol{g}) + \boldsymbol{F} = 0 \tag{3.17}$$

where $E = 2100\ Pa$ is the Young modulus, $\nu = 0.45$ is the Poisson ratio, $\boldsymbol{u}$ is displacement, ρ is the tissue density, $\Delta\mathbf{g}$ is the change in gravity, and $\boldsymbol{F}$ is the applied force. In this thesis, the preoperative and intraoperative states are both in the supine position and the change in gravity, $\Delta\mathbf{g}$, from operating room table rotations is assumed to be negligible.

For the finite element method the domain is divided into smaller components, or elements, and a solution to the partial differential equation is estimated. In this work, the domain is meshed into tetrahedral elements with 4mm edge lengths using a custom mesh generator [233], that provides a set of points, or nodes, and connections between those nodes that define the individual sub-compartments, or elements. For a conventional forward-solved finite element model, intraoperative displacements are measured, applied to the points on the boundary of the domain, and then interpolated throughout the discretized domain using polynomials. The result is a displacement field across the whole organ. Using the Galerkin method of weighted residuals for discretization [234], 3.17 simplifies to a weak formulation of the partial differential equation in Equation 3.17:

$$\boldsymbol{K}\boldsymbol{u} = \boldsymbol{f} \tag{3.18}$$

where $\boldsymbol{K}$ is the stiffness matrix and $\boldsymbol{f}$ represents the forces acting on the system.

While these forward model approximations are valuable, they can fail to capture the true nature of how deformations were induced. For instance, as intraoperative breast deformations during arm motion are caused by underlying muscle and surrounding tissues acting on the organ, applying measured displacements to the skin surface in a breast finite element model would not be representative of the true physics involved. Approximating the true distribution of loads is important in solving for the true displacement field. The inverse problem addresses this concern. As opposed to directly applying measured displacements, the inverse approach attempts to reconstruct the distributed loads necessary to create the observed displacements. In a forward modeling approach, the material properties and boundary conditions are assumed to be known, and the model outputs volumetric displacements. Alternatively, in a reconstructive inverse model, the displacements and material properties are known, and the ideal boundary conditions to achieve these displacements are presumed to be unknown.

3.3.2 Linearized Iterative Boundary Reconstruction (LIBR)

Existing inverse modeling work and advances in other organ systems can be leveraged for the breast clinical problem. In liver guidance, a recent inverse modeling approach was presented by Heiselman *et. al.* [28] using a model discretized from a preoperative image and a series of control points distributed across the model surface, or boundary. Preoperatively, a library of small potential deformations is calculated. This is accomplished by slightly perturbing one control point and computing and storing the resulting effect on the mesh. A control point perturbation is treated as a Type 1 (i.e. Dirichlet) boundary condition, where the displacement is prescribed in one of the three coordinate directions. The Saint-Venant principle is employed to relax these point loads to be evenly distributed locally, removing exaggerated effects near the control point loading while keeping identical far-field behavior. This process is then repeated for all control points: perturbing, solving a forward model, relaxing, and saving the volumetric effect on the organ. This creates a set of precomputed deformation modes. Intraoperatively, these precomputed perturbations are weighted and combined to recreate the observed deformations. Levenberg-Marquardt optimization is used to solve for the optimal mode weights, iteratively minimizing model-data error and system strain energy in a scheme that also optimizes rigid transformation parameters.

This thesis modifies the LIBR method for data inputs and loading conditions specific to the BCS application. Here, forces are assumed to be applied from all boundaries except for where the breast skin interfaces with air. The skin interface with air is assumed to be stress free, while 45 control points are evenly distributed across all other boundaries. In short, displacements to drive the model are measured with sparse intraoperative data and assumed to be collected at the chest wall boundary and the skin surface.

3.4 Proposed Workflow

To understand the logistics of using this BCS guidance system, this section discusses the proposed workflow. Before imaging, MR-visible fiducials are evenly distributed across the breast. The number of fiducials should provide sufficient coverage to accurately describe breast displacements. Here fiducials will be used to capture nonrigid motion, so a larger number of fiducials are needed [171, 235]; 26 fiducials are used. To be sure that all fiducials are visible in the image, fiducials should be placed keeping in mind the field of view of the MR scanner. The center of each toroidal MR-visible fiducial is marked with colored ink. This semi-permanent ink can remain on the skin surface for days. For longer times between imaging and surgery, henna tattooing can be used to temporarily stain the fiducial locations on the skin surface.

If available, an open bore MR scanner should be used to image the patient in surgical position with the arm extended at 90°. In a closed bore scanner, images should be acquired with the ipsilateral arm fully adducted down at the patient's side. Padding may also be placed under the torso to simulate the anticipated rotated angle of the operating room table to reduce imaging-to-OR deformations due to rotations. When available, a plastic cage is recommended to support the coil and eliminate breast compression, otherwise padding can be placed on the sternum to reduce contact between the coil and the breast surface. Breast tissue is be imaged in the supine position using a 16 channel torso coil and a T1-weighted, 3D turbo field echo sequence with fat suppression. The imaging field of view is adjusted to maximize the number of visible fiducials. After imaging, the synthetic fiducials are removed leaving behind the temporarily tattooed fiducial centroids.

Preoperative data processing then begins. This can take place in the hour before surgery, or in the days prior if imaging is performed days in advance of surgery. The breast volume is segmented from the skin surface to the chest wall and the fiducial positions are designated and labeled with alphabetic characters A–Z. Fiducial labels provide naturally understandable correspondence between the model on the screen and the patient in physical space. The segmented volume is then input into the custom mesh generator to create a discretized volume of tetrahedral elements with 4 mm edge length[233]. Viewing the mesh and the image volume simultaneously, tissue types at mesh boundaries are designated for skin, sternum, chest wall, and transected internal tissues (adipose and glandular tissues at inferior, superior, and lateral mesh boundaries). The modes of deformation are precomputed using the LIBR method with control points distributed at all boundaries except the skin's interface with air.

On the day of surgery, the fiducial centroids should be re-marked with colored ink to ensure good visibility. Using the labeled fiducials from the MR image as a guide, fiducials should be correspondingly labeled on the skin surface in a secondary colored ink with hand-written capital letters.

In the operating room, the stereo cameras must be calibrated, ideally with a checkerboard tracked by

the optical tracker. Twelve images are collected at various checkerboard angles, and input into MATLAB's calibration function [228]. The calibration process, explained in detail in Appendix A, takes only a few minutes. This calibration defines the relationship between camera and optical tracker spaces. Ultrasound calibration (to define the relationship between ultrasound image pixels and physical space) does not need to be performed intraoperatively, provided the tracked attachment has not been removed, or can be detached and re-attached with no degradation in calibration accuracy. Tracked ultrasound images of the chest wall are collected, and the contours of the chest are designated. The guidance module fits a curved spline to a few manually selected points, or ducks, for each ultrasound image. The stereo camera video stream is then started, and the collection is initialized by briefly setting a region of interest around the breast surface and limits to constrain the allowable size of bounding boxes around letter labels. Automatic bounding box detection can be optionally augmented with manually designated bounding boxes, and the user is then prompted to input the inked letter for each bounding box (in one camera's image).

The skin surface, as measured with the stereo cameras, and the chest wall contours are then used as data input into the model-correction framework. The model-optimized deformation corrected images are loaded into the guidance module in the place of the preoperative supine MR images. The guidance system can then be used to visualize anatomy, and probe the available data to understand the tumor position. For echogenic tumors, tracked ultrasound can also be used to delineate the intraoperative tumor location with minimized compression or leveraging probe compression correction approaches presented in [236].

3.5 Data Collection

The workflow proposed above was carried out with minor adjustments to collect additional validation data. The data in this thesis was collected on 7 healthy volunteers from 23 to 57 years of age (average age of 29 $\pm$ 12) with breast volumes of 398 to 1228 cm^3. Before the volunteer arrived, the cameras were calibrated in the mock-OR setting and centered on the anticipated field of view. MR-visible fiducials were placed and inked on both breasts, and volumetric images were acquired using closed bore 3T MR scanner (Philips Healthcare, Best, The Netherlands) using a T1-weighted, 3D turbo field echo sequence with fat suppression and a 16-channel torso coil. One volunteer was imaged with an Ingenia Elition D-Stream wide bore with a voxel size of $0.357\times0.357\times1$ mm^3, and the remaining six volunteers were imaged with an Ingenia D-Stream with a $0.391\times0.391\times1$ mm^3 voxel size. To capture deformations from arm abduction, instead of just one supine image, each breast was imaged in two configurations: with the ipsilateral arm down by the torso, and ipsilateral arm up by the head. This resulted in a total of four scans per subject. The contralateral arm was down for both scans. The arm down image was considered the preoperative image, and the arm up image was considered a surrogate for intraoperative data in Chapter 5. Prospectively, the first MR image, typically

the right breast with the arm down by the torso, was processed during the remaining three imaging scans. Fiducials were localized and labeled, the breast tissue was segmented, and a mesh was generated to represent the breast volume. For one case, a mock-tumor was delineated within the MR image volume to simulate a non-palpable lesion visible on imaging during a prospective demonstration of system utility.

After imaging, the MR-visible synthetic fiducials were removed leaving behind red-inked centroids. These centroids were labeled with capital alphabetic characters in blue ink, drawn directly onto the skin surface. The volunteer was positioned with padded support under the ipsilateral shoulder to simulate rotation of the OR table and present the breast at a more favorable viewing angle for the surgeon and the overhead cameras. The mock-OR data collection surveyed the breast in three arm positions: arm down, surgical position, and arm up. In each position, the chest wall was measured with tracked ultrasound imaging, and surface fiducials were measured with static images from the stereo cameras and manually designated with a tracked stylus. Video recordings were taken with the stereo cameras to include each static position, deformations between positions, and ultrasound data collection.

For five cases, a demonstration was set up after data collection to test usability of the guidance module. The breast surface was acquired prospectively with two measurement techniques: a tracked stylus and the stereo cameras. The stereo-camera measurements at patient-bedside used semi-automatic fiducial detection and manual labeling. Fiducials were detected using thresholding with user-defined parameters including: region of interest, threshold bounds, and the minimum and maximum size of letters. A custom graphical user interface was then used to manually select the fiducials in alphabetical order, and augment the automatically detected data by manually selecting any missed fiducial centroids. This process, though interactive, was generally less time consuming than fiducial designation with a tracked stylus. Because fiducial positions were collected with a tracked stylus for validation, fiducials were used to register optical tracker and camera spaces in lieu of an optically tracked checkerboard. Surface data was incorporated into the guidance display to present real-time guidance based on rigid registration between the preoperative and intraoperative fiducial locations. All intraoperative data was co-registered to the preoperative imaging data. Tracked instruments were used to scroll through the imaging volume and probe the breast anatomy. In the case with a mock-tumor, the guidance system was used to understand 3D lesion position. The system was evaluated by a breast surgeon for two cases. The surgeon reported that this prototype system would be useful for surgical planning and resection, that it improved understanding of breast anatomy, and that it presented useful localization information that is not currently accessible.

Retrospectively, fiducials were localized and labeled with English characters in all images. After the breast volume was meshed and the boundary tissue types were designated, the boundary nodes were extracted as unstructured point clouds to represent the skin and chest wall surfaces. The full extent of these data clouds

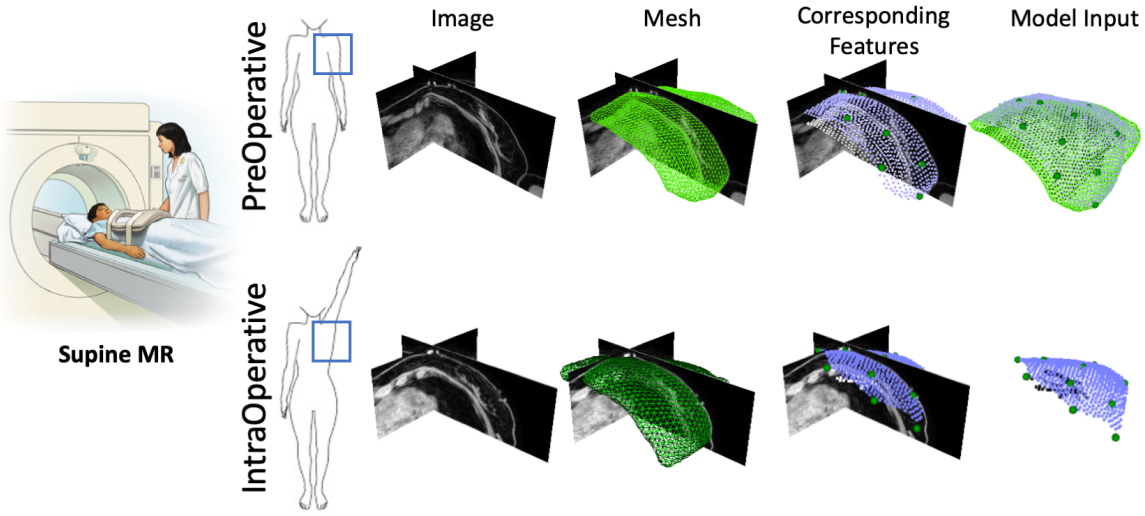

Figure 3.5: Data extracted from supine MR images and used to drive model optimizations. Drawing of the supine MR scanner is reprinted from [237].

was used for the preoperative image. The intraoperative image data were then subsampled to represent realistic collection feasible from intraoperative data sources. The skin surface was cropped to contain only intraoperative skin nodes. The chest wall was segmented in the tracked ultrasound planes, and these contours were manually aligned with the MR data and projected onto the mesh boundary to simulate collection of 7-10 tracked ultrasound planes. This processed data is visualized in Figure 3.5.

CHAPTER 4

Characterization of Supine Breast Deformations

4.1 Summary and Contributions

This chapter investigates the nature of breast deformations in the supine position characterizing the shape changes from imaging to surgery and associated with arm motion in the surgical position. The findings in this chapter quantify the necessity of nonrigid correction, and provide insights into the nature of supine breast deformations to inform future frameworks to correct these shape changes. While breast deformations from prone imaging to supine imaging have been well described [18, 19, 42, 43], the nature of breast deformations from supine imaging to the supine surgical position have not been previously described. Many guidance approaches assume that supine MR images are representative of the breast anatomy during surgery, though these deformations have not been quantified and rigid registration results in noticeable misalignments [139].

First, the nature of breast deformations is studied in the supine position. The magnitude of displacements from arm abduction is measured and the relationships between shift in different breast quadrants are quantified. These results have implications in the mechanics of modeling breast shift, and also describe if these deformations are rigid in nature. The deformations are found to be nonrigid, with the upper outer quadrant deforming significantly more than other quadrants, and the lower inner quadrant deforming significantly less than other quadrants. For a 90° abduction of the arm, the anticipated image-to-surgery arm pose change, displacements in the inferior/superior direction account for about 50% of shift, with the remaining shift approximately evenly split between the anterior/posterior direction and the medial/lateral direction. These findings suggest than a correction approach should take into account all three directionalities of shift and allow for uneven distributions of shift directions.

Next, the alignment accuracy after rigid registration is quantified, and found to be insufficient for surgical guidance with large errors that vary widely across subjects and across positions on the breast. Each case has regions of the breast with over 10 mm of misalignment after image-to-physical registration, and many cases have regions with error on the order of 20 mm. Even simple rotations of the operating room table can result in significant shifts and shape changes in breast tissue. When arm configurations are kept consistent from imaging to the mock-OR setting, error at surface fiducials is as high as 8-17 mm. In an image guidance system, such inaccuracies in tissue localization would likely result in larger resected volumes, incomplete tumor excisions, or both.

While image guidance systems provide useful information during surgery, significant misalignment re-

mains between a supine MR image and the surgical presentation of breast tissue after rigid registration. The contributions of this chapter elucidate a need for nonrigid correction to compensate for these motions as presented in the Chapter 5, and begin to capture mechanical behavior of breast tissue durring arm motion to inform correction approaches. These contributions also indicate that a larger number of fiducials may be necessary to capture nonrigid motions, emphasizing the need for a workflow friendly data capture method that is realized in Chapter 6.

This chapter is adapted from "Impact of deformation on a supine-positioned image guided breast surgery approach" published in the International Journal for Computer Aided Diagnostics and Surgery [238] and has been reproduced with the permission from the publisher, Springer Nature, and the co-authors Jon S Heiselman, Ma Luo, Ingrid M Meszoely, and Michael I Miga. This adaptation includes additional visualization of results in Figure 4.5.

> Winona L Richey, Jon S Heiselman, Ma Luo, Ingrid M Meszoely, and Michael I Miga. Impact of deformation on a supine-positioned image guided breast surgery approach. *International Journal of Computer Assisted Radiology and Surgery*, 16(11):2055–2066, 2021. ISSN 1861–6429.

4.1.1 Abstract

Purpose. To reduce reoperation rates for image guided breast conserving surgery, the enhanced sensitivity of magnetic resonance (MR) supine imaging may be leveraged. However, accurate tissue correspondence between images and their physical counterpart in the surgical presentation is challenging due to breast deformations (e.g. from patient/arm position changes, and operating room table rotation differences). In this study, standard rigid registration methods are employed and tissue deformation is characterized. *Methods*. On n=10 healthy breasts, surface displacements were measured by comparing intraoperative fiducial locations as the arm was moved from conventional MR scanning positions (arm-down and arm-up) to the laterally extended surgical configuration. Supine MR images in the arm-down and arm-up positions were registered to mock intraoperative presentations. *Results*. Breast displacements from a supine MR imaging configuration to a mock surgical presentation were 28.9 ± 9.2 mm with shifts occurring primarily in the inferior/superior direction. With respect to supine MR-to-surgical alignment, the average fiducial, target, and maximum target registration errors were 9.0 $\pm$ 1.7 mm, 9.3 $\pm$ 1.7 mm, and 20.0 $\pm$ 7.6 mm, respectively. Even when maintaining similar arm positions in the MR image and mock surgery, the respective averages were 6.0 ± 1.0 mm, 6.5 $\pm$ 1.1 mm and 12.5 $\pm$ 2.8 mm. *Conclusion*. From supine MR positioning to surgical presentation, the breast undergoes large displacements (9.9 – 70.1 mm). The data also suggest that significant nonrigid deformations (9.3 $\pm$ 1.7 mm with 20.0 mm average maximum) exist that need to be considered in image guidance and modeling applications.

4.1.2 Introduction

High reoperation rates in breast conserving surgery have been referred to as "the other breast cancer epidemic," [17] and have been reported as 10–29% in recent years [33, 34, 36]. Newly adopted localization strategies are largely based on preoperative placement of invasive markers [35, 102, 103, 122, 126, 141]. However, with these approaches it can be difficult to understand lesion position and extent, particularly at depth. An alternative approach is to leverage medical imaging data in real-time to guide surgery. For example, ultrasound image guidance has been shown to outperform seed-based methods with positive margin rates ranging from 0–14% [20–25]. Unfortunately, only 50% of non-palpable tumors are visible on ultrasound [26].

An image guidance platform that could integrate magnetic resonance (MR) imaging would provide more comprehensive guidance for the majority of patients. Such a system would provide detailed subsurface anatomy, higher sensitivity [45], and enhanced lesion location and extent with methods like dynamic contrast enhanced MR [64], particularly for ultrasound-occult cancer. The use of MR data to enhance localization in real time is limited by differences between the diagnostic (prone) and surgical theater (supine) presentations. From prone to supine imaging, breast tissue shifts range 10–85 mm [18, 19, 43]. Additional confounding factors include differences in tumor volume, surface area, sphericity, and distances from the only available landmarks (the chest wall, skin, and nipple) [18, 19, 43].

Several surgical guidance frameworks have been introduced to register, or align, breast MR data to the surgical presentation (primarily prone to supine registration [169, 170]). Recent advances have led groups to pursue supine MR [41, 62, 132, 239] due to comparable imaging sensitivity and better initial alignment to surgical presentation. Barth et al. [50] expanded on the system of Pallone et al. [41, 239] creating a custom supine MR image guidance system for breast conserving surgery relying on rigid registration, and achieving 9% positive margin rates, compared with 19% by wire guidance. In a similar work, Conley et al. developed a custom image-to-physical nonrigid registration method and demonstrated tumor centroid localization errors of 5.3 and 5.5 mm, outperforming rigid alignment error of 6.5 and 12.5 mm respectively [60, 240]. Ebrahimi et al. implemented a thin-plate spline registration to predict tumor motion due to abduction of the arm [171]. While supine MR offers improved alignment, the above works suggest there are still uncharacterized discrepancies in tissue location between imaging and surgery presentations (e.g. effects from patient position, arm position, and surgical table rotation). This paper reports the nature of breast deformation from supine imaging-to-surgical presentation and evaluates the accuracy of rigid registration in the context of a supine MR image-guided approach.

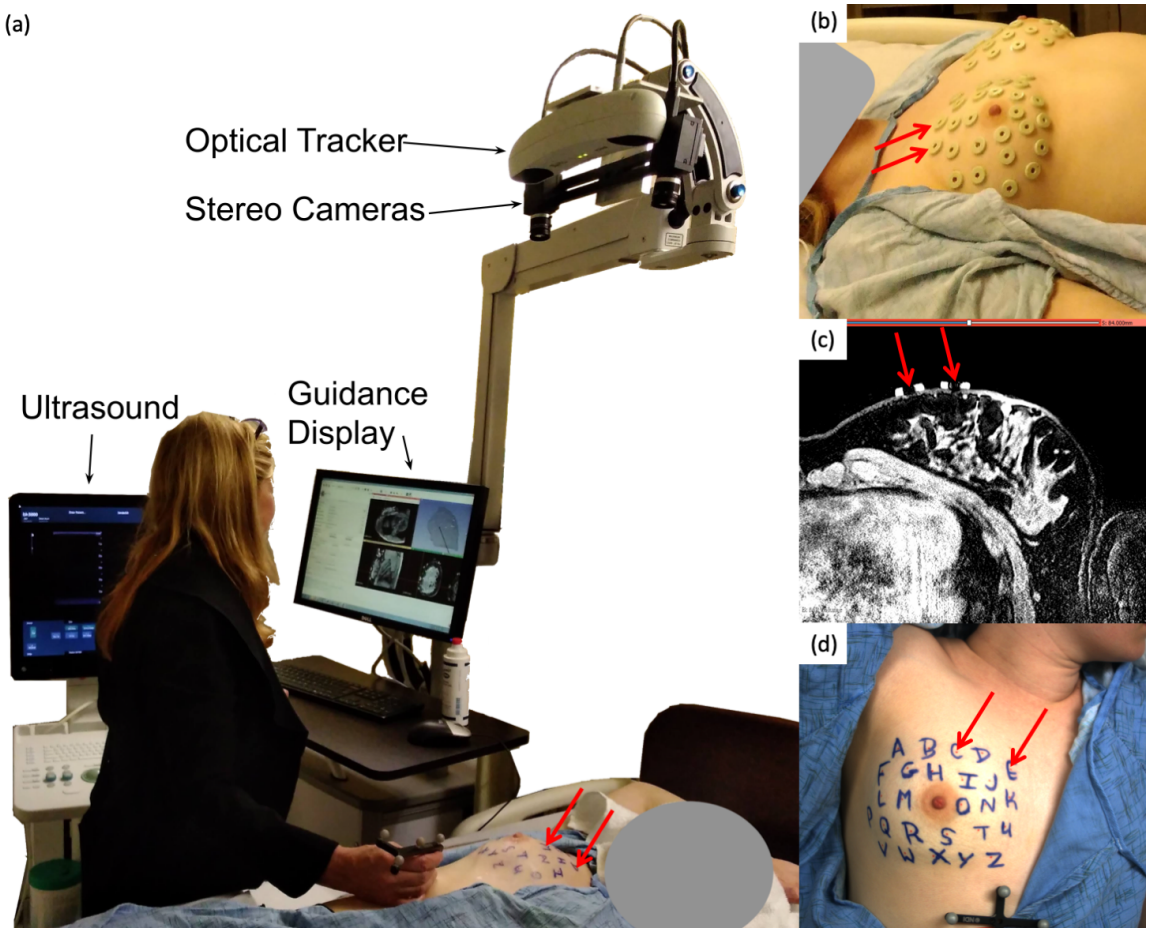

Figure 4.1: Data collection system and fiducial distribution. Red arrows indicate fiducial locations. (a) Data collection in the arm-up position with the rigidly coupled instrument tracker and stereo camera pair, ultrasound machine, and guidance display. (b) Twenty six MR visible fiducials distributed across each breast. (c) Two fiducials visible on an axial slice of a supine MR image. (d) Anterior view from one RGB camera in the mock intraoperative setting; the center of each MR fiducial marked with red ink, and labeled with a blue hand drawn letter.

4.1.3 Methods

4.1.3.1 Intraoperative Surgical Monitoring Platform

A custom data collection system [241] (Figure 4.1a) was developed with stereo cameras (FLIR, Richmond, BC, Canada) for breast surface acquisition, optically tracked instruments (Northern Digital Inc., Waterloo, ON, Canada), intraoperative ultrasound (BK Medical, Peabody, MA, USA), and a guidance module implemented in 3D Slicer [224]. The module registers all patient data to MR image space, and presents the surgeon with the position of their tracked tool in relation to all other aspects of the scene including the breast model, lesion model, fiducial positions, and tracked ultrasound images. The system in Figure 4.1a is in use with a tracked stylus.

4.1.3.2 Human Data Collection

Experimental protocols were approved by the Vanderbilt University Institutional Review Board and six healthy volunteers were enrolled with informed consent. Of the twelve breasts, two were excluded from analysis: one due to subject movement during data collection, and one due to incomplete data. Volunteers ranged in age from 23–57 (average 30 $\pm$ 13) years. Breast volumes, as manually segmented from an arm-down supine MR, ranged from 459–1230 cm^3 (mean: 681 $\pm$ 214 cm^3). With each case, 26 adhesive synthetic MR-visible fiducial markers (IZI Medical Products, Owing Mills, MD) were placed on the skin with approximately equal sampling across the breast surface (Figure 4.1b). The number of fiducials was chosen to sufficiently sample the surface based on three previous works [171, 235, 242]. To adequately and densely cover the surface of the breast, while providing precise point-to-point correspondence, 26 fiducial points were used. All measurements successfully identified at least 23 fiducials, and 82% contained all 26 fiducials.

MR data were collected in conventional closed bore 3T MR scanners (Philips Healthcare, Best, The Netherlands) using a T1-weighted, 3D turbo field echo sequence with fat suppression. One volunteer was imaged with an Ingenia Elition D-Stream wide bore, and the remaining five volunteers were imaged with an Ingenia D-Stream. A 16-channel torso coil was laid over the chest and supported with padding placed on the sternum to reduce breast compression. Multiple available clinical scanners were used across subjects with one of two voxel resolutions, $0.357\times0.357\times1$ mm^3, or $0.391\times0.391\times1$ mm^3 voxel size. To effectively capture the full range of breast motion between two arm position extremes, MR data were collected in two positions: with the ipsilateral arm down by the torso and then up by the head. The contralateral arm was down for both scans. Full lateral extension was not possible due to bore constraints. In both MR images, locations of the MR-visible fiducials (Fig. 4.1c) were manually localized, and labeled in 3D Slicer with an English alphabet character-based label (A–Z). Fiducial labels provide intuitive correspondence between the model and physical space.

Less than 24 hours after MR imaging, the subject was moved to a mock surgical presentation area for additional data collection. The center of each fiducial was marked as a distinct ink dot, then the MR-visible fiducials were removed. Once removed, a letter label was then specifically inked onto the skin surrounding each inked fiducial dot (Figure 4.1d). This process allowed the fiducial center to be identified on the subject using manual digitization via an optically tracked wand (stylus) as well as determined (potentially automatically) with the stereo cameras using optical character detection. In surgery, patients are typically oriented in an oblique supine position, with the operating table tilted slightly such that the ipsilateral arm is raised. This rotation of the table brings the breast to a more favorable position for lesion excision. To simulate this rotation, in our mock surgical presentation, padding was placed underneath the ipsilateral shoulder and upper

torso. Data were then collected in three positions: with the ipsilateral arm down, abducted to 90 degrees from the torso (T-shape, the typical surgical presentation), and up by the head. Fiducial locations in the mock surgical setting were collected with a handheld optically tracked stylus. To allow quadrantized analysis, each fiducial location was manually assigned to one of the four conventional anatomical breast quadrants (upper outer, upper inner, lower outer, lower inner). Fiducials were assigned to quadrants by assessing fiducial locations in 3D space relative to the nipple and referencing RGB stereo camera images.

4.1.3.3 Breast Shift Among Range of Arm Positions

Breast surface displacements were measured by comparing intraoperative fiducial locations as the arm was moved in a mock surgical setting. Euclidean distances between corresponding points were computed for 3 shifts: (i) arm-down to T-shape, (ii) T-shape to arm-up, and (iii) arm-down to arm-up. The first measured shift represents the typical arm motion from preoperative supine MR imaging to surgical position. The second measured shift was performed to capture an alternative preoperative supine MR position with the arm-up. The third breast shift represents the effect of the full range of arm motion. The magnitude and direction of displacement were measured for each shift, and compared between shifts. The directionality of displacement was analyzed by comparing the three orthogonal components of displacement in the MR image space: medial/lateral, anterior/posterior, and superior/inferior. The directionality is reported in each anatomical direction as the percentage of the total displacement. Additionally, for each case the average displacement was computed in each quadrant. Displacements were compared among the four breast quadrants.

4.1.3.4 Image-to-Physical Registration Associated with Conventional Image-Guided Surgery Approaches

While the section "Breast Shift Among Range of Arm Positions" measured breast shift magnitude, it is important to distinguish rigid translations and rotations from nonrigid deformations. To study this, spatial discrepancies in breast fiducials were investigated after registering the fiducials between conventional supine MR imaging and mock surgical presentation. Using traditional point-based registration techniques, fiducial locations in MR image space were aligned with their corresponding positions that were optically digitized in the physical mock surgical setting. The rigid registration method is described in [230] and is an accepted standard in the field. Traditional metrics of fiducial registration error (FRE) and target registration error (TRE) are reported [230]. Briefly, the fiducial registration error (FRE) measures the general misalignment of fiducials as $FRE = \sqrt{\frac{1}{N}\sum_{i=1}^{N}|T(x_i) - y_i|}$ where N is the number of corresponding fiducial points, $T(x_i)$ represents the rigidly transformed ith fiducial point x_i into the same space as corresponding point y_i. The target registration error (TRE) represents an equivalent calculation but the point being compared in the two

spaces is a novel point that was not used in determination of the rigid registration transformation, $T(*)$. Here, TRE was determined using a leave-one-out strategy where the transformation $T(*)$ is determined using $N-1$ fiducials. The N^{th} fiducial is treated as a novel target. This process is repeated iteratively treating each fiducial as a target to evaluate accuracy. TRE is established as the root mean square error over the entire cohort.

Registration error metrics are reported for each of the four image-to-physical registrations involving the mock operating room (OR) and conventional MR settings: (1) arm-down mock OR to arm-down MR (2) arm-up mock OR to arm-up MR, (3) T-shape mock OR (surgical position) to arm-down MR, and (4) T-shape mock OR to arm-up MR. For registration (3)—a likely surgical protocol—TRE is further evaluated by varying the number and distribution of fiducials to establish potential lower bounds required for good registration fidelity. These additional analyses focus particularly on the impact of fiducial distribution across the four breast quadrants. Beginning with a lower limit of using only $n = 4$ fiducials and proceeding to an upper limit of n=23 fiducials, registrations were performed for each possible combination of n fiducials. Any fiducials not used in the registration were treated as novel targets for the determination of TRE. Here, since all cases have at least 24 corresponding fiducials recognized for registration (3), the upper limit of $n = 23$ is used to ensure that registration accuracy may be computed on at least one target for each case. TRE was averaged by case, and then across all cases. Some of these combinations represent unrealistic and unbalanced fiducial distributions. Therefore, an alternative combinatorial approach was also used to evaluate the impact of systematically distributing fiducials across quadrants. The process begins by requesting one fiducial from each quadrant to be used in registration, then incrementing. This quadrantized approach includes all combinations where the differences among the number of fiducials requested from each quadrant are no more than one. When the number of fiducials from a quadrant requested for registration exceeds the number of fiducials in the quadrant, all fiducials in that quadrant are drawn and additional combinations are included reserving one fiducial in that quadrant as a target. All combinations are ensured to be unique.

4.1.3.5 Statistical Tests

For each metric reported, the distribution of samples was tested for normality using a one-sample Kolmogorov-Smirnov test. Each distribution was found to be approximately normally distributed. A paired-t test ($\alpha = .05$) was used to test significance and power, given the sample size of 10 breasts. Magnitude and direction of displacement were compared with paired t-tests ($p < 0.05$). Displacements were compared among the four breast quadrants with a paired t-test ($p < 0.008$ with Bonferroni correction). Tests with power greater than 80% are considered strongly powered.

4.1.4 Results

4.1.4.1 Breast Shift Among Range of Arm Positions

With the subject otherwise stationary in the mock OR setting, the average displacement, i.e. shift, from the arm-down to T-shape position was 28.9 $\pm$ 9.2 mm (range: 9.9–70.1 mm), while the average displacement from the arm-up to T-shape position was 27.6 $\pm$ 8.9 mm. This difference was not statistically significant ($p > .05$). The average displacement from the arm-down to arm-up position was 42.0 $\pm$ 15.4 mm, which was significantly greater ($p < 0.05$) than the shift from arm-down to T-shape ($power = 0.79$) and the shift from arm-up to T-shape ($power = 0.99$). For reference, each volunteer is assigned a lowercase letter and subjects are presented in the order of decreasing breast volume (a–f). Subjects are consistently labeled with this convention across all figures and tables. Results are reported in Table 4.1.

Table 4.1: Surface fiducial displacements in the supine position and registration error metrics for image-to-physical registrations reported in millimeters (mm).

Case		Breast Volume (cm^3)	**Displacement (mm) Mean ± Std**		
			Arm-down to T-shape	Arm-up to T-shape	Arm-down to Arm-up
a	L	1,230	26.8 $\pm$ 5.2	39.4 $\pm$ 13.1	8.0 $\pm$ 14.8
b	R	730	39.5 $\pm$ 10.1	29.1 $\pm$ 8.9	55.8 $\pm$ 17.9
	L	694	33.5 $\pm$ 10.0	24.3 $\pm$ 9.4	54.7 $\pm$ 16.6
c	R	693	40.5 $\pm$ 6.4	26.3 $\pm$ 6.1	38.5 $\pm$ 11.4
	L	668	38.5 $\pm$ 6.2	22.9 $\pm$ 2.9	36.9 $\pm$ 8.2
d	R	688	14.5 $\pm$ 2.6	19.7 $\pm$ 5.1	21.9 $\pm$ 5.4
	L	581	17.4 $\pm$ 1.9	13.2 $\pm$ 5.2	18.2 $\pm$ 3.9
e	R	595	21.3 $\pm$ 3.5	30.4 $\pm$ 7.3	42.4 $\pm$ 8.6
	L	474	29.0 $\pm$ 5.0	43.9 $\pm$ 10.5	62.1 $\pm$ 14.8
f	L	459	28.4 $\pm$ 3.5	26.7 $\pm$ 6.7	31.6 $\pm$ 8.7

For the left breast of each volunteer, displacement magnitude and direction are displayed on the breast model segmented from the MR image (Figure 4.2). Fiducial displacements, shown with arrows, were interpolated across the model surface using natural neighbor interpolation, as implemented in MATLAB, to produce the colored meshes. For each mesh, the sternum is on the left with the armpit towards the top right, as shown by the human outline in the bottom right of Figure 4.2.

The percentage of displacement in each of the three orthogonal directions (medial/lateral, anterior/posterior, superior/inferior) is shown in Figure 4.3. The percentage of displacement in the medial/lateral direction was statistically larger in the arm-up to T-shape shift when compared to the two other shifts ($power = 0.66$ when compared to arm-down to T-shape shift and $power = 0.98$ when compared to arm-down to arm-up shift). The percentage of displacement in the superior/inferior direction was significantly larger in the arm-down to arm-up position change when compared to the two other positional changes ($power = 0.87$ when

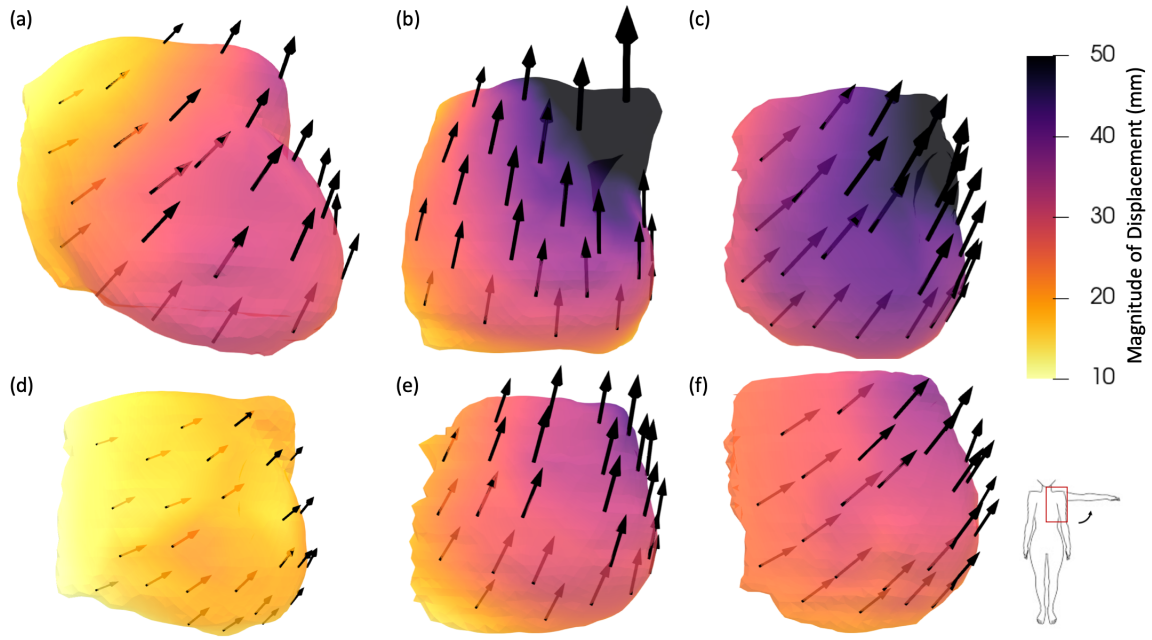

Figure 4.2: Breast surface displacements associated with arm movement from the arm-down position to intraoperative position. Arrow vectors placed at fiducial locations show the direction of displacement and are scaled according to the magnitude of displacement.

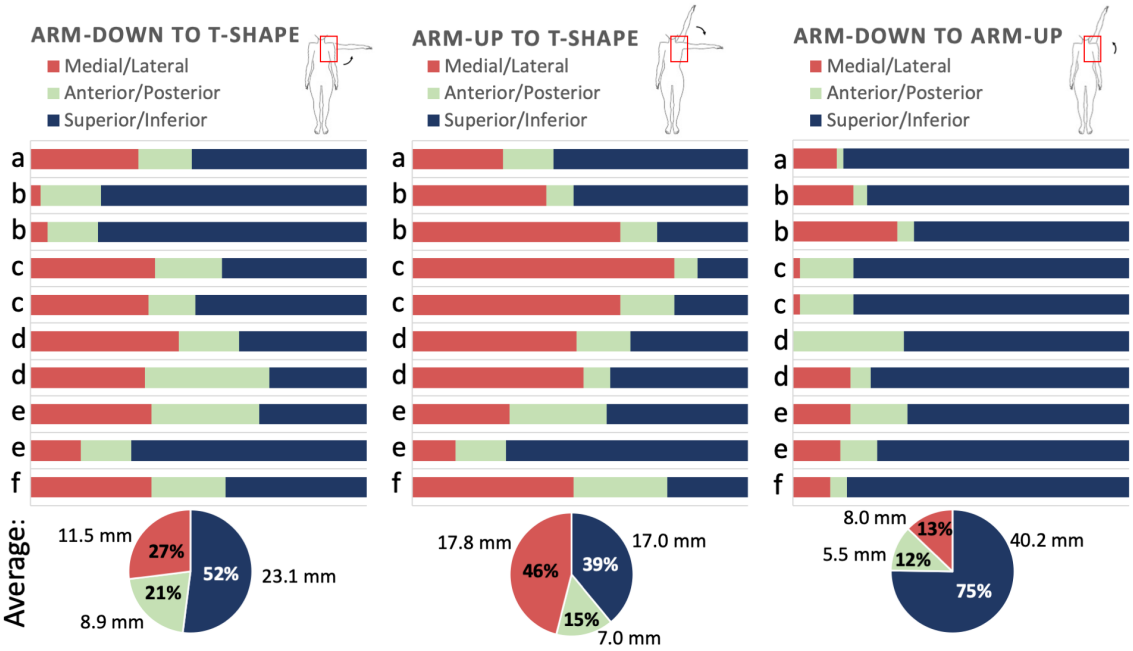

Figure 4.3: Directionality of breast surface displacements associated with arm movement in the supine position with arm motion illustrated for each of the three positional changes. Average percentage and magnitude of displacement in each direction is displayed at the bottom.

compared to arm-down to T-shape shift and $power = 0.99$ when compared to arm-up to T-shape shift). In the anterior/posterior direction, the percentage of displacement was significantly larger for the arm-down to T-shape shift only when compared to the arm-down to arm-up shift ($power = 0.91$).

4.1.4.2 Analysis of Breast Shift by Anatomical Quadrant

Average displacement differed among the four conventional anatomical quadrants, illustrated in Fig 4.4a. For the arm-down to T-shape pose change, average displacements in the upper outer quadrant were significantly larger than averages in all other quadrants ($power > 0.98$) as shown in Figure 4.4b. From T-shape to the arm-up position, the upper outer quadrant shifted significantly more and the lower inner quadrant shifted significantly less than all other quadrants ($power > 0.99$). When comparing average quadrant displacements from the arm-down to arm-up positions, all comparisons were significantly different ($power > 0.90$) as shown in 4.4c. The line of equivalence is plotted as a reference, showing where the displacement associated with quadrant A on the y-axis is equivalent to the displacement of the comparator quadrant B on the x-axis. Deviations from this line of equivalence are readily visualized in Figure 4.4.

4.1.4.3 Image-to-Physical Registration Results Associated with Conventional Image-Guided Surgery Approaches

Registration error metrics are reported (Table 4.2) for each combination of preoperative and intraoperative data: (1) arm-down mock OR to arm-down MR (2) arm-up mock OR to arm-up MR, (3) T-shape mock OR (surgical position) to arm-up MR, and (4) T-shape mock OR to arm-down MR. The first two registrations quantify breast deformations for equivalent arm poses; the third and fourth registrations quantify the deformation from the preoperative images to surgical positioning. Fiducial registration error (FRE) values were 5.8 $\pm$ 0.8 mm and 6.2 $\pm$ 1.2 mm for registrations (1) and (2) respectively. Target registration error (TRE) values were 6.3 $\pm$ 0.9 mm and 6.7 $\pm$ 1.3 mm for registrations (1) and (2) respectively. For registrations from image space to surgical presentation (T-shape), FRE was 7.9 $\pm$ 1.6 mm using the arm-up MR image (3), and 9.0 $\pm$ 1.7 mm using the arm-down MR image (4). TREs were 8.6 $\pm$ 1.8 mm and 9.3 $\pm$ 1.7 mm for registrations (3) and (4) respectively. On average for deformation (4), the maximum target error was 20.0 $\pm$ 7.6 mm. Figure 4.6 shows TRE at each fiducial location on a wireframe representation of the breast surface. Furthermore, image to physical registrations in the same arm pose were compared to registrations with differing arm poses (imaging to surgical position). More specifically, (1) was compared to (4) and similarly (2) was compared to (3). These registration errors were significantly different ($power > 0.95$), indicating significant nonrigid deformations are due to arm motion in the supine position.

In registrations for the arm-down to T-shape deformation, the most likely surgical protocol, average TRE

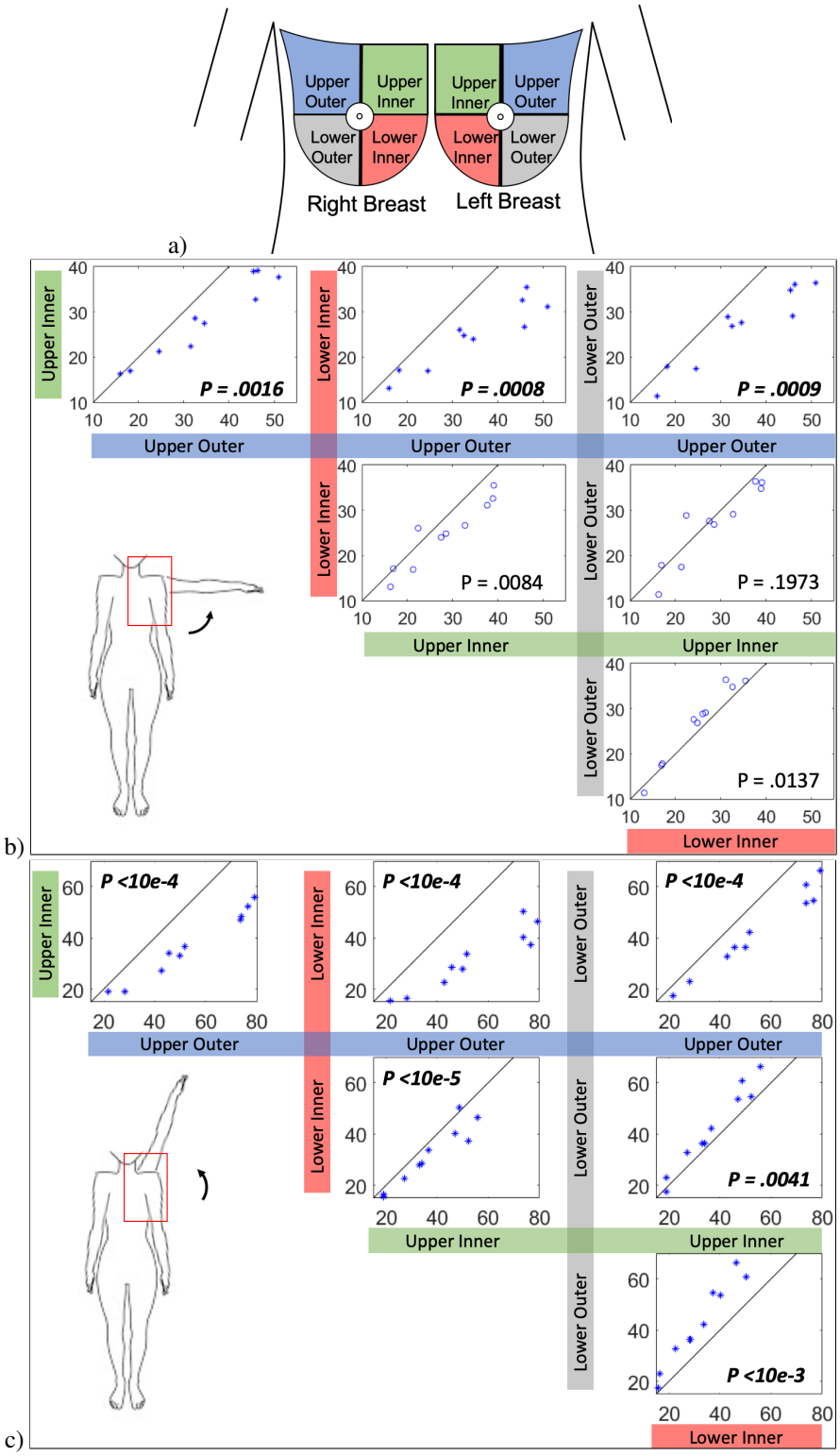

Figure 4.4: Comparison of average displacements for each pair of quadrants. Each plot point represents the average displacement in two quadrants for one case. Significantly different shifts are plotted as asterisks (*), and p-values are reported. The line y=x, where quadrant displacements are equivalent, is shown in black. (a) Color coded quadrants of the breast (b) Comparison of average quadrant displacements from arm-down to T-shape (c) comparison of average quadrant displacements from arm-down to arm-up

Table 4.2: Registration error metrics (in millimeters, mm) for image-to-physical registrations of surface points.

Case		Breast Volume (cm^3)	Registration Error (mm) RMS											
			Arm-down MR to Arm-down Mock OR			Arm-up MR to Arm-up Mock OR			Arm-down MR to Surgical Position			Arm-up MR to Surgical Position		
			FRE	TRE	Max TRE	FRE	TRE	Max TRE	FRE	TRE	Max TRE	FRE	TRE	Max TRE
a	L	1,230	7.4	7.9	14.8	5.8	6.2	9.9	10.0	10.9	17.7	10.3	10.9	21.0
b	R	730	5.3	5.8	10.9	3.9	4.2	7.4	5.0	5.6	11.9	9.7	10.4	27.8
	L	694	6.3	6.9	13.9	5.5	6.2	11.8	8.2	9.2	16.3	11.3	12.1	36.4
c	R	693	4.9	5.3	10.0	5.7	6.2	12.0	8.0	8.8	13.2	9.4	10.1	23.3
	L	668	5.5	5.9	10.0	7.9	8.6	16.1	7.6	8.2	18.4	9.6	10.3	20.1
d	R	688	5.2	5.5	8.1	6.3	6.7	10.0	6.6	7.0	10.7	10.5	8.0	11.1
	L	581	5.3	5.7	14.4	7.5	8.1	17.4	9.1	9.9	19.3	6.0	6.5	14.4
e	R	595	6.4	6.8	15.3	7.6	8.3	14.3	10.4	11.3	19.8	7.2	7.7	13.9
	L	474	6.7	7.1	15.6	5.8	6.2	12.8	7.0	7.6	16.3	8.1	8.6	16.8
f	L	459	5.4	5.8	14.3	6.0	6.5	11.3	7.3	7.8	14.4	7.7	8.2	15.6
Mean		*681 cm^3*	*5.8*	*6.3*	*12.7*	*6.2*	*6.7*	*12.3*	*7.9*	*8.6*	*15.8*	*9.0*	*9.3*	*20.0*

decreased asymptotically with an increasing number of fiducials with a final limit of 8.5 mm. The quadrantized method approached the limit faster than the non-quadrantized method, as shown in Figure 4.5. For $n > 10$ fiducials the two approaches are not statistically different.

4.1.4.4 Impact of Instrumentation Error on Analysis

Registration error due to instrumentation was evaluated by rigidly aligning five sets of skin fiducial points collected with the subject in exactly the same position. Two main sources of error are possible: intrinsic instrumentation error associated with optical tracking and MR imaging resolution, and localization error associated with an individual designating the location of a fiducial marker either using an optically tracked stylus on the patient or demarking the fiducial marker in a corresponding MR imaging set. While the error associated with intrinsic instrumentation error is documented by device characteristics [243], the impact of localization error needs to be assessed in practical use. To evaluate accuracy of fiducial localization on a subject in the T-shape surgical presentation position, the same fiducial locations were collected repeatedly for a total of five point sets. All combinations of point sets (5 choose 2) were registered, and the average FRE was determined to be 1.5 ± 0.1 mm. Similarly, the locations of the fiducials were designated in an MR image with the subject arm down and all combinations of point sets (5 choose 2) were registered providing a counterpart average FRE of 1.6 ± 0.4 mm.

For each measurement approach, an approximation standard of the upper limit of instrumentation error was defined as one standard deviation greater than the mean. This results in 1.6 mm and 2.0 mm for optical-

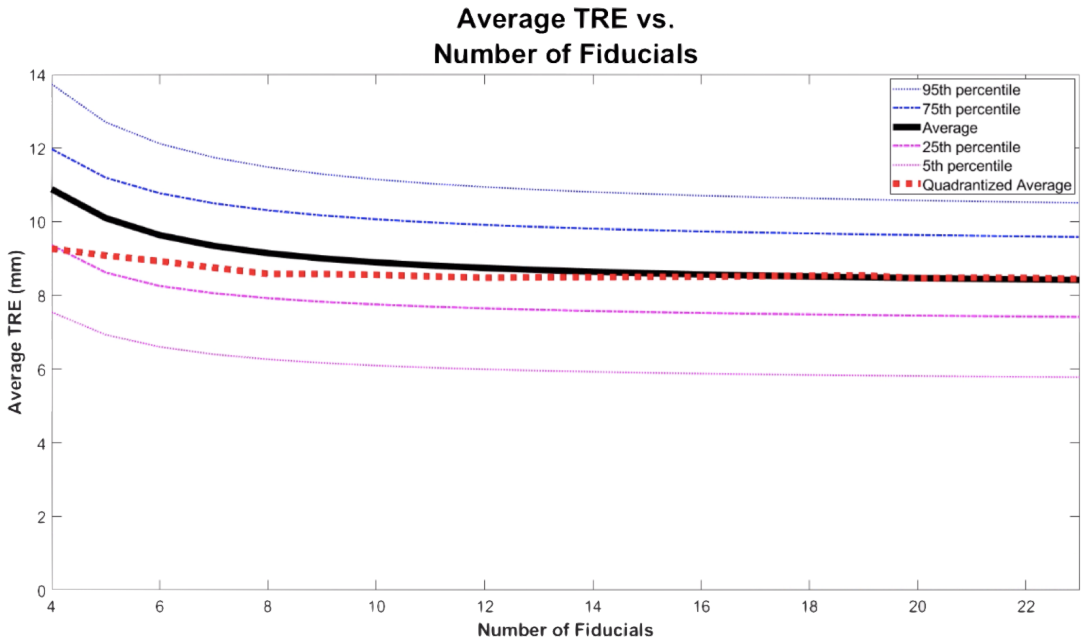

Figure 4.5: Average TRE for supine MR to intraoperative position as it varies with the number of fiducials used in rigid registration. In a few cases, fiducials were missing in the MR and/or the mock OR dataset, limiting the evaluation to maximum of 23 fiducials.

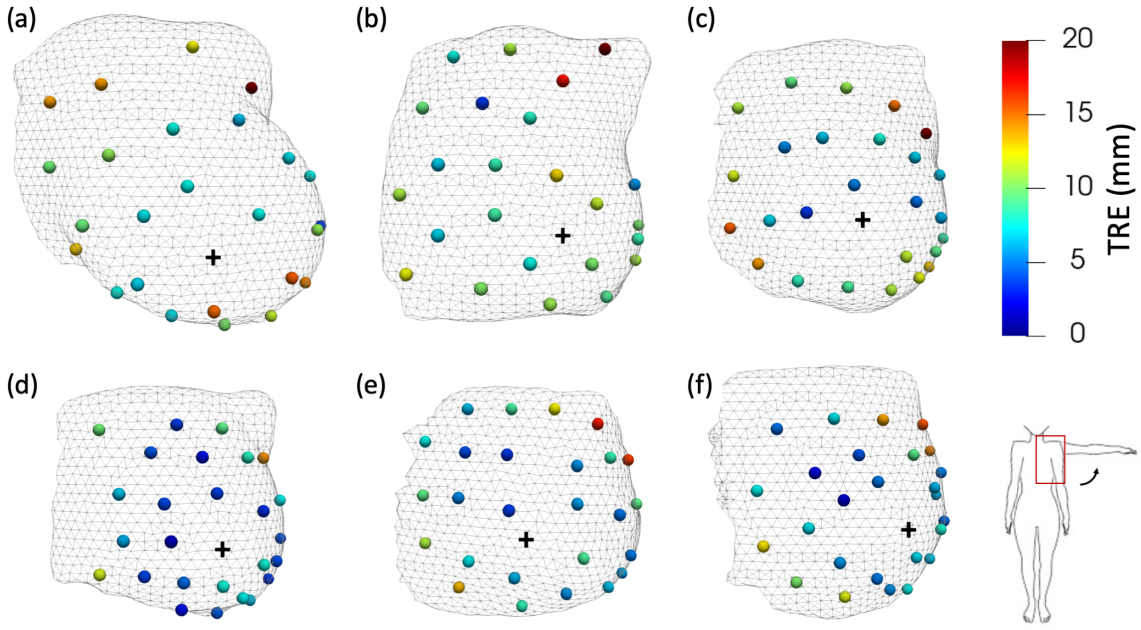

Figure 4.6: Target registration error for arm-down supine MR to intraoperative position (T-shape mock OR) for the left breast of each subject. The nipple is marked by (+).

stylus digitized and MR points respectively. In a worst-case scenario, these errors would sum to represent a combined instrumentation error, i.e. approximately 3.6 mm. When considering the remaining error after registering the supine MR images and surgical T-shape presentation, errors that are significantly greater than this 3.6 mm instrumentation error (paired t-test, $p < .05$) are assumed to be associated with deformations, i.e. nonrigid shape change. All registrations produced significantly greater errors; therefore, nonrigid components of deformation are significant and cannot be completely compensated for using a rigid registration approach. This analysis shows that nonrigid deformation between imaging and surgery is significant even for registrations between the same pose (i.e. (1) and (2)).

4.1.5 Discussion

At a fundamental level, the components of rigid and nonrigid deformation are considerable between MR-supine and OR-supine configurations. Across subjects, displacement and registration error varied in magnitude (9.0 mm average FRE with average maximum TRE of 20.0 mm) and spatial distribution suggesting that patient-specificity and real-time monitoring are likely needed within a resection guidance approach. Displacements were also largest in the upper outer quadrant, where disproportionately 38–54% of breast cancers occur [244–246]. This uneven shift among quadrants would also likely make rigid-registration based image guidance approaches particularly prone to error. Even with a high number of well-distributed fiducials, when registering conventional supine breast MR to surgical presentation each subject had a region with TRE above 10 mm, and many had regions with TRE above 20 mm. Comparing image-to-physical registration errors in the same vs. differing arm poses demonstrated that there are significant nonrigid deformations due to arm motion. Going further, even when the arm poses were kept consistent between MR and mock surgery positions, nonrigid error was still present (average errors of 6.5 mm with average maximum TRE of 12.5 mm) and significantly greater than instrumentation error. This suggests that even under ideal conditions, nonrigid deformation is likely an important factor to consider. Other important considerations are number of fiducials and preferred MR position. For rigid registration, greater than 10 fiducials and distribution across all four quadrants is recommended. Neither arm-up nor arm-down supine MR position is preferred when considering displacement magnitude or registration error. However, the significant difference in directionality could impact the difficulty of modeling these deformations.

To the best of our knowledge, this work is the first to report such a comprehensive characterization of image-to-surgical deformations. While limited to the breast surface, displacements and registration errors are reported for densely sampled corresponding points. In a related work, Ebrahimi et al measured tumor displacement from the arm-down position, to an arm up position in supine MR images [171]. The center of mass displacements for six tumors were reported between 10.9 and 46.8 millimeters from full abduction of

the arm. Rigid registration errors (TRE) for tumors' centers of mass were between 2.6 and 17.9 mm. The magnitudes of these subsurface measurements are remarkably comparable and consistent with our measurements provided here thus proving a similar scale and range for both displacement and registration error.

There are several limitations to this work. The sample size is small and not representative of breast cancer patient demographics. Breast cancer patients are typically older than the average age of the reported cohort, with most patients in the age range of 50–70 years old [247] and subject to differing breast consistency. Further study remains to conclusively evaluate the effects of numerous anatomical factors on breast displacement and registration error (e.g. volume, density, and placement/distribution of breast tissue). The position of the breast on the torso was an unexpected confounding factor in this dataset. Larger, and particularly more laterally set breasts are deformed by contact with the arm in the arm down position. Similarly, these breasts could also experience larger forces during arm motion due to spatial relationships to ligaments and axillary skin. Breast shape and the position of breast tissue on the rib cage likely impact deformation and registration error as well, but these effects have not been investigated in this work. Expanding this data set is a next step to establish trends regarding the impact of breast volume on displacement or registration error.

Another limitation of the work is associated with workflow. In practice, some seed-based targets can be implanted up to 30 days before surgery [126, 248] allowing workflow and cost benefits by enabling scheduling flexibility [142]. Comparatively, fiducial placement likely reduces patient discomfort but with more restrictive scheduling. In the framework discussed herein, there would also be modifications to necessary imaging. Supine MR is not standard of surgical care and would likely increase imaging costs. However, workflow modifications must also be considered within the context of current reoperation rates. A single-pass negative-margin breast conserving surgery procedure would have great potential patient and cost benefits. Lastly, this work has been limited to breast surface analysis. Integration of tracked intraoperative ultrasound, as in Figure 4.1, allows subsurface features to be incorporated (i.e. tumor margins, implanted biopsy clips, etc.). While rigid registration often relies on surface fiducials, the addition of subsurface ultrasound data could help to constrain a nonrigid modeling approach. Figure 4.7 shows an example under development and awaits further study.

4.1.6 Conclusions

While work is ongoing with supine MR and rigid registration guidance [50, 60, 62], results here have demonstrated that for supine MR-to-OR alignment strategies, nonrigid deformations are present and significant. Navigation systems will need to improve accuracy to compete with, and improve beyond, implanted marker-based guidance. Future strategies that use sparse readily-available localization and imaging data coupled to nonrigid registration approaches could potentially offer the next cost-effective revolution in improved surgical

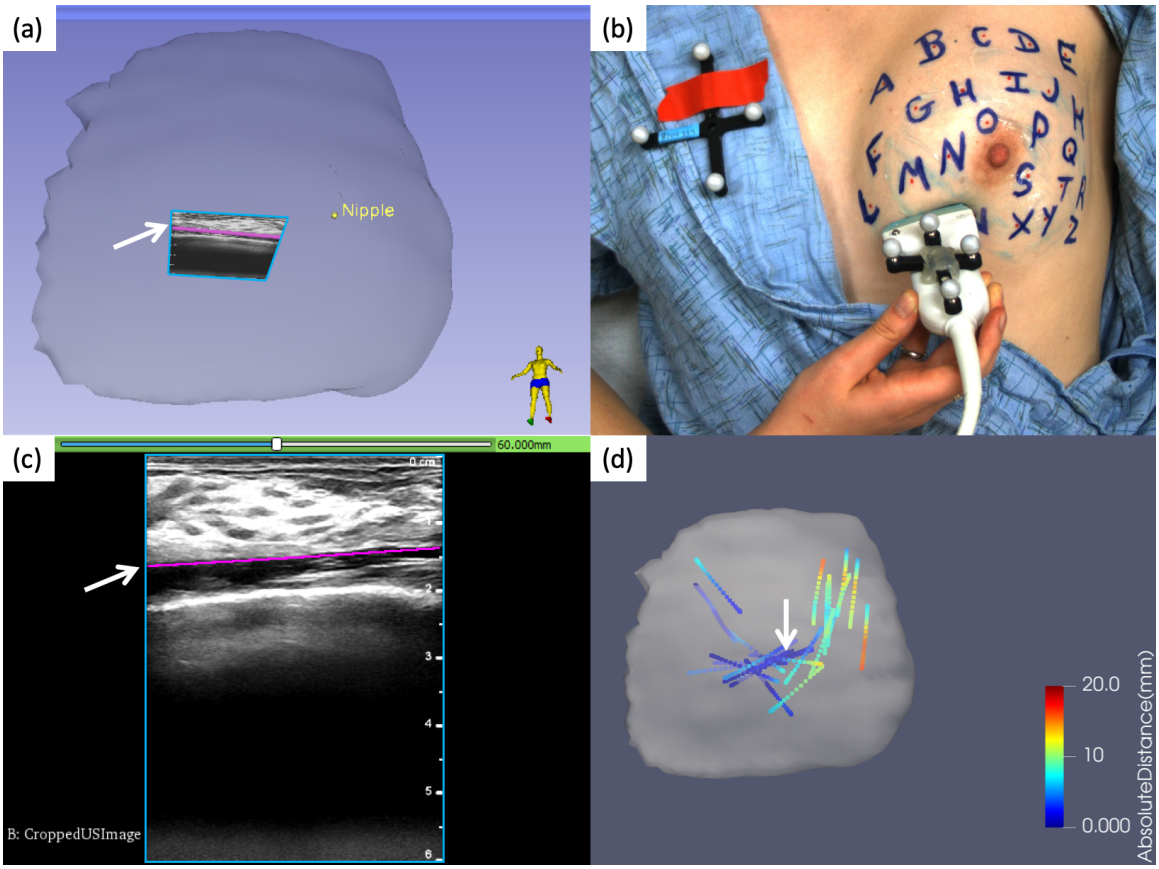

Figure 4.7: Ultrasound data in an image guidance system, with a white arrow indicating this chest wall segmentation: (a) breast model as segmented from the MR image with tracked ultrasound plane in blue, and the chest wall segmented in magenta; (b) ultrasound image acquisition in the mock OR; (c) ultrasound image outlined in blue with the segmented chest wall surface in magenta; (d) acquired chest wall contour data on the breast model where color indicates the closest point residual with its MR counterpart after rigid registration.

accuracy.

Acknowledgments

This work was supported by NIH-NIBIB awards T32EB021937, R21EB022380, R01EB027498, and Vanderbilt grant 1S10OD021771-01.

CHAPTER 5

Model-Based Correction of Breast Deformations

5.1 Summary and Contributions

With deformations from imaging to surgery shown to be large and nonrigid in Chapter 4, in this chapter a modeling framework is developed to compensate for these shape changes and improve intraoperative localization accuracy. The framework presented here can be integrated into a guidance module display to quickly correct preoperative images based on sparse measurements of image-to-OR deformations. These deformation corrected images display a more accurate representation of the breast anatomy in the operating room.

A patient-specific biomechanical model is derived from a preoperative supine MR image volume. In the operating room, the deformed shape of the breast can be measured with the data collection system presented in Chapter 3 consisting of tracked ultrasound imaging of subsurface anatomy, and stereo camera measurements of the skin surface. The developed approach then uses the LIBR deformation correction method [28] with breast-specific boundary conditions to model the volumetric deformations across the entire organ. Localization accuracy of the proposed nonrigid correction method is compared to accuracy with a rigid registration alignment. Driven with intraoperatively feasible sparse-data distributions, nonrigid correction significantly improves surface and subsurface alignment beyond rigid predictions.

The first section in this chapter demonstrates that nonrigid correction provides significantly improved accuracy over rigid registration, and shows that integrating subsurface data near the tumor can significantly improve accuracy even further. The model is evaluated across 7 healthy volunteers. This study is the first to use an inverse model to correct for breast deformations in the supine position, iteratively predicting forces that produce the observed intraoperative breast state and minimizing model error in less than a minute. By sampling realistic sparse data from dense MR image volumes, this study was able to evaluate accuracy across over 150 subsurface regions of interest. This is the first study to comprehensively evaluate registration alignment across such a high number of surface and subsurface points well distributed throughout breast volumes.

Evaluation of model performance is then extended by including biopsy clips as subsurface data inputs. When a lesion is suspected to be cancerous, a biopsy is generally performed. During the biopsy, a sample of tissue is removed from the lesion and a biopsy clip is left behind in the location that was sampled. This clip is currently not used for intraoperative localization. Instead, a secondary appointment in radiology is needed to place a separate localization device: either a marker seed or a guide-wire as described in Section 2.3.3. These localization devices are compatible with a method of intraoperative guidance. The method here

proposes to shift this standard, to leverage biopsy clips visible on ultrasound imaging to inform guidance and improve correction accuracy in a region of interest surrounding the tumor. This section investigates the impact of incorporating this information as an additional driving input to the model correction framework, demonstrating that one localized point near the tumor can significantly improve accuracy even further beyond correction driven with boundary-data alone (surface and chest wall data). Model performance is evaluated in the context of clinically relevant regions of interest, in light of reported lesion sizes as previously discussed in Section 2.3.4.

The second section in this chapter demonstrates model performance in a breast cancer patient. This section evaluates performance with 9 surface fiducials instead of the 26 surface fiducials used in the previous section, showing that the model still improves alignment for surface fiducials, subsurface features and a tumor volume.

These contributions, in tandem with the contributions from Chapter 4, have continued to motivate additional works investigating more complex modeling approaches that incorporate additional factors such as anisotropy and heterogeneity. The fast speed of model correction presented here sets the stage for prospective intraoperative correction and motivates investigations into rapid, automated data collection to acquire high numbers of surface fiducials. To fully leverage the accuracy reported here, a rapid surface measurement approach is realized in Chapter 6.

5.2 Computational Imaging to Compensate for Soft-Tissue Deformations in Image-Guided Breast Conserving Surgery

5.2.1 Abstract

Objective: During breast conserving surgery (BCS), magnetic resonance (MR) images aligned to accurately display intraoperative lesion locations can offer improved understanding of tumor extent and position relative to breast anatomy. Unfortunately, even under consistent supine conditions, soft tissue deformation compromises image-to-physical alignment and results in positional errors. *Methods*: A finite element inverse modeling technique has been developed to nonrigidly register preoperative supine MR imaging data to the surgical scene for improved localization accuracy during surgery. Registration is driven using sparse data compatible with acquisition during BCS, including corresponding surface fiducials, sparse chest wall contours, and the intra-fiducial skin surface. Deformation predictions were evaluated at surface fiducial locations and subsurface tissue features that were expertly identified and tracked. Among $n = 7$ different human subjects, an average of 22 ± 3 distributed subsurface targets were analyzed in each breast volume. *Results*: The average target registration error (TRE) decreased significantly when comparing rigid registration to this nonrigid approach (10.4 ± 2.3 mm vs 6.3 ± 1.4 mm TRE, respectively). When including a single subsurface feature as

additional input data, the TRE significantly improved further (4.2 ± 1.0 mm TRE), and in a region of interest within 15 mm of a mock biopsy clip TRE was 3.9 ± 0.9 mm. *Conclusion*: These results demonstrate accurate breast deformation estimates based on sparse-data-driven model predictions. *Significance*: The data suggest that a computational imaging approach can account for image-to-surgery shape changes to enhance surgical guidance during BCS.

5.2.2 Introduction

In the United States, breast cancer is the most common cancer in women and will be diagnosed in an estimated 290,560 people this year [1]. The majority of these patients will be recommended for breast conserving surgery (BCS) [2, 3], a tissue-sparing procedure that consists of surgical removal of the lesion and a margin of healthy tissue surrounding that lesion. Unfortunately, the patient position in surgery is very different from the position for most diagnostic breast imaging, making imaging information underutilized in surgery. For diagnostic magnetic resonance (MR) imaging, a patient is lying prone, or face down, with the breast pendant within an imaging radiofrequency coil. For diagnostic ultrasound imaging, the patient lies supine, or face up, with the arm fully abducted beside the head. For mammography, the patient is standing with the breast compressed between two plates. None of these imaging positions are representative of surgical position. In surgery, a patient lies supine with the arm outstretched laterally at 90°, i.e. in a T-shape. As a result of this incongruence between diagnostic imaging and surgical presentation, it can be challenging for surgeons to relate the tumor location in a medical image volume to its intraoperative counterpart on the operating table. In addition, studies have emerged demonstrating that switching from prone to supine imaging presentations induces tumor shape and size differences, as well as a shift in the tumor position with respect to all available anatomical landmarks [18, 42, 64]. Even under ideal circumstances when a patient remains in a supine configuration during imaging, simple 90°abduction of the arm results in significant shifts and shape changes in breast tissue [238]. In fact, even simple intraprocedural changes such as small rotations of the operating room table can result in significant remaining alignment errors after rigid registration [238].

In an effort to overcome difficulties surrounding intraoperative lesion localization during BCS, several techniques have been established to provide positional information during surgery. Wire-guided localization involves inserting a guide wire into the center of a tumor using cross-sectional image guidance. In surgery, the surgeon uses the wire as a guide path to the region of interest. However, in radiology the guide wire placement technology is geometrically constrained and can lead to resection paths that are suboptimal. Additionally, as these wires are placed potentially hours before the surgery, the protruding wire can become displaced. Most importantly, even with optimal wire placement and successful resection along the wire path, the surgeon must estimate the relative position of the wire tip within the lesion and must also approximate the exact

tumor boundary surrounding the unseen wire tip when resecting a suitable surgical margin.

Though guide wire approaches are still in use, in the past decade, the expanding use of implanted seed-based markers (e.g. radioactive, magnetic, and radar reflector seeds) is beginning to replace guide wire approaches. For seed-based methods, a small localization marker is implanted near the lesion by radiology in the days or weeks before surgery. The placement of the marker is then confirmed with imaging. The seed is localized intraoperatively using a handheld probe that reports the seed-to-probe distance. Though these seed-based techniques offer improvement over wire guidance, reoperation rates remain high due to residual disease after resection, or positive margins. Average reoperation rates are reported up to 30%, with most averages around 10–20% [13, 14, 16]. These methods provide seed location and allow for unconstrained trajectory to a target, but they cannot provide guidance for boundary management during resection to excise the precise deformed lesion shape. In recent years, reoperation rates have plateaued around 10–20% [14, 72, 73], suggesting that these approaches may be at their resolution limit.

Intraoperative MR imaging can provide the shape of the tumor on the operating table, but requires the use of nonmagnetic tools and interruption of surgery for imaging [18]. Additionally, intraoperative MR is not widely available, as most operating rooms are not equipped with MR scanners. Alternatively, ultrasound can be used within the sterile field throughout the procedure to visualize echogenic tumors intraoperatively. The transducer can also be used to investigate the resection cavity for remaining tumor after the initial excision. One of the largest drawbacks to intraoperative ultrasound is that not all lesions are visible on ultrasound. Though intraoperative ultrasound provides low rates of positive margins (2–14%) [23–25], only 50% of non-palpable tumors are visible on ultrasound [26]. There remains a need for 3D guidance that can be used for a larger majority of patients.

Image guidance systems can provide information about full tumor boundaries by registering, or aligning, preoperative imaging with the physical patient space. For BCS, these research systems typically use preoperative MR imaging [50, 60, 139] as it offers high sensitivity [45, 47] and, when performed in a supine position, can provide an improved understanding of intraoperative tumor shape and position [19, 46, 64]. There are several ways supine MR data have been leveraged in the operating room. Sakakibara et al. positioned patients in a surgical pose for MR imaging and used a projector to display tumor extent directly onto the breast surface during surgery. This method produced smaller resection volumes and lower positive margin rates than wire guidance [132]. Recently, Wu et al. achieved 18% positive margin rates by tracing tumor positions onto the skin surface using a patient specific 3D printed breast mold derived from supine MR imaging [134]. These methods show the value of supine MR in determining intraoperative tumor extent. However, their reliance on a skin surface projection still provides limited understanding of tumor depth and makes them inadequate for complete 3D margin management during resection.

Image guidance systems that incorporate 3D renderings can show the full tumor extent based on preoperative imaging. An image guidance system from Pallone et al. expanded upon these skin surface projections by including a 3D model view and tracked tools [41]. When evaluated on 69 patients in a randomized controlled prospective study, their system showed a 9% positive margin rate under current margin guidelines, which was lower than for wire-guided BCS. Though this did not meet a level of statistical significance ($p = 0.08$), it is certainly suggestive [50]. In separate work, Perkins et al. integrated MR imaging into an augmented reality system for BCS with promising qualitative validation [139].

Although the aforementioned approaches aim to display preoperative tumor extent registered to the intraoperative space, the reliance on rigid registration between image and physical spaces represents a substantial limitation. Though simple linear shifts are easily accommodated with rigid approaches, there is a considerable degree of nonrigid deformation that occurs between imaging positioning and surgical presentation, even for supine-to-supine registrations [238]. Abduction of the arm, re-positioning of the patient, and rotation of the operating table all contribute to discrepancies between imaging and surgical tumor location. Due to these nonrigid shifts, residual error after rigid registration can be large—on the order of 10–30 mm on the surface [238]. Localization inaccuracies can lead to larger resected specimen volumes, positive margins, or both. In fact, in qualitative evaluation, [139] notes the conspicuous need for nonrigid correction due to obvious misalignments after rigid registration.

Nonrigid deformation correction for breast cancer surgery has been limitedly explored, especially within the context of the clinically relevant supine-to-supine registration problem. However, initial findings suggest that nonrigid registration approaches can improve accuracy for BCS. Ebrahimi et al. observed deformations from full abduction of the arm in supine MR images, and used thin plate splines on 24–34 fiducials well distributed across the breast surface to correct for deformations. Though the method had no biophysical link, accuracy at tumor centroids in six patients improved from 3–18 mm with rigid registration to 1–10 mm. However, improvement across all cases was variable [171]. Although the approach performed very well for some cases, in one case error actually increased with nonrigid registration.

Conley et al. introduced a nonrigid correction method that employed a forward solved finite element method (FEM) using sparse data collection in a mock-intraoperative setting [60]. Following preoperative supine MR imaging, mock-intraoperative data were collected including surface fiducial locations marked with tracked tools, surface collection with a laser range scanner, and the chest wall position measured with tracked ultrasound. An initial image-to-physical rigid registration was performed, and the remaining fiducial mismatch was used to estimate surface displacements. A patient specific breast mesh was assumed to experience loading in the craniocaudal direction only at inferior and superior mesh boundaries. This work reduced two tumor centroid errors from 6.5 and 12.5 mm with rigid registration to 5.5 and 5.3 mm after correction,

respectively [60]. Although the nonrigid approach offered improvement, the number of cases was limited and the value of the method was inconsistent, offering 15% and 58% improvement in the two cases evaluated. While the work was interesting, unfortunately, the assumption of only craniocaudal boundary forces from observed surface fiducial movements is likely a limitation. The approach did not account for displacements in the medial-lateral, and anterior-posterior directions which collectively are approximately equal to the craniocaudal displacements according to a recent study by Richey et. al. [238].

In the work presented here, an inverse modeling approach is employed to predict breast deformation from abduction of the arm. In contrast to forward models, inverse modeling approaches can be designed to reconstruct forces at the anatomical locations that experience true mechanical loading. Here, the linearized iterative boundary reconstruction (LIBR) method, as presented in [28], has been modified for clinical application in BCS. The LIBR method solves for a distributed profile of applied mechanical loading that produces the observed intraoperative breast shape change given a set of sparse data constraints. Once the shape change has been reconstructed, a navigation system can be updated with a deformed image volume that constitutes a computational image of the new tissue state. Another important contribution of this work is the degree of validation that is offered in the evaluation. Previous work in nonrigid breast registration has been very limited. Here, the modified LIBR approach is evaluated on 157 subsurface targets well distributed within the breast volumes of $n = 7$ human subjects, thus providing a global volumetric evaluation of target registration errors.

5.2.3 Methods

5.2.3.1 Overview of Experimental Protocol

A mock operating room (OR) experiment was conducted on $n = 7$ healthy volunteers. Supine MR imaging provided a mock-preoperative scan with the arm at the subject's side. Repeat imaging was conducted with the subject in an alternate configuration with the ipsilateral arm fully abducted. The supine MR with fully abducted arm was treated as a mock-intraoperative configuration, from which sparse data were extracted to represent an extent feasible for intraoperative collection. This extent is representative of acquisition in physical surgical space that would remain minimally disruptive to surgical workflow. With data obtained in the mock-preoperative and the mock-intraoperative states, a novel image-to-physical registration approach was performed and evaluated. Accuracy assessment involved transforming novel (not used as part of the registration) subsurface targets from the mock-preoperative location to their predicted mock-intraoperative location and then comparing to the manually measured counterpart in the acquired mock-intraoperative state. The evaluation involved on average 22 ± 3 subsurface targets across the data set, comprising a total number of 157 corresponding target points. Lastly, as patients generally have biopsy clips and/or a localization marker

implanted in the breast prior to surgery, the evaluation experiment was extended to include the impact on alignment if a single subsurface feature could also be incorporated into the sparse set of intraoperatively acquired data.

5.2.3.2 Human Imaging

Data were collected on seven healthy volunteers as approved by the Institutional Review Board at Vanderbilt University (protocol code 130038, date of approval 11/11/2015). Volunteers ranged from 23 to 57 years of age (average age of 29 $\pm$ 12) with breast volumes of 398 to 1228 cm^3 (average volume of 688 $\pm$ 256 cm^3). As noted above, the mock-preoperative imaging state involves supine imaging with the arms down within the closed MR bore. As discussed, surgical positioning involves the arm abducted 90°in a T-shape orientation and previous work supports significant shape change between these two states [238]. This configuration is not possible within the scanner. Here, to provide full volumetric MR data for comprehensive subsurface validation, the fully abducted position was used to approximate the surgical position. It should be noted that this represents a more considerable challenge than the T-shape surgical presentation. In previous work, the shape change for the fully abducted arm is approximately 45% larger in magnitude than the halfway abducted surgical presentation [238].

With respect to specific protocol, two supine MR images were obtained sequentially: one with the arm down beside the torso, and a second with the arm up beside the head. In both scans, the contralateral arm was down. Before scanning, 26 fiducials (IZI Medical Products, Owing Mills, MD) were evenly distributed across the breast surface. These fiducials are visible in both MR images and serve as corresponding surface points. Due to the significant breast shifts, after abduction some fiducials moved to outside the image field of view; at least 23 corresponding fiducials were recognized in each case. Images were obtained on closed bore 3T Phillips scanners using a 16-channel torso coil with padded support to reduce compression of the breasts. In one case a plastic cage was placed around the subject's torso to fully suspend the coil, eliminating tissue compression. It should be noted that the plastic cage wholly eliminated breast compression for this case (similar to proper application of padded coil support) with the added benefit of simplifying subject repositioning. A THRIVE sequence was used with one of two voxel resolutions, $0.357\times0.357\times1$ mm^3, or $0.391\times0.391\times1$ mm^3 voxel size. The THRIVE pulse sequence does not compensate for respiratory and cardiac motions. However, motion artifacts were not noticeable for the majority of volunteers in this study. Though one subject had noticeable respiratory artifact, this artifact was small enough that image features were still able to be selected with no change to the imaging procedure (e.g. respiratory gating).

5.2.3.3 Image Derived Data

The breast volumes of both the mock preoperative and intraoperative breast state were segmented manually to include the skin, ligaments and adipose tissues. Chest wall was not included in the breast tissue segmentation. To improve the speed of segmentation, automatic interpolation in ITK-SNAP [249] was used, segmenting every 5-10 slices in the axial direction. Generally, an experienced user takes 15-30 minutes to segment the breast depending on complexity of the breast shape. Custom mesh generation software was used to generate patient specific 3D meshes from the breast segmentations of both states [233]. Meshes were discretized to tetrahedral elements with 4 mm edge length. Mock-preoperative breast meshes ranged from approximately 6,500–18,000 vertices.

The supine MR images provided the following data as shown in Figure 5.1: (1) corresponding locations of the MR-visible synthetic surface fiducials, (2) the breast skin surface, (3) the chest wall, and (4) subsurface feature locations used for validation. All features were designated manually, and all surfaces were subsampled from the boundary of the patient specific 3D mesh. To simulate realistic intraoperative data collection, a sparse data set was taken from the mock-intraoperative state (arm-abducted MR image). For the mock-intraoperative state, the sparse chest wall data included a set of chest wall contours simulating collection from 7–10 linear probe ultrasound images with 40 mm width. It should be noted that the distribution of chest wall sample contours was based on previous work in a tracked ultrasound study measuring the chest wall in a mock-intraoperative setting using a BK5000 18L5 linear probe (BK Medical UK Ltd., Peabody, MA) [238]. Contours were designated manually, each contour taking only a few seconds to segment. With respect to the breast skin surface, intraoperative segmentations were subsampled from the breast mesh boundary nodes to only include intrafiducial surface points. This process ensures that the extent of the intraoperative skin surface is entirely contained on the preoperative mesh. Lastly, the subsurface features used for validation were selected manually, choosing an average of 22 ± 3 (ranging from 18–26 across the data) well distributed homologous points for each subject. Throughout the seven breast volumes, a total of 157 corresponding points were identified.

5.2.3.4 Nonrigid Deformation Correction

This work employs the linearized iterative boundary reconstruction (LIBR) method, recently presented by Heiselman et al. [28], modified for breast-specific data. Here, breast deformations are assumed to be isotropic, homogeneous, and linearly elastic. The method supposes that tissue deforms according to the Navier Cauchy equations, which govern linear elasticity at static equilibrium [232]. Here, the Galerkin method of weighted residuals [234] using conventional linear local Lagrange polynomial interpolants with tetrahedra is used to determine approximate displacements which come close to the unknown true displace-

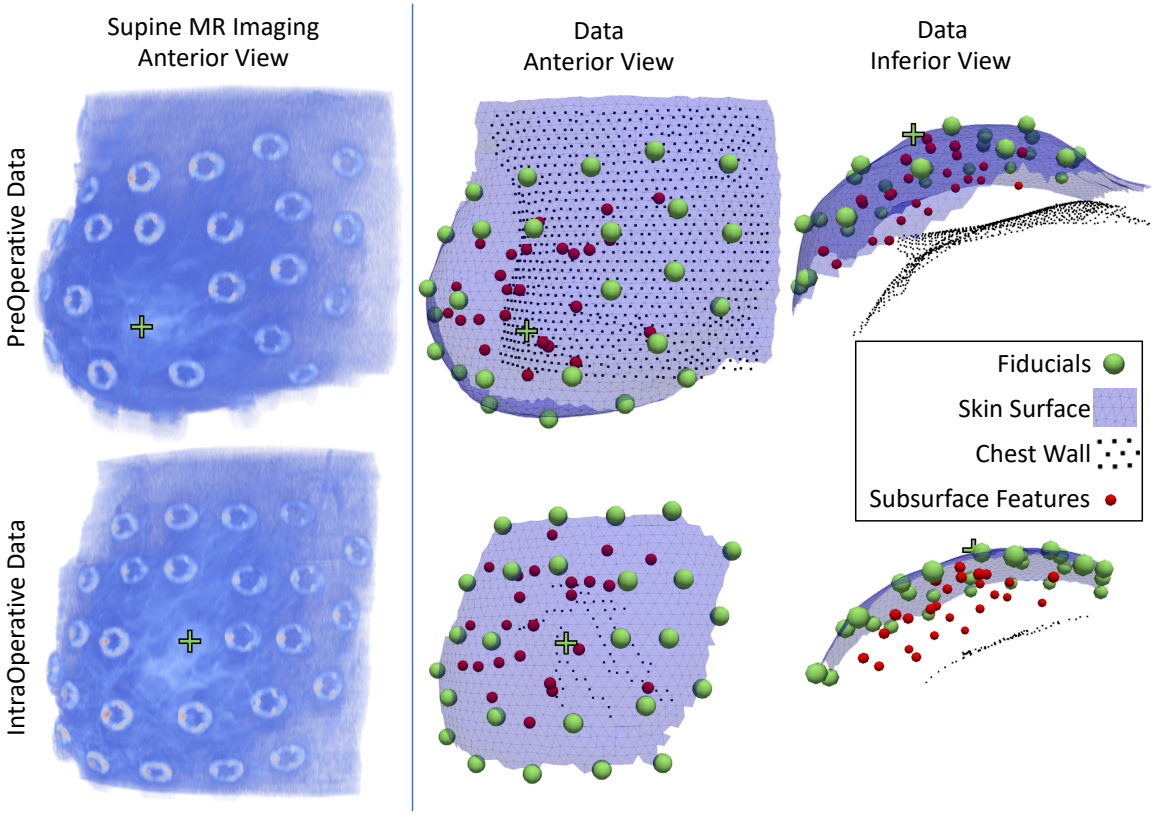

Figure 5.1: Exemplar data for one subject, rendered in ParaView [250]. Supine MR projection images (left) with nipple displayed as +, and extracted data (right). The model is evaluated at the subsurface features (red), which were not used to drive the correction.

ment field.

Briefly, the LIBR method solves for a set of boundary condition displacements that produce the observed intraoperative deformation state. A series of control points on the model surface are perturbed in each of the three Cartesian directions. Perturbations are in the form of displacement boundary conditions, i.e. Dirichlet conditions, and the resulting deformation solution is computed using the finite element method. Each point loading is relaxed to establish an equivalent distributed load with identical far-field behavior as the point source. The relaxed displacements resulting from each control point perturbation embody independent modes that characterize local responses to forces applied to the tissue. These deformation solutions can be linearly combined to iteratively reconstruct intraoperative organ deformations based on optimizing the objective function from [28],

$$\Omega(\alpha,\tau,\theta) = \sum_{F} \frac{\omega_F}{N_F} \sum_{t=1}^{N_F} {f_i}^2 + \omega_E {f_E}^2 \tag{5.1}$$

where f_i represents the distance between the position of an intraoperative data point provided to the correction algorithm and its counterpart on the registered preoperative model, f_E represents the strain energy of the deformation, ω_F represents the weight of a feature F, N_F represents the number of points within feature F, and ω_E represents the strain energy weight. The objective function is parameterized over a weight vector α that encodes the deformation state, and rigid transformation parameters τ and θ, which represent rigid translations and rigid rotations of the deforming model, respectively. Levenberg-Marquardt optimization is used, terminating when the step-wise error tolerance $\Delta\Omega < 10^{-12}$ is satisfied. Material parameters in the Navier Cauchy equations are set as in [28], with Young's Modulus $E = 2100\ Pa$ and Poisson's ratio, $v = 0.45$.

The LIBR method reported in [28] is modified to reflect the breast localization data described above, and Equation 5.1 becomes

$$\Omega(\alpha,\tau,\theta) = \frac{1}{N_{fids}} \sum_{i=1}^{N_{fids}} {f_i}^2 + \frac{1}{N_{skin}} \sum_{i=1}^{N_{skin}} {f_i}^2 + \frac{1}{N_{chest}} \sum_{i=1}^{N_{chest}} {f_i}^2 + \omega_E {f_E}^2 \tag{5.2}$$

with the assumption that each data component of the objective function equally impacts its evaluation (i.e. $\omega_F = 1.0\ m^{-2}$). The model-data misfit error, f_i, for each feature is computed based on the type of correspondence, with MR-visible fiducials (abbreviated as fids) treated as corresponding points, and skin and chest wall data treated as point-to-surface correspondences (or sliding constraints) as described in [28]. The strain energy weighting factor, ω_E, has been empirically determined and is fixed at $10^{-9}\ Pa^{-2}$. The modeling workflow is summarized in Figure 5.2.

Control points serve as the action points of applied perturbations, and consist of 45 discrete locations dispersed across all the boundaries of the mesh, except for the skin surface. As in Heiselman et al., k-means

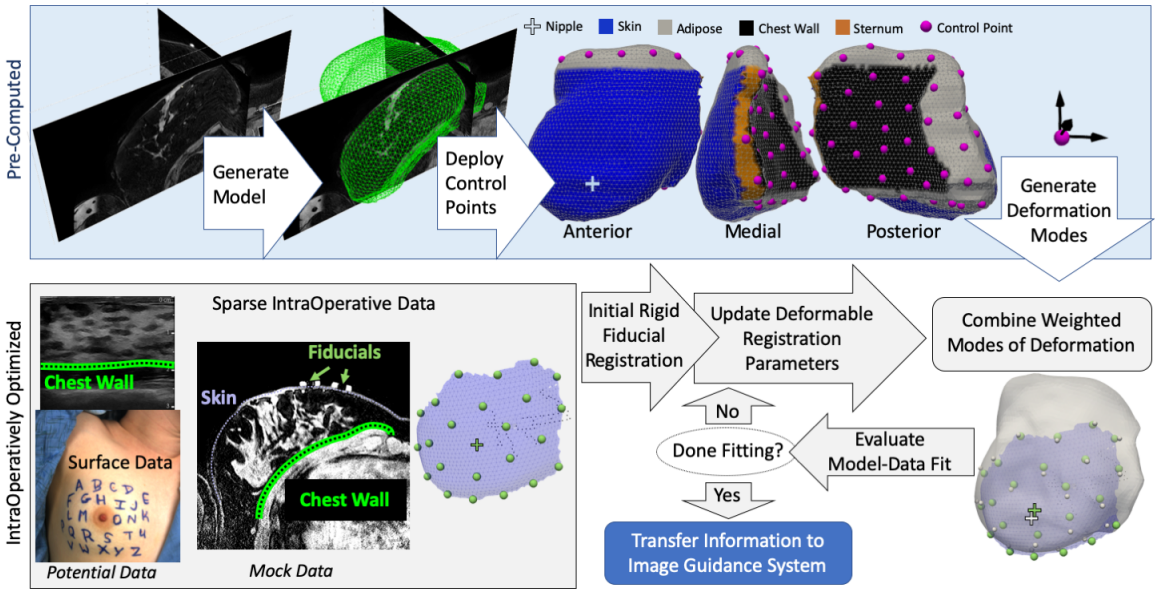

Figure 5.2: Schematic of the method workflow, with precomputed steps (top) and intraoperative optimization steps (bottom). The nipple is consistently marked +.

clustering was used to evenly distribute control points across the control surfaces [28]. The distribution of 45 control points, in magenta, on a preoperative breast mesh is shown in the top right of Figure 5.2 in anterior, medial, and posterior views. Tissue types are designated with skin in blue, sternum in orange, and chest wall in black. Internal tissue that is transected by the mesh is marked in grey. This control point distribution represents the boundary of the computational domain where mechanical displacements are applied with remaining areas assumed stress-free. Applied displacements ideally capture the forces internal to the subject's body but external to the meshed computational domain, i.e. forces exerted by ligaments or tension on tissue adjacent to the meshed domain. It should also be noted that in some cases the breast surface did come into contact with the MR torso coil. However, these forces were minimized with the weight of the coil supported by padding or a plastic cage. Therefore, this contact was considered to have negligible influence on the registration.

Throughout this work, surface fiducial registration error (FRE) and subsurface target registration error (TRE) are computed as the arithmetic mean and standard deviation of Euclidean distances between predicted data positions and the ground truth positions as measured in the mock-intraoperative MR.

5.2.3.5 Impact from Including a Single Nearest Neighbor Subsurface Feature

Clinically, it is quite possible to localize a subsurface point near the lesion intraoperatively. For example, before surgery, patients routinely have biopsy clips and/or localization markers implanted in the breast in close proximity of the tumor. These subsurface features serve to assist in localization during tissue resection and can be localized either with tracked ultrasound images or with other intraoperative localization approaches.

On the former, approaches to account for deformations induced by ultrasound probe compression have been developed to enable accurate localization of subsurface targets with ultrasound [251]. With respect to the latter, investigators have developed custom seeds capable of being wirelessly tracked in 3D space during breast surgery [140, 252].

Given the common availability of a subsurface target near the region of interest, the impact of including a single subsurface feature on the LIBR approach was evaluated. For a given target, the nearest neighbor ($k = 1$) subsurface feature was considered another tracked point and included as an additional input to the model. Thus $k = 0$ indicates that no corresponding subsurface points were used. To accommodate, when $k = 1$ the objective function (Equation 5.2) is modified to include this

$$\Omega(\alpha, \tau, \theta) = {f_{feature}}^2 \frac{1}{N_{fids}} \sum_{i=1}^{N_{fids}} {f_i}^2 + \frac{1}{N_{skin}} \sum_{i=1}^{N_{skin}} {f_i}^2 + \frac{1}{N_{chest}} \sum_{i=1}^{N_{chest}} {f_i}^2 + \omega_E {f_E}^2 \tag{5.3}$$

where $f_{feature}$ is the model-data fit at one subsurface feature point, treated as a corresponding point as outlined in [28].

Here, the additional feature is the target's nearest neighbor, i.e. the subsurface point closest to the evaluation target of interest. The average distance from a target to its nearest neighbor was 15.0 ± 6.6 mm. One subsurface feature was considered a target and a model optimization was performed. The model optimization included the data outlined in Equation 5.3, where $f_{feature}$ is the model-data fit at the single target's nearest neighbor. Model accuracy was evaluated at the target of interest and across all surface fiducials. This process was then repeated, iterating through each target in the complete list of subsurface features.

Throughout this study, the subsurface TRE was only ever evaluated at novel points, i.e. it is never evaluated at any subsurface points used to drive the optimization. However, surface FRE is reported separately as residual error at surface fiducials that were used to drive the optimization.

5.2.3.6 Accuracy in Regions of Interest

Approximately 50% of breast lesions have radii smaller than 5 *mm*, and 77–87% have radii under 10 *mm* [150, 155]. Therefore, if planning to resect 10 mm of healthy tissue surrounding a lesion, as suggested in [38, 64, 132], over 50% of lesions would have planned resection volumes within an $r = 15$ *mm* region of interest (ROI), and over 75% of lesions would fall well within an $r = 30$ *mm* ROI. This means that the localization accuracy in these smaller regions of interest are clinically important.

As subsurface features in this work were selected to offer full coverage of the breast volume, distances between subsurface features are generally larger than the expected distance from a lesion to its implanted biopsy clip or localization seed. Conventional standard of care considers localization markers to be accurately

placed when they are within 10 mm of a lesion, but here the average distance between a target and its driving nearest neighbor was 15.0 ± 6.6 mm. To extend the analysis, each subsurface feature was treated as a mock biopsy clip that was localized in the operating room (hereafter referred to as a clip). The model's predictive accuracy was then evaluated by considering all targets within a region of interest (ROI) surrounding each clip. While the nearest neighbor analysis in the previous subsection provides an evaluation framework at every subsurface point, the ROI analysis provides analysis only locally in the immediate tissue neighborhood near a clip of interest.

Radii were selected based on breast lesion sizes, offering localization accuracy within the ranges of realistic excision volumes (accounting for over 50% and 75% of patients for $r = 15$ *mm* and $r = 30$ *mm* respectively). A region of interest was defined centered around each clip using radii of $r = 15$ *mm*,$r = 30$ *mm*, and $r = \infty$ *mm*. While this section focuses on local accuracy, it should be noted that a radius of $r = \infty$ gives the full field improvement across the entire breast volume from the inclusion of one subsurface mock biopsy clip. As noted above, smaller radii describe accuracy in a local region of interest surrounding a mock biopsy clip.

The model-based registration approach was then implemented using breast surface and chest wall data in addition to the single subsurface mock clip as the driving spatial information. The objective function for this analysis still utilizes Equation 5.3. Here, the additional feature is the subsurface clip of interest, and $f_{feature}$ is the model-data fit at that clip. The model evaluation differs with r, as all target errors within the ROI are reported. This process was repeated with each model implementation using a different subsurface feature as the mock surgical clip. On average, $r = 15$ *mm* ROIs included 1 ± 1 targets, and $r = 30$ *mm* ROIs included 4 ± 2 targets. At $r = \infty$, the number of included data points is 21 ± 3, i.e. all subsurface points are targets expect for the feature included in the optimization. Evaluating with a small radius ($r = 15$ *mm*) limits the coverage of evaluation, discarding points with no nearby subsurface data since these more isolated features are outside the scope of what would be realistic in the clinic. If a localization marker were more than 10 *mm* away from the target lesion, an additional marker would be placed closer to the target.

Though both the nearest neighbor and ROI approaches include one subsurface feature in each model optimization, they provide complimentary components of analysis. The nearest neighbor approach guarantees each subsurface feature is treated as an evaluation target exactly once. On the other hand, the ROI approach guarantees each subsurface feature is treated as an acquired data point included in the optimization function. The ROI approach, however, does not guarantee that every subsurface target is evaluated. As an example of this, if a subsurface feature is more than 15 mm away from all other targets, it will not be within any set of evaluation data at $r = 15$ *mm*. The number of ROIs (i.e. number of model optimizations) evaluated for each subject is reported.

5.2.4 Results

5.2.4.1 Minimal Data-Driven Optimization

Mean registration errors were compared with paired t-tests ($\alpha = 0.05$). When compared to point based rigid registration, the nonrigid deformation correction without subsurface feature drivers offers significant improvement in fiducial registration error (FRE) and target registration error (TRE) ($p < 0.001$), from FRE of 7.9 ± 1.6 to 2.4 ± 1.3 and TRE of 10.4 ± 2.3 mm to 6.3 ± 1.4 mm (Table 5.1 and Table 5.2). Precomputing the modes of deformation takes, on average 13 ± 4 minutes using 64 processors on a 2.20 Ghz Intel® Xenon® CPU. The deformable correction takes, on average, 21 ± 18 seconds (median 14 s) for optimization on a single thread of a 2.20 Ghz Intel® Xenon® CPU. Additionally, for each method the model improvement over rigid registration is reported as

$$\frac{(error_{rigid} - error_{nonrigid})}{error_{rigid}} \times 100\%. \tag{5.4}$$

Table 5.1: Subsurface target registration error (TRE) mean $\pm$ standard deviation (maximum) in millimeters

Case	Breast Volume (cm^3)	Point Based Rigid Registration TRE	Nonrigid Registration TRE	
			k=0	k=1
a	1,228	9.1 ± 2.8 (15.0)	6.2 ± 2.4 (10.7)	4.0 ± 2.0 (8.8)
b	692	11.3 ± 4.1 (19.5)	6.1 ± 3.4 (13.1)	3.8 ± 1.6 (6.8)
c	663	9.7 ± 3.6 (21.0)	6.1 ± 3.3 (13.1)	3.8 ± 1.8 (8.1)
d	638	11.4 ± 7.2 (24.5)	7.4 ± 4.0 (15.3)	4.3 ± 2.0 (9.2)
e	614	10.8 ± 3.3 (15.9)	7.2 ± 2.7 (13.3)	5.2 ± 2.5 (9.9)
f	588	14.0 ± 3.8 (19.0)	7.5 ± 2.7 (12.1)	5.7 ± 2.5 (10.2)
g	398	6.5 ± 4.1 (14.2)	3.5 ± 1.9 (8.0)	2.5 ± 0.9 (4.4)
Mean	*689 cm^3*	*10.4 ± 2.3*	*6.3 ± 1.4*	*4.2 ± 1.0*
Improvement over rigid registration			*39%*	*60%*

Table 5.2: Surface target registration error (FRE) mean $\pm$ standard deviation (maximum) in millimeters

Case	Point Based Rigid Registration TRE	Nonrigid Registration FRE	
		k=0	k=1
a	9.3 ± 2.8 (13.6)	5.1 ± 2.4 (10.7)	6.0 ± 2.5 (12.8)
b	9.6 ± 3.2 (17.3)	6.1 ± 3.4 (4.0)	2.9 ± 1.5 (8.5)
c	6.9 ± 2.2 (11.4)	6.1 ± 3.3 (5.4)	3.7 ± 1.7 (9.3)
d	6.3 ± 2.5 (14.4)	7.4 ± 4.0 (3.7)	2.4 ± 1.2 (8.1)
e	9.0 ± 4.4 (24.6)	7.2 ± 2.7 (6.6)	3.4 ± 1.7 (12.4)
f	8.3 ± 3.0 (13.6)	7.5 ± 2.7 (4.8)	2.9 ± 1.5 (7.7)
g	5.5 ± 1.7 (9.5)	3.5 ± 1.0 (4.7)	1.8 ± 1.1 (6.3)
Mean	*7.9 ± 1.6*	*2.4 ± 1.3*	*3.6 ± 1.5*
Improvement over rigid registration		*69%*	*54%*

5.2.4.2 Inclusion of a Single Nearest Neighbor Subsurface Feature

The TRE significantly improves with the addition of subsurface feature data from $k = 0$ to $k = 1$ ($p < 0.001$). Conversely, the FRE significantly worsens with the inclusion of a subsurface feature point from $k = 0$ to $k = 1$ ($p < 0.001$). Subsurface TREs are presented in Table 5.1, and residual surface FREs are presented in Table 5.2. Spatial distribution of subsurface target error with the inclusion of the nearest neighbor subsurface point ($k = 1$) is visualized in Figure 5.3. This figure shows both the broad distribution of targets, as well as the distances between targets and their nearest neighbors. Left breasts are reflected so each breast mesh is in the same anatomical orientation, with the arm on the left and the sternum on the right of the image, as indicated on the full-body diagram. Breast volumes are also reported in Table 5.1. While the model performs best in the smallest breast volume, for this dataset there is no observable trend with respect to volumes. Figure 5.4 shows the distribution of average error across the seven cases, and statistical comparisons. For all registration methods reported in Figure 5.4 , each target is evaluated exactly once.

5.2.4.3 Accuracy in Regions of Interest

When evaluation was limited to a region of interest ($r = 30$ *mm*), registration error significantly decreased in comparison to evaluation across the whole breast with $r = \infty$ ($p < 0.001$). As the radius decreases, the TRE continues to significantly improve from $r = 30$ *mm* to $r = 15$ *mm* ($p = 0.001$). For $r = \infty$, the addition of one subsurface clip resulted in higher error when compared to TRE for the model run with no subsurface clip ($p = 0.026$). In other words, although local target errors improve, far field errors worsen.

Results for regions of interest with decreasing radii are presented in Table 5.3 and distribution of average target error is shown in Figure 5.5. As previously discussed, as the radius decreases, some clips no longer have targets within the region of interest and are therefore not included in evaluation. This behavior is reflected in the number of ROIs, also presented in Table 5.3. Though the average number of regions evaluated remains constant from $r = \infty$ *mm* to $r = 30$ *mm*, the average TRE drops significantly, reflecting higher accuracy in a region of interest, even when model accuracy is evaluated across a wide spatial distribution of regions. While the average TRE improves significantly again when the radius is reduced to $r = 15$ *mm*, the number of evaluated regions drops down to 14 ± 5. This reduction in the number of regions evaluated means that our analysis is limited to the more central regions of the breast where subsurface features are more densely distributed. The density of subsurface points can be observed in Figure 5.3.

5.2.5 Discussion

The method presented here demonstrates state-of-the art localization in seven human breasts, with comprehensive target sampling in varying volumes. The method offers consistent, significant improvement with

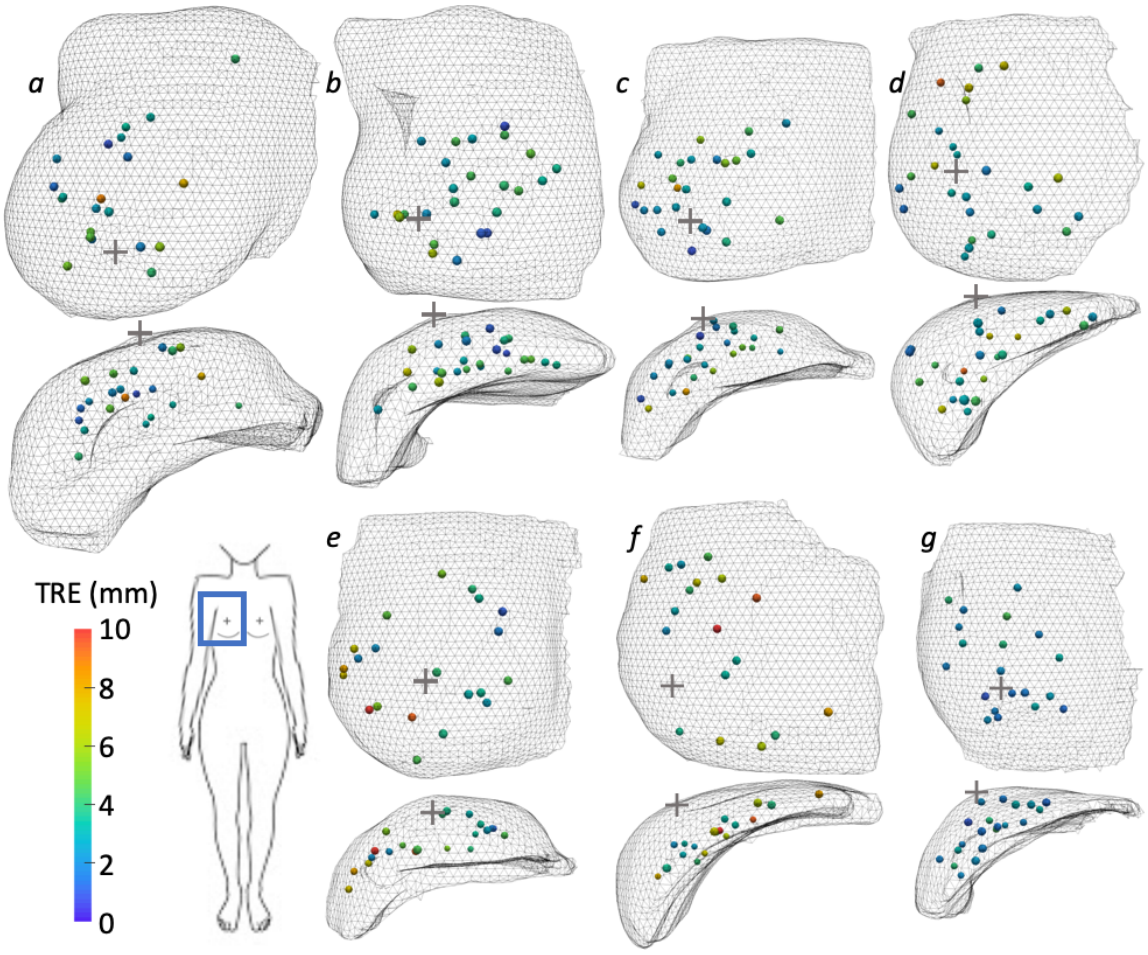

Figure 5.3: Distribution of subsurface target registration error (mm) with the $k = 1$ nearest neighbor subsurface feature included as model input for each target evaluation. For each case the target locations are shown in the preoperative, or arm down, breast mesh from the anterior view (top) and inferior view (bottom). The subject's orientation is on the full-body diagram at the bottom left, with the blue box showing the approximate anterior field of view. The nipple is consistently marked +.

Table 5.3: Subsurface target registration error (TRE) for nonrigid correction in a region of interest (ROI) with radius r around 1 clip. Mean ± standard deviation (maximum) are reported in millimeters, with average improvement over rigid registration shown as a percentage.

Case	$r = \infty$ mm		$r = 30$ mm		$r = 15$ mm	
	Avg ± std (Max)	# of ROIs	Avg ± std (Max)	# of ROIs	Avg ± std (Max)	# of ROIs
a	6.6 ± 2.4 (12.7)	22	5.3 ± 2.3 (10.9)	21	4.0 ± 2.1 (8.8)	15
b	6.3 ± 3.1 (13.7)	25	5.0 ± 2.2 (10.6)	25	4.3 ± 1.9 (7.7)	21
c	6.2 ± 2.8 (13.4)	25	4.9 ± 2.8 (10.7)	24	3.9 ± 1.6 (6.7)	14
d	7.8 ± 3.7 (17.6)	26	5.8 ± 2.4 (11.3)	26	2.9 ± 0.9 (4.3)	17
e	7.2 ± 2.8 (14.0)	21	5.8 ± 2.8 (12.5)	20	4.2 ± 2.0 (8.0)	13
f	7.6 ± 2.7 (13.4)	18	6.1 ± 2.6 (11.4)	17	4.1 ± 1.6 (6.8)	8
g	3.7 ± 1.8 (8.3)	20	2.6 ± 1.1 (5.8)	20	1.8 ± 0.7 (3.0)	8
Mean	*6.5 ± 1.4*	22	*5.0 ± 1.1*	22	*3.6 ± 0.9*	14
Improvement	*38%*		*52%*		*65%*	

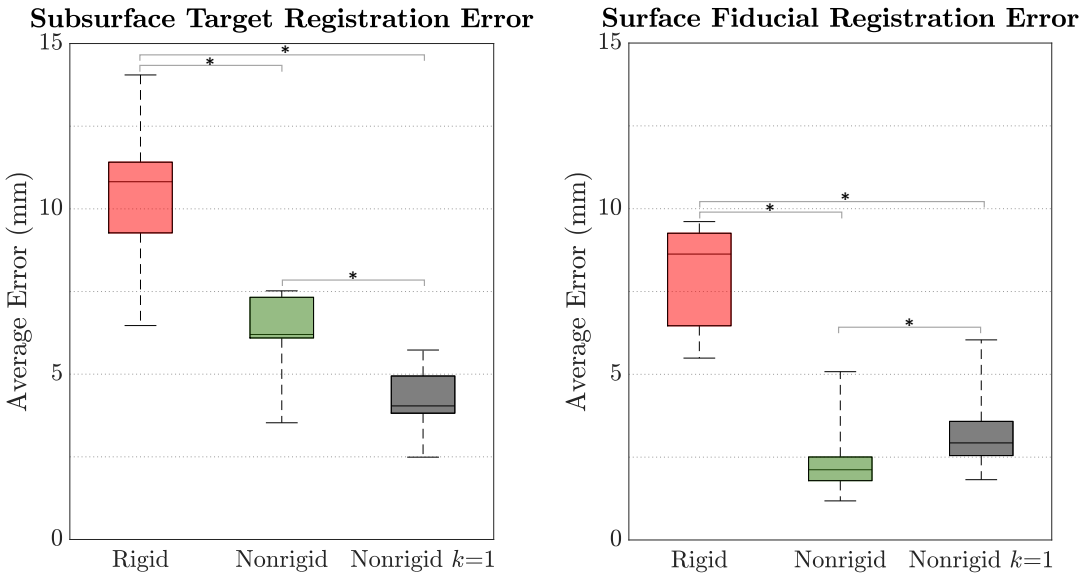

Figure 5.4: Comparison of registration error (mm) for point based rigid versus nonrigid registration with varied amounts of subsurface features, where $k = 1$ indicates that a neighboring subsurface feature is included in the model optimization. Significant differences exceeding $p < 0.001$ are reported with *.

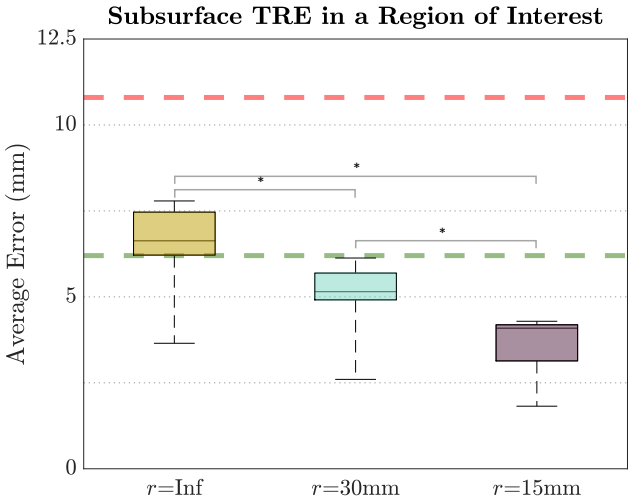

Figure 5.5: Comparison of subsurface target registration error (TRE) in millimeters, varying the radius of the region of interest, r, centered on a subsurface clip included in driving the model. Dashed lines represent median TRE for rigid (red) and nonrigid (green) registration with no subsurface clips included. Significant differences exceeding $p \leq 0.001$ are reported with *.

50–60% correction over conventional rigid registration. This algorithm provides subsurface target errors consistently on the order of 1 cm or less in targets well distributed throughout seven breast volumes undergoing mock preoperative-to-surgical deformations. This modeling framework can correct for nonrigid deformations fast enough to provide accurate guidance at patient bedside. The presented method outperforms previous findings with less variability.

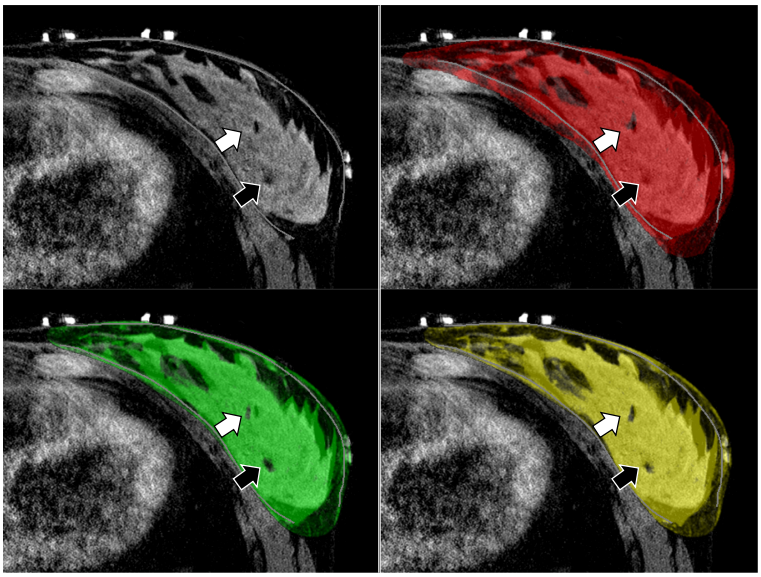

Figure 5.6: An axial slice of registered computational images overlaid on the ground truth image in the fully abducted arm position for case *d*. In all panels, segmentations of the chest wall and skin surface are outlined in gray. The rigidly registered image is shown in red. The model deformed image computed without subsurface features ($k = 0$) is shown in green. In yellow is the model deformed image computed with one additional subsurface point ($k = 1$) approximately 10 mm from the feature indicated by the white arrow.

This model correction technique combined with sparse intraprocedural data can be used to reconstruct computational images of the deformed anatomy for use in intraoperative guidance. An example of deformed computational images is shown in Figure 5.6 for case *d*. Qualitatively, the subsurface feature alignment improves significantly, along with the alignment of the skin surface and chest wall, displayed as grey contours in all panels. The feature indicated by the black arrow is not aligned for rigid registration (red) but becomes aligned when the nonrigid correction methods are employed (green and yellow). It should be noted that the feature indicated by the white arrow appears to be potentially aligned with rigid registration (red). However, in further multi-slice examination, there is still significant misalignment in the inferior/superior direction that cannot be visualized in this 2D example. With careful observation, there is a noticeable shape discrepancy and this is a result of the rigidly aligned feature being located several image slices inferior to the true feature location. Similarly, the nonrigid correction with no subsurface feature points included ($k = 0$, green) is notably misaligned in the medial-lateral (left-right) direction near the white arrow; however, the two nonrigidly

corrected images more closely predict the true shape of that feature and better align that feature in the inferior/superior direction. Finally, observing the same structure with the nearest subsurface neighbor ($k = 1$) included as additional data, the reconstructed computational image shows excellent agreement in location and shape (yellow). It is also important to note that the included subsurface data point was approximately 10 mm from the feature of interest designated by the white arrow. Whereas the far-field accuracy is slightly compromised at the surface above the well-fit features, the k=1 approach improves alignment for the feature further away (designated by the black arrow) at approximately 30 mm away. It is this regional accuracy that is most clinically relevant within the context of margin management. Though even without the use of an additional subsurface feature, the $k = 0$ approach (green) still shows significant improvement over conventional rigid registration (red).

Model accuracy is clinically relevant across the whole volume but demonstrates even higher fidelity in a region of interest around subsurface data. Results using the proposed method suggest that localization error of the tumor boundary is achievable to less than 4 mm on average within a 15 mm radius of a biopsy clip, and to 5 mm on average within a 30 mm radius. In the context of breast lesion sizes as discussed in Section 5.2.3.6 with the planned margin of healthy tissue included, the large majority of patients would have resection volumes smaller than the regions of interest discussed here. Intraoperative localization accuracy for over 75% of patients can be expected to be on the order of 5 mm. For patients with smaller lesions – still over 50% of patients – accuracy of a guidance system using this method could be expected to be less than 4 mm on average [150, 155].

Previous works evaluated performance solely based on tumor overlap metrics, limiting error analysis to one region of interest around the tumor. While tumor overlap is valuable for evaluating final oncological margins, it is incomplete for evaluating the general accuracy of a localization strategy. Point-based measurements instead provide precise accuracy measurements that are not subject to the ambiguities associated with surface or volume alignments. Additionally, because the full volumetric data provided many subsurface points, the analysis here was extended to include at least 8 regions of interest in each breast volume. Though the proposed method remains to be evaluated in patients, local accuracy is reported in many regions of interest, and full-field accuracy is quantified across well-sampled precise points.

Limitations of this study largely fall into the following categories: the use of full volumetric data from supine MR images, model assumptions, limited population, and the shift to existing standard of care. First, while the use of full volumetric data provides realistic extent and thorough validation targets, it does come with limitations. Although clinically acquired intraoperative data would likely provide fewer evaluation targets, true intraoperative measurement sources may include additional noise or localization errors. Tracked ultrasound measurements with probe deformation correction have reported localization accuracy on the order

of 3 mm in vivo [251], and electromagnetically tracked seeds have reported accuracies below 1 mm, though accuracy degrades with distance [253]. In the mock intraoperative setup in [238], reproducibility of surface fiducials manually designated with a stylus was measured to be 1.5 ± 0.1 mm (case *d* here). While these localization errors are not considered in this work, segmentation error may add similar noise and impact the results. In that same instrumentation analysis in [238], reproducibility of surface point picking in supine MR images was measured as 1.6 ± 0.4 mm, though this quantification cannot be directly translated to the localization error of subsurface points. Related to the use of MR data in this study, other limiting factors include image quality, segmentation error, and spatial distribution of validation targets. Many cases had few or no distinct features in the medial breast tissue as visible in Figure 5.3. Fortunately, this area of the breast experiences smaller displacements, and the bulk of breast shift occurs farther from the sternum [238].

Second, in this model, precomputed modes of deformation are generated based on isotropic, homogeneous, and linear elastic assumptions. The results may be improved with a model that incorporates anisotropy, heterogeneity, co-rotational or nonlinear elasticity, body forces, or a different distribution of boundary conditions. Though breast tissue is often considered hyperelastic, the linear elastic assumption here allows modes of deformation to be quickly scaled and combined for improved intraoperative localization. Despite this reduction in complexity, the model performance still significantly improves upon conventional registration and the approach using superposition of these linear modes makes model predictions fast enough to be feasible in the operating room. While outside the scope here, it would be interesting to compare performance with a superposition of hyperelastic modes, though a non-linear combination of these modes would be complex and a linear combination of these modes would alter some hyperelastic behavior. Similarly, accounting for local rigid body motion with techniques such as co-rotational finite elements may improve results further [168]. Constitutive models and large deformations are important considerations but their election must also be influenced by other considerations (e.g. computational speed, anisotropy, anatomical structures – Cooper's ligaments, glandular tissue milk perfusion, etc.)

Another limitation of current assumptions is that this registration approach is not well suited to account for volume changes, though breast volume varies with the menstrual cycle [254, 255]. Depending on the time between imaging and surgery, preoperative and intraoperative breast volumes may differ. While, the majority of breast cancer patients are postmenopausal [256], if hormonal changes in breast volume are later determined to be paramount within an image guidance framework, additional deformation modes could be considered to allow for volume changes without additional strain energy penalty as suggested in [257]. Alternatively, supine MR imaging could feasibly be conducted on the same day to minimize volume change effects. The suggested or allowable time between preoperative imaging and surgery remains to be investigated.

Though the current the implementation does not consider intraoperative deformations due to incisions,

future work should incorporate modes to model resection. Interestingly, there are some initial efforts toward this that also use deformation modes in the context of tissue retraction [258]. However, in related work, even a rigid registration framework at surgical onset was able to obtain reoperation rates lower than wire-guided localization (9% and 19% respectively) [50]. The work presented here shows a significant improvement beyond the accuracy of rigid registration, suggesting that a nonrigid correction framework could provide the accuracy required to push the field beyond the current 10-20% reoperation rates.

Similarly, model performance was not investigated with varied levels of input data sparsity. Effects of denser sparse data density and extent, especially along the chest wall, remain to be studied more completely. Though it should be noted, in results not presented here, deformable correction was also evaluated using only the breast surface fiducials and skin surface. In these surface-driven corrections, the surface points are allowed to fit more closely at the expense of unpenalized subsurface structural misalignment. When compared to rigid registration, surface-driven correction still significantly improves FRE and TRE ($p < 0.001$) with FRE of 2.2 ± 1.3 mm providing 72% improvement, and TRE of 6.6 ± 1.5 mm providing 39% improvement. When compared to deformable correction with surface and chest wall information (i.e. compared to model correction results reported in Section 5.2.4.1 with $k = 0$) surface-driven correction improves FRE ($p = 0.006$) and worsens TRE ($p = 0.049$). Though these results demonstrate that model correction is valuable with surface data alone, more data and analyses are required to fully investigate the importance of intraoperative measurements of the chest wall position.

The effect of more limited surface data also remains to be evaluated. Feasibility of collecting the full breast surface has been demonstrated by several groups [50, 60, 139], but a stationary camera as in [241] is more practical for re-collecting surfaces without interfering with workflow to provide continued alignment beyond an initial registration. Surfaces collected with stationary cameras are often limited by line-of-sight constraints, especially for larger breast volumes. The effect of these line-of-sight constraints on data collection are not considered here, but should be investigated in future works. If necessary, tracked instruments could be used to collect intraoperative data to augment a camera-acquired surface.

Third, the population of subjects included in this study is limited; the average age of volunteers in this study was 29 years, and there are only seven subjects. The majority of breast cancer patients are between 50 and 70 years of age [247], and only one of the healthy volunteers here is in that age range, at 57 years. As tissue properties are known to vary with age and menopausal status, future works may investigate correction accuracy on breast cancer patients. With respect to the number of subjects, this limited sample size was sufficient for strongly powered statistical tests indicating nonrigid registration improves beyond rigid registration, and that the inclusion of one subsurface point improves prediction accuracy even further. Future work could include correction accuracy across a wider range of ages and breast volumes.

Lastly, there are a few considerations within the context of the existing standard of care for breast cancer. Though the proposed method necessitates supine MR imaging, it is not currently standard of care. However, in a recent study comparing diagnostic value of contrast-enhanced breast MR in 120 patients with lesions undergoing both prone and supine imaging, interestingly there was no difference in image quality between prone and supine positions for both image resolution and diagnostic value [63]. The only difference was in geometric lesion extension which was to be expected given the change in loading conditions. Studies like the one presented here offer a rationale for changing diagnostic protocols for surgical candidates in the future. In addition, a paradigm shift that improves localization would likely result in improved patient outcomes and reduced costs associated with reoperations. Furthermore, if one could generate localizable biopsy clips, it would take full advantage of our findings regarding the impact of subsurface data. It would also have the benefit of eliminating the painful device placement procedures for seed-based methods used by many hospitals, and reduce the growing burden placed on radiology departments.

5.2.5.1 Conclusion

Existing image-guided breast surgery investigations have largely employed conventional image-guided surgery techniques that used rigid registration. These early investigations reflect accuracy and margin management similar to that of seed-based methods [50]. While anecdotal results using nonrigid approaches and sparse data have been promising [60, 171], the work herein is the first to significantly demonstrate the potential for better margin management by accounting for volumetric nonrigid deformations. When compared to conventional rigid registration, the method consistently provides significantly improved registration accuracy across all subjects. Furthermore, including just one nearby subsurface feature significantly improves registration accuracy even further and opens the possibility of integrating the capability with seed-based methods or similar alternatives. Another important strength of the work is that the approach is driven with realistic sparse mock-intraoperative data, and the registrations can be produced at clinically feasible speeds. While advancements are still needed, the proposed approach is robust, accurate, and compatible with intraoperative workflows such that it is quite reasonable to see this framework becoming a surgical technology as ubiquitous as image guidance has already become within neurosurgical standard of care.

Acknowledgments

This research was funded by NIH-NIBIB awards T32EB021937, R21EB022380, R01EB027498, Vanderbilt Ingram Cancer Center Scholarship 3450804 and Vanderbilt grant 1S10OD021771-01 for the 3T MRI, housed in the Vanderbilt Center for Human Imaging.

5.3 Tumor deformation correction for an image guidance system in breast conserving surgery

This section is adapted from "Tumor deformation correction for an image guidance system in breast conserving surgery" published in Medical Imaging 2022: Image-Guided Procedures, Robotic Interventions, and Modeling [259] and has been reproduced with permission from the publisher, the International Society for Optics and Photonics, and the co-authors Jon S Heiselman, Morgan J Ringel, Ingrid M Meszoely, and Michael I Miga.

5.3.1 Abstract

Breast cancer is the most common cancer in women, and surgical resection is standard of care for the majority of breast cancer patients. Unfortunately, current reoperation rates are 10-29%. Uncertainty in lesion localization is one of the main factors contributing to these high reoperation rates. This work uses the linearized iterative boundary reconstruction approach to model patient breast deformation due to abduction of the ipsilateral arm. A preoperative supine magnetic resonance (MR) image was obtained with the patient's arms down near the torso. A mock intraoperative breast shape was measured from a supine MR image obtained with the patient's arm up near the head. Sparse data was subsampled from the full volumetric image to represent realistic intraoperative data collection: surface fiducial points, the intra-fiducial skin surface, and the chest wall as measured with 7 tracked ultrasound images. The deformed preoperative arm-down data was compared to the ground truth arm-up data. From rigid registration to model correction the tumor centroid distance improves from 7.3 mm to 3.3 mm, average surface fiducial error across 9 synthetic fiducials and the nipple improves from 7.4 ± 2.2 to 1.3 ± 0.7, and average subsurface error across 14 corresponding features improves from 6.2 ± 1.4 mm to 3.5 ± 1.1 mm. Using preoperative supine MR imaging and sparse data in the deformed position, this modeling framework can correct for breast shape changes between imaging and surgery to more accurately predict intraoperative position of the tumor as well as 10 surface fiducials and 14 subsurface features.

5.3.2 Introduction

In the United States, over 287,000 people are expected to be diagnosed with breast cancer in 2022 [1]. Of these cases, approximately two thirds will undergo breast conserving surgery [2]. Current lesion localization strategies for breast conserving surgery (e.g. radioactive seed, magnetic seed, SAVI Scout) use a seed-based marker or guidewire preoperatively implanted under serial cross-sectional image guidance. While these methods provide valuable subsurface information, they cannot provide full intraoperative tumor boundaries, which are essential to reliably obtain complete resection. This difficulty in localizing tumor boundaries intraoperatively leads to uncertainty in the oncological margin, incomplete resections, and high reoperation rates of

10-29% [33, 34, 36, 260].

Magnetic resonance imaging offers high sensitivity for breast cancer [45, 47], and provides improved understanding of intraoperative tumor shape and position when scans are performed in a supine position [19, 46, 64]. Several groups have demonstrated the utility of viewing information from supine MR during breast conserving surgery [50, 132, 134, 139]. Image-to-physical image guidance platforms that align these high contrast and high-resolution preoperative imaging with the intraoperative patient can predict the full tumor extent in the operating room and assist surgeons with localizing more exact tumor boundaries. However, such image-to-physical guidance platforms to date have utilized rigid registration to describe breast motions between imaging and surgery that are inherently nonrigid. Although there have been indications of growing interest in preoperative supine MR so that imaging more closely aligns with the supine patient presentation in surgery [50, 132, 134, 139], significant deformations occur between imaging and surgery even in the context of preoperative supine MR [238]. These image-to-surgical deformations arise due to changes in patient positioning, arm motion, and rotation of the operating room (OR) table. In particular, while supine imaging is performed with the arms down within the closed MR bore, supine operative position places the arm abducted 90 degrees in a T-shape orientation.

Nonrigid deformation-corrected registration methods offer improvement over conventional rigid registration. A method presented by Ebrahimi et al. improved registration error evaluated at the centroid of six tumors from 3–18 mm with rigid registration to 1–10 mm using thin plate splines on surface fiducials [171]. Conley et al. presented a nonrigid finite element method (FEM) correction approach utilizing the chest wall from tracked ultrasound and MR-visible surface fiducials digitized with a stylus, and demonstrated reduction in the centroid errors of two tumors from 6.5 and 12.5 mm after rigid registration to 5.5 and 5.3 mm after correction, respectively [60]. In the method of Conley et al., displacements on the skin surface were estimated via fiducial misalignment after rigid registration. This fiducial misalignment was used in a forward FEM solution approach, with displacements prescribed on the superior and inferior boundaries of the organ. While this approach reduced errors when compared to rigid registration, the true loading on breast tissue is more complex.

In contrast, inverse modeling approaches aim to reconstruct these complex true loading conditions. Given a set of sparse data constraints supplied to the algorithm, the linearized iterative boundary reconstruction (LIBR) method, as presented in Heiselman et al. [28], solves for a profile of applied distributed loads that produce the observed intraoperative organ shape. Here the LIBR method is employed to predict breast deformation from abduction of the arm. The framework presented here is tailored to applications in breast conserving surgery, with consideration to the sparse data sources that are amenable to workflow in this intraoperative environment. This work presents this novel deformation correction framework to predict breast

shape changes due to arm motion in the supine position.

5.3.3 Methods

5.3.3.1 Patient Data Collection

One 71-year-old breast cancer patient was enrolled with informed consent in this study approved by the Institutional Review Board at Vanderbilt University. The patient had biopsy-confirmed invasive mammary carcinoma in the left breast. Nine MR-visible fiducials were placed on the breast surface. A THRIVE (T1-weighted, high resolution isotropic volume excitation) sequence with fat suppression was used to obtain supine MR images. A 16-channel sensitivity encoding torso coil (SENSE XL Torso Coil, Philips Healthcare) was placed over the patient's torso and suspended with padding to avoid breast compression. The field of view was 200 mm $\times$ 200 mm $\times$ 160 mm, centered around the left breast, and the reconstructed voxel size was 0.391 mm $\times$ 0.391 mm $\times$ 1 mm. The patient was imaged in the supine position with her arm down at her side. This image was used as the preoperative image. The patient's ipsilateral arm was then moved above the head and she was imaged again. This second image was used to obtain mock intraoperative data. In both images the breast tissue was segmented semi-automatically in ITK-Snap and the segmentation was manually corrected. Using a custom built software [233], the segmentation was discretized into a 3D mesh of 40,336 tetrahedral elements with edge lengths of 4 mm and a total internal volume of 503 cm^3.

In the preoperative (arm-down) supine MR image, the following features can be designated: surface fiducials, nipple, and the tumor boundary. These data are shown in Figure 5.7. The segmented tumor volume was 646 mm^3. The roughly ellipsoid shape had a major axis of about 26 mm and both minor axes approximately 10 mm. Additionally, the chest wall and skin surfaces can be designated and subsampled from the breast model boundary.

In the intraoperative (arm-up) supine MR image, the same features are identified. The surface fiducials are identified, and the chest wall and skin surfaces are subsampled from the breast model boundary to mimic feasible intraoperative data collection. The chest wall surface is subsampled to represent chest wall segmentations in seven tracked ultrasound images, and the skin surface is subsampled to only include data within the fiducials (the intra-fiducial surface points). Additionally, 14 subsurface homologous points are identified in both images to be used for validation.

5.3.3.2 Registration Method

To correct for nonrigid deformations, the linearized iterative boundary reconstruction (LIBR) method introduced by Heiselman et al. [28] is employed. At static equilibrium, linear elasticity is governed by the Navier

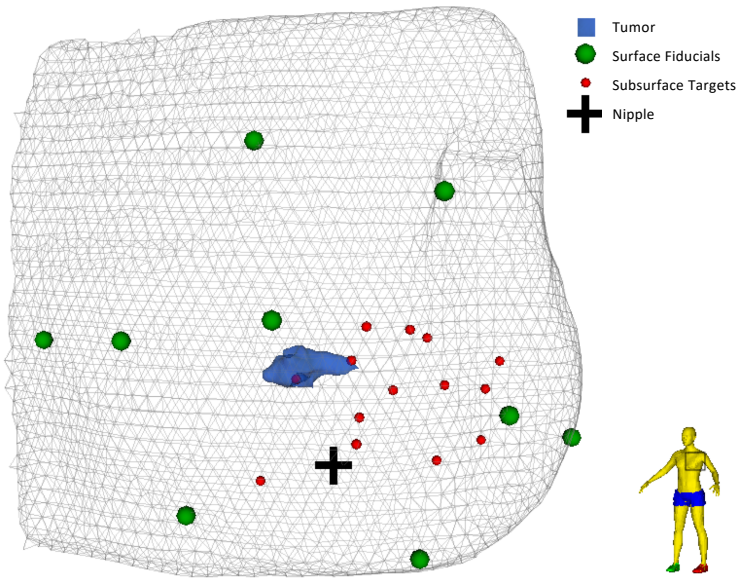

Figure 5.7: Validation points in the preoperative data designated from a supine MR image, including locations of tumor, surface fiducials, subsurface features (targets) and the nipple (+) on the preoperative breast model.

Cauchy equations,

$$\frac{E}{2(1+\nu)}\nabla^2\boldsymbol{u}+\frac{E}{2(1+\nu)(1-2\nu)}\nabla(\nabla\cdot\boldsymbol{u})+\boldsymbol{F}=0 \tag{5.5}$$

with $E = 2100\ Pa$ as Young's Modulus, $\nu = 0.45$ as Poisson's ratio, $\boldsymbol{u}$ as the displacements, and $\boldsymbol{F}$ as the applied forces. In short, the LIBR method iteratively reconstructs the intraoperative position from a superposed formulation of boundary conditions. A series of control points are distributed on the surface of the organ and every control point is perturbed in each of the three cartesian directions. For each of these perturbations, deformation solutions are pre-computed with a forward solved finite element approach. At runtime the optimal linear combination of these deformation solutions is determined by minimizing the objective function,

$$\Omega(\alpha,\tau,\theta)=\sum_F\frac{\omega_F}{N_F}\sum_{t=1}^{N_F}f_i^2+\omega_E{f_E}^2 \tag{5.6}$$

where f_i represents the distance between an intraoperative data point and the registered preoperative model, f_E represents the strain energy of the deformation, ω_F represents the weight of a feature F, N_F represents the number of points within feature F, and ω_E represents the strain energy weight. The parameters for the objective function are the weight vector α that encodes the deformation state, τ which represents the rigid translations, and θ which represents rigid rotations. All features are weighted equally, with $\omega_F = 1.0\ m^{-2}$, and the strain energy is weighted with $\omega_E = 10^{-9}\ Pa^{-2}$.

Framework feasibility is demonstrated with sparse data that could be realistically obtained in the operating

room. The features used to drive the model are the chest wall, the skin surface, and surface fiducials. The chest wall as segmented from the supine MR image is down-sampled to mimic chest wall segmentations in seven ultrasound images with 40 mm width and the skin surface is limited to the intra-fiducial skin nodes. The model-data error, f_i, for each feature is computed based on the type of correspondence, with fiducials treated as corresponding points, and skin and chest wall data treated as point-to-surface correspondences as described in Heiselman et al. [28].

The nonrigid model accuracy is compared to two rigid registration approaches: point-based registration using the fiducials, and iterative closest point (ICP) registration of the fully tumor surface. For point-based registration, the preoperative and intraoperative spaces are rigidly registered using 10 corresponding surface points: nine surface fiducials and the nipple. Though ICP registration of full tumor volumes is not feasible intraoperatively, this alignment of the tumor surfaces represents the rigid mismatch in segmentations of the tumor in the two MR images. Note that ICP was performed directly between segmented tumor volumes, not between the outer breast surfaces.

The nonrigid model accuracy is evaluated using differing amounts of intraoperative data. The fiducials, intra-fiducial skin surface, and seven chest-wall segments are used in all three nonrigid correction approaches. In practice, breast cancer patients often have an implanted marker in or near the tumor—either a biopsy clip or a specific localization device such as a magnetic, radioactive, or infrared-reflecting seed. These devices can be localized intraoperatively in tracked ultrasound images. Analysis is therefore extended, including a subsurface feature as additional point-based input to the model. Here, the tumor's nearest neighbor is considered, with the number of included subsurface features k=1. Conversely, when k=0, the model is run as previously described with no subsurface feature points included. Finally, the full tumor surface is included as a point-to-surface correspondence. While this data collection is not feasible intraoperatively, this analysis provides a nonrigid comparator to the rigid ICP alignment, though the nonrigid correction includes a larger distribution of data. No subsurface feature points were included in either of the registration approaches that include the full tumor surface as input to the registration.

5.3.3.3 Subsurface Validation: Tumors and Targets

To evaluate model performance, the predicted tumor location was compared with the observed tumor location in the mock-intraoperative image. Boundary nodes of the predicted tumor are evaluated with tumor centroid distance, as well as the modified, maximum, average and $K_{95\%}$ Hausdorff Distances [261]. The DICE coefficient is also reported. Alignment of the homologous subsurface points was compared where target registration error is reported as the average distance between the intraoperative point location, and the model deformed point location.

5.3.4 Results

With rigid registration, the tumor centroid distance was 7.3 mm. Average target errors across the 14 corresponding subsurface features, and average fiducial registration errors across the 10 corresponding surface fiducials are displayed in Table 5.4. As shown in Figure 5.8, and demonstrated by the 2% DICE coefficient in Table 5.5, the tumor volumes are largely not overlapping with rigid alignment.

Table 5.4: Registration error values in millimeters (average $\pm$ standard deviation) at surface and subsurface features. Rigid registration methods include iterative closest point (ICP) and point-based. For nonrigid registration methods, k denotes the number of subsurface neighbors included in driving the model.

	Rigid Correction		Nonrigid Correction		
	Point-Based	ICP	$k=0$	$k=1$	Tumor Surface
Surface Fiducials	7.4 ± 2.0	10.3 ± 6.7	1.0 ± 0.4	1.3 ± 0.7	1.3 ± 0.7
Subsurface Features	6.2 ± 1.4	4.8 ± 3.5	3.5 ± 1.1	3.3 ± 1.1	3.1 ± 1.4

Table 5.5: Tumor overlap metrics after registration. Rigid registration methods include iterative closest point (ICP) and point-based. For nonrigid registration methods, k denotes the number of subsurface neighbors included in driving the model.

	Rigid Correction		Nonrigid Correction		
	Point-Based	ICP	$k=0$	$k=1$	Tumor Surface
Tumor Centroid Distance (mm)	7.3	0.5	4.4	3.3	2.4
DICE Coefficient	2%	84%	32%	40%	62%
Hausdorff Distance (mm)					
Modified	4.1	0.6	2.3	1.9	1.3
Maximum	9.3	3.1	6.2	4.9	4.4
Average	3.9	0.4	2.0	1.6	1.0
$K_{95\%}$	7.0	1.1	4.4	3.2	2.4

Iterative closest point (ICP) registration provides a high overlap between the two tumor surfaces with a DICE coefficient of 84%, though intraoperative measurement of the full, dense tumor surface is not practical. Importantly, this volume overlap comes at the cost of fiducial and target error. Compared to rigid registration, ICP registration error at the fiducials is *increased* by 39%. Though we see an improvement in target error with the ICP registration, note that the targets are mainly distributed in the same local region as the tumor, as shown in Figure 5.7.

With deformation correction and no included subsurface feature points ($k = 0$), subsurface feature error becomes 3.5 $\pm$ 1.1 mm, providing 44% improvement over rigid registration. Fiducial registration error becomes 1.0 ± 0.4 mm with deformation correction, providing 86% improvement over rigid correction. At the tumor, point-based rigid registration error was reduced 40% to 4.4 *mm*with nonrigid correction.

The tumor centroid distance continues to improve when including a subsurface feature near the tumor

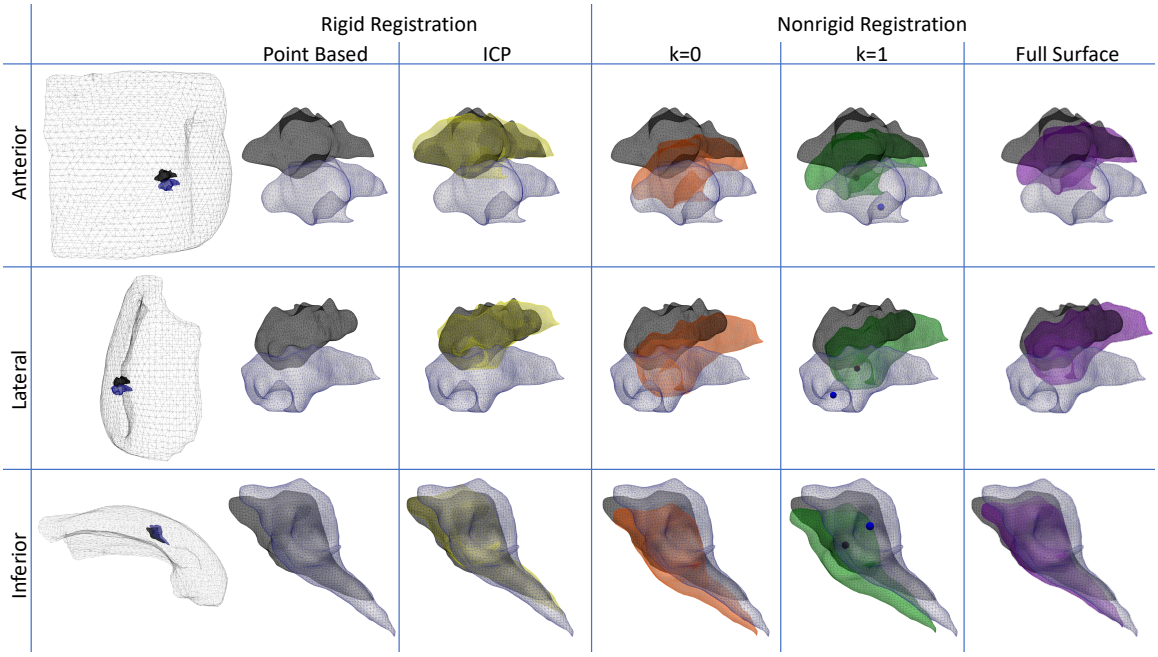

Figure 5.8: Tumor overlap after registration. Leftmost images show the preoperative breast mesh with preoperative tumor (blue) and ground truth intraoperative tumor position (black) after rigid point-based registration. For $k = 1$, the mock biopsy clip position is displayed as a point with the preoperative location in blue and the intraoperative location in black.

($k = 1$), improving 55% over point-based rigid registration as shown in Table 5.5. Table 5.4 shows the small detriment to surface alignment with a small improvement in subsurface alignment. In Table 5.4, subsurface error is still computed at all 14 subsurface features, though one of these features is considered a mock biopsy clip (and therefore added to the data driving model correction). If this driving feature point is excluded from the subsurface error computation, a true measurement of TRE, the subsurface registration error is 3.4 ± 1.0 mm (compared to 3.3 ± 1.1 mm as reported in Table 5.4).

Though not feasible in the operating room, including the full tumor surface provides a theoretical best-case scenario for the current modeling approach, while the iterative closest point registration offers a theoretical best-case scenario for tumor overlap with rigid registration. Although the rigid ICP approach outperforms model correction at the tumor, all nonrigid approaches outperform rigid alignment at fiducials and subsurface features.

5.3.5 Conclusion

This work presents a novel deformation correction approach in breast conserving surgery that achieves clinically relevant registration accuracy using realistically obtainable intraoperative data. Moreover, this demonstrates an initial investigation into the impact of providing subsurface features to a model to improve lo-

calization accuracy; including subsurface features in a modeling approach has the potential to offer even further improvement. This deformation correction framework has the potential to significantly improve intra-operative tumor localization in breast conserving surgery by better predicting image-to-surgery breast shape changes.

Acknowledgments

This work was supported by NIH-NIBIB awards T32EB021937, R21EB022380, R01EB027498, and Vanderbilt grant 1S10OD021771-01.

CHAPTER 6

Monitoring Soft Tissue Deformations with Computer Vision

6.1 Summary and Contributions

This chapter presents methods for tracking fiducials on soft tissue using computer vision. Tracking precise fiducial locations with high accuracy enables workflow friendly data collection for input into the model-based approach presented in Chapter 5 that corrects for image-to-surgery breast deformations. This chapter investigates several approaches for automatic point localization and labeling in a mock operating room using stereo cameras. This task can be considered as two subtasks: detection and labeling. Detection provides accurate fiducial locations, while labeling points determines correspondence between intraoperative and preoperative data (i.e. which intraoperative fiducial matches a given preoperative fiducial). This correspondence must be known in order to minimize the point-wise distance between these locations during model-based correction. Here, to provide image-to-physical correspondence, data in the preoperative MR image is labeled manually, and the fiducial locations in the mock operating room setting are labeled with tracking based approaches that either propagate labels (as in Sections 6.2 and 6.4) or rely on optical character recognition (as in Section 6.3).

In Section 6.2, an existing feature tracking algorithm, OpenTLD [262], is used to track five surface fiducials with 6 mm diameters throughout a series of deformations. Each fiducial is tracked individually, determining a trajectory throughout the video. This work compares the localization accuracy of two stereo camera systems and outlines initial investigations into image processing techniques for fiducial centroid localization within object-tracking bounding boxes. This work also demonstrates that the higher resolution of the Grasshopper cameras provides improved localization accuracy compared to the lower resolution Bumblebee cameras, though the Grasshopper cameras need to be calibrated for each use. This work demonstrates the utility of localizing a fiducial by calculating the centroid of an automatically-segmented fiducial region. This automated fiducial localization outperforms user-identified fiducial centroids. Processing speeds are slow (more than 3 seconds to locate one fiducial in a single image) and dependent on the number of fiducials, and validation dataset is limited to small deformations on a phantom with high stiffness. The results in this section show initial promise of fiducial tracking for surgical guidance applications with relevant localization accuracy when compared to an optically tracked stylus, while the methods set the stage for future developments into automatic centroid detection fully realized in the following sections.

In Section 6.3, this phantom analysis is extended to a higher number of more precise fiducials. A novel method for fiducial marking on skin is presented taking advantage of multiple color channels, small fiducials

for precise localization, and larger labels for easy fiducial detection. Blue fiducials can be readily detected by computing a blue color percentage, or blue color component image. This fiducial detection considers the contribution of the blue color channel in relation to the pixel's other color channel values (red and green). Using this color component image, blue inked fiducials can be localized across three skin tone variations in a phantom setting. Fiducial points approximately 2mm in diameter are inked in a separate color, and similarly show high detection rates. Here optical character recognition (OCR) is used to label each detected fiducial in the 2D images. Letter regions, as detected with simple thresholding, are converted into binary masks for labeling. The letter assigned by OCR is used to match fiducials in the left and right video streams. The algorithm takes the stereo camera video feed and outputs letter-labeled 3D fiducial locations that can be registered to letter-labeled fiducial locations in the preoperative image. While still preliminary, this work shows initial success of an OCR approach even without data-specific training.

In the final section, Section 6.4, a novel tracking algorithm is introduced for near-real time tracking of inked-skin fiducials and performance is is evaluated on eight breasts from six human subjects. The fiducial detection method presented in the previous section is paired with a robust feature-matching approach to determine correspondence. The framework relies on KAZE feature detection and matching [263] to determine correspondence between left and right fiducial candidates to provide triangulated 3D fiducial positions. Similarly, KAZE features combined with a custom feature history framework provide frame-to-frame point matching to propagate labels for reliable registration. This section demonstrates reliable fiducial localization robust to tool interference, large motions, and fiducial distortions, with 1.6 mm accuracy when compared to a tracked stylus.

The contributions of this chapter provide a reliable surface measurement method for intraoperative data collection. This framework can be integrated into a guidance system for near-real-time guidance updates with a rigid registration framework, or on-demand guidance updates with a nonrigid correction approach. This method extends the utility of guidance beyond initial alignments, and dramatically reduces the data-collection burden. Incorporating a guidance system into the existing surgical workflow becomes increasingly easy with the surface measurement method in this chapter requiring less than a minute of initialization for continuous surgical field monitoring. The ability to collect near-real-time data opens the door for faster and more complex modeling approaches. With surface data collection no longer a limiting factor in breast guidance, this work poses a new need for correction approaches that incorporate resection and retraction to provide a guidance system that can continuously update with the dynamic intraoperative environment.

6.2 A system for automatic monitoring of surgical instruments and dynamic, non-rigid surface deformations in breast cancer surgery

This section is adapted from "A system for automatic monitoring of surgical instruments and dynamic, non-rigid surface deformations in breast cancer surgery" published in Medical Imaging 2018: Image-Guided Procedures, Robotic Interventions, and Modeling [264] and has been reproduced with permission from the publisher, the International Society for Optics and Photonics, and the co-authors Ma Luo, Sarah E Goodale, Logan W Clements, Ingrid M Meszoely, and Michael I Miga.

> Winona L Richey, Ma Luo, Sarah E Goodale, Logan W Clements, Ingrid M Meszoely, and Michael I Miga. A system for automatic monitoring of surgical instruments and dynamic, non-rigid surface deformations in breast cancer surgery. In *Medical Imaging 2018: Image-Guided Procedures, Robotic Interventions, and Modeling*, volume 10576, page 105761H. International Society for Optics and Photonics.

6.2.1 Abstract

When negative tumor margins are achieved at the time of resection, breast conserving therapy (lumpectomy followed with radiation therapy) offers patients improved cosmetic outcomes and quality of life with equivalent survival outcomes to mastectomy. However, high reoperation rates ranging 10-59% continue to challenge adoption and suggest that improved intraoperative tumor localization is a pressing need. We propose to couple an optical tracker and stereo camera system for automated monitoring of surgical instruments and non-rigid breast surface deformations. A bracket was designed to rigidly pair an optical tracker with a stereo camera, optimizing overlap volume. Utilizing both devices allowed for precise instrument tracking of multiple objects with reliable, workflow friendly tracking of dynamic breast movements. Computer vision techniques were employed to automatically track fiducials, requiring one-time initialization with bounding boxes in stereo camera images. Point based rigid registration was performed between fiducial locations triangulated from stereo camera images and fiducial locations recorded with an optically tracked stylus. We measured fiducial registration error (FRE) and target registration error (TRE) with two different stereo camera devices using a phantom breast with five fiducials. Average FREs of 2.7 ± 0.4 mm and 2.4 ± 0.6 mm with each stereo-camera device demonstrate considerable promise for this approach in monitoring the surgical field. Automated tracking was shown to reduce error when compared to manually selected fiducial locations in stereo camera image-based localization. The proposed instrumentation framework demonstrated potential for the continuous measurement of surgical instruments in relation to the dynamic deformations of a breast during lumpectomy.

6.2.2 Introduction

Breast cancer is the most common cancer among women, second only to lung cancer in mortality[265]. With advancements in detection, an increasing number of cases are being diagnosed at early stages. These early stage diagnoses result in more operations on smaller tumors, and a rising number of candidates eligible for breast conserving therapy, which includes surgical resection and radiation therapy[266, 267]. For patients who are eligible, breast conserving therapy with negative margins has been shown to be as effective as mastectomy, the complete removal of breast tissue[4, 8, 162, 268, 269]. With respect to the surgical goals of lumpectomy, success is determined by the presence of pathologically negative margins occurring when there are no cancer cells at the edges of the resected tissue. Breast conserving therapy also offers patients favorable cosmetic outcomes and equivalent survival outcomes in the case of negative margins. However, the re-operation rates for lumpectomy are currently estimated at 10-59% [270–275] and returning to the operating room negatively impacts patient satisfaction, cosmetic outcomes, and reintroduces risk of surgical complications. It is commonly accepted that improved localization reduces reoperation rates, as localization procedures are often measured by their effect on reoperation rates [20, 90]. Therefore, the high re-resection rates of BCT indicate the need for improved intraoperative tumor localization.

Breast cancer tumor localization proves difficult for two main reasons: the huge differences between diagnostic and intraoperative presentations and the limited extent of geometric and spatial cues during surgery to guide resection. Magnetic resonance is generally considered the most sensitive imaging modality for breast cancer[44, 276]. While not a standard diagnostic, diagnostic magnetic resonance images are often taken and in the prone position, with the breast pendant. Additionally, a patient's arms are either at their sides or extended above their head in order to enter the imaging bore. For surgery, the patient is in a supine position with the arm extended laterally. Tumor displacements between prone and supine breasts are reported between 18-60 mm [41–43]. In addition, mammographic examination is another common breast cancer image screening method. In this case, a standing patient will place the breast between two compressive plates. This process also introduces large tissue displacements and shape change from its preoperative counterpart due to tissue compression.

With respect to intraoperative localization methods, the most common form of surgical guidance is the use of guide wires. A guide wire is placed in the center of the tumor by a radiologist during diagnostic imaging, and the patient waits with a wire protruding from the breast until surgery. There is discomfort during preoperative wait time and guide wires can shift during that period. In addition, the implanted wire path to the center of the tumor is constrained by the diagnostic presentation and may not be the best surgical path. Guide wires also only provide localization of tumor center and do not provide information about

tumor margins. Intraoperative ultrasound visualizes tumor margins in the operating room but takes time, can require a radiologist, and most importantly, approximately half of breast tumors are not echogenic[26]. Intraoperative supine MRI offers clear location information, but is costly, cumbersome, time inefficient, and only offers initial tumor location, i.e. the location and deformations are not tracked or updated throughout surgery. Alternatively, imprint cytology is the practice of pressing a tumor to a glass slide following removal; cancerous cells stick to the slide and non-cancerous cells come off clean. This method is good for evaluating tumor margins, but interferes with workflow and, most importantly, is not always effective.

Non-rigid, dynamic deformation of breast tissue during surgery makes tumor localization difficult. Further, these deformations are challenging to compensate for, especially with the large variance in material properties across patients due to age, genetics and hormonal changes [277, 278]. Existing modeling and prediction is often driven by surface deformations. The relationship between surface and subsurface measurements has been previously explored in a trial done with 12 patient volunteers. In that study, surface and subsurface feature deformations were quantified and compared, showing that surface deformations are predictive of subsurface deformations[166]. Initial registrations offer surgeons improved localization at the start of surgery, but if registrations are not updated, tumor margins remain difficult to ascertain and the guidance becomes less valuable upon incision. Continuous monitoring of the breast surface is needed for registration and modeling updates to maintain accuracy after the initial data collection and throughout the procedure.

In this work, we couple optical instrument tracking with a stereo camera's visual surface tracking. Conventional tracking can be used for surgical instruments and the deforming breast surface can be more readily monitored with a stereo camera. Stereo camera point localization has been previously shown to be reliable[225], and we extend this work to hypothesize that a computer vision tracking algorithm can be applied to automatically and continuously monitor the breast surface. The surface information provided throughout surgery would allow for ongoing non-rigid registration with a computational model. Registration between preoperative and intraoperative data would give the surgeon access to continuously updating spatial information. This work is an important and exciting first step towards automatic and continuous surgical guidance in real-time for breast cancer surgery.

6.2.3 Methods

A bracket was designed to maximize the overlap between the volume of a Polaris Vicra optical tracker (Northern Digital, Waterloo, ON, Canada) and the volumetric field of view of the Bumblebee XB3 (FLIR, formerly Point Grey Research, Richmond, BC, Canada). The stereo cameras offer point reconstruction capabilities from triangulation of stereo camera images and the automated tracking algorithms of OpenTLD software [262]. The stereo camera and optical tracker were rigidly paired and registration was performed on a phantom

breast (Breast Probe, SIMULAB Corporation, Seattle, WA) with five fiducials. To evaluate the performance of this system with the Bumblebee XB3 stereo camera, three trials were conducted, each consisting of a deformed and undeformed state. To further evaluate the capabilities of optical tracking paired with stereo camera automated tracking, the Bumblebee XB3 was replaced with two Grasshopper cameras (FLIR, formerly Point Grey Research, Richmond, BC, Canada). The grasshoppers, shown attached to the bracket in Figure 6.1A and 6.1B , offer improved resolution with 1600 $\times$ 1200 pixels, compared to the 1280 $\times$ 960 pixels of Bumblebee XB3 images. Three trials were conducted with the two Grasshopper cameras, each trial consisted of five deformation states.

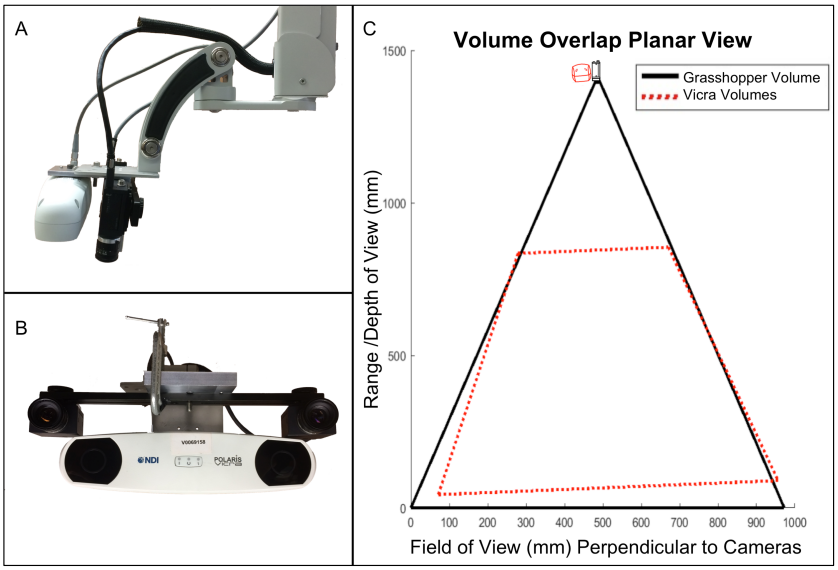

Figure 6.1: Bracket designed to optimally pair instrument and surface tracking (A) 2D lateral view of the optical tracker and stereo camera coupled with our designed bracket attached to a surgical arm (B) inferior view (C) 2D lateral view of the overlap between the volume of the optical tracker (red) and the volume of the stereo camera (black); this plot corresponds to the orientation shown in A.

6.2.3.1 Bracket Design

The Polaris Vicra was angled towards the Bumblebee XB3's field of view. The angle that maximizes volume overlap was calculated to be 3 degrees, and a bracket was designed and machined to rigidly couple the two devices. With the y-axis as the range, or depth, of view, and x-axis as the plane perpendicular to the cameras, the Z dimension was parallel to the cameras and was optimized by centering the two devices (i.e. the center of the Polaris Vicra is aligned with the center of the set of stereo cameras). The volume was therefore optimized as an area in the XY plane with most overlap. The volume overlap in the XY plane is shown in Figure 6.1C with the Grasshopper cameras.

6.2.3.2 Stereo Camera Points

Bumblebee XB3 stereo camera images were collected through a modified version of Point Grey software, displaying output from all three cameras of the Bumblebee. Example output of the Bumblebee can be seen in Figure 6.2C, with superimposed arrows to describe locations where forces were applied. Stereo camera images from two grasshopper cameras were collected with a custom-built image capture software [225]. The coupled devices were centered over the phantom and each Grasshopper was tilted until the right camera's field of view was about 1 cm to the right of the left field of view, and both views were approximately centered on the deformation apparatus. Calibration for both sets of cameras was performed with stereo camera calibration algorithms from Matlab's Computer Vision System Toolbox. Sixteen images were used for Bumblebee XB3 calibration resulting in a mean reprojection error of 0.29 pixels, and twelve images were used for Grasshopper images resulting in a mean reprojection error of 0.46 pixels.

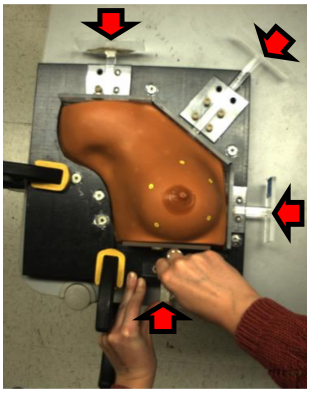

Figure 6.2: Breast phantom deformation apparatus shown with five yellow fiducials. Red arrows indicate the directions in which deformations may be applied.

Each fiducial was automatically tracked with computer vision software, OpenTLD[262], after manually defining bounding boxes in the initial left and right frames. Images from left and right cameras were used to triangulate three-dimensional fiducial locations. The left and right points used for triangulation were taken from the bounding boxes defined by the tracking algorithm. Three methods were used to determine the fiducial centers within each bounding box: two automatic methods, and manual selection. The automatic fiducial localization methods were bounding box averaging and region growth. For the bounding box averaging method, the top left and bottom right corners of each bounding box were averaged to calculate the center, and these centers were used in the triangulation process. For the region growth technique, a fast marching algorithm was used to produce a fiducial region segmented from the image. This segmentation process uses gray scale intensity difference weights calculated from the intensity values at the seed locations via Matlab's Image Processing toolbox (utilizing graydiffweight with a roll-off factor of 0.2). Because bright fiducial markers were used, this method was automated by using the brightest pixel as a seed point for the algorithm.

The centroid of the fiducial of interest can then be computed by determining the centroid of this region. To evaluate the accuracy of our automated methods, manually selected fiducial centroids were also collected at each point for each deformation.

6.2.3.3 Optical Tracker Points

The Polaris Vicra and an optical tracking stylus shown in Figure 6.3A and 6.3D were used to record optical tracker fiducial locations. The optical tracking system detects the location of retro-reflective markers by emitting infrared light and detecting the reflections from the markers on a specific instrument. Each instrument has a specific geometry of reflective markers to allow for simultaneous tracking of multiple instruments. At each fiducial point, the optically tracked fiducial location was computed by averaging 8 rapid acquisitions via the optical tracking system.

6.2.3.4 Experimental Setup

Five yellow fiducials with 6 mm diameters were used as shown in Figure 6.3C. With the Bumblebee XB3, three tests were performed, each with two deformation states. Tests 1 and 2 induced deformation to produce the second states, while Test 3 was a relaxation from a deformed state to a second, undeformed state. With the two Grasshopper cameras, three tests were performed, each with five deformation states. All three tests consisted of an undeformed state, and then a deformation at each of the arrows shown in Figure 6.2. The experimental setup is shown in Figure 6.3.

6.2.3.5 Registration Technique

All three sets of triangulated fiducial locations were registered to optically tracked points via a point based rigid registration. Stereo camera triangulated points from the initial left and right frames were registered to the optically tracked NDI points from the first deformation state. A point set results from each method of fiducial localization in stereo images: bounding box averaging, region growth, and manual selection. The transformation that results from registering each of these three point sets to optically tracked NDI points, each define the relationship between the stereo camera space and the optical tracker instrumentation space. However, given that each method has disparate sources of error, slight differences in these transformations are to be expected. For this reason, these point sets were, separately, each registered to the optically tracked NDI points. The registration computed with the 5 fiducial points in the first frame, served as the calibration transformation between Vicra and stereo-pair and was applied to all successive frames in the trial. This registration defines a transformation T consisting of a rotation and transformation to relate the two sets of points: x, the stereo camera point set, and y, the optically tracked NDI point set. $T(x)$ represents the transformed

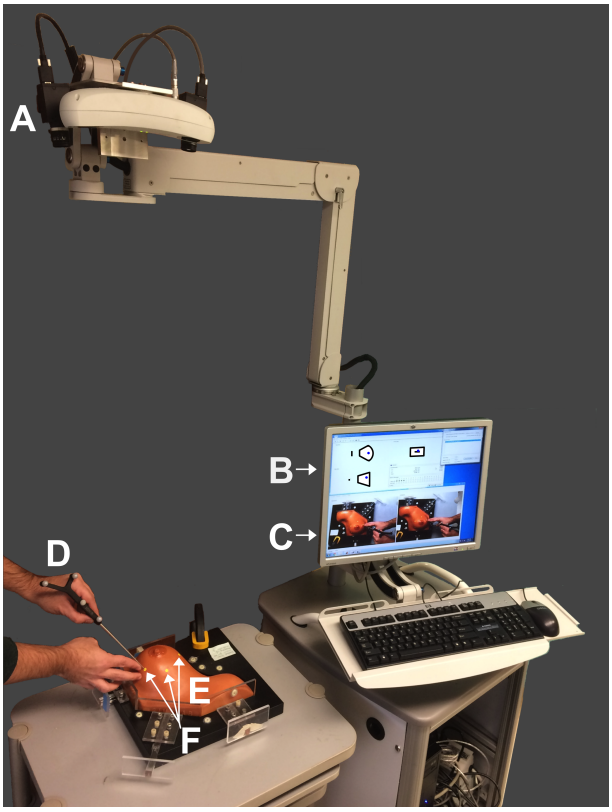

Figure 6.3: Coupled device prototype (A) coupled stereo camera and optical tracker attached to a surgical arm (B) monitor displaying the location of the instrument tip within the optical tracker's volume (C) monitor displaying stereo camera images for surface tracking (D) tracked surgical instrument (E) breast phantom (F) fiducial markers.

stereo camera points, i.e. the stereo camera points represented in the optically tracked instrumentation space. Fidelity was reported as a fiducial registration error (FRE) a measure of overall landmark misalignment, and is shown below, with N representing the number of fiducials [223].

$$FRE = \sqrt{\frac{1}{N}\sum_{i=1}^{N}(T(x_i) - y_i)} \tag{6.1}$$

To evaluate target localization, target registration error (TRE), a measure of target misalignment, was computed using a leave-one-out method. Coordinates from four fiducials across all deformation states were used to register, and the calculated transformation, T_i , was applied to the fifth fiducial with i ranging from 1 to N, the number of fiducials. This means that the TRE for a target point is the magnitude of the vector between the transformed stereo camera point, $T_i(p)$, and the optically tracked NDI point, q. The equation for TRE is shown below [223].

$$TRE = ||(T_i(p) - q))|| \tag{6.2}$$

6.2.3.6 Optical Tracker Point Localization Evaluation

In these experiments we use optically tracked NDI points to evaluate the accuracy of our computer vision tracking system, considering the optically tracked NDI points to be the true, or "gold standard", point locations. Therefore, it is useful to evaluate the same five points localized multiple times with the optically tracked NDI stylus to provide some sense of the fidelity of the "gold standard". Five fiducial locations were collected following the same procedure as outlined in Section 6.2.3.3. These same, undeformed points were recollected four additional times for a total of five point sets each with five fiducials. All combinations of point sets were registered systematically to establish an estimate of FRE. In addition, a leave-one-out test was performed to establish an estimate of TRE.

6.2.4 Results

Comparing NDI tracked points and triangulated stereo camera points can be reliably registered with an FRE of 2.7 ± 0.4 mm for the Grasshopper Cameras and 2.4 ± 0.6 mm for the Bumblebee, using the region growth method to calculate fiducial centroids on stereo camera images. FREs for each camera were averaged across all deformations and are presented in Figure 6.4. TRE averages were of 2.8 ± 1.1 mm for the Grasshopper Cameras and 2.7 ± 1.4 mm for the Bumblebee using the region growth method to calculate fiducial centroids on stereo camera images.

Our "gold standard" validation of the optically tracked NDI point accuracy yielded an average FRE of 0.8 ± 0.3 mm, with a leave-one out TRE of 1.0 ± 0.3 mm.

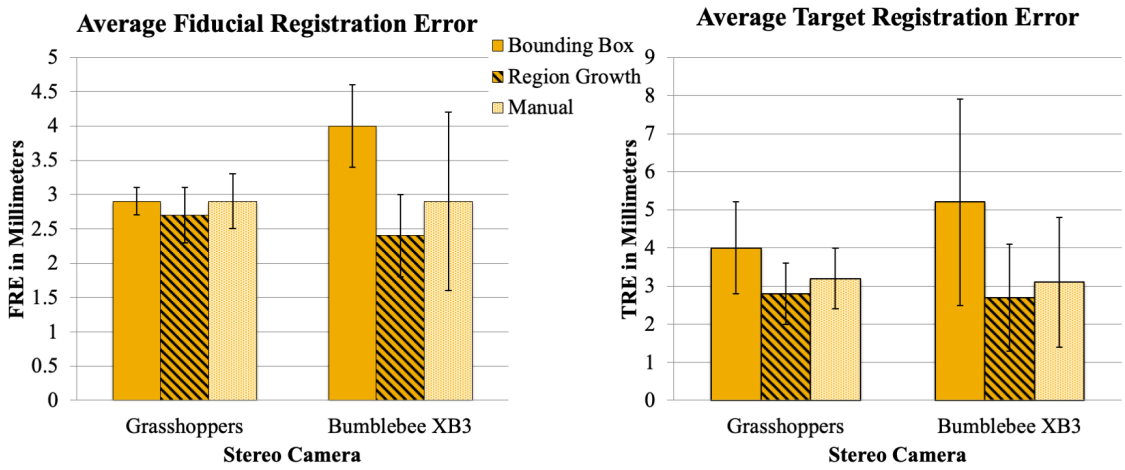

Figure 6.4: Errors reported averaged across all deformation states, in millimeters with error bars reflecting standard deviation; Fiducial Registration Error (Left) and Target Registration Error (Right).

The first state contains the stereo-camera points that were localized from user-defined bounding boxes for the automated fiducial localization methods. To evaluate the accuracy of our tracking method alone, average FREs and TREs were also computed without the point sets from the first state. Registration was still performed using the first state. For the Bumblebee camera, FRE averaged 2.7 ± 0.9 mm and TRE averaged 2.7 ± 1.0 mm. For the Grasshopper cameras, FRE averaged 2.9 ± 0.9 mm and TRE averaged 2.8 ± 1.1 mm.

A two-sample t-test with unequal variances was performed to compare the two stereo camera systems. The camera systems were compared using the results from the automatic region growth fiducial localization. The Bumblebee FRE was found to be significantly less than that of the Grasshoppers ($p < 0.01$), while TRE was not found to be significantly different between the two camera systems.

6.2.5 Discussion

As was somewhat expected, the region growth algorithm outperformed the bounding box algorithm. As a more precise alternative, it suffers less subjective error with user-defined bounding box. Even for bounding boxes initialized with the fiducial center exactly in the center, as the tracking algorithm progresses there is the potential for the bounding box to shift with subtle shape and location changes that could create error in the bounding box method. More surprisingly perhaps, is that the region growth method outperforms the manual selection process. Upon further investigation, the difference between manually selected points and automatically selected points is generally minimal in the plane of the camera image. However, the manually selected method suffered higher error in the triangulated depth than the automatic region growth method. Even with great care taken to select the centroids of fiducials, we hypothesize this error stems from discrepancies in correspondences. That is, the same point must be selected in the left and right images for

triangulation to be correct; automatic methods lend themselves to more reliably selecting the same pixel at the center, provided that the bounding boxes are reasonably similar. A two-sample t-test with unequal variances showed the Bumblebee XB3 had statistically significantly lower average error (2.4 mm average FRE) than the two Grasshoppers (2.7 mm average FRE) for the region growth method. However, overall, the Grasshoppers produced more reliable results with lower standard deviations, and more consistent results with less average error across all three methods. Because the grasshopper cameras can be angled toward each other to create more overlap in their field of view, we have found in results not reported here that the point cloud reconstructions have been more satisfying, which will prove valuable as we move forward. For future work, we will likely adopt the Grasshopper configuration.

While care was taken to minimize deformation from stylus contact with the phantom breast, it should be noted that the optical tracker stylus is a contact method and potentially introduces error due to deformations. A stylus was used to collect points as opposed to fixing near infrared-visible markers to the breast phantom which could have improved localization and consequently calibration. The registration of the repeated optically tracked points (Section 2.3) allows us to determine the baseline for accuracy of our validation method. Our ground truth has an average error of 0.8 ± 0.3 mm.

It is well known that target error is minimized when targets are surrounded by localized fiducials [230]. Because registration accuracy decreases as the target moves further from the centroid of the fiducials, the leave one-out method for TRE presented here has an inherent error, i.e. the target in our experiments was always completely distant from the centroid of the fiducials. To evaluate the target error without this bias, an additional data point was collected at the nipple of our mock breast phantom setup. With the nipple as a target, the bounding box method was used to locate the center of the fiducial resulting in an average TRE of 2.0 mm (note region growth could not be used due to the phantom coloring in this case). When using the "gold standard" registration, TRE of the nipple was 0.6 mm.

6.2.6 Conclusion

The proposed approach is an important step towards real-time, automated monitoring of dynamic intraoperative breast deformation. The tracking method is robust to occlusions of fiducials and multiple fiducials of similar size and shape. Visual fiducials adhered to the breast and tracked with computer vision are extremely practical for intraoperative breast tracking, allowing for easy demarcation of fiducial points and reliable tracking with computer vision. Using passive optical tracking, multiple tools can be simultaneously monitored with minimized surface tracking interference. Additionally, because the instrumentation tracking volume extends outside the stereo camera's field of view (in the Z direction, or left-right axis of images), the tip of surgical instruments can continue to be tracked even if their reflective markers fall outside the view of

the stereo camera.

Computer vision applications in image guided breast surgery have not been well investigated. The system presented is a realization of a novel pairing of computer vision technologies and instrumentation tracking, each focused at different aspects of the surgical problem. By monitoring instrumentation and surgical field separately, each modality takes advantage of the different tracking strengths. Conventional optical tracking gives precise instrument locations of multiple objects. The stereo camera allows automation of the surface tracking process for real time intraoperative image guidance in dynamic, non-rigid breast deformation. The functionality to track the instrument tip with precision is not new, but its incorporation into an automatically deforming image guidance system is novel.

This system is workflow friendly; it does not require expensive imaging equipment and personnel to operate (as in intraoperative MR), sits away from the clinician's surgical field, and requires less than one minute of initialization and then no further interaction. This technique could be easily managed by a surgeon or surgical assistant, taking less than a minute for the one-time initialization of surface markers. The results here show that points can be tracked and localized reliably with an average FRE below 3.0 mm. Both vision approaches (Grasshopper or Bumblebee XB3) are acceptable and the region growth method is the best for fiducial localization in stereo camera images. This work shows promise toward computer vision surface tracking in breast cancer lumpectomy and breast cancer therapy. This system shows the potential to provide the surgeon with tumor localization even as the tissue moves due to gravity and surgical instruments. If this system is fully realized and validated, surgeons could be presented with real-time changes to surface and subsurface breast features in relation to their surgical instruments.

Acknowledgments

This work was supported in part by the NIH-NCI grant R01CA162477 and NIH-NIBIB grant R21EB022380.

6.3 Textual fiducial detection in breast conserving surgery for a near-real time image guidance system

This section is adapted from "Textual fiducial detection in breast conserving surgery for a near-real time image guidance system" published in Medical Imaging 2020: Image-Guided Procedures, Robotic Interventions, and Modeling [264] and has been reproduced with permission from the publisher, the International Society for Optics and Photonics, and the co-authors Jon S Heiselman, Ma Luo, Ingrid M Meszoely, and Michael I Miga.

> Winona L Richey, Jon S Heiselman, Ma Luo, Logan W Clements, Ingrid M Meszoely, and Michael I Miga. Textual fiducial detection in breast conserving surgery for a near-real time image guidance system. In *Medical Imaging 2020: Image-Guided Procedures, Robotic Interventions, and Modeling*, volume 11315, page 113151L. International Society for Optics and Photonics.

6.3.1 Abstract

Breast cancer is the most common cancer in American women, and is the second most deadly. Current guidance approaches for breast cancer surgery provide distance to a seed implanted near the tumor centroid. Large deformations between preoperative imaging and surgical presentation, coupled with the lack of tumor extent information leads to difficulty in ensuring complete tumor resection. Here we propose a novel image guidance platform that utilizes character-based fiducials for easy detection and small fiducial points for precise and accurate localization. Our system is work-flow friendly, and near-real time with use of stereo cameras for surface acquisition. Using simple image processing techniques, the proposed technique can localize fiducials and character labels, providing updates without relying on video history. Character based fiducial labels can be recognized and used to determine correspondence between left and right images in a pair of stereo cameras, and frame to frame in a sequence of images during a procedure. Letters can be recognized with 89% accuracy using the MATLAB built in optical character recognition function, and an average of 81% of points can be accurately labeled and localized. The stereo camera system can determine surface points with accuracy below 2 mm when compared to optically tracked stylus points. These surface points are incorporated to a four-panel guidance display that includes preoperative supine MR, tracked ultrasound, and a model view of the breast and tumor with respect to optically tracked instrumentation.

6.3.2 Introduction

In the United States, breast cancer is the most commonly diagnosed cancer in women and has the second highest rate of mortality [279]. For women worldwide, breast cancer has the highest incidence and highest morality [280]. Surgery is the standard of care for these patients. Most breast cancer patients are faced with two surgical options: mastectomy or breast conserving therapy (BCT). Mastectomy involves removal of the breast tissue, areola, and skin. While BCT is the removal of the tumor and a margin of healthy tissue surrounding the tumor, with follow-up radiation treatment. Margins are considered negative if there are no tumor cells on the border of the excised mass. Given negative margins, BCT has been shown to have equivalent outcomes to mastectomy [4, 7] with shorter surgical times, shorter post-operative hospital stays, and improved cosmetic outcomes, as the breast usually retains its original shape and symmetry with the contralateral breast[8–10, 30, 31]. High reoperation rates set breast cancer apart from other common general surgeries with an observed versus expected morbidity (O/E) ratio nearly three times higher than that of other general surgeries [12]. In the last six years, BCT reoperation rates have been reported from 8-27% [33–37]. These high rates of positive margins in breast cancer surgeries have been referred to as ”the other breast cancer epidemic” [17].

Unfortunately, tumor position and extent can be very difficult to visualize intraoperatively. None of the

standard preoperative imaging techniques—mammography, ultrasound, prone magnetic resonance (MR)—have the patient in surgical position. Tumor displacements between imaging position and surgical position are reported between 18 - 68 mm [18, 19, 41–43]. Intraoperative ultrasound (US), which provides tumor extent, has been shown to reduce reoperation rates, but 50% of nonpalpable breast lesions are nonechogenic [277]. Furthermore, it can be difficult to visualize the exact orientation of the US imaging plane, especially for deeper tumors. Current state-of-the-art guidance techniques for breast conserving surgery (BCS) provide distance from a handheld wand to an implanted seed, but do not provide tumor orientation or extent [101, 127, 248]. Image guidance solutions are moving towards the use of supine MR and optical tracking [41, 50, 264]. However, these systems do not allow for real time updates. Optically tracked fiducials can only provide surgical planning information, as they must be removed from the breast surface at the start of surgery. We have previously shown retrospectively that tracked fiducials in stereo camera images can provide surface points throughout a video [264]. However, for larger numbers of fiducials, correspondence becomes confounded. High frame rates are used to improve video tracking, and for high numbers of fiducials video processing lags behind real time. While use of a GPU, or more optimized algorithms could reduce processing time, an ideal solution would be independent of video framerate and maintain correspondence even for large numbers of fiducials.

6.3.3 Methods

This work consists of two main components: (1) continual, automated intraoperative monitoring and (2) providing surgeons with tumor location, position and extent before and during BCS. We propose the use of stereo cameras to capture the breast surface in surgery, and we pair these stereo cameras with conventional instrument tracking. This intraoperative monitoring system can be combined with preoperative and intraoperative imaging as well as patient specific models to provide tumor location, position and extent before and during BCS. A four-panel display including MR data, ultrasound data, and a 3D patient specific breast model brings all of the available information into the same space to help the surgeon plan and perform BCS.

Three different skin-tones were painted onto a deformable breast phantom (Breast Probe, SIMULAB Corporation, Seattle, WA). For each skin-tone, the phantom was deformed 4 times using the plungers shown in Figure 6.5. This resulted in a total of five deformation states: no deformation and deformations from plungers 1-4. Fiducials were marked as small red dots and labels were drawn as blue capital English letters (Figure 6.5).

Our system uses the Polaris Vicra optical tracker (Northern Digital, Waterloo, ON, Canada) and two Grasshopper cameras (FLIR, formerly Point Grey Research, Richmond, BC, Canada). These two devices are coupled with a rigid bracket as previously presented in 27. For each deformation state, and for each

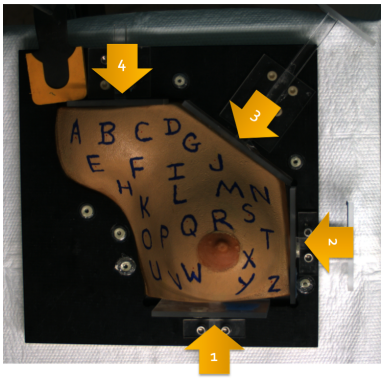

Figure 6.5: The breast phantom with blue letters and red fiducials; the plungers are indicated with yellow arrows.

phantom skin tone, stereo camera images were obtained. Fiducials and their labels were localized with simple thresholding and bounding boxes. These bounding boxes provided image patches. From these image patches, the fiducial location and the letter label were identified. This process is performed in the right and left stereo camera images, and the labels were used to guide correspondence to obtain a set of 3D surface points by triangulation. This process is outlined in Figure 6.6.

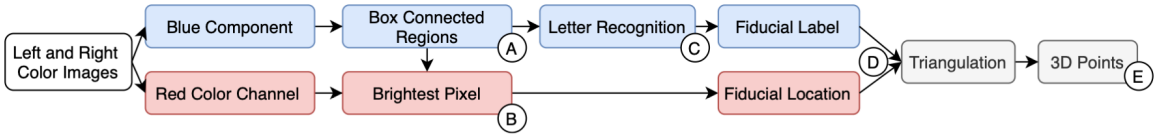

Figure 6.6: The process to generate three dimensional points from the left and right stereo camera images. Circled letters represent the steps at which results are reported.

To evaluate the accuracy of our system, points obtained from the stereo camera images were registered with points manually collected with an optically tracked stylus. These points can then be integrated into a four-panel guidance display to aid surgeons in visualizing tumor location. Our four-panel image guidance display was implemented using 3D Slicer [224].

6.3.3.1 Defining Bounding Boxes

Regions of interest were defined using the blue color component. The blue color component, or the blue percentage of each pixel, was computed with Equation 6.3.

$$Blue\ Color\ Component = \frac{BlueValue}{RedValue + GreenValue + BlueValue} \tag{6.3}$$

Blue pixels have high blue color components, while other colors have lower blue color components. This blue color component allows for easy thresholding of the blue letters, as shown in Figure 6.7. For

example, white pixels are bright in the blue color channel but dark in the blue color component. Case-specific parameters were manually designated including a blue color component threshold, a region of interest outlining the phantom, maximum and minimum bounding box sizes, and padding. The region of interest was used to mask the blue color component image, and the threshold was used to create a binary representation of the blue letter pixels from that masked image. The connected components in this binary image were boxed individually. Boxes that are too big, or too small are removed. This process provides a box around each letter. Parameters were set in the first (non-deformed) frame, and maintained for the remaining 4 images of each experiment.

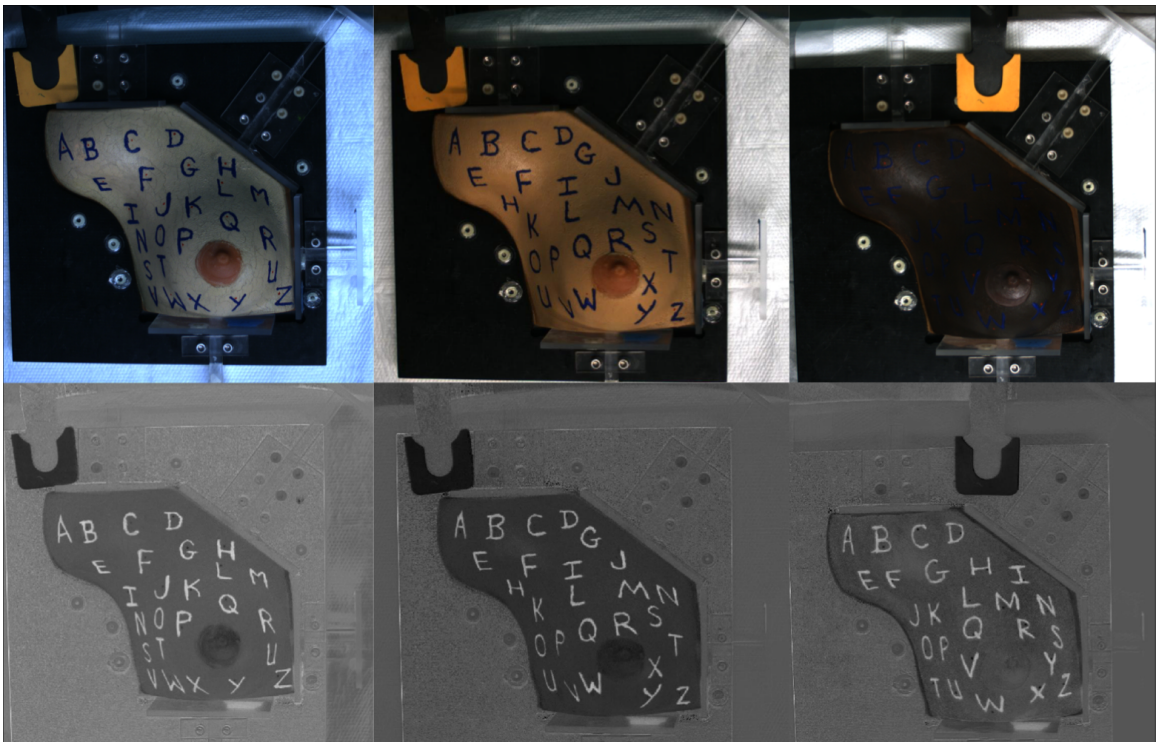

Figure 6.7: The three phantoms with blue letter labels and red fiducial dots (top row), with their corresponding blue color components (bottom row).

6.3.3.2 Fiducial Localization and Labeling

Red pixels display brightly in the red color channel. For each image patch, the brightest pixel in the red color channel is considered the fiducial center and is used as the fiducial's 2D location. This method is fast and reliable. To determine the label for each fiducial, the MATLAB built-in optical character recognition (OCR) method was used. The region inside each bounding box is fed into the OCR function, specifying the limited character set (the alphabet of capital letters), and that the letters are "block" letters. The bounding boxes, with fiducials localized and letters labeled are shown in Figure 6.8.

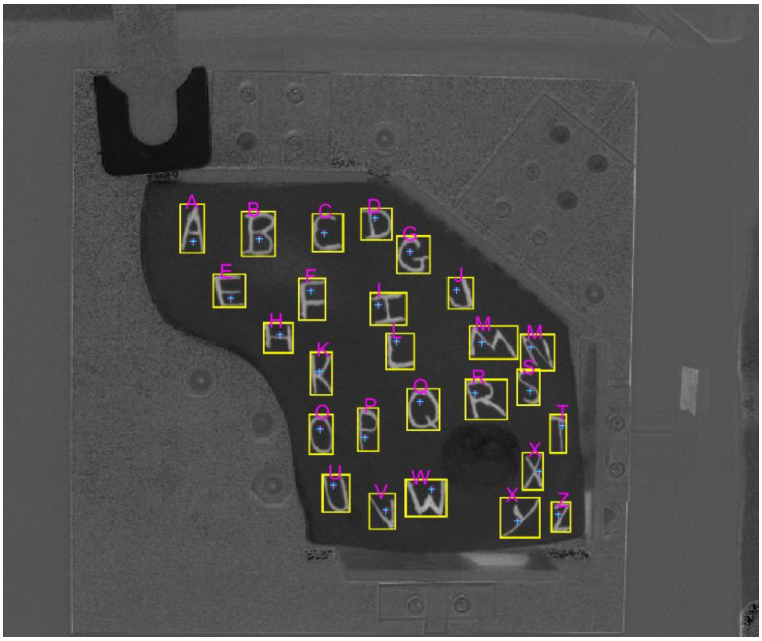

Figure 6.8: Example output of fiducial and label detection. The blue color component is shown, with boxed connected components in yellow. The fiducial locations are indicated as cyan and magenta asterisks. Letter labels, as output from the letter recognition function, are shown above the image patch in magenta. Here, all labels are correct except for "N", which is mislabeled as "M".

6.3.3.3 Generating Labeled 3D Points

A very straightforward approach was implemented to handle letter recognition errors. All incorrectly labeled 2D points are not used to triangulate 3D points. When the image patch is labeled as more than one letter or no letter (space), it is considered incorrect. When the incorrect label is a single letter, it can result in a conflict where multiple single-letter labels are identical. With this simplistic correspondence approach, any non-unique single letter label is discarded. For example, if there are two points labeled 'N' in the left image, both those points will not be used, and the point labeled 'N' in the right image will also remain unused; 'N' will not be included in the generated 3D point set. If letter correspondence is incorrect, the triangulated depth is generally quite noticeably an outlier. Therefore, if the triangulated 3D point is more than 3 standard deviations from the mean of the point set, it is considered an error and discarded. While this approach may seem overly simple, it makes the output points reliable without the need for more complicated error checks.

6.3.3.4 Validation

To evaluate the capabilities of our stereo camera system, manual intervention was used to obtain all 26 alphabetical points for all deformation states, on all three phantom skin-tones. Instead of using the automated letter labeling method (OCR), points were manually labeled. For the few cases where there was no bounding box around a letter, the fiducial point was identified manually. This provided a set of 3D points from the stereo

camera system. Fiducial locations were also collected manually with an optically tracked stylus (Northern Digital Inc, Waterloo, ON, Canada) and registered to the fiducial locations collected with the stereo camera system. This registration defines a transformation matrix, T, consisting of a rotation and transformation to align the two sets of points: $\boldsymbol{x}$, the stereo camera point set, and $\boldsymbol{y}$, the optically tracked point set. $T(\mathbf{x})$ represents the stereo camera points that have been transformed into the optically tracked instrumentation space. Fidelity is reported as fiducial registration error (FRE), a measure of overall landmark misalignment, and is shown below, with N representing the number of fiducials, which is 26 for all our trials [230].

$$FRE = \sqrt{\frac{1}{N}\sum_{i=1}^{N}(T(x_i) - y_i)} \tag{6.4}$$

In these experiments, the optically tracked stylus points were considered the gold standard. To evaluate the accuracy of this gold standard, the same fiducial locations on the breast phantom were collected five times with no deformation between collections. Registration was performed with each pair of these validation point sets, and the FRE is reported.

6.3.3.5 Four-Panel Display

The points collected with the stereo camera pair inform a four panel display for intraoperative guidance. We propose the use of supine MR performed preoperatively with MR-visible fiducials. This supine MR can be used to generate a patient-specific 3D breast model. The positions of the MR visible fiducials can be marked on the skin with marker (such as the red dot fiducials in Figure 6.5 and Figure 6.7), the MR-visible fiducials are removed, and a blue letter label is written beside each dot. During the surgical procedure, the preoperative MR can be registered to the intraoperative surface points collected with our system.

6.3.4 Results

This process successfully boxed 99% of letters. Using the reddest pixel to identify the fiducial location was found to be very reliable, as every fiducial that was boxed had a correct fiducial location. This effectiveness can be seen on the histograms in Figure 6.9 A and B. Figure 6.9A shows the histogram of letters that were correctly and completely boxed. Occasionally extraneous boxes were identified, but these boxes were always eliminated at a later step without specific intervention. These extraneous boxes occurred around the edges of our phantoms, mostly near plungers that had entered the region of interest and were reflecting overhead light.

Letters in the blue component image patches were successfully labeled with an average of 89% accuracy, and the accuracy distribution can be seen in Figure 6.9C. Examples of image patches that were incorrectly labeled are shown in Figure 6.10. An average of 81% of 3D fiducial points were correctly labeled and localized with the accuracy distribution shown in Figure 6.9D. To be correctly labeled and localized, the label

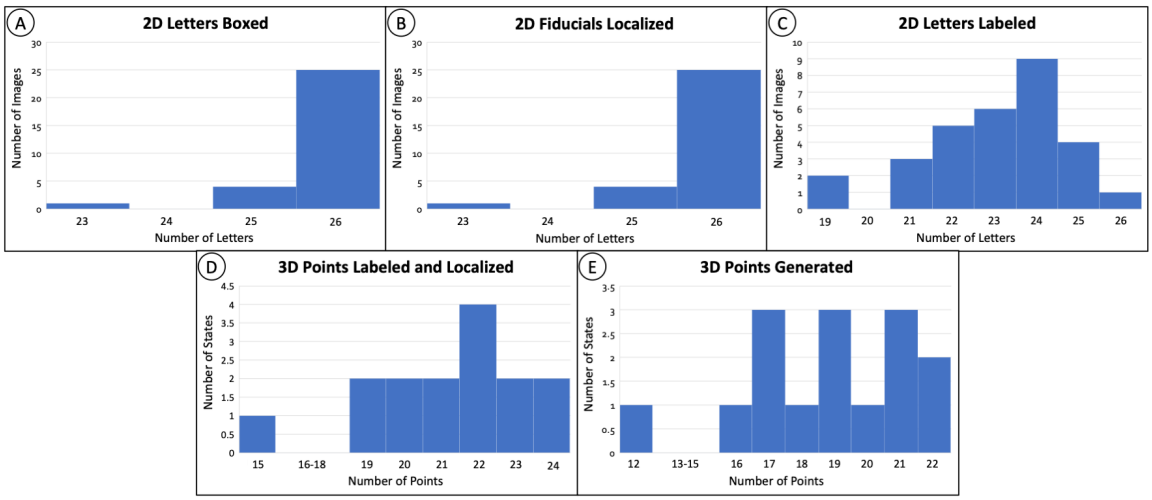

Figure 6.9: Accuracy at five steps in the process of identifying fiducial points on our phantoms. Circled letters correspond to the locations of circled letters in the steps shown in Figure 6.6. The top row (A-C) shows metrics all in 2D space, considering left and right frames individually, for a total of 30 frames (3 phantoms, 5 deformation states each, and a left and right image for each state). The y-axes for the top row are number of images. The bottom row (D and E) shows metrics all in 3D space, considering triangulated points, for a total of 15 point sets (3 phantoms, 5 deformation states each).

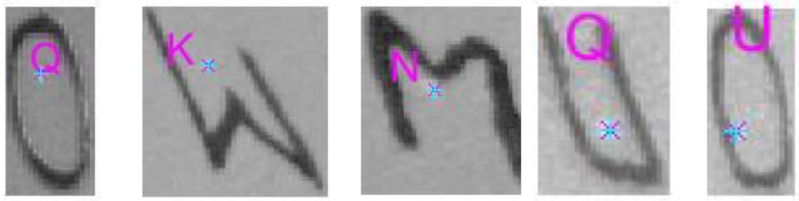

Figure 6.10: Examples of blue color component image patches that were fed into the optical character recognition function and mislabeled. The output label is displayed in magenta. The fiducial location, as determined by the brightest pixel in the red color channel (not shown), is indicated with a cyan and magenta asterisk.

and red fiducial location must be correct in the left and right images. Incorrect labels lead to confounding correspondence, and were handled as described in Section 6.3.3.3 to generate 3D points with 73% success rate, as shown in Figure 6.9E.

The FRE between the stereo camera points and the points manually collected with the optically tracked stylus was 1.9 ± 0.2 mm. The FRE between the five validation point sets manually collected with the optically tracked stylus was 1.4 ± 0.1 mm.

Figure 6.11 displays a sample of the image guidance system with human data, gathered with IRB approval and patient consent. Using optically tracked tools, instruments can also be registered to and displayed in model space, as shown by the black stylus, and the orange transparent model of the tracked ultrasound plane.

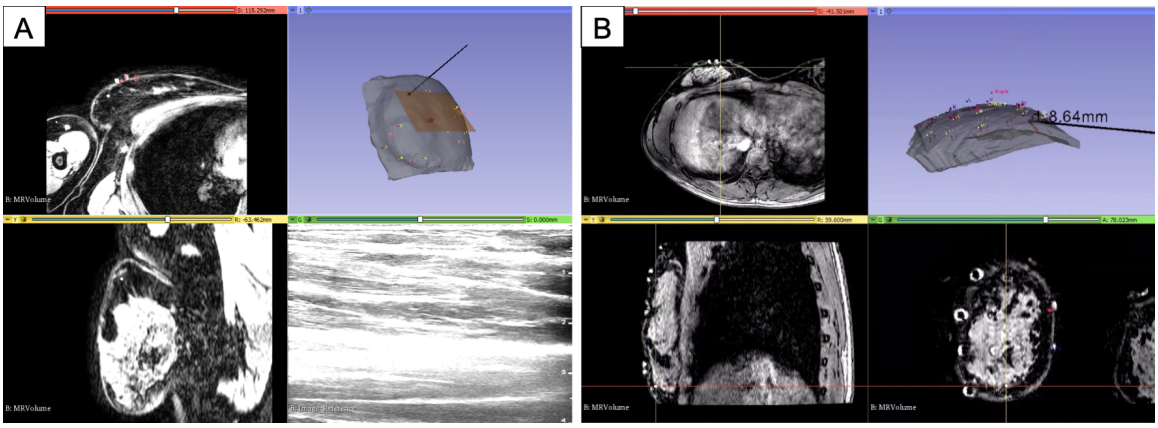

Figure 6.11: Image guidance system four-panel displays. (A) Display using tracked US probe: MR axial and sagittal slice views (left), live ultrasound feed (right bottom) and 3D rendering, with tumor segmentation in red, surface points, stylus in black, and model of the tracked ultrasound plane in transparent orange (right top). (B) Display using tracked stylus: MR axial, sagittal and coronal slice views each with cross-hair positioning of the tracked stylus (left top, left bottom, right bottom, respectively), and model of the breast, tumor, and tracked stylus with surface points and the distance from stylus to tumor (top right).

6.3.5 Discussion

To the best of our knowledge, this work presents the novel use of lettered fiducials in a stereo camera system. Stereo cameras are out of the surgical field, and can measure the surgical position without the use of a seed or probe. Because the field is monitored with RGB cameras, fiducials can be drawn on to the skin with marker. Drawn fiducials are cheap, sterile, and do not interfere with surgical incisions.

Character based fiducial labels allow detection to substitute for tracking, eliminating the need for object history. With each frame processed independently, frames need not be processed in order, or at high frame rates. This allows the system to provide intraoperative surface points at near real time speed, while continuously updating a guidance display with each set of collected points. Letters also provide intuitive features on a previously featureless surface. These letters serve as easy reference points between the patient on the table

and the tumor and breast models on the screen.

Letters also allow us to leverage existing work in Optical Character Recognition (OCR) – a large image processing field. The letters in these digital images can be isolated and recognized, applying this existing OCR knowledge to help localize fiducials. Letters are relatively easy to detect, and can be drawn large in size to improve detection while fiducial points can be drawn as small points nearby for accurate and precise fiducial location measurements.

We also present a novel four panel display including tracked ultrasound, registered preoperative MR, and a patient specific 3D breast model in a module written for 3D Slicer [224]. While standard directions treat the breast surface as a clock face to give angle and distance relative to the nipple, letters allow for the addition of more intuitive directions relative to more proximal concrete landmarks. The tracked stylus, displayed with respect to the patient specific breast and tumor models, can be used to help understand lesion, extent, position and depth with respect to the surface by means of the nearby letter landmarks.

While paint was used for our experiments, we propose the use of indelible markers for use on human skin, similar to the markers that are currently used for surgical planning. For the use of this system during surgery, other colors may be more suitable than red, to reduce the impact of blood in the image. We expect this method to be similarly successful using other colored fiducials, particularly with the use of other color channels, and other color spaces. Future work may benefit from green fiducials in the green color channel, or the use of the hue saturation value color space.

While these results show promise, we acknowledge there is much room for improvement. The two main sources of error are poor letter recognition and the compounding nature of errors in the left and right images. The nature of stereo cameras requires the cameras to have slightly different perspectives. In our system, the cameras are at an angle that provides great depth perception, but relatively large distortion in letters on steep surfaces, such as the sides of the breast phantom. This large distortion contributes to many letter recognition errors. These recognition errors are to be expected, as the OCR method implemented in MATLAB is not optimized for letter recognition in grayscale image patches of handwritten letters. These errors could potentially be reduced using another method. Other methods for OCR have achieved high success ranging up to near human-levels of accuracy, even for handwritten text [281, 282]. Letter distortion also means that recognition errors are likely to only occur on one of the two images. Utilizing the left image to inform the right image labels, and vice versa could dramatically improve performance.

Finally, the FRE reported here was affected by the deformable properties of the phantom. These experiments use a nonrigid breast phantom. The deformable properties of our phantom allow us to evaluate how our system is affected by motion and slight variations in letter configuration and lighting. However, the deformable nature of our phantom causes localization error when using the optically tracked stylus, as the stylus

tip needs to be positioned touching the surface without deforming the surface. The registration error between our stylus collected validation point sets was 1.4 ± 0.1 mm. This means that the majority of the error in our stereo camera evaluation, is actually from our validation method, and our cameras are capable of getting reasonably accurate points. Furthermore, conventional optical tracking is widely accepted and used in image guidance. The proposed method of intraoperative surface acquisition performs with comparable accuracy but with significantly reduced workflow interruption.

6.3.6 Conclusion

This stereo camera system can accurately localize surface points with 1.9 ± 0.2 mm FRE when compared to points manually collected with an optically tracked stylus. On average, 23 of 26 letters correctly (89%) can be detected and labeled correctly. The system can correctly detect and label 21 three-dimensional points (81%). Using this simplistic approach to handling mislabeling, an average of 19 fiducials (73%) can be generated as labeled 3D points with a minimum of 12 fiducials. While 12 fiducials is enough for a rigid registration, more fiducials would provide more information and better alignment between image and physical space. More exploration is necessary to investigate improved approaches and robustness to lighting variations and obstruction. While still in preliminary stages, this system has the potential to be the first continually updating image guidance system for breast cancer surgery.

Acknowledgements

This work has been supported by NIH-NIBIB awards T32EB021937, R21EB022380, R01EB027498, and NIH-NCI award R01CA162477.

6.4 Soft tissue monitoring of the surgical field: detection and tracking of breast surface deformations

6.4.1 Abstract

Objective: Most computer vision approaches for point localization are optimized for rigid, planar objects and are not well suited for soft tissue tracking within surgical workflows. However, skin fiducial localization is needed to align preoperative data with the dynamic intraoperative scene. This work presents a contactless, automated fiducial acquisition method using stereo video of the operating field to provide precise, reliable fiducial localization for an image guidance framework in breast conserving surgery. *Methods*: On n=8 breasts from six healthy volunteers, the breast surface was measured throughout the full range of arm motion in a supine mock-surgical position. Using hand-drawn inked fiducials, adaptive thresholding, and KAZE feature matching, precise three-dimensional fiducial locations were detected and tracked through tool interference, partial and complete marker occlusions, significant displacements and nonrigid shape distortions. *Results*:

Compared to digitization with a conventional optically tracked stylus, fiducials were automatically localized with 1.6 $\pm$ 0.5 mm accuracy and the two measurement methods did not significantly differ. The algorithm provided an average false discovery rate < 0.1 with all cases below 0.2%. On average, 85.6 $\pm$ 5.9% of all visible fiducials were automatically detected and tracked, and 99.1 $\pm$ 1.1% of frames provided only true positive fiducial measurements, which indicates the algorithm achieves a data stream that can be used for reliable on-line registration. *Conclusions*: Tracking is robust to occlusions, displacements, and most shape distortions. *Significance*: This work-flow friendly data collection method provides highly accurate and precise three-dimensional surface data to drive an image guidance system for breast conserving surgery.

6.4.2 Introduction

Computer vision has been increasingly utilized in surgery for a wide variety of applications ranging from understanding surgical process to computer aided detection and navigation [283]. While its use in tool tracking has been a key component in standard-of-care guidance systems for decades, computer vision methods for soft tissue tracking has had more limited development. Several recent surgical technologies have utilized unique printed markers (e.g. ArUco [185] or ARTag [212] fiducials) to localize skin surface information during surgical procedures [137, 139, 284]. However, even in rigid scenarios, localization errors for these types of fiducials can be high. In a study comparing 12 common marker dictionaries, localization error was over 7 mm on average for 0-75° viewing angles. Though two methods achieved accuracy suitable for surgical applications (below 2 mm), results are reported for relatively large tags (5 cm) mounted onto rigid, planar boards and viewed from close distances (0.05 – 0.5 m) [188]. Commercial systems for computer vision tracking of rigid tools, such as the Claronav MicronTracker, report 0.2 mm calibration accuracy from 0.4-1.0 m distances, though viewing angles and lighting conditions are not reported [177].

While many vision-based toolkits for tracking markers are freely available and easily adoptable, their accuracy is limited [187], especially in the context of the dynamic surgical environment. These tags are designed to be mounted on rigid and planar surfaces. These rigid assumptions result in reduced detection rate and accuracy when fixed to nonrigid surfaces, such as skin in deforming surgical applications. Recently, a marker detection system has been proposed using deformable fiducial tags, [189], but surgical use would still rely on a cumbersome process of printing and mounting specialized, large, and obstructive tags to skin in the sterile operating environment. Furthermore, when using these tag-based approaches in the context of image guidance systems, point correspondence to their preoperative imaging counterpart is not intuitive to users because the marker patterns have no immediate relationship to the imaging data. The work herein presents a fiducial detection and tracking algorithm customized for surgical guidance applications with intuitive ink-based alphabetic labels hand drawn directly onto the skin surface. These letter-based fiducials enable three-

dimensional point measurements during surgery, so that information rich preoperative images can be aligned with the patient on the operating room (OR) table, enhancing surgeon understanding of tumor position and subsurface anatomy. While this automated skin-fiducial localization method can be used in the context of many surgical domains for image-to-physical registration, in this work it will be evaluated in the context of breast conserving surgery (BCS) due to the deformable nature of breast tissue.

With regard to the clinical application, there has been recognition that BCS could benefit from the addition of improved surgical guidance in the process of tumor resection. In recent years, breast conserving surgery reoperation rates have plateaued at approximately 10-20% [15]. Primary contributors to these reoperation rates are the vast shape changes and deformations between diagnostic and surgical settings that make it difficult to reliably determine intraoperative tumor positioning and extent [18, 19, 42, 43]. To address these shortcomings, an automated surface acquisition method is needed to continuously inform a rigid image alignment approach to assist in visualizing approximate intraoperative tumor boundaries. Better yet, a system that could measure 15–25 precise fiducials over the breast surface would potentially enable deformable soft tissue alignment techniques to facilitate surgical lesion localization in the deforming breast. Since registration accuracy is ultimately dependent on data sparsity and coverage, the ability to quickly and accurately measure sufficient intraoperative localization data is critical for the utilization of image guidance. Corresponding points, i.e. points visible both in the preoperative image and on the breast in the OR, are an essential data source for guidance and correction frameworks.

To visualize intraoperative tumor boundaries, several research systems for image guidance in breast conserving surgery have emerged using corresponding fiducial points [41, 50, 132, 137, 139]. Typically, these initial image guidance systems for BCS have used rigid registration to align preoperative supine MR images to the patient in the surgical position. For example, Barth *et al.* developed a guidance approach using skin fiducials and rigid registration to actively guide surgery in comparison to conventional wire-guided localization. The results nearly halved positive margin rates of residual cancer after resection when compared to conventional wire guidance, from 23% to 12% [50]. Though this study showed great promise, it should be noted that the results were underpowered for statistical significance.

Another research prototype system for intraoperative breast tumor visualization used six ArUco tags to register a virtual reality breast scene to the patient [139]. These ArUco tag fiducials were not placed directly on the breast, but rather at the breast perimeter, i.e., on the surrounding rib cage and just inferior to the clavicle, likely to avoid the dynamic deformations associated with soft breast tissue. While this placement provided rigid alignment, these fiducials could not capture the nonrigid shape changes [139]. Furthermore, the authors acknowledged difficulties in placing ArUco tags on corresponding locations associated with MR-visible fiducial locations.

These rigid registration frameworks leave conspicuous residual misalignment after rigid registration [139]. To provide further context to the application, in BCS the patient's arms are outstretched at 90°(in a T-shape), whereas in a conventional closed-bore MR imaging system, the patient's arm would be positioned either down by the torso or up by the head to fit within the scanner. Even when imaging and surgery are both performed with a supine body orientation, there are still large imaging-to-OR deformations resulting in high residual registration errors that reflect nonrigid deformations. Quantitatively, in a breast alignment study using rigid registration in a mock imaging-to-OR framework [238], maximum target errors after registration were reported from 10.7–36.4 mm, indicating that a rigid registration approach is unlikely to be sufficiently accurate for resection.

Beyond providing landmarks for rigid alignment as in the above systems, fiducials that are properly distributed across the breast could be used as a valuable source of deformation measurement [238] toward correcting misalignment due to breast shape changes [171, 235]. For example, Conley *et al.* presented a modeling framework with an initial rigid alignment using fiducials and ultrasound measurements of the chest wall followed by nonrigid correction driven by 6–7 surface fiducials [60]. While quite preliminary, compared to rigid registration the method improved tumor localization in surgical positioning by 15% and 58% in two cases evaluated. A method presented by Ebrahimi *et al.* used thin plate splines to predict volumetric breast deformations from 24–34 surface fiducials alone. In six patients, the average estimate of a tumor centroid had 3–18 mm of error after rigid registration, and 1–10 mm of error after the thin plate spline registration scheme [171].

These advances toward sophisticated guidance approaches in BCS are encouraging, and common to the above systems is the localization of fiducials, either designated manually with an optically tracked stylus or directly tracked with the use of an adhered marker. With the former, designating fiducial positions manually during surgery is tedious and the precision is heavily dependent on the user. Additionally, for soft tissues, measurement methods that contact the surface have been shown to be less accurate than noncontact measurements [181]. Despite the impracticality of manual methods, the latter option of adhered fiducials is complicated by the fact that fiducials near the surgical region of interest must be removed prior to commencing surgery. In [50], all fiducials are removed for surgery, limiting correction to only an initial alignment. Additionally, both methods are limited by non-automatic measurement and labeling of fiducials, which consumes valuable time in the operating room for each additional fiducial identified during the procedure. The landscape of emerging guidance systems for BCS reveals a pressing need for measurement techniques that enable rapid soft-tissue measurements to enable novel alignment and localization approaches, which must also be easy to integrate into BCS workflow. The work presented here directly addresses this need by abandoning the concept of structured or printed fiducials, and instead investigating a novel approach with intuitive

fiducials (English alphabet) inked directly on the breast surface and then tracked using image processing methods. The strategy is easily integrated into current workflow and the inked letter-based fiducials on the patient inherently correspond to labels that can be rendered in an image-guided display to provide surgeons with a convenient, intuitive map on a previously featureless breast surface. The automatic surface acquisition method uses simple image processing to detect fiducial labels and fiducial positions, and leverages conventional feature detection and matching to track these precise fiducial positions on the nonrigidly deforming skin surface through time. These fiducials that consist only of sterile ink can be tracked to provide continuous, automated, simultaneous, and precise fiducial collection in a deformable OR setting.

6.4.3 Methods

6.4.3.1 Human Data Collection

Using the system shown in Figure 6.12a, data were collected on n=8 breasts across six healthy volunteers ages 23–57 (29 $\pm$ 14) with informed consent and approval from the Vanderbilt University Institutional Review Board. For each breast, 26 MR-visible fiducials (IZI Medical Products, Owing Mills, MD) were distributed on the breast surface. Supine MR images were obtained in two arm positions shown in Figure 6.12b: with the ipsilateral arm down resting beside the torso, and with the ipsilateral arm up resting beside the head. Fiducial positions were manually designated in each MR image. At least 24 fiducials were visible in each image, with some fiducials going out of view due to image size and large deformations from arm abduction. On average, 25.6 $\pm$ 0.6 fiducials (mean $\pm$ std) were designated within an individual MR image volume. It should be noted that the MR image data were used only to provide preoperative fiducial locations for error filtering as they would represent known priors in the image-guided application. The full protocol involving MR imaging data is provided here only to convey the complete procedural workflow of the approach.

After imaging, subjects were moved to a mock intraoperative setup where they lay supine with padding under the ipsilateral shoulder to simulate rotation of the OR table. The center of each toroidal MR-visible fiducial was marked with colored ink (red) shown in the center image of Figure 6.12b, and the fiducial was removed. Each fiducial, now a red dot, was then labeled with a capitalized English character in a second color ink (blue letter label) as in Figure 6.12c. The size of each character was approximately 3 cm in height. Visible skin markings (such as moles) that were the same color as fiducials were covered with a third ink color. Static fiducial locations were measured in three positions for each breast: arm up, surgical position (i.e. arm outstretched at 90°), and arm down. Fiducial locations were also designated manually using an optically tracked stylus, a tool typical in image guided surgery (Polaris Vicra optical tracker, Northern Digital, Waterloo, ON, Canada). Stereo images of the operative field were collected with two Grasshopper stereo cameras (FLIR, formerly Point Grey Research, Richmond, BC, Canada) placed 0.9-1.2 m above the skin

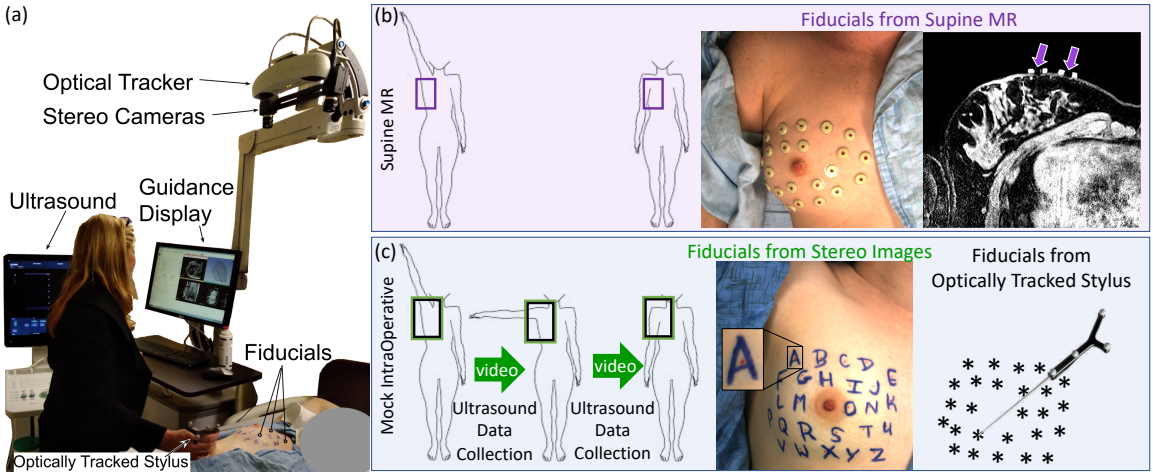

Figure 6.12: Overview of data collection and the arm configurations, or states, measured in each setting. (a) image guidance system (b) data collected from supine magnetic resonance (MR) images with the distribution of fiducials. In the top right, fiducial positions visible in an axial image slice are indicated with purple arrows (c) data collected in the mock intraoperative setting.

surface. Stereo cameras provided color images at 1200 $\times$ 1600 pixel resolution, and were calibrated using the method presented by Zhang *et al.* [226] in MATLAB's Computer Vision Toolbox [228]. Stereo cameras were used to record videos of fiducial positions in the three static arm positions and throughout arm adduction at about 5 frames per second. Intermittently during video collection, an ultrasound exam was conducted, providing procedural obstruction of the visual field. Video footage recorded during this process consisted of ultrasound gel application, probing the ultrasound transducer over the breast surface, and gel removal with a towel. Video frames were considered static if they contained breathing motion, but no other major motions, obstructions or interference with breast tissue. Thin layers of ultrasound gel were not considered an obstruction. With respect to evaluation of tracking performance, the algorithm tracks fiducial points throughout the full video duration, including arm adduction and ultrasound exams. This approach allows analysis before and after considerable motion and obstruction events.

6.4.3.2 Algorithm Overview

This surface tracking algorithm for image guided surgery uses handwritten inked fiducials that can be sterilized and remain on the skin throughout surgery. The algorithm is implemented in MATLAB 2021b using functions from the Computer Vision Toolbox [228]. Briefly, fiducials are localized in 2D images by leveraging the two ink colors and adaptive thresholding. Fiducials are matched and tracked using KAZE feature matching [285] and point history. An overview of the algorithm is shown in Figure 6.13, best viewed in color. The algorithm is considered in two parts: localization and labeling.

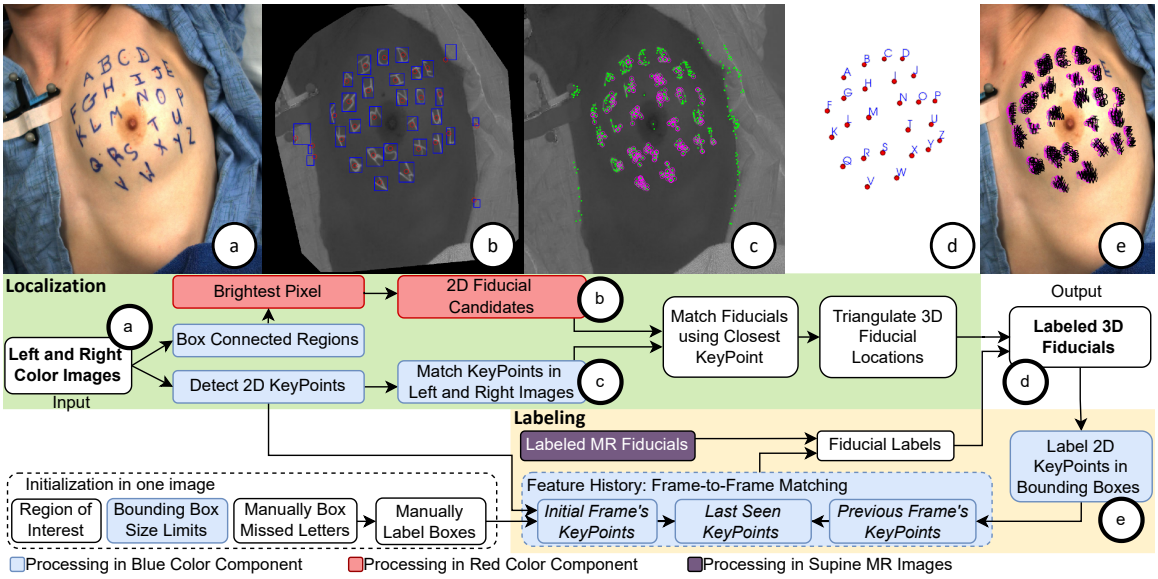

Figure 6.13: Detection and tracking algorithm. Images cropped for visualization. (a) A color image from one of the stereo cameras (b) blue color component of the masked region of interest with boxed connected regions (blue), and 2D fiducial candidates (red) (c) 2D KAZE keypoints (green) with successfully matched 3D keypoints circled (magenta) (d) Output labeled fiducials in 3D space and (e) 2D keypoints labeled by bounding box for input into the Feature History.

6.4.3.3 Fiducial Detection: Point Localization

The color component is computed from the raw RGB camera images as the color ratio of each pixel according to

$$Color\ Component(Channel \in \{R,G,B\}) = \frac{channel}{R+G+B} \tag{6.5}$$

for R, G, and B the red, green, and blue intensities, respectively, where *channel* is the desired color channel. The color component range is normalized to 256. In the blue color component (*channel=B*), adaptive thresholding is used to create a binary mask of the letter label regions. A bounding box is placed around each connected component. Within each bounding box, the red color component image is computed and individually normalized to 256. This process provides maximum contrast between fiducial pixels and surrounding skin, from which a 2D fiducial candidate is identified as the centroid point in the region grown around the brightest pixel in the red color component. In Figure 6.13b, the blue color component image shows the bounding boxes resulting from adaptive thresholding in blue and the identified 2D fiducial candidates circled in red.

KAZE feature detection and matching is used to obtain a sparse cloud of triangulated keypoints [285]. Detected KAZE keypoints (2D keypoints) are shown in Figure 6.13c in green, with successfully matched keypoints between left and right stereo images (3D keypoints) plotted as magenta circles. The 2D fiducial

candidates from the red centroids are matched as follows. For each 2D fiducial candidate in the left image (candidateL), the algorithm determines the closest successfully matched keypoint from KAZE (keypointL). In the right image, the 2D fiducial candidate (candidateR) closest to the keypointR is considered the correct match. Although KAZE produces a 3D point cloud (visualized in 2D space as the magenta circles in Figure 6.13c), the keypoints have no correspondence to the MR image. This process of fiducial detection and matching ensures measurements of the inked fiducial points that correspond to imaging data. However, it should be noted that the closest-keypoint assumption does yield some incorrect matches. Outliers are removed at this step by error filtering based on the difference in position (slope) between left and right matched points. Next, matches are ensured to be unique. For all nonunique matches between fiducial candidates, the best candidate is chosen by the match that provides a slope closest to the median slope of all matched keypoints.

6.4.3.4 Initialization

On initialization, the user manually defines a region of interest (ROI) for each camera and tunes the minimum and maximum bounding box sizes according to the size and variability of the letter labels. The main purpose of the ROI is to reduce the computational search space for several of the tracking steps. This reduction improves runtime for feature detection and eliminates many extraneous 2D fiducial candidates in an early phase of the algorithm. After the ROI is established, the ROI is dilated before applying the adaptive thresholding step on subsequent frames to ensure that the mask edge is sufficiently far from the letter labels and does not interfere with thresholding. Bounding box size limits are manually set to include all letter-labels, and are defined once and applied to both image streams.

Once the detection algorithm is initialized, the tracking algorithm is initialized in just one image. After automatic 3D fiducial detection, the 2D bounding boxes of these 3D candidates are presented to the user. The user is instructed to manually box undetected fiducial labels, and manually label each box with its letter label. This user input serves to initialize the feature history. All 2D keypoints that fall within bounding boxes are stored along with their features and labels. Examples of these labeled keypoints are shown in Figure 5.2e.

Finally, when fiducial candidates arise too close together, e.g. due to a letter-label appearing discontinuous in an image, the candidate with the highest average red color component is kept and all other candidates are discarded. The algorithm therefore requires one additional parameter that defines a minimum allowable distance between fiducial candidates in 3D space. For the majority of cases, this parameter can be zero (unconstrained). However, for one case (case 1L), the parameter was set so that 3D fiducial candidates must be at least 20 mm apart.

In summary, initialization requires manually annotating in the first image frame: (1) a region of interest for both cameras, (2) bounding box size limits, (3) minimum distance between fiducials, (4) bounding boxes

missed by automatic detection, and (5) letter labels for bounding boxes.

6.4.3.5 Fiducial Tracking: Point Labeling

Labeling the 3D fiducial candidates relies on frame-to-frame KAZE feature matching [285]. In summary, labels are propagated through one camera stream by matching the 2D keypoints within bounding boxes to previously labeled keypoints. The label of a fiducial candidate is the most common label in its bounding box.

Feature matching relies on storing feature history in three main phases: *Phase 1*: keypoints in the initial frame, *Phase 2*: keypoints in the previous frame, and *Phase 3*: the last seen keypoints. The feature history stores keypoint locations, feature vectors, and letter-labels. In *Phase 1*, keypoints in the initial frame are stored using user-defined letter-labels as described at the end of the previous section; these labels have the highest confidence since they are manually specified. Only unlabeled boxes continue on to be labeled by the next phase. Next, in *Phase 2*, keypoints in the remaining bounding boxes are matched to the keypoints of the previous frame. The previous frame is most likely to resemble the current presentation of features. Finally, the remaining unlabeled bounding boxes continue on to *Phase 3* where keypoints are labeled using the last seen keypoints. The list of last seen keypoints for a given letter is defined as the most recent n=100 points labeled with that letter. Since there are 26 fiducial letter-labels, the size of this matrix is therefore restricted to 2600 features, letters, and point locations (recall that the feature history is only maintained for one camera image stream). When constructing the last seen keypoint matrix, points are added in descending time order prioritizing points that were successfully matched to the current frame. In priority order, points are added from the following lists until 100 features are reached: (i) matched features from the previous frame, (ii) matched features from the last seen keypoints, (iii) unmatched features from the previous frame, and (iv) unmatched features from the last seen matrix. The last seen points add robustness to lighting variations and occlusions.

After all boxes are labeled, uniqueness is enforced again. Letter duplicates are evaluated and the 3D fiducial candidate closest to the historic 3D fiducial location is kept, while all other candidates labeled with that letter are discarded. If the letter has not been previously localized in 3D, the point location is considered uncertain and all candidates for this letter are discarded.

Here, a final stage of error catching is implemented that is unique to this application. Points that are sufficiently far from their MR counterpart are considered erroneous. More specifically, image-to-surgery rigid registration accuracy in the supine position has been previously measured with maximum surface target errors between 7.4 and 36.4 mm [238]. Using this characterization as a guide, fiducials were considered incorrectly localized if they were more than 40 mm from their MR fiducial counterpart. While this parameter is a constant in this work, if 40 mm proved inappropriate on another dataset, this parameter could be prescribed based on

fiducial registration error (FRE) after the point-based registration of the tracked fiducials to their positions in preoperative MR. This error catching largely serves to remove points with incorrect left-right matching causing erroneous triangulated 3D coordinates.

6.4.3.6 Evaluation

Three main performance metrics are evaluated: (A) localization accuracy of 3D fiducial detection, (B) tracking fidelity, and (C) tracking completeness. Beginning with the detection algorithm localization accuracy, 3D localized fiducial points were compared to the corresponding points localized using an optically tracked stylus tool (NDI Polaris Vicra, Waterloo, Ontario, Canada), which is a standard in image guided surgery due to its reliable accuracy [174]. In each static arm position, the fiducial positions as measured with the stereo cameras are automatically localized and manually labeled. These camera-based fiducial measurements are rigidly registered to positions measured with the optically tracked stylus and the residual error is reported. Registrations are computed using a conventional least-squares singular value decomposition point-based registration method [222], and fiducial registration error (FRE) is measured as the root mean square of the distances between registered point sets as defined by Fitzpatrick et al. [223].

Additionally, to measure the accuracy of the gold standard measurements, for one subject, fiducial positions were measured repeatedly with the optically tracked stylus. All combinations of these point sets were rigidly registered, and the average FRE is reported as a baseline error metric for this ground truth measurement technique.

With respect to assessing tracking fidelity, the rate of false positives, i.e. incorrect fiducial returned, was measured by examining fiducial positions in the 2D images, and by comparing 3D triangulated fiducial locations to stylus-designated locations. The number of frames with no false positives is reported and represents how often the automatically detected fiducials can be used for reliable image-to-physical registration. For a frame f, the average false discovery rate(1-precision), is also reported and is described as

$$False\ Discovery\ Rate_f = \frac{False\ Positives}{Total\ Detections} \times 100\% \tag{6.6}$$

Lastly, tracking completeness is evaluated with the number and distribution of visible fiducials not returned as output (i.e. how many fiducials are missed, and how are these missed fiducials distributed across the breast surface). To compare the automatic method to an ideal output from the stereo camera images, detection rate (recall) is considered as

$$Detection\ Rate_f = \frac{True\ Positives}{Total\ Visible} \times 100\% \tag{6.7}$$

where the total number of visible fiducials is determined as the number of fiducials that could be localized in the camera images by augmenting automatic detection with manual point picking. Fiducials are considered not visible if their red fiducial centroid cannot be picked manually in the stereo camera images for a state. The analysis is extended to investigate completeness with regards to the full extent that could be captured with an alternative method not limited by line-of-sight (e.g. manually designated with tracked stylus) with

$$Extent_f = \frac{True\ Positives}{26\ Fiducials} \times 100\% \tag{6.8}$$

It should be noted that the number of frames in each breast acquisition state analyzed is not necessarily evenly distributed as no specific protocol was in place for the length of time recorded in each static arm position. Since arm up configurations generally expose a greater number of fiducials to the cameras, an unweighted average may show that cases with more frames in the arm up position have better completeness metrics. To remove this bias, completeness metrics for each case are first averaged by state, then averaged across all three states. Additionally, the completeness metrics did not include phases of motion or obstruction.

6.4.4 Results

6.4.4.1 Detection: 3D Localization Accuracy

Localization accuracy was evaluated in the three static arm states (one evaluation per state) for seven of the eight cases. Case 5R was omitted due to missing still images time-synced with NDI collection. Accuracy is reported as the FRE (mm) associated with registering fiducial points localized from the stereo camera system and the corresponding points designated with an optically tracked stylus. On average, 22 $\pm$ 2.4 fiducials were automatically localized with the camera system. Table 6.1 reports the accuracy (FRE) and the average number of fiducials used to compute the rigid registration, averaged across all 3 states. After rigid registration, automatically localized fiducials differed from the ground truth stylus-designated positions by 1.6 $\pm$ 0.5 mm. As reported in [238], when static fiducial positions on the breast were measured with the optically tracked stylus repeatedly five times) FRE was 1.5 $\pm$ 0.1 mm. The two distributions of FRE were compared with an unpaired t-test ($\alpha = 0.05$) and were not significantly different ($p = 0.54$).

6.4.4.2 Tracking: Fidelity

Tracking fidelity is only evaluated in static frames as these are the only acquisition times where the corresponding ground truth 3D fiducial locations (stylus-designated) are available for verification. Though a tracking algorithm should successfully track through large deformations and obstructions, it is reasonable to assume that surface data will be collected during static, unobstructed scenes. Here, all video frames were processed for tracking, though performance during deformations and obstructions is only included in Figure

Table 6.1: Localization accuracy

Case	Average Accuracy (mm)	Average Number of Fiducials Localized
1L	2.6	20.0
2R	1.9	25.0
2L	1.5	22.7
3R	1.6	23.7
4R	1.2	21.3
5L	1.4	23.0
6L	1.3	18.0
Average	1.6 ± 0.5	22 ± 2.4

5.3. Figure 5.3 shows the true positive and false positives over time through the entire protocol for cases 1L and 3R. For case 1L, the video frames from various experimental phases are displayed, demonstrating how obstructions in the scene result in a lower number of localized fiducials. The total number of frames processed for tracking and the number of static frames analyzed are reported in Table 6.2 alongside the false discovery rate and the total number of false positives. Since no frames had more than one false positive, the number of false positives also represents the number of frames with unusable output for registration. In the worst case (5R) where 7/267 frames have false positives, still over 97% of frames are usable for reliable registration, and on average $99.1 \pm 1.1\%$ of frames are usable.

Table 6.2: Tracking Fidelity

Case	Total Frames Tracked	Static Frames Analyzed	Total alse Positives	False Discovery Rate(%)
1L*	1227	295	5	0.1
2R	1507	431	0	0.0
2L	874	206	0	0.0
3R*	1220	185	1	0.0
4R	582	132	3	0.1
5R	1312	267	7	0.2
5L	790	129	0	0.0
6L	575	171	0	0.0
Average	1011	218	2	0.1 ± 0.1

*performance visualized in Figure 6.14

6.4.4.3 Tracking: Completeness

The average detection rate was $85.6 \pm 5.9\%$, showing that a large majority of visible fiducials can be automatically detected and localized as visible in Figure 6.15. All static frames returned at least 10 fiducials for registration, with 75% of cases returning a minimum of 18 fiducials across all frames. In retrospective

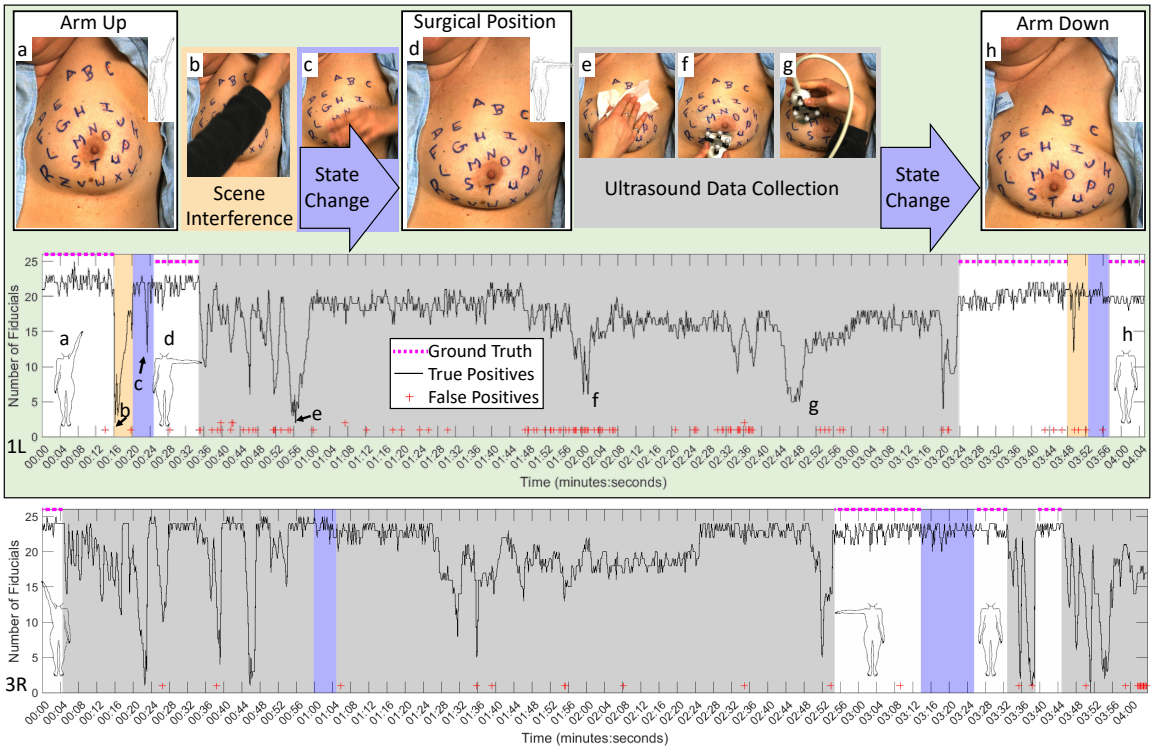

Figure 6.14: Data collection and processing throughout the entire video for two representative cases: 1L and 3R. Note performance recovery after obstructions and false positives. The three arm configurations where accuracy was measured are overlaid: arm up (left), surgical position, and arm down (right). Video content is classified into four categories: static frames (no highlight), adduction frames (blue), ultrasound collection (gray), and other scene interference (yellow). Number of fiducials that are true positives (black line), false positives (red +), and manually localized in static frames (magenta dashed line). Highlighted frames are processed but excluded from reported metrics.

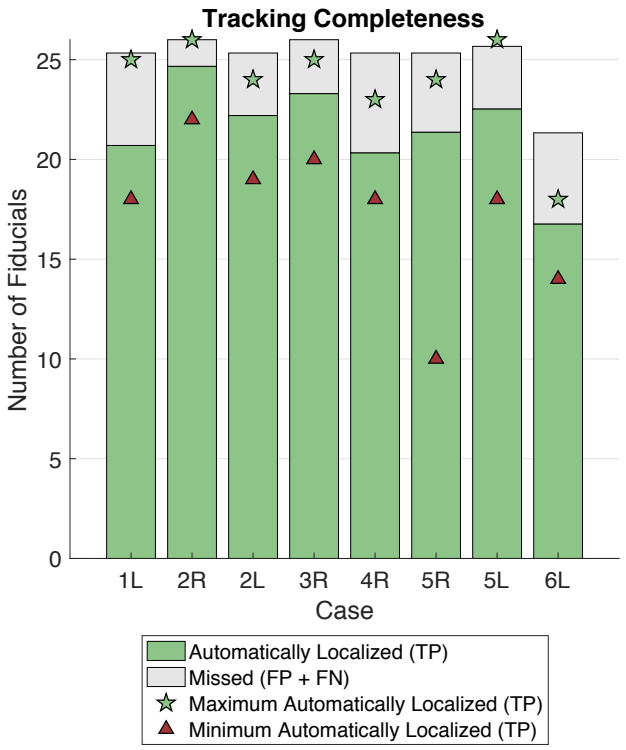

Figure 6.15: Average number of fiducials automatically localized (TP= true positives), compared to the average number of fiducials visible (top of gray bar). False negatives (FN) and false positives (FP) are considered missed fiducials.

analysis, the fiducials that were commonly missed resided on the lateral edge of the breast surface, closest to the arm, where the surface deviates from planarity and the frequency of missed localization increases as displayed in Figure 6.16. While highly performant, the algorithm was found to struggle with some letter distortions due to large fiducial deformations. To illustrate this trend, the magnitude of deformation due to arm adduction is shown in the right column of Figure 6.16 This drop-out due to distortion is most notable in the upper outer breast quadrant (i.e. fiducials closest to the armpit) like the letter "C" in the top row of Figure 6.16. Also, it is interesting that not all fiducials with large displacements suffer: more medial fiducials that undergo large deformations are able to be localized with low dropout rates (e.g. the letter "B" in the top row). With regards to extent, although the cameras suffer from line of sight constraints, $82.6 \pm 9.2\%$ of the full 26 fiducials can be localized automatically (Figure 6.16 – *Center* column).

6.4.5 Discussion

This work demonstrates a successful surgical field monitoring system that can capture nonrigid skin motion with accuracy, fidelity and completeness such that it can be used to promote new directions in surgical guidance. The inked fiducials are easy to place and are amenable to sterile processes, as they can remain on the

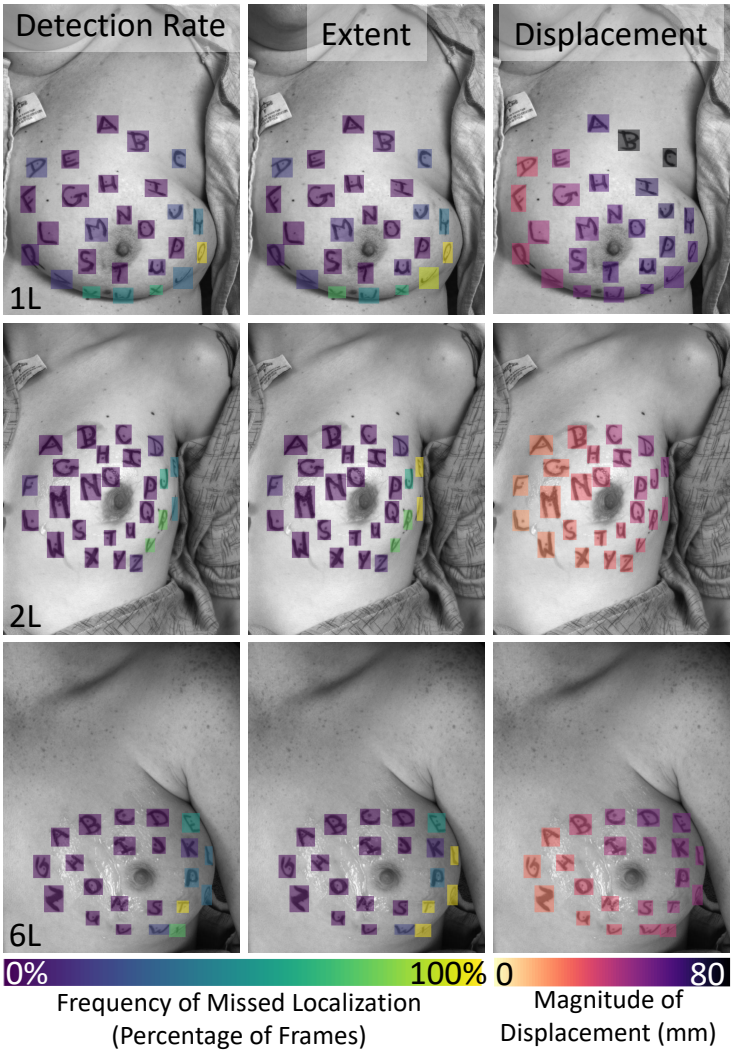

Figure 6.16: Distribution of missed fiducials for three cases, shown in the arm-down state. Left - detection rate, or missed fiducials with respect to all visible fiducials. Center - extent, or missed fiducials with respect to all 26 placed fiducials. Right - fiducial displacement from arm up to arm down states.

skin surface throughout surgery. The large letter label provides a feature rich surface and the small fiducial dot provides a precise localization target. While quite preliminary, initial surgeon impressions with the lettered fiducials integrated into a guidance system were met with considerable enthusiasm as letters provide naturally understandable landmarks between the patient and the guidance display.

In comparison to existing alternatives that are compatible with OR workflow for BCS, localization accuracy for automatic detection was not statistically different from manual digitization using an optically tracked stylus. However, it should be noted that the accuracy of stylus-designated data is user-dependent which was noted during data collection. For example, manual stylus digitization without deforming the surface while the subject is breathing was challenging.

As a general note, the tracking algorithm presented here was designed and evaluated within the context of utility in image guided surgery. While some algorithms may balance all evaluation metrics, utility in the surgical guidance application relies on a low false positive rate, as frames with false positives cannot be used for registration. Consequently, aggressive error catching was implemented to prioritize a low false positive rate over a high detection rate (i.e. it is preferable to miss some fiducials, as long as all fiducials are trustworthy).

The tracking algorithm is highly reliable with a low false positive rate suitable for use in surgery. The algorithm suffers most with completeness, as line-of-sight constraints can confound detection rate and extent. For example, for the two subjects that had both breasts processed, the breast with better line-of-sight (i.e. larger simulated rotation of the table to provide a more favorable viewing angle) performed better. For case 2, the right breast was more favorably angled than the left, and for case 5 the left breast was more favorably angled than the right. Intra-subject performance differences are visible in cases 2 and 5 in Figure 6.15, with 2R and 5L outperforming their counterparts.

Despite line-of-sight constraints, an adequate number of fiducials can be localized for a reliable registration. The minimum number of localized fiducials for most cases was above 15, far more than the 6-8 fiducials used for registration in initial breast guidance methods [50, 60], or the 11 fiducials necessary to fully describe rigid breast deformations [238]. On average, 21 fiducials could be localized, providing a distributed coverage of surface data to drive potential nonrigid correction frameworks.

For case 5R, there were two frames where only 10 fiducials could be automatically localized. This low minimum was due to a reduced point cloud returned from KAZE feature matching whereby fiducials were still correctly detected in each image, but the algorithm failed to successfully match keypoints between left and right images. This case suffered from a variety of confounding factors: white-balance discrepancies between left and right images, shadows, and subtle motion due to subject re-adjustment. Though all of these problems are visible in other cases, it is hypothesized that the combination of all three factors caused the

unusual dip in the number of localized fiducials.

As noted in Section 6.4.4.3, largely distorted fiducial labels become more difficult to match to the object's feature history. This effect may be particularly detrimental as points with large displacements are likely to be the most informative to registration. However, surface deformations would not be subjected to the full range of arm motion intraoperatively–only half the range of motion is needed to move from imaging position (arm up or down to fit within a closed bore scanner) to intraoperative position (90°abduction).

With respect to limitations, there are several aspects that are important to consider: (1) skin tone variations (2) ink colors (3) lighting variations (4) processing time, and (5) reproducibility.

Beginning with skin tone variations, these were not explored in this manuscript as all volunteers for this study were Caucasian. Evaluation on a variety of human skin colors remains to be evaluated. However, the algorithm is specifically designed with skin tone variations in mind, with fiducial detection performing well in the blue color component images across phantoms of various skin tones [241] from previous work. A predecessor to the detection process presented here is described in [241] though correspondence between 2D fiducial candidates was determined with optical character recognition. The previous approach showed that this 2D detection method was robust to phantoms of differing skin tones; however, the algorithm experienced large dropouts at the correspondence step due to the poor performance of the preliminary optical character recognition approach.

When considering the second limitation of ink colors, it is important to consider the use of red ink in light of the eventual presence of blood after incision. In this work, an algorithm that leveraged two ink colors on opposite sides of the color wheel was implemented. Though the concept of color channels is leveraged heavily in this approach, the color channels do not need to be prescribed to blue and red. Preliminary investigations, not reported here, show that alternative ink colors can be transformed into hue saturation value (HSV) space to map the label color to an equivalent of the blue color channel, while mapping the fiducial color to the red color channel. The use of purple letters and green fiducial centroids is under consideration currently. More comprehensive evaluation of algorithm performance under these conditions remains to be investigated further. In regards to scene interference in the letter-label color channel, note that the ultrasound gel was blue tinted, and in some cases residual gel remained spread across the breast during the static frames evaluated. While the algorithm sometimes struggled with specular reflections from ultrasound gel, the color tint generally did not interfere with adaptive thresholding. Scene interference in the red color channel (e.g. the cap of the ultrasound gel bottle) is generally more intrusive to performance, as obstructions close to the true fiducial location can cause false positives. This can be observed in the supplementary videos.

With respect to lighting variations, while some insight was gained from the introduction of ultrasound gel, more investigation is needed. Apart from glare on the gel, the videos acquired did include footage containing

moving shadows, but it is difficult to study the impact given that the bright overhead lights typically present in the OR were not part of our mock surgery experimental setting. With proper exposure, the breast surface should be clearly illuminated with little impact on algorithm performance although future investigations are warranted.

Runtime evaluation, the fourth limitation, also remains to be optimized. The current processing rate is about 2.5 seconds per frame, with the large majority of that time spent on KAZE feature detection and matching. Speed improvements could be achieved by implementing this algorithm on a graphical processing unit (GPU) in an a more efficient programming language than MATLAB and by using AKAZE feature matching. Accelerated KAZE has shown dramatically improved speeds with little effect on matching performance [263], and KAZE implementations on a GPU have been shown to offer tenfold speed improvements with no degradation in performance [286]. Nevertheless, the current implementation could be used to provide on-demand updates to a guidance framework with minimal wait times. Although surgery would be briefly paused for a registration update, an on-demand framework would be far less intrusive than current clinical seed-based guidance approaches that require the surgeon to halt surgery and use a handheld probe to survey the field manually. Additionally, these systems only provide a distance readout to a preoperatively implanted point-based target, which would be considerably inferior to accurately co-registered supine MR imaging data.

Lastly, when considering reproducibility there are several constraints that the algorithm assumes. As previously mentioned, each fiducial label should be continuous to provide an adequate bounding box. Labels should ideally be unique, to ensure that features are correctly matched. For best performance, fiducial labels should be uniform in size which allows more erroneous boxes and fiducial candidates to be eliminated based on size limits. Some cases here have relatively nonuniform letter size and thickness (as visible in Figure 6.16), and it should be noted that thicker inked lines provide better performance in the adaptive thresholding stage, as thin lines tend to break into multiple boxes creating erroneous 2D candidates. While the algorithm was generally robust to these variations, standardizing fiducial size and line thickness may reduce erroneous candidates and improve performance further.

In summary, protocol with respect to inked fiducial type, coloring, and arrangement can influence performance and remains to be further investigated. Despite these challenges, this methodology is evaluated on a challenging dataset that incorporates many realistic confounding factors from major and minor deformations, obstructions, and scene interference. The approach demonstrated accuracy and robustness (Tables 6.1 and 6.2) that make it a promising solution for soft tissue monitoring in the OR.

6.4.6 Conclusion

This work presents a novel method for precise intraoperative fiducial localization that is robust to interference from tools, occlusions, and most distortions of the skin surface. Fiducial inked-letter labels provide an intuitive mapping between landmarks written on the breast and landmarks on an image-guided display to more easily orient the surgeon during surgical navigation. This approach is contactless, automatic, and localizes all fiducials simultaneously providing one snapshot of the breathing cycle. The surface acquisition process is amenable to surgical workflows with fiducials that can be hand-drawn, sterilized, and remain on the breast surface throughout surgery. This method opens opportunities to move breast guidance beyond initial single-shot rigid alignments and towards continuous correction allowing for automatic updates to an image guidance system. Going even further, by providing dense fiducial coverage with high fidelity and precision, this data can serve as input into a deformable correction method to improve the accuracy of breast tumor localization. The work presented here demonstrates clinical utility of computer vision for monitoring soft tissue in the surgical field.

Acknowledgements

This research was funded by NIH-NIBIB awards T32EB021937, R21EB022380, R01EB027498, and Vanderbilt Ingram Cancer Center Scholarship 3450804 Vanderbilt grant 1S10OD021771-01for the 3T MRI, housed in the Vanderbilt Center for Human Imaging.

CHAPTER 7

Future Directions

7.1 Guidance System Improvements

While the system is currently capable of measuring the intraoperative environment at patient bedside, there are several improvements that could extend and improve system utility.

7.1.1 Camera Integration into 3D Slicer

Currently there are separate interfaces for the guidance system and the stereo camera surface measurement approach. The guidance system is implemented in 3D Slicer, while the user interfaces for the stereo cameras are mainly in MATLAB and a custom graphical user interface (GUI) implemented in C++ [225]. Integrating stereo camera image collection and data processing within the 3D Slicer framework would streamline the user experience. Currently, processed images output fiducial files that can be auto-loaded into the guidance module, though camera streams are viewed in the custom GUI window, and images are processed in MATLAB. An integrated camera view within the 3D Slicer program would allow the user to check camera field-of-view, and display processed image output within the four panel display. Alternatively, additional panels could be added to stream stereo camera output. Also, a larger monitor could be added to the cart computer and a six panel display could show stereo camera views, model view, and the orthogonal slices of an MR image volume.

This section discusses three proposed solutions to improve stereo camera integration in the guidance system: (1) command line executable video capture and processing triggered from the 3D Slicer GUI, (2) an integrated Python scripted 3D Slicer module, and (3) an integrated C++ loadable 3D Slicer module.

An executable has been developed to collect camera data on-demand from the command line, but has yet to be tied to a GUI control in 3D Slicer. The MATLAB processing could be similarly called from the command line, and triggered by a GUI control in the guidance module. This framework would allow the module to control stereo camera data collection. Though the stereo camera images would not be streamed directly into the guidance display, the live-stream could be viewed in a separate window (similarly on-demand and called from the guidance module), or displayed directly in the 3D Slicer window by loading in saved images. Loading in saved images may result in slower update rates on real time video streaming. However, the custom GUI stereo image capture rate is about 5 frames per second, and Slicer scene updates streaming from PLUS have been achieved at 15-24 frames per second with data streams from Plus Toolkit. Therefore, delayed feedback may be inconsequential when considering the current hardware limitations and the minimal

in-module camera needs. An on-demand camera image viewer would allow the user to check camera field of view when needed, but otherwise would only provide the processed fiducial output. This approach maximizes utility with minimal implementation costs.

Beyond simple call-back functions in Slicer to trigger camera image collection and MATLAB fiducial processing, the image streaming and processing could be implemented directly in 3D Slicer by importing the appropriate libraries (OpenCV for image processing and FlyCapture to interface directly with the FLIR cameras) and translating the detection and tracking code base from MATLAB to Python. A variation of the stereo camera fiducial detection algorithm has already been implemented in Python with OpenCV using bounding circles instead of bounding boxes, demonstrating similar success in preliminary tests. However, MATLAB's calibration parameters would need to be converted into OpenCV formats in order to also perform triangulation within OpenCV. Conversion to OpenCV may also reduce tracking runtime by facilitating the use of a graphical processing unit (GPU) as well as the switch from KAZE feature matching [285] to AKAZE feature matching [263].

Beyond an integrated Python scripted module in 3D Slicer, a solution to maximize efficiency and minimize image processing time would integrate all functionalities in a C++ loadable 3D Slicer module. Since the stereo camera live video stream cannot be accessed simultaneously by two programs, all functionality would need to be converted to C++ in order to allow C++ live-stream processing in conjunction with live-stream viewing within Slicer.

7.1.2 Optically Tracked Calibration Checkerboard

In the system presented in this thesis, because fiducial positions were collected with the optically tracked stylus for validation, the fiducial positions could be used to define the transformation between optical tracker and camera spaces. Point based registration using 26 fiducials is limited, especially since fiducial positions carry inherent error due to user hand motion, subject breathing motion, and induced skin deformations from stylus contact with the soft tissue surface. Furthermore, the stereo camera fiducial measurements, now demonstrated to be a viable source of surface data, can replace stylus-designated fiducials. The transformation between instrument and camera spaces should then be otherwise defined. As an alternative to fiducial point-picking, this transformation can be defined during camera calibration by optically tracking the standard calibration checkerboard.

Going forward, a new checkerboard is proposed to automate registration between camera and optical tracker spaces. This new board, also a checkerboard with 6x8 18mm squares, was printed on matte paper and mounted on a rigid board. Four optically tracked passive marker spheres are fastened to the corners, so this board may be simultaneously tracked by the cameras (via the checkerboard), and also by the optical tracker

(via the spheres). A calibration setup like this was fabricated using a metal board, though the heavier weight of this board makes it more difficult to prop up securely at steeper imaging angles necessary for calibration. In the future, a wooden board with a checkerboard and optically tracked passive marker spheres could serve the same purpose at a lighter weight.

7.1.3 Inked Reference Markers

Data collected in the scene is generally measured in relation to the origin of the measuring device. For optically tracked data, the x, y, and z coordinates of a data point reflect the distance between the instrument tip and the origin of the optical tracker. Similarly, for data collected with the stereo cameras, the position of a data point reflects the distance between the point and the origin of the calibrated stereo camera space. In the cases described, the measurement device is considered the ”reference frame”. When the measurement device (e.g. optical tracker, or stereo cameras) is moved, the frame of reference is lost. In other words, a tissue data point that was collected in front of the camera 1 meter away, will still be displayed 1 meter away from the camera, but the tissue is now in a different location. Thus, re-digitization of data will not inherently align with previously designated locations. To avoid this problem of losing the frame of reference, a tracked reference object (hereafter referred to as a reference) is often used in image-guided procedures. Data is then collected with respect to the reference, instead of the measurement device. As long as the positional relationship between the the patient and the reference remains undisturbed, this allows devices to be repositioned ad-hoc with no affect on measurements or visualization.

In other image guidance applications, the reference is able to be mounted in a location that minimally interferes with surgical workflow. For example, in neurosurgery the reference is attached to the operating room table, and the patient’s head remains stationary with respect to that reference.

For breast surgery, the reference can be particularly valuable. A reference target on the sternum would serve two main purposes (1) as described above, to serve as a conventional reference to the patient if the system is moved during the procedure, but also (2) to keep ultrasound data aligned with surface data throughout breathing motion. If the reference can be mounted to the patient’s chest directly, then the effect of respiratory motion can be accounted for during data capture, and associated errors can be eliminated. The effects of breathing motion are reduced with stereo cameras (compared to stylus point designation) because fiducials are measured simultaneously from a single time-point image capture. Though surface data is captured at one time-point in the breathing cycle, ultrasound images measuring the chest wall location may be captured at different time points. Using a reference target attached to the sternum can help minimize respiratory motion error during chest wall measurements.

In the data collected for this thesis, an optically tracked stylus was taped to the sternum and data was saved

with respect to both the tracker and the reference. Unfortunately, the optically tracked reference interfered with data collection in many cases. The reference position was frequently disturbed, and often obstructed during data collection, while the measurement device positions were never altered. In the future, additional MR-visible fiducials can be placed on the sternum and inked with numbers or symbols. With fiducials inked directly on the skin surface, the risk of unintended reference motion is eliminated. It would be most convenient to place these fiducials in a line, though 3D space ambiguities arise when registering only co-linear points. Along with fiducials on the sternum, at least one reference fiducial should be placed more laterally, either below the infra-mammary fold on the rib cage, a few centimeters lateral to the sternum, or in a combination of these locations. Potential locations and symbols are shown in Figure 7.1a. It should be noted that while there are no theoretical limits to the number of fiducials able to be detected and tracked with the algorithm in Section 6.4, the bounds of this theory have not been experimentally tested. Additional fiducial points increase the computational burden of feature matching and may increase the possibility of mismatches.

Alternatively, reference fiducials could leverage another kind of label as in Figure 7.1b, with minor alterations to the detection approach. A long line connecting sternum fiducials, or infra-mammary fiducials could be detected with an alternate set of bounding box size limits, and a set number of red-pixel fiducial candidates could be detected. Compared to the symbol-based reference scheme, the linear-based reference scheme could reduce feature matching burden, and could also provide larger features to automatically orient the image or determine the region of interest. Since these surfaces are relatively flat (reducing depth distortion in 2D image space), and the fiducial locations should be fairly consistent with respect to their linear label, fiducials may be able to be matched based on simple 2D affine transformations to align the blue lines in the left and right images and obtain left-right correspondence for triangulation. Another consideration of the linear-based reference marker is that current fiducial detection uses an intensity threshold in the red color component. Since the red color component is normalized within each bounding box, this intensity threshold is relative to the local lighting variations. Larger bounding boxes would alter this normalization process, potentially degrading localization precision when lighting variations are large across the bounding box (as visible in Figure 7.1b). In order for the fiducial centroids to be perceived with the accuracy reported in Section 6.4, the larger bounding box may need to be divided into smaller windows, based on relative fiducial positions in the preoperative MR image. If reference fiducial matching did not rely on the keypoint cloud, this would keep the sternum points out of the main region of interest, reducing feature matching computational burden, and eliminating possible mismatches between letters and symbols.

One main limitation of tracking ultrasound data with respect to the reference is that the act of ultrasound imaging often obstructs the reference. With reference fiducials on the sternum, the ultrosonographer is constrained to avoid imaging angles where their arm or hand obstructs this area. A final consideration on this

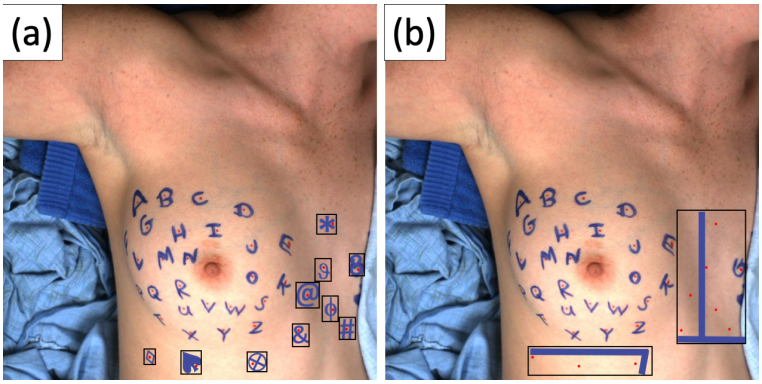

Figure 7.1: Possible locations for inked reference fiducials using the current symbol-based approach (a) and using a related line-based approach. Bounding boxes are overlaid for each type of reference fiducials.

topic is that reference fiducials should ideally be spread over a larger region to allow some reference fiducials to be obstructed at any given time, without interfering with data collection.

7.1.4 Optically Tracked Ultrasound Attachment

An ultrasound tracker attachment should be developed that can be sterilized for intraoperative use, detached and re-attached with no degradation in ultrasound calibration accuracy, and remain visible to the optical tracker when the transducer is perpendicular to the skin surface during ultrasound imaging.

The current attachment mechanism for fixing an optically tracked object to the ultrasound transducer uses semi-permanent glue that cannot be sterilized. Additionally, the current method has the optically tracked reference object fixed to the flat face of the transducer (i.e. parallel to the imaging plane). Unfortunately, during ultrasound imaging the transducer is often perpendicular to the optical tracker. Experimental use of the tracked ultrasound transducer revealed difficulties in collecting data with the current arrangement because the optimal probe angle for the optical tracker conflicts with the optimal probe angle for imaging.

For the laparoscopic transducer, other researchers in the laboratory have fabricated a custom device to reliably detach and re-attach an optical tracked reference object. The device showed reproducible accuracy after multiple detachment and re-attachment cycles, when calibrated with the tracked ultrasound calibration module presented in this thesis. A similar piece of hardware should be developed for the linear probe used for breast imaging.

7.2 Guidance System Extensions to Other Surgical Domains

The custom guidance software system presented in this thesis has been extended as a prototype navigation system for other surgical domains outside of breast specific uses. This framework is being extended for use in laparoscopic liver resection, and for neurosurgical tumor resection and deep brain stimulation. The

framework for automatically loading in patient data from a single directory, and displaying the data co-registered in a custom guidance display can be leveraged in both liver and brain surgery. All guidance modules built off the work in this thesis share a code base of functionalities that span the different surgical applications, though each has its own GUI and some unique application-specific functionalities.

An image guidance module for image guided liver surgery has been built upon the framework developed for this thesis. In this context, data collection with an optically tracked stylus has been modified and extended to incorporate in-module tool-tip calibration, surface swabbing, and real-time registration updates during data collection. The breast system's functionality for chest wall data collection with intraoperative ultrasound has been adapted and expanded for measurements of the posterior liver surface, blood vessels, and tumors. For blood vessels and tumors, in-module closed-surface segmentation ability has been incorporated (i.e. to represent closed objects instead of surfaces). Beyond these data collection extensions, novel visualization of registration error estimation has been implemented. Using the methods presented in [287], the uncertainty of nonrigid elastic registrations can be estimated based on the distribution of intraoperative data. This target error estimation is visualized within the liver guidance module, shown as a color map within the 3D organ model (Figure 7.2) [288]. This added functionality allows the surgeon to swab the organ with their tracked stylus and probe the navigational confidence in various regions of the organ.

The liver guidance system also integrates model-based deformation correction with the LIBR approach into the image-guidance user interface, allowing the user to run correction directly from the guidance module. The extension also enables comparison of corrected and uncorrected registrations, where the user is blinded to the current displayed registration approach for unbiased evaluation of perceived accuracy. In the future, liver-guidance functionalities for tumor segmentation in tracked ultrasound images and model-based correction should be incorporated into the breast module.

In the context of neurosurgery, the guidance framework here can also accept brain-specific data inputs for guidance during deep-brain stimulation and brain tumor resection. Several factors contribute to brain shift, or displacements between the brain position in preoperative imaging, and the brain presentation during surgery. These factors include changes in intracranial pressure, osmolarity, cerebral-spinal fluid levels and head orientation. Localization accuracy in neurosurgery is crucial, and sparse-data-driven model-correction frameworks can improve localization accuracy by correcting for these image-to-OR deformations. Tracked stylus measurements can serve as input into a deformation correction framework to account for brain shift [289, 290], and the data-loading and visualization aspects of the presented module can be used for intraoperative guidance. Additionally, the tracked ultrasound functionality presented here can be used to visualize brain anatomy using a burr-hole transducer for optimal electrode placement in deep brain stimulation. The module functionality could also be extended to track electrodes and display electrode information co-registered with

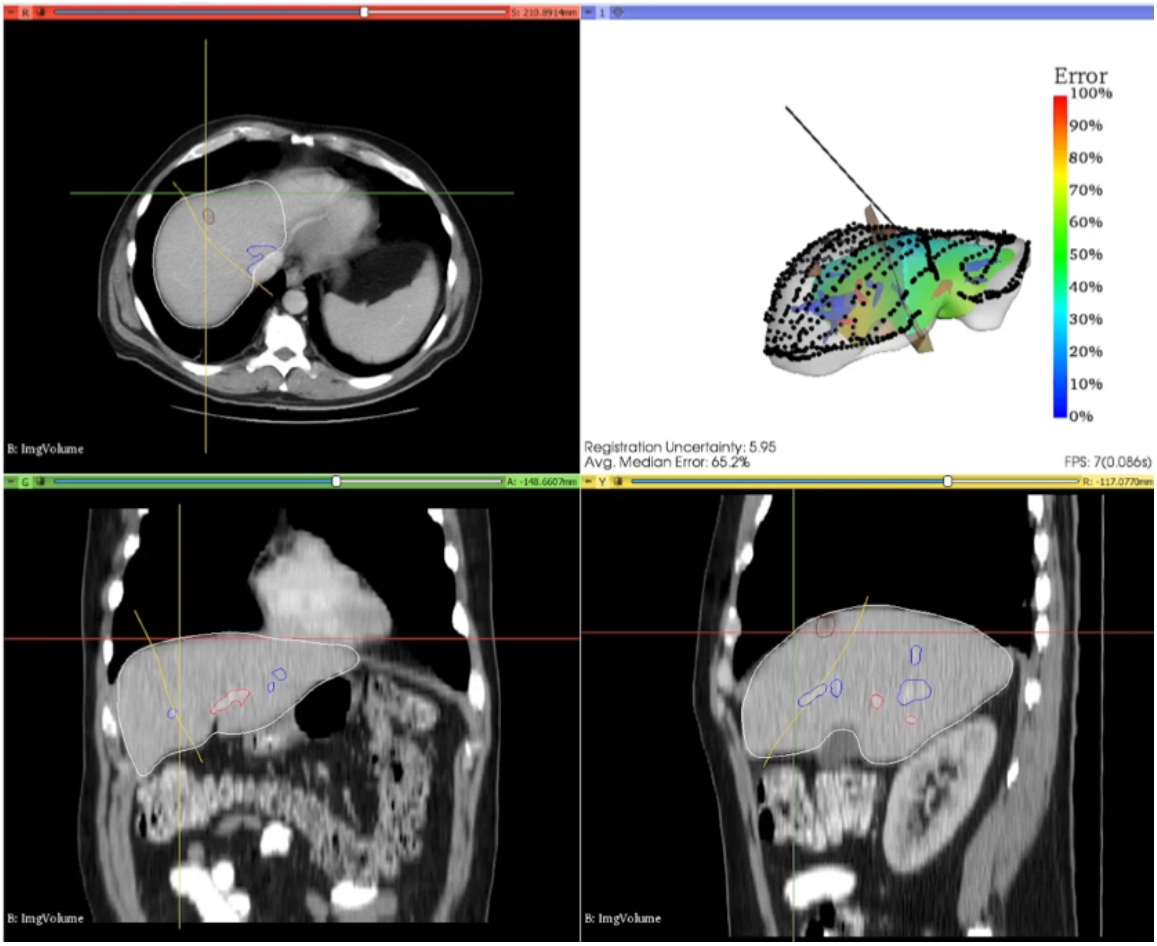

Figure 7.2: Image guidance module for liver resection, showing three cross-sections of an abdominal CT, with vessel segmentations shown in red and blue, and the planned resection plane in yellow. The stylus position is delineated with the cross hairs in the CT images, and with the black stylus model in the upper right 3D scene rendering. The 3D scene rendering shows the surface data collected with the tracked stylus, and the error estimation overlaid showing registration uncertainty.

intraoperative ultrasound images of necessary anatomy.

7.3 Further Characterizing Supine-to-Supine Deformations

Quantification of supine-to-supine deformations in Chapter 4 has also been extended to subsurface characterization. Image-to-image registration with advanced normalization tools (ANTs) framework [291] was performed to register arm adducted and arm abducted MR images [292] from the dataset of this thesis. The resulting deformation field was used to compute deformation metrics, quantifying the mechanical properties of the breast tissue. Comparing glandular and adipose tissues revealed a statistical difference in volume change between tissue types, indicating that the breast tissue is anisotropic in nature.

The analysis presented in Chapter 4 can also be extended to characterize subsurface deformations. With 18-26 subsurface points designated per subject in the MR images, a similar study to surface evaluations presented in Chapter 4 could be conducted on subsurface points. In conjunction with the ANTS informed deformation fields, point-wise displacements of the manually picked subsurface features could be measured and analyzed to report the directionality of subsurface displacement, as well as the relationship between surface and subsurface displacements. This quantification could serve to further inform modeling applications and elucidate the necessary penetrative depth of deformation modes.

Surface displacements from arm motion in the supine position could be further quantified beyond displacements at the marked fiducial centroids. In the camera videos of arm movement, corresponding features at keypoints on the letter-labels can be identified and used to describe surface rotations. Thoroughly describing local surface rotations around fiducial points could inform a framework for incorporating rotations into more complex model-based correction methods. This analysis would also provide a denser distribution of surface data, to help determine the fiducial density necessary to fully quantify non-rigid components of breast deformation.

7.4 Factors Influencing Model-Based Correction

In addition to the added model complexities covered in the discussion of Section 5.2 in Chapter 5, there are several future directions regarding the impact of integrating the modeling framework within context of the data-acquisition system presented.

7.4.1 Alternative Camera Positioning

As shown in Chapter 4, for image-to-surgical deformations, the largest displacements occur on the lateral side of the breast. Unfortunately, these lateral points can be some of the most difficult to capture with the stereo cameras mounted overhead. Placing the cameras in a more lateral, inferior position closer to the patient may

provide better sight lines for these lateral points without compromising the medial points.

For optical trackers with larger fields of view, an overhead view is rare. Commonly, trackers are placed beside the patient, angled toward the surgical site. The cameras may benefit from this angled placement; however, with the Polaris Vicra's more limited 3D field of view optical instrument tracking may become more difficult. Alternative camera positions may benefit from un-coupling the instrument tracker and stereo cameras, though such a re-design would also require reconsideration of the ideal orientation to maximize the overlapping volumes of the paired devices. Uncoupling the devices would also require additional fail-safes to ensure that camera and tool spaces remain correctly registered throughout the procedure. One simple change in this case would be to attach optically tracked fiducials to the sternum in conjunction with breast surface fiducials (as an alternative to the inked reference fiducials discussed in Section 7.1.3). Special consideration should be taken when combining inked reference fiducials with an alternative camera viewing angle, as sternum tracking is more likely to be obstructed from some angles.

7.4.2 Surface Extent

Camera-acquired intraoperative breast surface data will likely have smaller extents than those used in Chapter 5, especially for larger breasted patients. The camera data show that, when mounted overhead directly above the breast, fiducials on steeply curved surfaces may not be captured accurately. This is often due to line-of-sight constraints, but can also be caused by limitations of pixel-wise inaccuracies in fiducial localization. While strategic positioning of the stereo cameras can reduce line-of-sight constraints, steep curvature of the breast leaves inherent localization difficulties. At steep viewing angles, sub-pixel inaccuracies in 2D fiducial localization cause larger depth errors during triangulation. For better localization especially at steep viewing angles, more precise fiducial localization could be achieved with sub-pixel fiducial centroid estimation. This change may recover some lateral fiducials filtered out as errors in Section 6.4.

A benefit of the keypoint-matching approach presented in Section 6.4 is that it provides a sparse measurement of the skin surface in addition to the fiducial positions. However, this point cloud is considerably more sparse than the skin surface used for modeling deformations in Chapter 5. A sample KAZE keypoint cloud is shown in Figure 7.3. Resampling approaches, like that presented in [293] may be necessary to incorporate the keypoint surface cloud into a modeling framework, or alternative feature collection approach. To remove outlier points localized (e.g. keypoints along the surgical drapes), additional error filtering may need to be performed. Three such errors are visible on the left of Figure 7.3, noticeably beyond the breast model.

With respect to density of fiducials and surface points, data obtained from the camera images in the surgical position can be used to estimate realistic intraoperative data extent from an overhead camera angle. The sparse data used in Chapter 5 could be sub-sampled to replicate realistic line-of-sight constraints and algo-

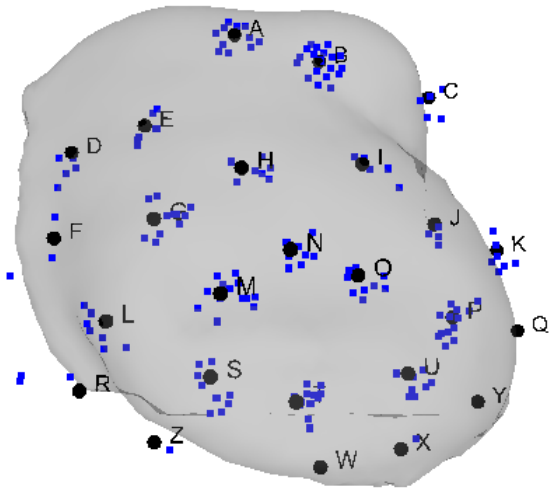

Figure 7.3: Breast model generated from preoperative supine MR with intraoperative data overlaid from the stereo cameras. The KAZE keypoint cloud in blue and fiducial locations are shown in black (automatic detection augmented with manual selection).

rithmic data-dropout, and evaluate these effects on model performance. Simulating various camera viewing angles in a 3D scene rendering of breast models and surface fiducials can also provide insights into optimal camera placement, and provide a theoretical upper bound for data extent.

If further analysis reveals that the cameras' line-of-sight constraints significantly impact the reported model accuracy, camera data could be augmented with a stylus point collection of fiducials outside the cameras field of view. If necessary, this would reduce automation, but would only require digitization of a few fiducials. These fiducials can also be collected with respect to a reference, limiting the need for repeated digitization, though the accuracy would degrade with nonrigid deformations after digitization since these points could not be continuously tracked.

7.4.3 Number of Fiducials

The number of fiducials necessary for nonrigid registration likely depends on the framework used for deformation correction, with a more accurate model potentially achieving clinically relevant accuracy while requiring less data. Investigating model performance as the number and placement of fiducials varies would inform the protocol for pre-operative fiducial placement. While for rigid registration, diminishing returns were observed for more than 11 fiducials, the ideal number of fiducials is likely different when considering a nonrigid registration approach. Similar to the analysis for rigid registration presented in Chapter 4, model-based registration can be evaluated with varying data distributions using all combinations of fiducials

comparing quadrantized and random subsampling schemes. The skin surface data can also be subsampled to still only include intra-fiducial surface points, using the subset of fiducials to constrain the surface data extent.

If more than 26 fiducials are found to be beneficial, further labeling schemes should be investigated to expand to symbols and potentially numbers. When expanding the set of labels, note that each label should be continuous. In other words, discontinuous labels (e.g."i" or "10") would not be sufficient for the current computer vision algorithm as the two segments would be boxed separately. It is possible that reusing letters with sufficient distance between them (e.g. top left and bottom right of a region of interest) may not confound matching, though this remains to be investigated. The number of fiducials necessary should be used to inform future algorithmic developments in stereo video processing. If less than 26 fiducials yielded similar model accuracy, then the protocol could be optimized to identify and include only the most distinct letters (e.g. "W" may be excluded as a label, since it is likely to be become discontinuous with partial obstructions or shadows).

7.4.4 Chest Wall Extent

Optimal chest wall data extent is a balance between minimizing the burden of intraoperative data collection and maximizing available data that improves the model's predictive accuracy. In Chapter 5, sparse chest wall data was used as input to the model with data distribution that mimics feasible intraoperative data collection. The chest wall measurements were based on 7-10 tracked ultrasound images in a mock intraoperative setting. Though, additional analysis in Section 5.2.5 revealed that excluding the chest wall data entirely had significant impact on the registration approach. This suggests that model accuracy should be evaluated with varied amounts of chest wall data. For stronger powered statistics, this analysis should include more subjects ideally with larger breast volumes.

In Chapter 5, intraoperative data provided to the model is assumed to directly map to a corresponding point within the preoperative data set. In other organ systems, such as the liver and brain, the tissue is a fixed volume. In the breast, certain boundaries are fixed and obvious across imaging domains (e.g. the skin and chest wall), and other boundaries are dictated by user discretion and the field of view in the preoperative imaging volume (e.g. inferior, superior, and lateral boundaries). These boundary ambiguities result in correspondence concerns when intraoperative data extents may extend beyond the data extent in preoperative imaging. In this thesis, intraoperative data is specifically collected with this limitation in mind to ensure correspondence. Surface data is constrained to the intra-fiducial surface, and ultrasound data is sampled near the center of the organ, to ensure that intraoperative measurements are within the breast volume designated in the preoperative images. In the case of an extensive chest wall sampling, the algorithm would need to be

altered in order to correctly determine correspondence. One simple approach to address this is to project the intra-fiducial skin surface onto the underlying collected chest wall surface and use this projection to crop the extent.

7.5 Workflow Considerations

As discussed in Chapter 6, Section 6.4.5 , the tracking algorithm is affected by parameter variability and fiducial inking protocol, though these effects remain to be more thoroughly explored. Based on the experiences here, future data collection should ink letters with uniform sizing and thick lines ($\geq 4mm$).

Increasing the range of allowable bounding boxes at the initialization stage increases completeness but simultaneously can increase the rate of false positives. In Section 6.4, wide regions of interest were set to include the full range of motion, and a wide range of bounding box sizes were considered viable candidates in order to accommodate the variable letter sizes. In this thesis, the true size of letters ranged from about 2-4 cm, and size differences in the 2D image were exacerbated by letters' position (depth) with respect to the cameras. Inking letter labels thick lines and uniform sizing may improve results.

Another consideration is that skin markings the same color as ink should be covered with a third colored ink (not black). In the first case presented in Section 6.4, black ink was used to cover red skin markings. Unfortunately, depending on lighting variations and underlying skin tone black ink can have a high value in the red color component. Even with this coloring scenario causing 2 additional false positives (out of 5 total) in case 1L, false positives were still rare occurring in only 1.7% of static frames. Across all frames for case 1L as shown in Figure 6.14, false positives occur in 8% of frames, and this coloring causes 66% of these false positives. While perhaps algorithmic improvements could be made to filter out black ink, future data collection should cover the skin markings with a third colored ink (e.g. green), or include the marking as the fiducial dot or part of the label (note that label resemblance to English characters currently does not affect performance).

7.5.1 Alternative Ink Colors

Red-inked fiducials, as presented in this thesis, are limited to only provide guidance before the initial incision. Once blood enters the surgical scene, red fiducial localization will be compromised. Though the presented approach leverages color channels, ink colors are not limited to the conventional RGB color channels. By converting pixel intensities into hue saturation value space, pixel intensity positions can be rotated to align any ink color (hue) with a desired color channel. Then, the pixel intensities with distorted hue values can be converted back to a three color channel space, so that one color channel represents the letter ink color, and another color channel represents the fiducial ink color. Alternatively, by choosing colors on opposite sides

of the color wheel, a single color channel can simultaneously represent the color component for both the letter-labels and the fiducial centers. Initial investigations into this approach have demonstrated success, but remain to be fully explored. This color alignment technique can be evaluated first in the human data for blue and red ink colors; aligning the letter-ink color with the maximum value in the blue color component (i.e. true blue, or [0 0 1] in RGB space) may also be beneficial even for blue and red ink color combinations to maximize feature visibility in the respective color component images. Beyond this, color combinations that avoid red (e.g. purple labels and green fiducials) should be investigated to verify feasibility after blood enters the scene.

7.6 Alternative Labeling Schemes

Alternative approaches to the tracking algorithm presented in Section 6.4 may leverage machine learning for bounding box detection and tracking or custom optical character recognition for correspondence and labeling. While machine learning approaches could prove valuable with an abundance of data, they may be limited by a small mock-intraoperative dataset. A system such as the one presented in this thesis could be deployed in surgery and used for guidance while simultaneously collecting a representative dataset for future investigations into machine learning approaches. The approach presented herein is generalizable and largely predictable – both valuable attributes for system use during surgery.

It should be noted here that improvements to various aspects of the algorithm may also potentially introduce new pitfalls. The current approach is most limited not by fiducial detection but by matching, both left-to-right and frame-to-frame. As seen in Figure 6.13B, all fiducial labels are detected and their fiducial candidates are correctly identified. However, due to the sparsity of the point cloud around letter “E”, this point cannot be localized. This trend is common: fiducials can be correctly identified in 2D, but are unsuccessfully matched due to the sparsity of the point cloud made from KAZE keypoints. This effect is also visible in Figure 7.3, where they keypoint cloud does not extend to include all the fiducials that could be manually localized in the camera images. This keypoint cloud extent is responsible for the difference between manually localized points in that state, and automatically localized points in that state (visible as the gap between the magenta dotted lines and the black lines in Figure 6.14, note that Figure 6.14 corresponds to Figure 7.3). The difference in view angles between the left and right images causes large differences in letter presentation—especially at the edges of the breast—reducing the number of matched keypoints. A feature matching algorithm – perhaps a custom feature descriptor – that provided more matches in these areas could provide more points overall. However, it also must be considered that these edges – particularly edges that fall on steeply curved surfaces (i.e. the lateral edge of the breast), are also the most susceptible to mislocalization. These points are much more likely to have fiducial centers out of view, even if part of the letter

label is visible. Beyond that, even when a fiducial is visible, triangulating the 3D fiducial location becomes increasingly challenging as the curvature steepens, with single pixel inaccuracies resulting in increasingly large depth reconstruction errors. Therefore, an algorithm that produced a more extensive point cloud may also result in decreased localization accuracy or higher rates of false positives. Likely, sub-pixel centroid estimation and additional error filtering steps would need to be considered.

7.6.1 Custom Feature Descriptors

A custom feature descriptor, in lieu of KAZE, may be able to provide more matched points in the keypoint cloud. The algorithm presented here detects features in the blue color component image, but color information is lost in the conversion to grayscale. In other domains, researchers have incorporated color information to improve upon conventional feature detection approaches [294]. A custom feature descriptor could be centered on the fiducial point, and incorporate color information, or an encoded representation of the nearby letter geometry. A custom feature descriptor may benefit from using nonlinear difusion, like KAZE. Smoothing the image using nonlinear diffusion that preserves high contrast feature edges while minimizing noise gives KAZE an edge over other feature detectors that use Gaussian smoothing (such as classic feature detection algorithms ORB [295], SIFT [296] and SURF [297]). However, since letter-labels are relatively uniform sizes, perhaps a more limited scale space could be explored to reduce processing time.

7.6.2 Optical Character Recognition

Another area for potential algorithm development is leveraging a custom network for optical character recognition (OCR). The work in Section 6.3 could be expanded by training a neural network on handwriting samples from the freely available NIST [298] or CEDAR [299] data sets as well as skin fiducial letters identified in camera images. Bounding boxes around skin fiducials can be quickly processed into binary images of the handwritten inked letters as shown in Figure 7.4, and a neural network could be trained to classify these images providing left-right correspondence and labeling at once. A preliminary version of an OCR method, such as the one presented in Section 6.3, could also be used to improve initialization in the first frame, reducing user-input by only requiring manual labels for low confidence fiducial labels.

Although the crude implementation of OCR correspondence in Section 6.3 is outperformed by the tracking algorithm in Section 6.4, more sophisticated implementations that tune a recognition network on this dataset of inked-letter fiducials would be a more realistic test of the feasibility of OCR. The large databases of handwriting data represent many of the challenging factors. Future work may investigate if an OCR approach can navigate the large letter distortions due to motion, camera viewing angles, and hand-writing degradation on this soft-tissue surface.

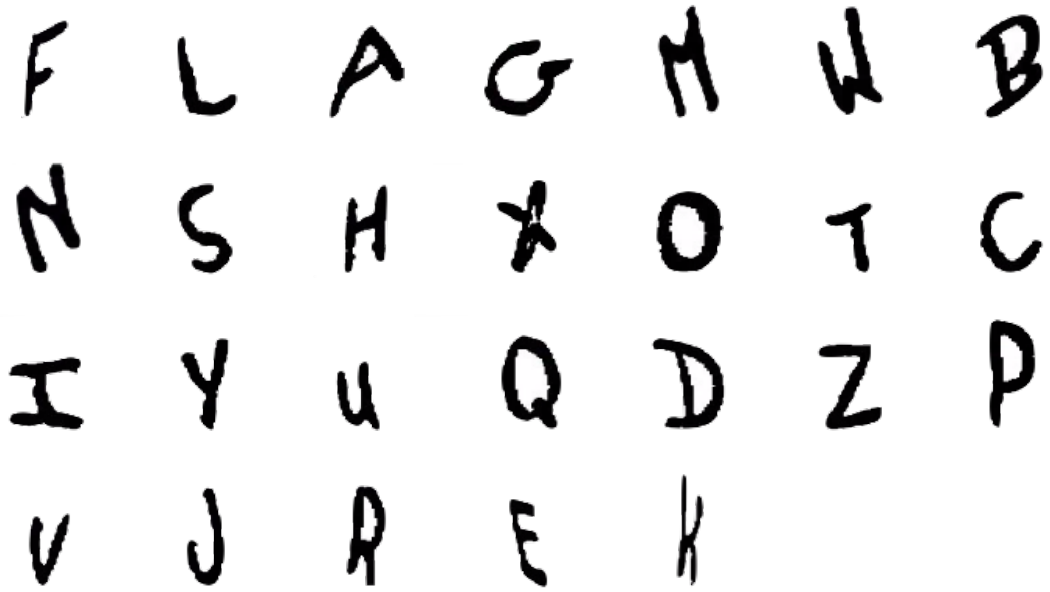

Figure 7.4: Binary masks of letters processed from human skin; sample input for an optical character recognition correspondence approach.

While only two different hand-writings were used in Section 6.4, since the algorithm relies on letter labels for features only – and not for optical character recognition – it is unaffected by inter-user handwriting differences. For a more realistic data set, additional hand-writings should be collected for inked letters on soft tissue surfaces. Furthermore, such an algorithm may benefit from protocol guidelines for the font of handwritten letters. In this thesis, letters were inked with a font type that yielded the best performance with the OCR approach in MATLAB's Computer Vision Tool Box [228], in limited testing on a white paper background. Though the thickness and size of letters varied, the font was consistent across all cases. As OCR capabilities and toolkits continue to improve, this option becomes increasingly realistic and straightforward to implement.

7.7 A Comprehensive Breast Guidance System

7.7.1 Utility in Radiology

Outside of the operating room, the system as proposed could be paired with a tracked needle for improved breast cancer localization in radiology for biopsy and preoperative localization procedures. In this context, the deformations between imaging and the procedure could potentially also be minimized, as the arm may be able to be placed in the same orientation as the imaging. As demonstrated in Chapter 4, residual registration error, though still present, would be minimized if the imaging arm-configuration is maintained for the procedure.

In this context, model accuracy in the same arm position could be evaluated with a study similar to the evaluation in Chapter 5, but with repeat imaging in the same arm configuration with the subject leaving the scanner and standing in between consecutive scans. Since deformations would be considerably smaller, localization accuracy would likely be improved.

Currently, preoperative biopsies and localization device placements are performed using real-time planar imaging while the patient is awake. These painful procedures are prolonged by uncertainty during navigation. Use of the system during device placement could reduce the time needed for device placement and improve patient experience. For surgical localization, the system could also be deployed outside the constraints of the dynamic operating room environment. The system could provide guidance for inserting a tracked dye-injection-needle to mark lesion boundaries, depositing dye within the tissue. Guided injections could be performed on all sides of the tumor to provide localization information during surgery.

7.7.2 Utility in Surgery

The system should be evaluated in the surgical context for which it was designed. To probe the perceived value of the guidance module, a surgeon perception study may be conducted on breast cancer patients in an OR setting before surgery with echoic lesions.

Experiment workflow could be similar to the data collection for this thesis, with preoperative imaging and data processing. Then in a intraoperative evaluation at the start of surgery, the system can be used to collect the sparse-intraoperative data to drive model correction. The model-corrected tumor position can be displayed via the 4-panel display with a tracked stylus and ultrasound transducer. Similar to the evaluation in [60], the model-predicted tumor location can be compared to the lesion location as measured on compression correction ultrasound images using the approach presented by Pheiffer *et al.* in [236].

Stereo camera video can be recorded during the entire procedure, to evaluate tracking performance in the true surgical environment. After the resection but before the incision is closed, the incision location should be measured with a tracked stylus and then all tools should be removed from the scene to obtain stereo-camera measurements of breast surface including the incision. This would allow further development into incision-mapping via computer vision. Future work on modeling resection could incorporate these incision measurements into a real-time framework for dynamic guidance throughout surgery. This data can also be used to predict the lesion position within the resected volume (i.e. predict margin width). These margin predictions can be compared to the measured margins in post-operative specimen evaluation in imaging and pathology.

7.8 Closing Remarks

This dissertation presents a robust, accurate image guidance system with a novel, automatic data collection framework compatible with surgical workflows. This system offers improved accuracy to localize breast tumor boundaries in the operating room and fundamentally shift BCS towards more precise tumor excision and lower reoperation rates.

Appendix A

Camera Calibration Protocol

A standardized protocol for calibration image collection was developed and used throughout this thesis. This protocol was optimized empirically for two GRAS-20S4C-C Grasshopper cameras (FLIR, formerly Point Grey Research, Richmond, BC, Canada) with FUJINON 1:1.4/16mm HFI6HA-1B lenses, spaced with a baseline of approximately 240 mm. Specific calibration protocols are not often reported as accuracy depends on many factors. While the development of this protocol took considerable trial and error, after its development, the calibration process was observed to be robust and reproducible, taking no more than a few minutes. While this protocol is dependent on the specific use case presented here, it is described for completeness in reporting methods as well as to serve as a starting point that may be tailored to another user's specific needs. Here, there is assumed to be no tangential distortion, meaning that the camera sensor is parallel to the lens, and there is assumed to be no skew, meaning that the image axes are exactly perpendicular.

A.1 Calibration Checkerboard

An 18mm 6x8 checkerboard was printed on standard 8.5 x 11 inch white printer paper. The whitespace surrounding the board was cropped, leaving a border of whitespace approximately 10 mm wide, and the checkerboard was mounted to a piece of 3 mm thick cardboard using a thin even layer of Elmer's glue. Several checkerboard sizes were tested and 18 mm performed best for reconstructing a point cloud of the phantom breast surface at distances of 0.75–1.5 meters from the cameras to the phantom.

A.2 Camera Set-up

Camera setup is prompted through a MATLAB script to ensure consistency.

- The lens aperture is opened fully to maximize light allowed to the sensor.
- Disparity is set to be approximately 10–20 mm at the height of the scene. Disparity between the two camera views is minimized to improve automatic feature matching, however it is important that the left camera's field of view is truly to the left of the right camera's field of view. In other words, be sure that the cameras' principal axes cross beyond the scene.
- The focal plane is set to the approximate height of the nipple.

A.3 Calibration Images

Images were collected using the software interface developed in [225]. Due to small delays between left and right image capture, it is very important that all images are taken with the checkerboard stationary. The checkerboard should never be held or touched while collecting images; holding the checkerboard can increase the reprojection error by 2–3 times.

Images for calibration are collected in 3 stages: flat, shallow angles, and steep angles. Four images are captured in each stage. Because the breast is generally highest in the center of the scene, in this calibration protocol, when the board is angled the raised section of the board is always towards the middle of the field of view and the lowered section of the board is always closer to the edges of the field of view. First, the checkerboard is imaged approximately flat at the far extent of the camera field of view. The board is imaged in each of the four corners, roughly square with the image corners. Second, one end of the board is raised up approximately 5 cm. For these shallow angled images, the board is positioned diagonally, with one short edge near the center of the field of view, and the other short edge pointed toward the corner of the image. This process is repeated, pointing the short edge at each of the four corners. Lastly, for the steep angles, the board is again square with the image. One short end of the board is raised 10 cm. An example set of these 12 calibration images is shown in Figure A.3.

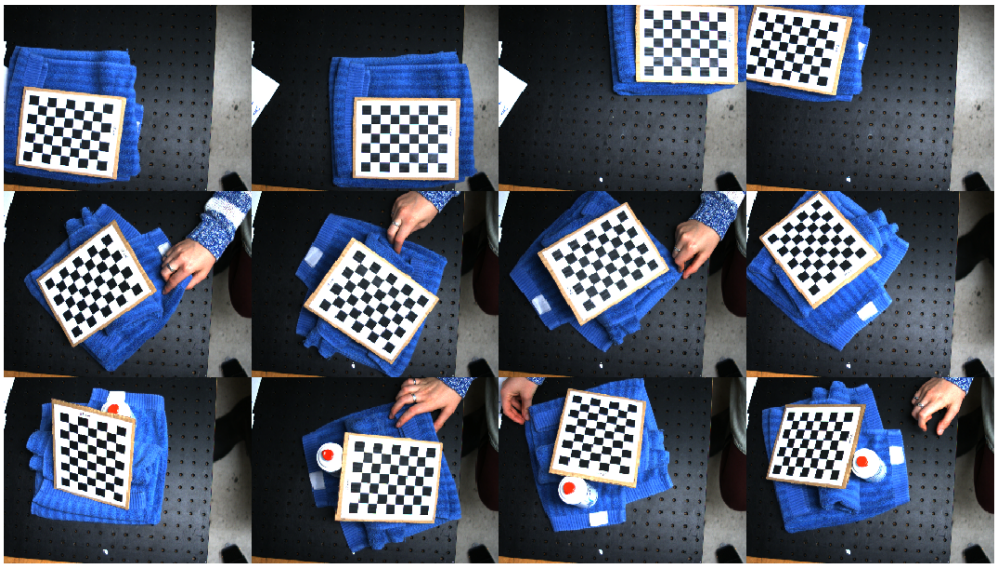

Figure A.1: Calibration images of the 18 mm checkerboard from one of the two stereo cameras.

A.4 Estimation of Theoretical Depth Error

Given the baseline (b) of the stereo camera, an anticipated distance (z) to the scene, and the focal length of the cameras (f) in pixels, depth error (ε_z) can be estimated from the equation presented in [300]

$$\varepsilon_z = \frac{z^2}{b \cdot f} \cdot \varepsilon_D \tag{A.1}$$

with a disparity error (ε_D).

Throughout experiments, reprojection error after calibration is on the order of 0.2–0.4 pixels, though disparity error is also impacted by an algorithm's ability to identify correctly corresponding pixels within each fiducial centroid. Here, several estimates for disparity error are used, as the true value is unknown. Human data was collected with the scene approximately 1.3 meters from the camera, though 750–1500 mm distances are reasonable for an overhead view in an operating room. The baseline between the cameras is approximately 240 mm. Using equation, Equation A.1, a theoretical limit for the stereo camera accuracy can be computed at varying depths and for various estimations of disparity error.

Table A.1: Depth error estimation (in mm) computed with Equation A.1 with varying disparity error and distance to scene.

Depth Error Estimation ε_z (mm)				
		Disparity Error ε_D (pixels)		
		0.3	0.5	1.0
Distance to Scene z (mm)	750	0.19	0.31	0.62
	1300	0.56	0.94	1.87
	1500	0.75	1.25	2.49

References

[1] Rebecca L Siegel, Kimberly D Miller, Hannah E Fuchs, and Ahmedin Jemal. Cancer statistics, 2022. *CA: a cancer journal for clinicians*, 2022. ISSN 0007-9235.

[2] Mehra Golshan, Constance T Cirrincione, William M Sikov, Donald A Berry, Sara Jasinski, Tracey F Weisberg, George Somlo, Clifford Hudis, Eric Winer, and David W Ollila. Impact of neoadjuvant chemotherapy in stage ii–iii triple negative breast cancer on eligibility for breast-conserving surgery and breast conservation rates: surgical results from calgb 40603 (alliance). *Annals of surgery*, 262(3): 434, 2015.

[3] Edward Guadagnoli, Jane C Weeks, Charles L Shapiro, Jerry H Gurwitz, Catherine Borbas, and Stephen B Soumerai. Use of breast-conserving surgery for treatment of stage i and stage ii breast cancer. *Journal of Clinical Oncology*, 16(1):101–106, 1998. ISSN 0732-183X.

[4] Bernard Fisher, Stewart Anderson, John Bryant, Richard G Margolese, Melvin Deutsch, Edwin R Fisher, Jong-Hyeon Jeong, and Norman Wolmark. Twenty-year follow-up of a randomized trial comparing total mastectomy, lumpectomy, and lumpectomy plus irradiation for the treatment of invasive breast cancer. *New England Journal of Medicine*, 347(16):1233–1241, 2002. ISSN 0028-4793.

[5] Bernard Fisher, Jong-Hyeon Jeong, Stewart Anderson, John Bryant, Edwin R Fisher, and Norman Wolmark. Twenty-five-year follow-up of a randomized trial comparing radical mastectomy, total mastectomy, and total mastectomy followed by irradiation. *New England Journal of Medicine*, 347(8): 567–575, 2002. ISSN 0028-4793.

[6] Kathrin Thöne, Anja Rudolph, Nadia Obi, Jenny Chang-Claude, and Dieter Flesch-Janys. Prognostic impact of surgery for early-stage invasive breast cancer on breast cancer-specific survival, overall survival, and recurrence risk: a population-based analysis. *Breast cancer research and treatment*, pages 1–10, 2018. ISSN 0167-6806.

[7] Jose Vila, Sara Gandini, and Oreste Gentilini. Overall survival according to type of surgery in young (leq 40 years) early breast cancer patients: a systematic meta-analysis comparing breast-conserving surgery versus mastectomy. *The Breast*, 24(3):175–181, 2015. ISSN 0960-9776.

[8] Shailesh Agarwal, Lisa Pappas, Leigh Neumayer, Kristine Kokeny, and Jayant Agarwal. Effect of breast conservation therapy vs mastectomy on disease-specific survival for early-stage breast cancer. *JAMA surgery*, 149(3):267–274, 2014. ISSN 2168-6254.

[9] Sanjay P Bagaria, Nabil Wasif, Bhupendra Rawal, Sarah A McLaughlin, and Armando E Giuliano. Is mastectomy undertreatment for low-risk breast cancers eligible for breast-conserving therapy? *Cancer*, 121(16):2705–2712, 2015. ISSN 1097-0142.

[10] Mahmoud B El-Tamer, B Marie Ward, Tracy Schifftner, Leigh Neumayer, Shukri Khuri, and William Henderson. Morbidity and mortality following breast cancer surgery in women: national benchmarks for standards of care. *Annals of surgery*, 245(5):665, 2007.

[11] Erica Wrubel, Raylene Natwick, and G Paul Wright. Breast-conserving therapy is associated with improved survival compared with mastectomy for early-stage breast cancer: A propensity score matched comparison using the national cancer database. *Annals of Surgical Oncology*, pages 1–6, 2020. ISSN 1534-4681.

[12] D. L. Eck, S. L. Koonce, R. F. Goldberg, S. Bagaria, T. Gibson, S. P. Bowers, and S. A. McLaughlin. Breast surgery outcomes as quality measures according to the nsqip database. *Ann Surg Oncol*, 19(10): 3212–7, 2012. ISSN 1534-4681 (Electronic) 1068-9265 (Linking). doi: 10.1245/s10434-012-2529-6. URL https://www.ncbi.nlm.nih.gov/pubmed/22829006.

[13] M Luke Marinovich, Naomi Noguchi, Monica Morrow, and Nehmat Houssami. Changes in reoperation after publication of consensus guidelines on margins for breast-conserving surgery: a systematic review and meta-analysis. *JAMA surgery*, 155(10):e203025–e203025, 2020. ISSN 2168-6254.

[14] Liska Havel, Himani Naik, Luis Ramirez, Monica Morrow, and Jeffrey Landercasper. Impact of the sso-astro margin guideline on rates of re-excision after lumpectomy for breast cancer: a meta-analysis. *Annals of surgical oncology*, 26(5):1238–1244, 2019. ISSN 1534-4681.

[15] Katerina Kaczmarski, Peiqi Wang, Richard Gilmore, Heidi N Overton, David M Euhus, Lisa K Jacobs, Mehran Habibi, Melissa Camp, Matthew J Weiss, and Martin A Makary. Surgeon re-excision rates after breast-conserving surgery: a measure of low-value care. *Journal of the American College of Surgeons*, 228(4):504–512. e2, 2019. ISSN 1072-7515.

[16] Susan G Brouwer de Koning, Marie-Jeanne TFD Vrancken Peeters, Katarzyna Jóźwiak, Patrick A Bhairosing, and Theo JM Ruers. Tumor resection margin definitions in breast-conserving surgery: systematic review and meta-analysis of the current literature. *Clinical breast cancer*, 18(4):e595–e600, 2018. ISSN 1526-8209.

[17] 3rd Cody, H. S. and K. J. Van Zee. Reexcision–the other breast cancer epidemic. *N Engl J Med*, 373 (6):568–9, 2015. ISSN 1533-4406 (Electronic) 0028-4793 (Linking). doi: 10.1056/NEJMe1507190. URL https://www.ncbi.nlm.nih.gov/pubmed/26244311.

[18] M. A. Mallory, Y. Sagara, F. Aydogan, S. DeSantis, J. Jayender, D. Caragacianu, E. Gombos, K. G. Vosburgh, F. A. Jolesz, and M. Golshan. Feasibility of intraoperative breast mri and the role of prone versus supine positioning in surgical planning for breast-conserving surgery. *Breast J*, 23(6):713–717, 2017. ISSN 1524-4741 (Electronic) 1075-122X (Linking). doi: 10.1111/tbj.12796. URL https://www.ncbi.nlm.nih.gov/pubmed/28295903.

[19] Eva C Gombos, Jagadeesan Jayender, Danielle M Richman, Diana L Caragacianu, Melissa A Mallory, Ferenc A Jolesz, and Mehra Golshan. Intraoperative supine breast mr imaging to quantify tumor deformation and detection of residual breast cancer: preliminary results. *Radiology*, 281(3):720–729, 2016. ISSN 0033-8419.

[20] Isabel T. Rubio, Antonio Esgueva-Colmenarejo, Martin Espinosa-Bravo, Juan Pablo Salazar, Ignacio Miranda, and Vicente Peg. Intraoperative ultrasound-guided lumpectomy versus mammographic wire localization for breast cancer patients after neoadjuvant treatment. *Annals of Surgical Oncology*, 23 (1):38–43, 2016. ISSN 1534-4681. doi: 10.1245/s10434-015-4935-z. URL https://doi.org/10.1245/s10434-015-4935-z.

[21] J. H. Volders, M. H. Haloua, N. M. A. Krekel, V. L. Negenborn, R. H. E. Kolk, Amfl Cardozo, A. M. Bosch, L. M. de Widt-Levert, H. van der Veen, H. Rijna, Ahmt van Amerongen, K. Jozwiak, S. Meijer, and M. P. van den Tol. Intraoperative ultrasound guidance in breast-conserving surgery shows superiority in oncological outcome, long-term cosmetic and patient-reported outcomes: Final outcomes of a randomized controlled trial (cobalt). *Ejso*, 43(4):649–657, 2017. ISSN 0748-7983. doi: 10.1016/j.ejso.2016.11.004. URL ⟨GotoISI⟩://WOS:000399853900006.

[22] Hasan Karanlik, Ilker Ozgur, Dilek Sahin, Merdan Fayda, Semen Onder, and Ekrem Yavuz. Intraoperative ultrasound reduces the need for re-excision in breast-conserving surgery. *World journal of surgical oncology*, 13(1):321, 2015. ISSN 1477-7819.

[23] Holm Eggemann, Tanja Ignatov, Serban Dan Costa, and Atanas Ignatov. Accuracy of ultrasound-guided breast-conserving surgery in the determination of adequate surgical margins. *Breast cancer research and treatment*, 145(1):129–136, 2014. ISSN 0167-6806.

[24] G. K. Cakmak, A. U. Emre, B. Bahadir, O. Tascilar, and S. Ozkan. Surgeon performed continuous intraoperative ultrasound guidance decreases re-excisions and mastectomy rates in breast cancer. *Breast*, 33:23–28, 2017. ISSN 0960-9776. doi: 10.1016/j.breast.2017.02.014. URL ⟨GotoISI⟩://WOS:000402210800004.

[25] M. W. Barentsz, T. van Dalen, P. D. Gobardhan, V. Bongers, C. I. Perre, R. M. Pijnappel, Maaj van den Bosch, and H. M. Verkooijen. Intraoperative ultrasound guidance for excision of non-palpable invasive breast cancer: a hospital-based series and an overview of the literature. *Breast Cancer Research and Treatment*, 135(1):209–219, 2012. ISSN 0167-6806. doi: 10.1007/s10549-012-2165-7. URL ⟨GotoISI⟩://WOS:000307333700020.

[26] V Suzanne Klimberg. Advances in the diagnosis and excision of breast cancer. *The American Surgeon*, 69(1):11, 2003. ISSN 0003-1348.

[27] J. Tseng, A. Kyrillos, E. Liederbach, G. G. Spear, J. Ecanow, C. H. Wang, T. Czechura, O. Kantor, M. Miller, D. J. Winchester, C. E. Pesce, S. Rabbitt, and K. Yao. Clinical accuracy of preoperative breast mri for breast cancer. *J Surg Oncol*, 115(8):924–931, 2017. ISSN 1096-9098 (Electronic) 0022-4790 (Linking). doi: 10.1002/jso.24616. URL https://www.ncbi.nlm.nih.gov/pubmed/28409837.

[28] Jon S Heiselman, William R Jarnagin, and Michael I Miga. Intraoperative correction of liver deformation using sparse surface and vascular features via linearized iterative boundary reconstruction. *IEEE Transactions on Medical Imaging*, 2020. ISSN 0278-0062.

[29] Hyuna Sung, Jacques Ferlay, Rebecca L Siegel, Mathieu Laversanne, Isabelle Soerjomataram, Ahmedin Jemal, and Freddie Bray. Global cancer statistics 2020: Globocan estimates of incidence and mortality worldwide for 36 cancers in 185 countries. *CA: a cancer journal for clinicians*, 71(3): 209–249, 2021. ISSN 0007-9235.

[30] S Hofvind, Â Holen, T Aas, M Roman, S Sebuødegård, and LA Akslen. Women treated with breast conserving surgery do better than those with mastectomy independent of detection mode, prognostic and predictive tumor characteristics. *European Journal of Surgical Oncology*, 41(10):1417–1422, 2015. ISSN 0748-7983.

[31] E Shelley Hwang, Daphne Y Lichtensztajn, Scarlett Lin Gomez, Barbara Fowble, and Christina A Clarke. Survival after lumpectomy and mastectomy for early stage invasive breast cancer. *Cancer*, 119(7):1402–1411, 2013. ISSN 1097-0142.

[32] André Hennigs, Valerie Fuchs, Hans-Peter Sinn, Fabian Riedel, Geraldine Rauch, Katharina Smetanay, Michael Golatta, Christoph Domschke, Florian Schuetz, and Andreas Schneeweiss. Do patients after reexcision due to involved or close margins have the same risk of local recurrence as those after one-step breast-conserving surgery? *Annals of surgical oncology*, 23(6):1831–1837, 2016. ISSN 1068-9265.

[33] Alicia A Heelan Gladden, Sharon Sams, Ana Gleisner, Christina Finlayson, Nicole Kounalakis, Patrick Hosokawa, Regina Brown, Tae Chong, David Mathes, and Colleen Murphy. Re-excision rates after breast conserving surgery following the 2014 sso-astro guidelines. *The American Journal of Surgery*, 214(6):1104–1109, 2017. ISSN 0002-9610.

[34] L Hughes, J Hamm, C McGahan, and C Baliski. Surgeon volume, patient age, and tumor-related factors influence the need for re-excision after breast-conserving surgery. *Annals of surgical oncology*, 23(5):656–664, 2016. ISSN 1068-9265.

[35] Linnea Langhans, Maj-Britt Jensen, Maj-Lis M Talman, Ilse Vejborg, Niels Kroman, and Tove F Tvedskov. Reoperation rates in ductal carcinoma in situ vs invasive breast cancer after wire-guided breast-conserving surgery. *JAMA surgery*, 152(4):378–384, 2017. ISSN 2168-6254.

[36] Marina T van Leeuwen, Michael O Falster, Claire M Vajdic, Philip J Crowe, Sanja Lujic, Elizabeth Klaes, Louisa Jorm, and Art Sedrakyan. Reoperation after breast-conserving surgery for cancer in australia: statewide cohort study of linked hospital data. *BMJ open*, 8(4):e020858, 2018. ISSN 2044-6055.

[37] Adam M Zysk, Kai Chen, Edward Gabrielson, Lorraine Tafra, Evelyn A May Gonzalez, Joseph K Canner, Eric B Schneider, Andrew J Cittadine, P Scott Carney, and Stephen A Boppart. Intraoperative

assessment of final margins with a handheld optical imaging probe during breast-conserving surgery may reduce the reoperation rate: Results of a multicenter study. *Annals of surgical oncology*, 22(10): 3356–3362, 2015. ISSN 1068-9265.

[38] N. M. Krekel, A. M. Lopes Cardozo, S. Muller, E. Bergers, S. Meijer, and M. P. van den Tol. Optimising surgical accuracy in palpable breast cancer with intra-operative breast ultrasound–feasibility and surgeons' learning curve. *Eur J Surg Oncol*, 37(12):1044–50, 2011. ISSN 1532-2157 (Electronic) 0748-7983 (Linking). doi: 10.1016/j.ejso.2011.08.127. URL https://www.ncbi.nlm.nih.gov/pubmed/21924854.

[39] N. Colakovic, D. Zdravkovic, Z. Skuric, D. Mrda, J. Gacic, and N. Ivanovic. Intraoperative ultrasound in breast cancer surgery-from localization of non-palpable tumors to objectively measurable excision. *World Journal of Surgical Oncology*, 16:7, 2018. ISSN 1477-7819. doi: 10.1186/s12957-018-1488-1. URL ⟨GotoISI⟩://WOS:000444642400001.

[40] D. Arko, N. C. Sikosek, N. Kozar, M. Sobocan, and I. Takac. The value of ultrasound-guided surgery for breast cancer. *European Journal of Obstetrics & Gynecology and Reproductive Biology*, 216:198–203, 2017. ISSN 0301-2115. doi: 10.1016/j.ejogrb.2017.07.034. URL ⟨GotoISI⟩://WOS:000411771700032.

[41] M. J. Pallone, S. P. Poplack, H. B. Avutu, K. D. Paulsen, and Jr. Barth, R. J. Supine breast mri and 3d optical scanning: a novel approach to improve tumor localization for breast conserving surgery. *Ann Surg Oncol*, 21(7):2203–8, 2014. ISSN 1534-4681 (Electronic) 1068-9265 (Linking). doi: 10.1245/s10434-014-3598-5. URL https://www.ncbi.nlm.nih.gov/pubmed/24619494.

[42] Luca Alessandro Carbonaro, Penampai Tannaphai, Rubina Manuela Trimboli, Nicola Verardi, Maria Paola Fedeli, and Francesco Sardanelli. Contrast enhanced breast mri: spatial displacement from prone to supine patient's position. preliminary results. *European journal of radiology*, 81(6): e771–e774, 2012. ISSN 0720-048X.

[43] Hiroko Satake, Satoko Ishigaki, Mariko Kitano, and Shinji Naganawa. Prediction of prone-to-supine tumor displacement in the breast using patient position change: investigation with prone mri and supine ct. *Breast Cancer*, 23(1):149–158, 2016. ISSN 1340-6868.

[44] MARIBS Study Group. Screening with magnetic resonance imaging and mammography of a uk population at high familial risk of breast cancer: a prospective multicentre cohort study (maribs). *The Lancet*, 365(9473):1769–1778, 2005. ISSN 0140-6736.

[45] Ritse M Mann, Christiane K Kuhl, and Linda Moy. Contrast-enhanced mri for breast cancer screening. *Journal of Magnetic Resonance Imaging*, 50(2):377–390, 2019. ISSN 1053-1807.

[46] S. Joukainen, A. Masarwah, M. Könönen, M. Husso, A. Sutela, V. Kärjä, R. Vanninen, and M. Sudah. Feasibility of mapping breast cancer with supine breast mri in patients scheduled for oncoplastic surgery. *European Radiology*, 2018. ISSN 1432-1084. doi: 10.1007/s00330-018-5681-y. URL https://doi.org/10.1007/s00330-018-5681-y.

[47] P. Siegler, C. M. Holloway, P. Causer, G. Thevathasan, and D. B. Plewes. Supine breast mri. *J Magn Reson Imaging*, 34(5):1212–7, 2011. ISSN 1522-2586 (Electronic) 1053-1807 (Linking). doi: 10.1002/jmri.22605. URL https://www.ncbi.nlm.nih.gov/pubmed/21928381.

[48] A. P. del Palomar, B. Calvo, J. Herrero, J. Lopez, and M. Doblare. A finite element model to accurately predict real deformations of the breast. *Medical Engineering & Physics*, 30(9):1089–1097, 2008. ISSN 1350-4533. doi: 10.1016/j.medengphy.2008.01.005. URL ⟨GotoISI⟩://WOS:000261746200001.

[49] Anna Mîra, Ann-Katherine Carton, Serge Muller, and Yohan Payan. A biomechanical breast model evaluated with respect to mri data collected in three different positions. *Clinical Biomechanics*, 60: 191–199, 2018. ISSN 0268-0033.

[50] Richard J Barth, Venkataramanan Krishnaswamy, Keith D Paulsen, Timothy B Rooney, Wendy A Wells, Christina V Angeles, Rebecca A Zuurbier, Kari Rosenkranz, Steven Poplack, and Tor D Tosteson. A randomized prospective trial of supine mri-guided versus wire-localized lumpectomy for breast cancer. *Annals of surgical oncology*, pages 1–10, 2019. ISSN 1068-9265.

[51] Robert Martí, Caroline ME Rubin, Erika Denton, and Reyer Zwiggelaar. *Mammographic X-ray and MR correspondence*, pages 527–529. Springer, 2003.

[52] Christian P Behrenbruch, Kostas Marias, Margaret Yam, and J Michael Brady. The use of magnetic resonance imaging to model breast compression in x-ray mammography for mr/x-ray data fusion. In *5th International Workshop on Digital Mammography*. Citeseer, 2000.

[53] Matthew D Barber, Jeremy Thomas, and Michael Dixon. *Breast cancer: an atlas of investigation and management*. Clinical Publishing, 2008.

[54] Terese Winslow. Breast cancer treatment during pregnancy (pdq®)–health professional version, 2011. URL https://www.cancer.gov/types/breast/hp/pregnancy-breast-treatment-pdq. Accessed: March 26, 2022.

[55] Alan Hoofring. Mammogram: Image details, 2003. URL https://visualsonline.cancer.gov/details.cfm?imageid=4361. Accessed: April 6, 2022, public domain.

[56] Breast mri, 2022. URL https://www.mayoclinic.org/tests-procedures/breast-mri/multimedia/breast-mri/img-20007363. Accessed: April 6, 2022.

[57] Private breast ultrasound scan, 2022. URL https://sonoworld.co.uk/women-scans/private-breast-ultrasound. Accessed: April 6, 2022.

[58] J K Fuller and J R Fuller. *Surgical technology: principles and practice*. Elsevier Health Sciences, 1986.

[59] H. Khatam, G. P. Reece, M. C. Fingeret, M. K. Markey, and K. Ravi-Chandar. In-vivo quantification of human breast deformation associated with the position change from supine to upright. *Medical Engineering & Physics*, 37(1):13–22, 2015. ISSN 1350-4533. doi: 10.1016/j.medengphy.2014.09.016. URL ⟨GotoISI⟩://WOS:000349585100003.

[60] R. H. Conley, I. M. Meszoely, J. A. Weis, T. S. Pheiffer, L. R. Arlinghaus, T. E. Yankeelov, and M. I. Miga. Realization of a biomechanical model-assisted image guidance system for breast cancer surgery using supine mri. *International Journal of Computer Assisted Radiology and Surgery*, 10 (12):1985–1996, 2015. ISSN 1861-6410. doi: 10.1007/s11548-015-1235-9. URL ⟨GotoISI⟩://WOS:000365087100009.

[61] Doris Leithner, Linda Moy, Elizabeth A Morris, Maria A Marino, Thomas H Helbich, and Katja Pinker. Abbreviated mri of the breast: does it provide value? *Journal of Magnetic Resonance Imaging*, 49(7):e85–e100, 2019. ISSN 1053-1807.

[62] T. Alderliesten, C. Loo, A. Paape, S. Muller, E. Rutgers, M. J. Peeters, and K. Gilhuijs. On the feasibility of mri-guided navigation to demarcate breast cancer for breast-conserving surgery. *Medical Physics*, 37(6):2617–26, 2010. ISSN 0094-2405 (Print) 0094-2405 (Linking). doi: 10.1118/1.3429048. URL https://www.ncbi.nlm.nih.gov/pubmed/20632573.

[63] Alfonso Fausto, Annarita Fanizzi, Luca Volterrani, Francesco Giuseppe Mazzei, Claudio Calabrese, Donato Casella, Marco Marcasciano, Raffaella Massafra, Daniele La Forgia, and Maria Antonietta Mazzei. Feasibility, image quality and clinical evaluation of contrast-enhanced breast mri performed in a supine position compared to the standard prone position. *Cancers*, 12(9):2364, 2020.

[64] Brook K Byrd, Venkataramanan Krishnaswamy, Jiang Gui, Timothy Rooney, Rebecca Zuurbier, Kari Rosenkranz, Keith Paulsen, and Richard J Barth. The shape of breast cancer. *Breast Cancer Research and Treatment*, pages 1–8, 2020. ISSN 1573-7217.

[65] Josip Fajdic, Drazen Djurovic, Nikola Gotovac, and Zlatko Hrgovic. Criteria and procedures for breast conserving surgery. *Acta Informatica Medica*, 21(1):16, 2013.

[66] F Cardoso, S Kyriakides, S Ohno, F Penault-Llorca, P Poortmans, IT Rubio, S Zackrisson, and E Senkus. Early breast cancer: Esmo clinical practice guidelines for diagnosis, treatment and follow-up. *Annals of Oncology*, 30(8):1194–1220, 2019. ISSN 0923-7534.

[67] Nehmat Houssami, Petra Macaskill, M Luke Marinovich, J Michael Dixon, Les Irwig, Meagan E Brennan, and Lawrence J Solin. Meta-analysis of the impact of surgical margins on local recurrence in women with early-stage invasive breast cancer treated with breast-conserving therapy. *European Journal of Cancer*, 46(18):3219–3232, 2010. ISSN 0959-8049.

[68] Meena S Moran, Stuart J Schnitt, Armando E Giuliano, Jay R Harris, Seema A Khan, Janet Horton, Suzanne Klimberg, Mariana Chavez-MacGregor, Gary Freedman, and Nehmat Houssami. Society of surgical oncology–american society for radiation oncology consensus guideline on margins for breast-conserving surgery with whole-breast irradiation in stages i and ii invasive breast cancer. *International Journal of Radiation Oncology• Biology• Physics*, 88(3):553–564, 2014. ISSN 0360-3016.

[69] Monica Morrow, Kimberly J Van Zee, Lawrence J Solin, Nehmat Houssami, Mariana Chavez-MacGregor, Jay R Harris, Janet Horton, Shelley Hwang, Peggy L Johnson, and M Luke Marinovich. Society of surgical oncology–american society for radiation oncology–american society of clinical oncology consensus guideline on margins for breast-conserving surgery with whole-breast irradiation in ductal carcinoma in situ. *Annals of surgical oncology*, 23(12):3801–3810, 2016. ISSN 1068-9265.

[70] Anne Kuritzky, Chantal Reyna, Kandace P McGuire, Weihong Sun, Sara M DeSnyder, Staci Aubry, Apoorve Nayyar, Paula Strassle, Kelly K Hunt, and Jun-Min Zhou. Evaluation of 2014 margin guidelines on re-excision and recurrence rates after breast conserving surgery: A multi-institution retrospective study. *The Breast*, 51:29–33, 2020. ISSN 0960-9776.

[71] Amanda M Schulman, Jennifer A Mirrielees, Glen Leverson, Jeffrey Landercasper, Caprice Greenberg, and Lee G Wilke. Reexcision surgery for breast cancer: an analysis of the american society of breast surgeons (asbrs) mastery sm database following the sso-astro "no ink on tumor" guidelines. *Annals of surgical oncology*, 24(1):52–58, 2017. ISSN 1068-9265.

[72] Monica Morrow, Paul Abrahamse, Timothy P Hofer, Kevin C Ward, Ann S Hamilton, Allison W Kurian, Steven J Katz, and Reshma Jagsi. Trends in reoperation after initial lumpectomy for breast cancer: addressing overtreatment in surgical management. *JAMA oncology*, 3(10):1352–1357, 2017. ISSN 2374-2437.

[73] Alex Monaghan, Núria Chapinal, Lauren Hughes, and Christopher Baliski. Impact of sso-astro margin guidelines on reoperation rates following breast-conserving surgery. *The American Journal of Surgery*, 217(5):862–867, 2019. ISSN 0002-9610.

[74] Andrea L Merrill, Suzanne B Coopey, Rong Tang, Maureen P McEvoy, Michele C Specht, Kevin S Hughes, Michelle A Gadd, and Barbara L Smith. Implications of new lumpectomy margin guidelines for breast-conserving surgery: changes in reexcision rates and predicted rates of residual tumor. *Annals of surgical oncology*, 23(3):729–734, 2016. ISSN 1068-9265.

[75] TP Olson, J Harter, A Munoz, DM Mahvi, and TM Breslin. Frozen section analysis for intraoperative margin assessment during breast-conserving surgery results in low rates of re-excision and local recurrence. *Annals of Surgical Oncology*, 14(10):2953, 2007. ISSN 1068-9265.

[76] K Motomura, H Inaji, Y Komoike, T Kasugai, S Nagumo, S Noguchi, and H Koyama. Intraoperative sentinel lymph node examination by imprint cytology and frozen sectioning during breast surgery. *British journal of surgery*, 87(5):597–601, 2000.

[77] PJ Van Diest, H Torrenga, PJ Borgstein, R Pijpers, RP Bleichrodt, FD Rahusen, and S Meijer. Reliability of intraoperative frozen section and imprint cytological investigation of sentinel lymph nodes in breast cancer. *Histopathology*, 35(1):14–18, 1999.

[78] CH Lee and D Carter. Detecting residual tumor after excisional biopsy of impalpable breast carcinoma: efficacy of comparing preoperative mammograms with radiographs of the biopsy specimen. *AJR. American journal of roentgenology*, 164(1):81–86, 1995.

[79] Fabio Corsi, Luca Sorrentino, Matteo Bonzini, Daniela Bossi, Marta Truffi, Rosella Amadori, Manuela Nebuloni, Barbara Brillat, and Serena Mazzucchelli. Cavity shaving reduces involved margins and reinterventions without increasing costs in breast-conserving surgery: a propensity score-matched study. *Annals of surgical oncology*, 24(6):1516–1524, 2017.

[80] F. Schnabel, S. K. Boolbol, M. Gittleman, T. Karni, L. Tafra, S. Feldman, A. Police, N. B. Friedman, S. Karlan, D. Holmes, S. C. Willey, M. Carmon, K. Fernandez, S. Akbari, J. Harness, L. Guerra, T. Frazier, K. Lane, R. M. Simmons, A. Estabrook, and T. Allweis. A randomized prospective study of lumpectomy margin assessment with use of marginprobe in patients with nonpalpable breast malignancies. *Annals of Surgical Oncology*, 21(5):1589–1595, 2014. ISSN 1068-9265. doi: 10.1245/s10434-014-3602-0. URL ⟨GotoISI⟩://WOS:000334224900031.

[81] Marc Thill, Christine Dittmer, Kristin Baumann, Kay Friedrichs, and Jens-Uwe Blohmer. Marginprobe® –final results of the german post-market study in breast conserving surgery of ductal carcinoma in situ. *The Breast*, 23(1):94–96, 2014. ISSN 0960-9776.

[82] A. R. Triki, M. B. Blaschko, Y. M. Jung, S. Song, H. J. Han, S. I. Kim, and C. Joo. Intraoperative margin assessment of human breast tissue in optical coherence tomography images using deep neural networks. *Computerized Medical Imaging and Graphics*, 69:21–32, 2018. ISSN 0895-6111. doi: 10.1016/j.compmedimag.2018.06.002. URL ⟨GotoISI⟩://WOS:000447578800003.

[83] Katheryne E Wilson, Sunitha V Bachawal, Lotfi Abou-Elkacem, Kristen Jensen, Steven Machtaler, Lu Tian, and Jürgen K Willmann. Spectroscopic photoacoustic molecular imaging of breast cancer using a b7-h3-targeted icg contrast agent. *Theranostics*, 7(6):1463, 2017.

[84] B. L. Smith, M. A. Gadd, C. R. Lanahan, U. Rai, R. Tang, T. Rice-Stitt, A. L. Merrill, D. B. Strasfeld, J. M. Ferrer, E. F. Brachtel, and M. C. Specht. Real-time, intraoperative detection of residual breast cancer in lumpectomy cavity walls using a novel cathepsin-activated fluorescent imaging system. *Breast Cancer Research and Treatment*, 171(2):413–420, 2018. ISSN 0167-6806. doi: 10.1007/s10549-018-4845-4. URL ⟨GotoISI⟩://WOS:000440766500016.

[85] Hans C Burkholder, Laura E Witherspoon, R Phillip Burns, Jeffrey S Horn, and Michael D Biderman. Breast surgery techniques: preoperative bracketing wire localization by surgeons. *The American surgeon*, 73(6):574–579, 2007. ISSN 0003-1348.

[86] TY Chu, CY Lui, WK Hung, SK Kei, CL Choi, and HS Lam. Localisation of occult breast lesion: a comparative analysis of hookwire and radioguided procedures. *Hong Kong Med J*, 16(5):367–72, 2010.

[87] E. L. Postma, H. M. Verkooijen, S. van Esser, M. G. Hobbelink, G. P. van der Schelling, R. Koelemij, A. J. Witkamp, C. Contant, P. J. van Diest, S. M. Willems, Ihmb Rinkes, Maaj van den Bosch, W. P. Mali, R. van Hillegersberg, and Roll Study Grp. Efficacy of 'radioguided occult lesion localisation' (roll) versus 'wire-guided localisation' (wgl) in breast conserving surgery for non-palpable breast cancer: a randomised controlled multicentre trial. *Breast Cancer Research and Treatment*, 136 (2):469–478, 2012. ISSN 0167-6806. doi: 10.1007/s10549-012-2225-z. URL ⟨GotoISI⟩://WOS: 000310378700014.

[88] JD Luiten, MA Beek, AC Voogd, PD Gobardhan, and EJT Luiten. Iodine seed-versus wire-guided localization in breast-conserving surgery for non-palpable ductal carcinoma in situ. *British Journal of Surgery*, 102(13):1665–1669, 2015. ISSN 0007-1323.

[89] B. A. In 't Hout, K. E. Schenk, A. N. van der Linden, and R. M. Roumen. Efficacy of localization of non-palpable, invasive breast cancer: Wire localization vs. iodine-125 seed: A historical comparison. *Breast*, 29:8–13, 2016. ISSN 0960-9776. doi: 10.1016/j.breast.2016.06.011.

[90] L. Langhans, T. F. Tvedskov, T. L. Klausen, M. B. Jensen, M. L. Talman, I. Vejborg, C. Benian, A. Roslind, J. Hermansen, P. S. Oturai, N. Bentzon, and N. Kroman. Radioactive seed localization or wire-guided localization of nonpalpable invasive and in situ breast cancer a randomized, multicenter, open-label trial. *Annals of Surgery*, 266(1):29–35, 2017. ISSN 0003-4932. doi: 10.1097/sla.0000000000002101. URL ⟨GotoISI⟩://WOS:000402885700022.

[91] Carla IJM Theunissen, Esther AZ Rust, Mireille A Edens, Caroline Bandel, Piet L Jager, Eva M Noorda, and Anne Brecht Francken. Radioactive seed localization is the preferred technique in nonpalpable breast cancer compared with wire-guided localization and radioguided occult lesion localization. *Nuclear medicine communications*, 38(5):396–401, 2017. ISSN 0143-3636.

[92] Vi Thuy Tran, Julie David, Erica Patocskai, Mathieu Zummo-Soucy, Rami Younan, Lucie Lalonde, Maude Labelle, Mona El Khoury, André Robidoux, and Isabelle Trop. Comparative evaluation of iodine-125 radioactive seed localization and wire localization for resection of breast lesions. *Canadian Association of Radiologists Journal*, 68(4):447–455, 2017. ISSN 0846-5371.

[93] Sejal N Patel, Victoria L Mango, Priya Jadeja, Lauren Friedlander, Elise Desperito, Ralph Wynn, Sheldon Feldman, and Richard Ha. Reflector-guided breast tumor localization versus wire localization for lumpectomies: A comparison of surgical outcomes. *Clinical imaging*, 47:14–17, 2018. ISSN 0899-7071.

[94] Lacey Stelle, Taylor Schoenheit, Allison Brubaker, Xiwei Tang, Peiyong Qu, Kimberly Cradock, and Anna Higham. Radioactive seed localization versus wire localization for nonpalpable breast lesions: A two-year initial experience at a large community hospital. *Annals of surgical oncology*, 25(1):131–136, 2018. ISSN 1068-9265.

[95] Konstantinos Zacharioudakis, Sue Down, Zaheerah Bholah, Sum Lee, Taherah Khan, Anthony J Maxwell, Miles Howe, and James Harvey. Is the future magnetic? magseed localisation for non palpable breast cancer. a multi-centre non randomised control study. *European Journal of Surgical Oncology*, 45(11):2016–2021, 2019. ISSN 0748-7983.

[96] Xin Hu, Si Li, Yi Jiang, Wei Wei, Yinan Ji, Qiuyun Li, and Zongbin Jiang. Intraoperative ultrasound-guided lumpectomy versus wire-guided excision for nonpalpable breast cancer. *Journal of International Medical Research*, 48(1):0300060519896707, 2020.

[97] Sarianna Joukainen, Hidemi Okuma, Outi Kaarela, Elina Laaksonen, Vesa Kärjä, Ritva Vanninen, Amro Masarwah, and Mazen Sudah. Can supine breast magnetic resonance imaging help hit the target in extreme oncoplastic surgery? *European Journal of Surgical Oncology*, 2021.

[98] L. J. McGhan, S. C. McKeever, B. A. Pockaj, N. Wasif, M. E. Giurescu, H. A. Walton, and R. J. Gray. Radioactive seed localization for nonpalpable breast lesions: Review of 1,000 consecutive procedures at a single institution. *Annals of Surgical Oncology*, 18(11):3096–3101, 2011. ISSN 1068-9265. doi: 10.1245/s10434-011-1910-1. URL ⟨GotoISI⟩://WOS:000295844200013.

[99] Janice S Sung, Valencia King, Cynthia M Thornton, Jennifer D Brooks, Charles W Fry, Mahmoud El-Tamer, Lawrence T Dauer, Edi Brogi, Jean M St Germain, and Elizabeth A Morris. Safety and efficacy of radioactive seed localization with i-125 prior to lumpectomy and/or excisional biopsy. *European journal of radiology*, 82(9):1453–1457, 2013. ISSN 0720-048X.

[100] M. E. M. van der Noordaa, K. E. Pengel, E. Groen, E. van Werkhoven, E. J. T. Rutgers, C. E. Loo, W. Vogel, and Mjtfdv Peeters. The use of radioactive iodine-125 seed localization in patients with non-palpable breast cancer: A comparison with the radioguided occult lesion localization with 99m technetium. *Ejso*, 41(4):553–558, 2015. ISSN 0748-7983. doi: 10.1016/j.ejso.2015.01.022. URL ⟨GotoISI⟩://WOS:000353097700019.

[101] S. E. Nolano, L. O. Thalhiemer, E. Yu, E. Grujic, W. B. Carter, and T. G. Frazier. A comparison of the micro-impulse radar savi scout to the radioactive i125 seed in localization of non-palpable breast cancer for breast conserving therapy. *Cancer Research*, 77:2, 2017. ISSN 0008-5472. doi: 10.1158/1538-7445.Sabcs16-p3-13-10. URL ⟨GotoISI⟩://WOS:000397999001222.

[102] Cristine S Velazco, Nabil Wasif, Barbara A Pockaj, and Richard J Gray. Radioactive seed localization for breast conservation surgery: Low positive margin rate with no learning curve. *The American Journal of Surgery*, 214(6):1091–1093, 2017. ISSN 0002-9610.

[103] C. E. Cox, N. Garcia-Henriquez, M. J. Glancy, P. Whitworth, J. M. Cox, M. Themar-Geck, R. Prati, M. Jung, S. Russell, K. Appleton, J. King, and S. C. Shivers. Pilot study of a new nonradioactive surgical guidance technology for locating nonpalpable breast lesions. *Ann Surg Oncol*, 23(6):1824–30, 2016. ISSN 1534-4681 (Electronic) 1068-9265 (Linking). doi: 10.1245/s10434-015-5079-x. URL https://www.ncbi.nlm.nih.gov/pubmed/26847680.

[104] Charles E Cox, Scott Russell, Vanessa Prowler, Ebonie Carter, Abby Beard, Ankur Mehindru, Peter Blumencranz, Kathleen Allen, Michael Portillo, and Pat Whitworth. A prospective, single arm, multi-site, clinical evaluation of a nonradioactive surgical guidance technology for the location of nonpalpable breast lesions during excision. *Annals of surgical oncology*, 23(10):3168–3174, 2016. ISSN 1068-9265.

[105] P. H. Jadeja, V. Mango, S. Patel, L. Friedlander, E. Desperito, E. Ayala-Bustamante, R. Wynn, M. Chen-Seetoo, B. Taback, S. Feldman, and R. Ha. Utilization of multiple savi scout surgical guidance system reflectors in the same breast: A single-institution feasibility study. *Breast Journal*, 24(4):531–534, 2018. ISSN 1075-122X. doi: 10.1111/tbj.12979. URL ⟨GotoISI⟩://WOS:000438372800012.

[106] Elissa R Price, Amal L Khoury, Laura J Esserman, Bonnie N Joe, and Michael D Alvarado. Initial clinical experience with an inducible magnetic seed system for preoperative breast lesion localization. *American Journal of Roentgenology*, 210(4):913–917, 2018. ISSN 0361-803X.

[107] Judith Reid, Sian Tovey, EJ Campbell, Sujata Pareek, Jacqueline Kelly, Penny Law, Jon Coldeway, Evaristo Mumba, and Suzanne Elgammal. 29. the magseed® experience: One year on. *European Journal of Surgical Oncology*, 45(5):884, 2019. ISSN 0748-7983.

[108] D Thekkinkattil, M Kaushik, MM Hoosein, M Al-Attar, S Pilgrim, A Gvaramadze, L Hyklova, and A Jibril. A prospective, single-arm, multicentre clinical evaluation of a new localisation technique using non-radioactive magseeds for surgery of clinically occult breast lesions. *Clinical Radiology*, 74 (12):974. e7–974. e11, 2019. ISSN 0009-9260.

[109] Adam D Gerrard and Anu Shrotri. Surgeon-led intraoperative ultrasound localization for nonpalpable breast cancers: Results of 5 years of practice. *Clinical Breast Cancer*, 19(6):e748–e752, 2019.

[110] Gabrielle Gauvin, Caitlin T Yeo, Tamas Ungi, Shaila Merchant, Andras Lasso, Doris Jabs, Thomas Vaughan, John F Rudan, Ross Walker, and Gabor Fichtinger. Real-time electromagnetic navigation for breast-conserving surgery using naviknife technology: A matched case-control study. *The breast journal*, 2019. ISSN 1075-122X.

[111] M. J. Homer. Transection of the localization hooked wire during breast biopsy. *American Journal of Roentgenology*, 141(5):929–930, 1983. ISSN 0361-803X. doi: 10.2214/ajr.141.5.929. URL ⟨GotoISI⟩://WOS:A1983RM63600012.

[112] J. S. Montrey, J. A. Levy, and R. J. Brenner. Wire fragments after needle localization. *American Journal of Roentgenology*, 167(5):1267–1269, 1996. ISSN 0361-803X. doi: 10.2214/ajr.167.5.8911193. URL ⟨GotoISI⟩://WOS:A1996VR32900040.

[113] P. S. Davis, R. J. Wechsler, S. A. Feig, and D. E. March. Migration of breast biopsy localization wire. *American Journal of Roentgenology*, 150(4):787–788, 1988. ISSN 0361-803X. doi: 10.2214/ajr.150.4.787. URL ⟨GotoISI⟩://WOS:A1988M591500013.

[114] R. Grassi, S. Romano, M. Massimo, M. Maglione, B. Cusati, and M. Violini. Unusual migration in abdomen of a wire for surgical localization of breast lesions. *Acta Radiologica*, 45(3):254–258, 2004. ISSN 0284-1851. doi: 10.1080/02841850410003085. URL ⟨GotoISI⟩://WOS:000221554500003.

[115] H. Banitalebi and P. Skaane. Migration of the breast biopsy localization wire to the pulmonary hilus. *Acta Radiologica*, 46(1):28–31, 2005. ISSN 0284-1851. doi: 10.1080/02841850510015956. URL ⟨GotoISI⟩://WOS:000227276400005.

[116] James W Jakub, Richard J Gray, Amy C Degnim, Judy C Boughey, Mary Gardner, and Charles E Cox. Current status of radioactive seed for localization of non palpable breast lesions. *The American Journal of Surgery*, 199(4):522–528, 2010. ISSN 0002-9610.

[117] M. Sheetz and C. Steiner. Compliance with the us nuclear regulatory commission revised licensing guidance for radioactive seed localization. *Health Physics*, 115(3):402–408, 2018. ISSN 0017-9078. URL ⟨GotoISI⟩://WOS:000440867700015.

[118] Joseph S Tingen, Brian P McKinley, John M Rinkliff, Wendy R Cornett, and Claiborne Lucas. Savi scout radar localization versus wire localization for breast biopsy regarding positive margin, complication, and reoperation rates. *The American Surgeon*, 86(8):1029–1031, 2020. ISSN 0003-1348.

[119] Iham Kasem and Kefah Mokbel. Savi scout® radar localisation of non-palpable breast lesions: Systematic review and pooled analysis of 842 cases. *Anticancer Research*, 40(7):3633–3643, 2020. ISSN 0250-7005.

[120] Megan Kalambo and Jay R Parikh. Implementing the savi scout system in community radiology practice. *Journal of the American College of Radiology*, 14(9):1234–1238, 2017. ISSN 1546-1440.

[121] Scout radar localization "how it works", 2022. URL https://www.merit.com/merit-oncology/localization/breast-soft-tissue-localization/scout-radar-localization/. Accessed: March 25, 2022.

[122] B Schermers, Jos A van der Hage, CE Loo, MTFD Vrancken Peeters, HAO Winter-Warnars, F van Duijnhoven, B Ten Haken, SH Muller, and TJM Ruers. Feasibility of magnetic marker localisation for non-palpable breast cancer. *The Breast*, 33:50–56, 2017. ISSN 0960-9776.

[123] Bridget N Kelly, Alexandra J Webster, Leslie Lamb, Tara Spivey, Jenna E Korotkin, Anthony Henriquez, Michele A Gadd, Kevin S Hughes, Constance R Lehman, and Barbara L Smith. Magnetic seeds: An alternative to wire localization for non-palpable breast lesions. *Clinical Breast Cancer*, 2022. ISSN 1526-8209.

[124] Megan E Miller, Nirav Patil, Pamela Li, Mary Freyvogel, Ian Greenwalt, Lisa Rock, Ashley Simpson, Mary Teresczuk, Stephanie Carlisle, and Maria Peñuela. Hospital system adoption of magnetic seeds for wireless breast and lymph node localization. *Annals of Surgical Oncology*, 28(6):3223–3229, 2021. ISSN 1534-4681.

[125] Edward Murphy, Edel Quinn, Maurice Stokes, Malcom Kell, Mitchel Barry, Fidelma Flanagan, and Siun M Walsh. Initial experience of magnetic seed localization for impalpable breast lesion excision: First 100 cases performed in a single irish tertiary referral centre. *The Surgeon*, 2021. ISSN 1479-666X.

[126] Leslie R Lamb, Manisha Bahl, and Constance D Lehman. Evaluation of a nonradioactive magnetic marker wireless localization program. *American Journal of Roentgenology*, 211(4):W202–W202, 2018. ISSN 0361-803X.

[127] James R Harvey, Yit Lim, John Murphy, Miles Howe, Julie Morris, Amit Goyal, and Anthony J Maxwell. Safety and feasibility of breast lesion localization using magnetic seeds (magseed): a multicentre, open-label cohort study. *Breast cancer research and treatment*, 169(3):531–536, 2018. ISSN 0167-6806.

[128] Bas Pouw, Marie-Jeanne TFD Vrancken Peeters, and Renato A Valdés Olmos. *Radioguided Surgery of Non-palpable Breast Lesions: Radio Occult Lesion Localization (ROLL)*, pages 139–148. Springer, 2016.

[129] M. S. Sajid, U. Parampalli, Z. Haider, and R. Bonomi. Comparison of radioguided occult lesion localization (roll) and wire localization for non-palpable breast cancers: a meta-analysis. *J Surg Oncol*, 105(8):852–8, 2012. ISSN 1096-9098 (Electronic) 0022-4790 (Linking). doi: 10.1002/jso.23016. URL https://www.ncbi.nlm.nih.gov/pubmed/22213057.

[130] D. Carrera, L. Martin, M. de la Flor, F. Guspi, J. Picas, V. Izquierdo, S. Martinez, C. Jorda, R. Siurana, M. Martinez-Casals, J. M. Jaen, A. Pujol, and A. Benitez. Use of the roll technique for lumpectomy in non-palpable breast lesions. *Revista Espanola De Medicina Nuclear E Imagen Molecular*, 36(5):285–291, 2017. ISSN 2253-654X. doi: 10.1016/j.remn.2017.02.004. URL ⟨GotoISI⟩://WOS:000411045800003.

[131] F. Aydogan, M. Velidedeoglu, F. Kilic, and H. Yilmaz. Radio-guided localization of clinically occult breast lesions: current modalities and future directions. *Expert Review of Medical Devices*, 11 (1):53–63, 2014. ISSN 1743-4440. doi: 10.1586/17434440.2014.864233. URL ⟨GotoISI⟩://WOS: 000338293200008.

[132] Masahiro Sakakibara, Takeshi Nagashima, Takafumi Sangai, Rikiya Nakamura, Hiroshi Fujimoto, Manabu Arai, Toshiki Kazama, Hideyuki Hashimoto, Yukio Nakatani, and Masaru Miyazaki. Breast-conserving surgery using projection and reproduction techniques of surgical-position breast mri in patients with ductal carcinoma in situ of the breast. *Journal of the American College of Surgeons*, 207(1):62–68, 2008. ISSN 1072-7515. doi: https://doi.org/10.1016/j.jamcollsurg.2007.12.034. URL http://www.sciencedirect.com/science/article/pii/S1072751508000124.

[133] Rikiya Nakamura, Takeshi Nagashima, Masahiro Sakakibara, Takafumi Sangai, Hiroshi Fujimoto, Manabu Arai, Takashi Shida, Katsuhiko Kaneoya, Takuya Ueda, and Yukio Nakatani. Breast-conserving surgery using supine magnetic resonance imaging in breast cancer patients receiving neoadjuvant chemotherapy. *The Breast*, 17(3):245–251, 2008. ISSN 0960-9776.

[134] Zhen-Yu Wu, Hee Jeong Kim, Jongwon Lee, Il Yong Chung, Jisun Kim, Saebyeol Lee, Byung Ho Son, Sei-Hyun Ahn, Hak Hee Kim, and Joon Beom Seo. Breast-conserving surgery with 3d-printed surgical guide: a single-center, prospective clinical study. *Scientific Reports*, 11(1):1–8, 2021. ISSN 2045-2322.

[135] Richard J Barth, Venkataramanan Krishnaswamy, Keith D Paulsen, Timothy B Rooney, Wendy A Wells, Elizabeth Rizzo, Christina V Angeles, Jonathan D Marotti, Rebecca A Zuurbier, and Candice C Black. A patient-specific 3d-printed form accurately transfers supine mri-derived tumor localization information to guide breast-conserving surgery. *Annals of surgical oncology*, 24(10):2950–2956, 2017. ISSN 1534-4681.

[136] Beom Seok Ko, Namkug Kim, Jong Won Lee, Hee Jeong Kim, Il-Young Chung, Jisun Kim, Sae Byul Lee, Byung Ho Son, Hak Hee Kim, and Joon Beom Seo. Mri-based 3d-printed surgical guides for breast cancer patients who received neoadjuvant chemotherapy. *Scientific Reports*, 9(1):1–6, 2019. ISSN 2045-2322.

[137] Pedro F Gouveia, Joana Costa, Pedro Morgado, Ronald Kates, David Pinto, Carlos Mavioso, João Anacleto, Marta Martinho, Daniel Simões Lopes, and Arlindo R Ferreira. Breast cancer surgery with augmented reality. *The Breast*, 56:14–17, 2021. ISSN 0960-9776.

[138] Stephanie L Perkins, Michael A Lin, Subashini Srinivasan, Amanda J Wheeler, Brian A Hargreaves, and Bruce L Daniel. Perceptual accuracy of a mixed-reality system for mr-guided breast surgical planning in the operating room. In *Proceedings of the 26th Annual Meeting of the ISMRM, Paris, France*, page 607, 2018.

[139] Stephanie L Perkins, Michael A Lin, Subashini Srinivasan, Amanda J Wheeler, Brian A Hargreaves, and Bruce L Daniel. A mixed-reality system for breast surgical planning. In *2017 IEEE International Symposium on Mixed and Augmented Reality (ISMAR-Adjunct)*, pages 269–274. IEEE, 2017. ISBN 0769563279.

[140] 2021. URL https://elucentmedical.com/.

[141] Victoria L Mango, Ralph T Wynn, Sheldon Feldman, Lauren Friedlander, Elise Desperito, Sejal N Patel, Ameer Gomberawalla, and Richard Ha. Beyond wires and seeds: reflector-guided breast lesion localization and excision. *Radiology*, 284(2):365–371, 2017. ISSN 0033-8419.

[142] Danielle Sharek, Margarita L Zuley, Janie Yue Zhang, Atilla Soran, Gretchen M Ahrendt, and Marie A Ganott. Radioactive seed localization versus wire localization for lumpectomies: a comparison of outcomes. *American Journal of Roentgenology*, 204(4):872–877, 2015. ISSN 0361-803X.

[143] FA Ross, S Elgammal, J Reid, S Henderson, J Kelly, R Flinn, G Miller, H Sarafilovic, and SM Tovey. Magseed localisation of non-palpable breast lesions: experience from a single centre. *Clinical Radiology*, 2022. ISSN 0009-9260.

[144] Alexandra J Webster, Bridget N Kelly, Caroline McGugin, Suzanne B Coopey, Barbara L Smith, Michele A Gadd, and Michelle C Specht. Comparison of wireless localization alternatives to wire localization for non-palpable breast lesions. *Journal of the American College of Surgeons*, page 10.1097, 2022. ISSN 1879-1190.

[145] Y. M. Zhang, J. Seely, E. Cordeiro, J. Hefler, K. Thavorn, M. Mahajan, S. Domina, J. Aro, A. M. Ibrahim, A. Arnaout, D. Gravel, and C. Nessim. Radioactive seed localization versus wire-guided localization for nonpalpable breast cancer: A cost and operating room efficiency analysis. *Annals of Surgical Oncology*, 24(12):3567–3573, 2017. ISSN 1068-9265. doi: 10.1245/s10434-017-6084-z. URL ⟨GotoISI⟩://WOS:000413946700017.

[146] E. L. Postma, H. Koffijberg, H. M. Verkooijen, A. J. Witkamp, Maaj van den Bosch, and R. van Hillegersberg. Cost-effectiveness of radioguided occult lesion localization (roll) versus wire-guided localization (wgl) in breast conserving surgery for nonpalpable breast cancer: Results from a randomized controlled multicenter trial. *Annals of Surgical Oncology*, 20(7):2219–2226, 2013. ISSN 1068-9265. doi: 10.1245/s10434-013-2888-7. URL ⟨GotoISI⟩://WOS:000320040700019.

[147] J. S. L. Ong, J. Teh, C. Saunders, A. G. Bourke, C. Lizama, J. Newton, M. Phillips, and D. B. Taylor. Patient satisfaction with radioguided occult lesion localisation using iodine-125 seeds ('rollis') versus conventional hookwire localisation. *Ejso*, 43(12):2261–2269, 2017. ISSN 0748-7983. doi: 10.1016/j.ejso.2017.09.021. URL ⟨GotoISI⟩://WOS:000418982000004.

[148] Afsaneh Alikhassi, Farzanefar Saeed, Mehrshad Abbasi, Ramesh Omranipour, Habibollah Mahmoodzadeh, Massoome Najafi, Masoumeh Gity, and Ali Kheradmand. Applicability of radioguided occult lesion localization for non-palpable benign breast lesions, comparison with wire localization, a clinical trial. *Asian Pacific Journal of Cancer Prevention*, 17(7):3185–3190, 2016.

[149] Ray C Mayo III, Megan J Kalambo, and Jay R Parikh. Preoperative localization of breast lesions: current techniques. *Clinical imaging*, 56:1–8, 2019. ISSN 0899-7071.

[150] Rachel F Brem, Jeffrey W Hoffmeister, Gilat Zisman, Martin P DeSimio, and Steven K Rogers. A computer-aided detection system for the evaluation of breast cancer by mammographic appearance and lesion size. *American Journal of Roentgenology*, 184(3):893–896, 2005. ISSN 0361-803X.

[151] Susanne Wienbeck, Johannes Uhlig, Uwe Fischer, Martin Hellriegel, Eva von Fintel, Dietrich Kulenkampff, Alexey Surov, Joachim Lotz, and Christina Perske. Breast lesion size assessment in mastectomy specimens. *Medicine*, 98(37), 2019.

[152] L Li, R Roth, P Germaine, S Ren, M Lee, K Hunter, E Tinney, and L Liao. Contrast-enhanced spectral mammography (cesm) versus breast magnetic resonance imaging (mri): a retrospective comparison in 66 breast lesions. *Diagnostic and interventional imaging*, 98(2):113–123, 2017. ISSN 2211-5684.

[153] EM Fallenberg, C Dromain, F Diekmann, F Engelken, M Krohn, JM Singh, B Ingold-Heppner, KJ Winzer, U Bick, Renz, and DM. Contrast-enhanced spectral mammography versus mri: initial results in the detection of breast cancer and assessment of tumour size. *European radiology*, 24(1):256–264, 2014. ISSN 0938-7994.

[154] Han Song Mun, HH Kim, HJ Shin, JH Cha, PL Ruppel, HY Oh, and EY Chae. Assessment of extent of breast cancer: comparison between digital breast tomosynthesis and full-field digital mammography. *Clinical radiology*, 68(12):1254–1259, 2013. ISSN 0009-9260.

[155] Laura Liberman, Gary Mason, Elizabeth A Morris, and D David Dershaw. Does size matter? positive predictive value of mri-detected breast lesions as a function of lesion size. *American Journal of Roentgenology*, 186(2):426–430, 2006. ISSN 0361-803X.

[156] Tomas Cortadellas, Paula Argacha, Juan Acosta, Jordi Rabasa, Ricardo Peiró, Margarita Gomez, Laura Rodellar, Sandra Gomez, Alejandra Navarro-Golobart, and Sonia Sanchez-Mendez. Estimation of tumor size in breast cancer comparing clinical examination, mammography, ultrasound and mri—correlation with the pathological analysis of the surgical specimen. *Gland surgery*, 6(4):330, 2017.

[157] Björn Eiben, Lianghao Han, J Hipwell, Thomy Mertzanidou, Sven Kabus, Thomas Bülow, Cristian Lorenz, GM Newstead, Hiroyuki Abe, and Mohammed Keshtgar. Biomechanically guided prone-to-supine image registration of breast mri using an estimated reference state. In *Biomedical Imaging (ISBI), 2013 IEEE 10th International Symposium on*, pages 214–217. IEEE, 2013. ISBN 146736455X.

[158] T. P. B. Gamage, R. Boyes, V. Rajagopal, P. M. F. Nielsen, and M. P. Nash. Modelling prone to supine breast deformation under gravity loading using heterogeneous finite element models. *Computational Biomechanics for Medicine: Deformation and Flow*, pages 29–38, 2012. doi: 10.1007/978-1-4614-3172-5_5. URL ⟨GotoISI⟩://WOS:000392537800005.

[159] Lianghao Han, John Hipwell, Thomy Mertzanidou, Tim Carter, Marc Modat, Sebastien Ourselin, and David Hawkes. A hybrid fem-based method for aligning prone and supine images for image guided breast surgery. In *Biomedical Imaging: From Nano to Macro, 2011 IEEE International Symposium on*, pages 1239–1242. IEEE, 2011. ISBN 1424441277.

[160] L. Han, J. H. Hipwell, C. Tanner, Z. Taylor, T. Mertzanidou, J. Cardoso, S. Ourselin, and D. J. Hawkes. Development of patient-specific biomechanical models for predicting large breast deformation. *Phys Med Biol*, 57(2):455–72, 2012. ISSN 1361-6560 (Electronic) 0031-9155 (Linking). doi: 10.1088/0031-9155/57/2/455. URL https://www.ncbi.nlm.nih.gov/pubmed/22173131.

[161] Lianghao Han, John H Hipwell, Björn Eiben, Dean Barratt, Marc Modat, Sebastien Ourselin, and David J Hawkes. A nonlinear biomechanical model based registration method for aligning prone and supine mr breast images. *IEEE transactions on medical imaging*, 33(3):682–694, 2013. ISSN 0278-0062.

[162] T. Hopp, M. Dietzel, P. A. Baltzer, P. Kreisel, W. A. Kaiser, H. Gemmeke, and N. V. Ruiter. Automatic multimodal 2d/3d breast image registration using biomechanical fem models and intensity-based optimization. *Med Image Anal*, 17(2):209–18, 2013. ISSN 1361-8423 (Electronic) 1361-8415 (Linking). doi: 10.1016/j.media.2012.10.003. URL https://www.ncbi.nlm.nih.gov/pubmed/23265802.

[163] T. Mertzanidou, J. Hipwell, S. Johnsen, L. H. Han, B. Eiben, Z. Taylor, S. Ourselin, H. Huisman, R. Mann, U. Bick, N. Karssemeijer, and D. Hawkes. Mri to x-ray mammography intensity-based registration with simultaneous optimisation of pose and biomechanical transformation parameters. *Medical Image Analysis*, 18(4):674–683, 2014. ISSN 1361-8415. doi: 10.1016/j.media.2014.03.003. URL ⟨GotoISI⟩://WOS:000336478000004.

[164] A. Samani, J. Zubovits, and D. Plewes. Elastic moduli of normal and pathological human breast tissues: an inversion-technique-based investigation of 169 samples. *Phys Med Biol*, 52(6):1565–76, 2007. ISSN 0031-9155 (Print) 0031-9155 (Linking). doi: 10.1088/0031-9155/52/6/002. URL https://www.ncbi.nlm.nih.gov/pubmed/17327649.

[165] Fred S Azar, Dimitris N Metaxas, and Mitchell D Schnall. A finite element model of the breast for predicting mechanical deformations during biopsy procedures. In *Mathematical Methods in Biomedical Image Analysis, 2000. Proceedings. IEEE Workshop on*, pages 38–45. IEEE, 2000. ISBN 0769507379.

[166] Rebekah H Conley Griesenauer. *Development of an Image Guidance System for Breast Cancer Surgery*. Thesis, Vanderbilt University, 2017.

[167] N. V. Ruiter, R. Stotzka, T. O. Muller, H. Gemmeke, J. R. Reichenbach, and W. A. Kaiser. Model-based registration of x-ray mammograms and mr images of the female breast. *Ieee Transactions on Nuclear Science*, 53(1):204–211, 2006. ISSN 0018-9499. doi: 10.1109/tns.2005.862983. URL ⟨GotoISI⟩://WOS:000236473800033.

[168] J. Georgii, T. Paetz, M. Harz, C. Stoecker, M. Rothgang, J. Colletta, K. Schilling, M. Schlooz-Vries, R. M. Mann, and H. K. Hahn. Simulation and visualization to support breast surgery planning. *Breast Imaging, Iwdm 2016*, 9699:257–264, 2016. ISSN 0302-9743. doi: 10.1007/978-3-319-41546-8_33. URL ⟨GotoISI⟩://WOS:000386324200033.

[169] Timothy J Carter, Christine Tanner, William R Crum, Nicolas Beechey-Newman, and David J Hawkes. A framework for image-guided breast surgery. In *International Workshop on Medical Imaging and Virtual Reality*, pages 203–210. Springer, 2006.

[170] Timothy Carter, Christine Tanner, Nicolas Beechey-Newman, Dean Barratt, and David Hawkes. Mr navigated breast surgery: method and initial clinical experience. In *International Conference on Medical Image Computing and Computer-Assisted Intervention*, pages 356–363. Springer, 2008.

[171] M. Ebrahimi, P. Siegler, A. Modhafar, C. M. Holloway, D. B. Plewes, and A. L. Martel. Using surface markers for mri guided breast conserving surgery: a feasibility survey. *Phys Med Biol*, 59(7):1589–605, 2014. ISSN 1361-6560 (Electronic) 0031-9155 (Linking). doi: 10.1088/0031-9155/59/7/1589. URL https://www.ncbi.nlm.nih.gov/pubmed/24614540.

[172] Northern Digital Inc. Passive spheres, 2021. URL https://www.ndigital.com/products/passive-marker-spheres/. Accessed: March 9, 2022.

[173] Northern Digital Inc. Radix lenses, 2021. URL https://www.ndigital.com/products/radix-lens/. Accessed: March 9, 2022.

[174] Northern Digital Inc. Polaris vicra, 2021. URL https://www.ndigital.com/products/polaris-vicra/. Accessed: March 9, 2022.

[175] Angela Sorriento, Maria Bianca Porfido, Stefano Mazzoleni, Giuseppe Calvosa, Miria Tenucci, Gastone Ciuti, and Paolo Dario. Optical and electromagnetic tracking systems for biomedical applications: A critical review on potentialities and limitations. *IEEE reviews in biomedical engineering*, 13:212–232, 2019. ISSN 1937-3333.

[176] Northern Digital Inc. Polaris vega® st, 2021. URL https://www.ndigital.com/products/polaris-vega/polaris-vega-st/. Accessed: March 9, 2022.

[177] ClaronNav Inc. Microntracker specifications, 2022. URL https://www.claronav.com/microntracker/microntracker-specifications/. Accessed: March 22, 2022.

[178] Lena Maier-Hein, Alfred Franz, H-P Meinzer, and Ivo Wolf. Comparative assessment of optical tracking systems for soft tissue navigation with fiducial needles. In *Medical Imaging 2008: Visualization, Image-Guided Procedures, and Modeling*, volume 6918, pages 664–672. SPIE, 2008.

[179] Northern Digital Inc. Electromagnetic tracking, 2021. URL https://www.ndigital.com/technology/em-overview/. Accessed: March 9, 2022.

[180] Konstantin Christoph Koban, Philipp Perko, Lucas Etzel, Zhouxiao Li, Thilo Ludwig Schenck, and Riccardo Enzo Giunta. Validation of two handheld devices against a non-portable three-dimensional surface scanner and assessment of potential use for intraoperative facial imaging. *Journal of Plastic, Reconstructive & Aesthetic Surgery*, 73(1):141–148, 2020. ISSN 1748-6815.

[181] Amber L Simpson, Jessica Burgner, Courtenay L Glisson, S Duke Herrell, Burton Ma, Thomas S Pheiffer, Robert J Webster III, and Michael I Miga. Comparison study of intraoperative surface acquisition methods for surgical navigation. *IEEE Transactions on Biomedical Engineering*, 60(4):1090–1099, 2012. ISSN 0018-9294.

[182] Thomas S Pheiffer, Amber L Simpson, Brian Lennon, Reid C Thompson, and Michael I Miga. Design and evaluation of an optically-tracked single-ccd laser range scanner. *Medical physics*, 39(2):636–642, 2012.

[183] Sergio Garrido-Jurado, Rafael Muñoz-Salinas, Francisco José Madrid-Cuevas, and Manuel Jesús Marín-Jiménez. Automatic generation and detection of highly reliable fiducial markers under occlusion. *Pattern Recognition*, 47(6):2280–2292, 2014.

[184] Sergio Garrido-Jurado, Rafael Muñoz-Salinas, Francisco José Madrid-Cuevas, and Rafael Medina-Carnicer. Generation of fiducial marker dictionaries using mixed integer linear programming. *Pattern recognition*, 51:481–491, 2016.

[185] Francisco J Romero-Ramirez, Rafael Muñoz-Salinas, and Rafael Medina-Carnicer. Speeded up detection of squared fiducial markers. *Image and vision Computing*, 76:38–47, 2018.

[186] G. Bradski. The OpenCV Library. *Dr. Dobb's Journal of Software Tools*, 2000.

[187] Michail Kalaitzakis, Brennan Cain, Sabrina Carroll, Anand Ambrosi, Camden Whitehead, and Nikolaos Vitzilaios. Fiducial markers for pose estimation. *Journal of Intelligent & Robotic Systems*, 101 (4):71, 2021. ISSN 1573-0409. doi: 10.1007/s10846-020-01307-9. URL https://doi.org/10.1007/s10846-020-01307-9.

[188] Guoxing Yu, Yongtao Hu, and Jingwen Dai. Topotag: A robust and scalable topological fiducial marker system. *IEEE transactions on visualization and computer graphics*, 27(9):3769–3780, 2020. ISSN 1077-2626.

[189] Mustafa B Yaldiz, Andreas Meuleman, Hyeonjoong Jang, Hyunho Ha, and Min H Kim. Deepformabletag: end-to-end generation and recognition of deformable fiducial markers. *ACM Transactions on Graphics (TOG)*, 40(4):1–14, 2021. ISSN 0730-0301.

[190] Pengju Jin, Pyry Matikainen, and Siddhartha S Srinivasa. Sensor fusion for fiducial tags: Highly robust pose estimation from single frame rgbd. In *2017 IEEE/RSJ International Conference on Intelligent Robots and Systems (IROS)*, pages 5770–5776. IEEE, 2017. ISBN 1538626829.

[191] Yixian Su, Yu Sun, Mohamed Hosny, Wenpeng Gao, and Yili Fu. Facial landmark-guided surface matching for image-to-patient registration with an rgb-d camera. *The International Journal of Medical Robotics and Computer Assisted Surgery*, page e2373, 2022. ISSN 1478-5951.

[192] Lance B Gatrell, William A Hoff, and Cheryl W Sklair. Robust image features: Concentric contrasting circles and their image extraction. In *Cooperative Intelligent Robotics in Space II*, volume 1612, pages 235–244. International Society for Optics and Photonics, 1992.

[193] Youngkwan Cho, Jongweon Lee, and Ulrich Neumann. A multi-ring color fiducial system and an intensity-invariant detection method for scalable fiducial-tracking augmented reality. In *In IWAR*. Citeseer, 1998.

[194] Vladimir A Knyaz. The development of new coded targets for automated point identification and non-contact 3d surface measurements. *IAPRS*, 5:80–85, 1998.

[195] Leonid Naimark and Eric Foxlin. Circular data matrix fiducial system and robust image processing for a wearable vision-inertial self-tracker. In *Proceedings. International Symposium on Mixed and Augmented Reality*, pages 27–36. IEEE, 2002.

[196] Junaed Sattar, Eric Bourque, Philippe Giguere, and Gregory Dudek. Fourier tags: Smoothly degradable fiducial markers for use in human-robot interaction. In *Fourth Canadian Conference on Computer and Robot Vision (CRV'07)*, pages 165–174. IEEE, 2007.

[197] Anqi Xu and Gregory Dudek. Fourier tag: A smoothly degradable fiducial marker system with configurable payload capacity. In *2011 Canadian Conference on Computer and Robot Vision*, pages 40–47. IEEE, 2011.

[198] Filippo Bergamasco, Andrea Albarelli, Emanuele Rodola, and Andrea Torsello. Rune-tag: A high accuracy fiducial marker with strong occlusion resilience. In *CVPR 2011*, pages 113–120. IEEE, 2011.

[199] Filippo Bergamasco, Andrea Albarelli, Luca Cosmo, Emanuele Rodola, and Andrea Torsello. An accurate and robust artificial marker based on cyclic codes. *IEEE transactions on pattern analysis and machine intelligence*, 38(12):2359–2373, 2016.

[200] Lilian Calvet, Pierre Gurdjos, and Vincent Charvillat. Camera tracking using concentric circle markers: Paradigms and algorithms. In *2012 19th IEEE International Conference on Image Processing*, pages 1361–1364. IEEE, 2012.

[201] Lilian Calvet, Pierre Gurdjos, Carsten Griwodz, and Simone Gasparini. Detection and accurate localization of circular fiducials under highly challenging conditions. In *Proceedings of the IEEE Conference on Computer Vision and Pattern Recognition*, pages 562–570, 2016.

[202] Filippo Bergamasco, Andrea Albarelli, and Andrea Torsello. Pi-tag: a fast image-space marker design based on projective invariants. *Machine vision and applications*, 24(6):1295–1310, 2013.

[203] Meghshyam G Prasad, Sharat Chandran, and Michael S Brown. A motion blur resilient fiducial for quadcopter imaging. In *2015 IEEE Winter Conference on Applications of Computer Vision*, pages 254–261. IEEE, 2015.

[204] Jun Rekimoto. Matrix: A realtime object identification and registration method for augmented reality. In *Proceedings. 3rd Asia Pacific Computer Human Interaction (Cat. No. 98EX110)*, pages 63–68. IEEE, 1998.

[205] Hirokazu Kato and Mark Billinghurst. Marker tracking and hmd calibration for a video-based augmented reality conferencing system. In *Proceedings 2nd IEEE and ACM International Workshop on Augmented Reality (IWAR'99)*, pages 85–94. IEEE, 1999.

[206] Jun Rekimoto and Yuji Ayatsuka. Cybercode: designing augmented reality environments with visual tags. In *Proceedings of DARE 2000 on Designing augmented reality environments*, pages 1–10, 2000.

[207] Michael Rohs and Beat Gfeller. *Using camera-equipped mobile phones for interacting with real-world objects*. na, 2004.

[208] Daniel Wagner and Dieter Schmalstieg. Artoolkitplus for pose tracking on mobile devices. In *Proceedings of 12th Computer Vision Winter Workshop*, pages 139–146. Citeseer, 2007.

[209] Daniel Flohr and Jan Fischer. A lightweight id-based extension for marker tracking systems. In *Short Paper Proceedings of the Eurographics Symposium on Virtual Environments*, page 59–64. The Eurographics Association, 2007.

[210] Keisuke Tateno, Itaru Kitahara, and Yuichi Ohta. A nested marker for augmented reality. In *2007 IEEE Virtual Reality Conference*, pages 259–262. IEEE, 2007.

[211] Florian Schweiger, Bernhard Zeisl, Pierre Fite Georgel, Georg Schroth, Eckehard G Steinbach, and Nassir Navab. Maximum detector response markers for sift and surf. In *VMV*, volume 10, pages 145–154. Citeseer, 2009.

[212] Mark Fiala. Artag, a fiducial marker system using digital techniques. In *2005 IEEE Computer Society Conference on Computer Vision and Pattern Recognition (CVPR'05)*, volume 2, pages 590–596. IEEE, 2005.

[213] Edwin Olson. Apriltag: A robust and flexible visual fiducial system. In *2011 IEEE international conference on robotics and automation*, pages 3400–3407. IEEE, 2011.

[214] John Wang and Edwin Olson. Apriltag 2: Efficient and robust fiducial detection. In *2016 IEEE/RSJ International Conference on Intelligent Robots and Systems (IROS)*, pages 4193–4198. IEEE, 2016.

[215] Joseph DeGol, Timothy Bretl, and Derek Hoiem. Chromatag: A colored marker and fast detection algorithm. In *Proceedings of the IEEE International Conference on Computer Vision*, pages 1472–1481, 2017.

[216] Enrico Costanza, Simon B Shelley, and John Robinson. D-touch: A consumer-grade tangible interface module and musical applications. In *Proceedings of Conference on Human-Computer Interaction*. Citeseer, 2003.

[217] Enrico Costanza and John Robinson. A region adjacency tree approach to the detection and design of fiducials. *Vision Video and Graphics*, pages 63–70, 2003.

[218] Ross Bencina and Martin Kaltenbrunner. The design and evolution of fiducials for the reactivision system. In *Proceedings of the Third International Conference on Generative Systems in the Electronic Arts*, volume 2. Monash University Publishing Melbourne, VIC, Australia, 2005.

[219] Ross Bencina, Martin Kaltenbrunner, and Sergi Jorda. Improved topological fiducial tracking in the reactivision system. In *2005 IEEE Computer Society Conference on Computer Vision and Pattern Recognition (CVPR'05)-Workshops*, pages 99–99. IEEE, 2005.

[220] Martin Kaltenbrunner and Ross Bencina. reactivision: a computer-vision framework for table-based tangible interaction. In *Proceedings of the 1st international conference on Tangible and embedded interaction*, pages 69–74, 2007.

[221] Clemens Nylandsted Klokmose, Janus Bager Kristensen, Rolf Bagge, and Kim Halskov. Bullseye: high-precision fiducial tracking for table-based tangible interaction. In *Proceedings of the Ninth ACM international conference on interactive tabletops and surfaces*, pages 269–278, 2014.

[222] K Somani Arun, Thomas S Huang, and Steven D Blostein. Least-squares fitting of two 3-d point sets. *IEEE Transactions on pattern analysis and machine intelligence*, PAMI-9(5):698–700, 1987. ISSN 0162-8828. doi: 10.1109/TPAMI.1987.4767965.

[223] J Michael Fitzpatrick, Jay B West, and Calvin R Maurer. Predicting error in rigid-body point-based registration. *IEEE Transactions on Medical Imaging*, 17(5):694–702, 1998. ISSN 0278-0062.

[224] Andriy Fedorov, Reinhard Beichel, Jayashree Kalpathy-Cramer, Julien Finet, Jean-Christophe Fillion-Robin, Sonia Pujol, Christian Bauer, Dominique Jennings, Fiona Fennessy, and Milan Sonka. 3d slicer as an image computing platform for the quantitative imaging network. *Magnetic resonance imaging*, 30(9):1323–1341, 2012. ISSN 0730-725X.

[225] Xiaochen Yang, Logan W Clements, Rebekah H Conley, Reid C Thompson, Benoit M Dawant, and Michael I Miga. A novel craniotomy simulation system for evaluation of stereo-pair reconstruction fidelity and tracking. In *Medical Imaging 2016: Image-Guided Procedures, Robotic Interventions, and Modeling*, volume 9786, page 978612. International Society for Optics and Photonics, 2016.

[226] Zhengyou Zhang. A flexible new technique for camera calibration. *IEEE Transactions on pattern analysis and machine intelligence*, 22(11):1330–1334, 2000. ISSN 0162-8828.

[227] Richard Hartley and Andrew Zisserman. *Multiple view geometry in computer vision*. Cambridge university press, 2003.

[228] 2019. URL https://www.mathworks.com/products/computer-vision.html.

[229] Thomas Kuiran Chen, Adrian D Thurston, Randy E Ellis, and Purang Abolmaesumi. A real-time freehand ultrasound calibration system with automatic accuracy feedback and control. *Ultrasound in medicine & biology*, 35(1):79–93, 2009. ISSN 0301-5629.

[230] J Michael Fitzpatrick, Derek LG Hill, and Calvin R Maurer Jr. Image registration. *Handbook of Medical Imaging*, 2:447–513, 2000.

[231] Andras Lasso, Tamas Heffter, Adam Rankin, Csaba Pinter, Tamas Ungi, and Gabor Fichtinger. Plus: open-source toolkit for ultrasound-guided intervention systems. *IEEE transactions on biomedical engineering*, 61(10):2527–2537, 2014. ISSN 0018-9294.

[232] Stuart S Antman, DE Carlson, G Fichera, ME Gurtin, and PM Naghdi. *Mechanics of Solids: Volume II: Linear Theories of Elasticity and Thermoelasticity, Linear and Nonlinear Theories of Rods, Plates, and Shells*, volume 2. Springer, 1972. ISBN 3540055355.

[233] John M Sullivan Jr, Geoffrey Charron, and Keith D Paulsen. A three-dimensional mesh generator for arbitrary multiple material domains. *Finite Elements in Analysis and Design*, 25(3-4):219–241, 1997. ISSN 0168-874X.

[234] Daniel R Lynch. *Numerical partial differential equations for environmental scientists and engineers: a first practical course*. Springer Science & Business Media, 2004. ISBN 0387236198.

[235] Rowena E Ong, Jao J Ou, and Michael I Miga. Non-rigid registration of breast surfaces using the laplace and diffusion equations. *Biomedical engineering online*, 9(1):8, 2010. ISSN 1475-925X.

[236] Thomas S Pheiffer and Michael I Miga. Toward a generic real-time compression correction framework for tracked ultrasound. *International journal of computer assisted radiology and surgery*, 10(11): 1777–1792, 2015. ISSN 1861-6429.

[237] Mr scanning – questions and answers in mri, 2021. URL https://mriquestions.com/what-are-the-steps.html. Accessed: April 1, 2022.

[238] Winona L Richey, Jon S Heiselman, Ma Luo, Ingrid M Meszoely, and Michael I Miga. Impact of deformation on a supine-positioned image guided breast surgery approach. *International Journal of Computer Assisted Radiology and Surgery*, 16(11):2055—2066, 2021. ISSN 1861-6429.

[239] Matthew J Pallone, Steven P Poplack, Richard J Barth Jr, and Keith D Paulsen. Combining supine mri and 3d optical scanning for improved surgical planning of breast conserving surgeries. In *Medical Imaging 2012: Image-Guided Procedures, Robotic Interventions, and Modeling*, volume 8316, page 83163B. International Society for Optics and Photonics, 2012.

[240] Rebekah H Conley, Ingrid M Meszoely, Thomas S Pheiffer, Jared A Weis, Thomas E Yankeelov, and Michael I Miga. Image to physical space registration of supine breast mri for image guided breast surgery. In *Medical Imaging 2014: Image-Guided Procedures, Robotic Interventions, and Modeling*, volume 9036, page 90362N. International Society for Optics and Photonics, 2014.

[241] Winona L Richey, Jon Heiselman, Ma Luo, Ingrid M Meszoely, and Michael I Miga. Textual fiducial detection in breast conserving surgery for a near-real time image guidance system. In *Medical Imaging 2020: Image-Guided Procedures, Robotic Interventions, and Modeling*, volume 11315, page 113151L. International Society for Optics and Photonics, 2020.

[242] Jon S Heiselman and Michael I Miga. The image-to-physical liver registration sparse data challenge: characterizing inverse biomechanical model resolution. In *Medical Imaging 2020: Image-Guided Procedures, Robotic Interventions, and Modeling*, volume 11315, page 113151F. International Society for Optics and Photonics, 2020.

[243] 2020. URL https://www.ndigital.com/products/polaris-vicra/.

[244] Siwa Chan, Jeon-Hor Chen, Shunshan Li, Rita Chang, Darh-Cherng Yeh, Ruey-Feng Chang, Lee-Ren Yeh, Jessica Kwong, and Min-Ying Su. Evaluation of the association between quantitative mammographic density and breast cancer occurred in different quadrants. *BMC cancer*, 17(1):274, 2017. ISSN 1471-2407.

[245] Philippa D Darbre. Recorded quadrant incidence of female breast cancer in great britain suggests a disproportionate increase in the upper outer quadrant of the breast. *Anticancer Research*, 25(3C): 2543–2550, 2005. ISSN 0250-7005.

[246] Andrew HS Lee. Why is carcinoma of the breast more frequent in the upper outer quadrant? a case series based on needle core biopsy diagnoses. *The Breast*, 14(2):151–152, 2005. ISSN 0960-9776.

[247] Carol E DeSantis, Jiemin Ma, Mia M Gaudet, Lisa A Newman, Kimberly D Miller, Ann Goding Sauer, Ahmedin Jemal, and Rebecca L Siegel. Breast cancer statistics, 2019. *CA: A Cancer Journal for Clinicians*, 69(6):438–451, 2019. ISSN 0007-9235.

[248] Victoria Mango, Richard Ha, Ameer Gomberawalla, Ralph Wynn, and Sheldon Feldman. Evaluation of the savi scout surgical guidance system for localization and excision of nonpalpable breast lesions: a feasibility study. *American Journal of Roentgenology*, 207(4):W69–W72, 2016. ISSN 0361-803X.

[249] Paul A Yushkevich, Joseph Piven, Heather Cody Hazlett, Rachel Gimpel Smith, Sean Ho, James C Gee, and Guido Gerig. User-guided 3d active contour segmentation of anatomical structures: significantly improved efficiency and reliability. *Neuroimage*, 31(3):1116–1128, 2006. ISSN 1053-8119.

[250] Utkarsh Ayachit. *The paraview guide: a parallel visualization application*. Kitware, Inc., 2015. ISBN 1930934300.

[251] Thomas S Pheiffer, Reid C Thompson, Daniel C Rucker, Amber L Simpson, and Michael I Miga. Model-based correction of tissue compression for tracked ultrasound in soft tissue image-guided surgery. *Ultrasound in Medicine and Biology*, 40(4):788–803, 2014. ISSN 0301-5629.

[252] Natasja Janssen, Roeland Eppenga, Marie-Jeanne Vrancken Peeters, Frederieke van Duijnhoven, Hester Oldenburg, Jos van der Hage, Emiel Rutgers, Jan-Jakob Sonke, Koert Kuhlmann, and Theo Ruers. Real-time wireless tumor tracking during breast conserving surgery. *International journal of computer assisted radiology and surgery*, 13(4):531–539, 2018. ISSN 1861-6429.

[253] Alfred M Franz, Tamas Haidegger, Wolfgang Birkfellner, Kevin Cleary, Terry M Peters, and Lena Maier-Hein. Electromagnetic tracking in medicine—a review of technology, validation, and applications. *IEEE transactions on medical imaging*, 33(8):1702–1725, 2014. ISSN 0278-0062.

[254] Z Hussain, N Roberts, GH Whitehouse, M Garcia-Finana, and D Percy. Estimation of breast volume and its variation during the menstrual cycle using mri and stereology. *The British journal of radiology*, 72(855):236–245, 1999. ISSN 0007-1285.

[255] D Milligan, JO Drife, and RV Short. Changes in breast volume during normal menstrual cycle and after oral contraceptives. *Br Med J*, 4(5995):494–496, 1975. ISSN 0007-1447.

[256] Reza Ghiasvand, Hans-Olov Adami, Iraj Harirchi, Rahim Akrami, and Kazem Zendehdel. Higher incidence of premenopausal breast cancer in less developed countries; myth or truth? *BMC cancer*, 14 (1):1–8, 2014. ISSN 1471-2407.

[257] Jon S Heiselman. *Mechanics-based estimation of intraoperative soft tissue deformation for enhancing navigation during image-guided liver intervention*. Thesis, Vanderbilt University, 2020.

[258] Ishita Chen, Rowena E Ong, Amber L Simpson, Kay Sun, Reid C Thompson, and Michael I Miga. Integrating retraction modeling into an atlas-based framework for brain shift prediction. *IEEE Transactions on Biomedical Engineering*, 60(12):3494–3504, 2013. ISSN 0018-9294.

[259] Winona L Richey, Jon S Heiselman, Morgan J Ringel, Ingrid M Meszoely, and Michael I Miga. Tumor deformation correction for an image guidance system in breast conserving surgery. In *Medical Imaging 2022: Image-Guided Procedures, Robotic Interventions, and Modeling*, volume 12034, page 120340K. International Society for Optics and Photonics, 2022. doi: 10.1117/12.2611570.

[260] Olga Kantor, Catherine Pesce, Katherine Kopkash, Ermilo Barrera, David J Winchester, Kristine Kuchta, and Katharine Yao. Impact of the society of surgical oncology-american society for radiation oncology margin guidelines on breast-conserving surgery and mastectomy trends. *Journal of the American College of Surgeons*, 229(1):104–114, 2019. ISSN 1072-7515.

[261] M-P Dubuisson and Anil K Jain. A modified hausdorff distance for object matching. In *Proceedings of 12th international conference on pattern recognition*, volume 1, pages 566–568. IEEE, 1994. ISBN 0818662654.

[262] Zdenek Kalal, Krystian Mikolajczyk, and Jiri Matas. Tracking-learning-detection. *IEEE transactions on pattern analysis and machine intelligence*, 34(7):1409–1422, 2012. ISSN 0162-8828.

[263] P. F. Alcantarilla, Pablo Alcantarilla, Jesus Nuevo, and Adrien Bartoli. Fast explicit diffusion for accelerated features in nonlinear scale spaces. In *Proceedings of the British Machine Vision Conference 2013*, British Machine Vision Conference 2013. British Machine Vision Association, 2013. ISBN 1-901725-49-9.

[264] Winona L Richey, Ma Luo, Sarah E Goodale, Logan W Clements, Ingrid M Meszoely, and Michael I Miga. A system for automatic monitoring of surgical instruments and dynamic, non-rigid surface deformations in breast cancer surgery. In *Medical Imaging 2018: Image-Guided Procedures, Robotic Interventions, and Modeling*, volume 10576, page 105761H. International Society for Optics and Photonics, 2018.

[265] R. L. Siegel, K. D. Miller, and A. Jemal. Cancer statistics, 2016. *CA Cancer J Clin*, 66(1):7–30, 2016. ISSN 0007-9235. doi: 10.3322/caac.21332.

[266] Heriberto Medina-Franco, Leonardo Abarca-Pérez, Miriam N García-Alvarez, José L Ulloa-Gómez, Cecilia Romero-Trejo, and Jesús Sepúlveda-Méndez. Radioguided occult lesion localization (roll) versus wire-guided lumpectomy for non-palpable breast lesions: A randomized prospective evaluation. *Journal of surgical oncology*, 97(2):108–111, 2008. ISSN 0022-4790.

[267] S Eva Singletary. Surgical margins in patients with early-stage breast cancer treated with breast conservation therapy. *The American journal of surgery*, 184(5):383–393, 2002. ISSN 0002-9610.

[268] Joop A van Dongen, Adri C Voogd, Ian S Fentiman, Catherine Legrand, Richard J Sylvester, David Tong, Emmanuel van der Schueren, Peter A Helle, Kobus van Zijl, and Harry Bartelink. Long-term results of a randomized trial comparing breast-conserving therapy with mastectomy: European organization for research and treatment of cancer 10801 trial. *Journal of the National Cancer Institute*, 92 (14):1143–1150, 2000. ISSN 1460-2105.

[269] Umberto Veronesi, Natale Cascinelli, Luigi Mariani, Marco Greco, Roberto Saccozzi, Alberto Luini, Marisel Aguilar, and Ettore Marubini. Twenty-year follow-up of a randomized study comparing breast-conserving surgery with radical mastectomy for early breast cancer. *New England Journal of Medicine*, 347(16):1227–1232, 2002. ISSN 0028-4793.

[270] Mary F Dillon, Arnold DK Hill, Cecily M Quinn, Enda W McDermott, and Niall O'Higgins. A pathologic assessment of adequate margin status in breast-conserving therapy. *Annals of surgical oncology*, 13(3):333–339, 2006. ISSN 1534-4681.

[271] Gary Freedman, Barbara Fowble, Alexandra Hanlon, Nicos Nicolaou, Douglas Fein, John Hoffman, Elin Sigurdson, Marcia Boraas, and Lori Goldstein. Patients with early stage invasive cancer with close or positive margins treated with conservative surgery and radiation have an increased risk of breast recurrence that is delayed by adjuvant systemic therapy. *International Journal of Radiation Oncology* Biology* Physics*, 44(5):1005–1015, 1999. ISSN 0360-3016.

[272] Emil D Kurniawan, Matthew H Wong, Imogen Windle, Allison Rose, Arlene Mou, Malcolm Buchanan, John P Collins, Julie A Miller, Russell L Gruen, and G Bruce Mann. Predictors of surgical margin status in breast-conserving surgery within a breast screening program. *Annals of Surgical Oncology*, 15(9):2542–2549, 2008. ISSN 1534-4681.

[273] Catherine C Park, Michihide Mitsumori, Asa Nixon, Abram Recht, James Connolly, Rebecca Gelman, Barbara Silver, Stella Hetelekidis, Anthony Abner, and Jay R Harris. Outcome at 8 years after breast-conserving surgery and radiation therapy for invasive breast cancer: influence of margin status and systemic therapy on local recurrence. *Journal of Clinical Oncology*, 18(8):1668–1675, 2000. ISSN 0732-183X.

[274] DE Schiller, LW Le, BCJ Cho, BJ Youngson, and DR McCready. Factors associated with negative margins of lumpectomy specimen: potential use in selecting patients for intraoperative radiotherapy. *Annals of surgical oncology*, 15(3):833–842, 2008. ISSN 1534-4681.

[275] Melanie C Smitt and Kate Horst. Association of clinical and pathologic variables with lumpectomy surgical margin status after preoperative diagnosis or excisional biopsy of invasive breast cancer. *Annals of Surgical Oncology*, 14(3):1040–1044, 2007. ISSN 1534-4681.

[276] Christiane K Kuhl, Simone Schrading, Claudia C Leutner, Nuschin Morakkabati-Spitz, Eva Wardelmann, Rolf Fimmers, Walther Kuhn, and Hans H Schild. Mammography, breast ultrasound, and magnetic resonance imaging for surveillance of women at high familial risk for breast cancer. *Journal of clinical oncology*, 23(33):8469–8476, 2005. ISSN 0732-183X.

[277] Nancy A Lee, Henry Rusinek, Jeffrey Weinreb, Ramesh Chandra, Hildegard Toth, Cory Singer, and Gillian Newstead. Fatty and fibroglandular tissue volumes in the breasts of women 20-83 years old: comparison of x-ray mammography and computer-assisted mr imaging. *AJR. American journal of roentgenology*, 168(2):501–506, 1997. ISSN 0361-803X.

[278] Jörn Lorenzen, Ralph Sinkus, Maike Biesterfeldt, and Gerhard Adam. Menstrual-cycle dependence of breast parenchyma elasticity: estimation with magnetic resonance elastography of breast tissue during the menstrual cycle. *Investigative radiology*, 38(4):236–240, 2003. ISSN 0020-9996.

[279] Rebecca L Siegel, Kimberly D Miller, and Ahmedin Jemal. Cancer statistics, 2019. *CA: a cancer journal for clinicians*, 69(1):7–34, 2019. ISSN 0007-9235.

[280] Freddie Bray, Jacques Ferlay, Isabelle Soerjomataram, Rebecca L Siegel, Lindsey A Torre, and Ahmedin Jemal. Global cancer statistics 2018: Globocan estimates of incidence and mortality worldwide for 36 cancers in 185 countries. *CA: a cancer journal for clinicians*, 68(6):394–424, 2018. ISSN 0007-9235.

[281] Arindam Chaudhuri, Krupa Mandaviya, Pratixa Badelia, and Soumya K. Ghosh. *Optical Character Recognition Systems for Latin Language*, pages 165–191. Springer International Publishing, Cham, 2017. ISBN 978-3-319-50252-6. doi: 10.1007/978-3-319-50252-6_7. URL https://doi.org/10.1007/978-3-319-50252-6_7.

[282] Li Chen, Song Wang, Wei Fan, Jun Sun, and Satoshi Naoi. Beyond human recognition: A cnn-based framework for handwritten character recognition. In *2015 3rd IAPR Asian Conference on Pattern Recognition (ACPR)*, pages 695–699. IEEE, 2014. ISBN 1479961000.

[283] François Chadebecq, Francisco Vasconcelos, Evangelos Mazomenos, and Danail Stoyanov. Computer vision in the surgical operating room. *Visceral Medicine*, 36(6):456–462, 2020. ISSN 2297-4725.

[284] Marco Solbiati, Katia M Passera, Alessandro Rotilio, Francesco Oliva, Ilaria Marre, S Nahum Goldberg, Tiziana Ierace, and Luigi Solbiati. Augmented reality for interventional oncology: proof-of-concept study of a novel high-end guidance system platform. *European radiology experimental*, 2(1): 1–9, 2018. ISSN 2509-9280.

[285] Pablo Fernández Alcantarilla, Adrien Bartoli, and Andrew J Davison. Kaze features. In *European conference on computer vision*, pages 214–227. Springer, 2012.

[286] B Ramkumar, Rob Laber, Hristo Bojinov, and Ravi Sadananda Hegde. Gpu acceleration of the kaze image feature extraction algorithm. *Journal of Real-Time Image Processing*, 17(5):1169–1182, 2020. ISSN 1861-8219.

[287] Jon S Heiselman and Michael I Miga. Strain energy decay predicts elastic registration accuracy from intraoperative data constraints. *IEEE Transactions on Medical Imaging*, 40(4):1290–1302, 2021. ISSN 0278-0062.

[288] William R Heiselman, Jon S Jarnagin and Michael I Miga. Registration uncertainty in deforming organs: a novel approach for ensuring navigational confidence during image-guided procedures. In *Medical Imaging 2022: Image-Guided Procedures, Robotic Interventions, and Modeling*, volume 12034, page 120340Z. International Society for Optics and Photonics, 2022. doi: 10.1117/12.2612938.

[289] Ma Luo, Paul S Larson, Alastair J Martin, and Michael I Miga. Accounting for deformation in deep brain stimulation surgery with models: comparison to interventional magnetic resonance imaging. *IEEE Transactions on Biomedical Engineering*, 67(10):2934–2944, 2020. ISSN 0018-9294.

[290] Sarah Frisken, Ma Luo, Parikshit Juvekar, Adomas Bunevicius, Ines Machado, Prashin Unadkat, Melina M Bertotti, Matt Toews, William M Wells, Michael I Miga, et al. A comparison of thin-plate spline deformation and finite element modeling to compensate for brain shift during tumor resection. *International journal of computer assisted radiology and surgery*, 15(1):75–85, 2020.

[291] Brian B Avants, Nick Tustison, Gang Song, et al. Advanced normalization tools (ants). *Insight j*, 2 (365):1–35, 2009.

[292] Morgan J Ringel, Winona L Richey, Jon S Heiselman, Ma Luo, Ingrid M Meszoely, and Michael I Miga. Breast image registration for surgery: insights on material mechanics modeling. In *Medical Imaging 2022: Image-Guided Procedures, Robotic Interventions, and Modeling*, volume 12034, page 1203411. International Society for Optics and Photonics, 2022. doi: 10.1117/12.2611787.

[293] Jarrod A Collins, Jared A Weis, Jon S Heiselman, Logan W Clements, Amber L Simpson, William R Jarnagin, and Michael I Miga. Improving registration robustness for image-guided liver surgery in a novel human-to-phantom data framework. *IEEE transactions on medical imaging*, 36(7):1502–1510, 2017.

[294] Yan Zhao, Yuwei Zhai, Eric Dubois, and Shigang Wang. Image matching algorithm based on sift using color and exposure information. *Journal of systems engineering and electronics*, 27(3):691–699, 2016. ISSN 1004–4132.

[295] Ethan Rublee, Vincent Rabaud, Kurt Konolige, and Gary Bradski. Orb: An efficient alternative to sift or surf. In *2011 International conference on computer vision*, pages 2564–2571. Ieee, 2011. ISBN 1457711028.

[296] David G Lowe. Object recognition from local scale-invariant features. In *Proceedings of the seventh IEEE international conference on computer vision*, volume 2, pages 1150–1157. Ieee, 1999.

[297] Herbert Bay, Andreas Ess, Tinne Tuytelaars, and Luc Van Gool. Speeded-up robust features (surf). *Computer vision and image understanding*, 110(3):346–359, 2008.

[298] Patrick J Grother. Nist special database 19 - handprinted forms and characters database. *National Institute of Standards and Technology*, 1995.

[299] Jonathan J. Hull. A database for handwritten text recognition research. *IEEE Transactions on pattern analysis and machine intelligence*, 16(5):550–554, 1994.

[300] Chienchung Chang and Shankar Chatterjee. Quantization error analysis in stereo vision. In *Conference Record of the Twenty-Sixth Asilomar Conference on Signals, Systems & Computers*, pages 1037–1038. IEEE Computer Society, 1992.